

ИЗВЕСТИЯ ВЫСШИХ УЧЕБНЫХ ЗАВЕДЕНИЙ ЧЕРНАЯ МЕТАЛЛУРГИЯ

IZVESTIYA. FERROUS METALLURGY

fermet.misis.ru

2024 Том 67 № 4
Vol. No.

МЕТАЛЛУРГИЧЕСКИЕ ТЕХНОЛОГИИ

Термодинамическое моделирование восстановления кобальта и никеля при использовании концентратов гидрометаллургического обогащения для легирования стали

МАТЕРИАЛОВЕДЕНИЕ

Комплексная электронно-ионно-плазменная модификация поверхности нержавеющей высоколегированной стали

Физика упрочнения поверхности катания головки рельсов из заэвтектидной стали после эксплуатации

ФИЗИКО-ХИМИЧЕСКИЕ ОСНОВЫ МЕТАЛЛУРГИЧЕСКИХ ПРОЦЕССОВ

Термодинамические аспекты восстановления оксида вольфрама WO_3 углеродом, кремнием, алюминием и титаном

ИЗВЕСТИЯ ВЫСШИХ УЧЕБНЫХ ЗАВЕДЕНИЙ ЧЕРНАЯ МЕТАЛЛУРГИЯ

Научно-технический журнал

Издается с января 1958 г. Выпускается 6 раз в год

2024 Том 67 № 4
Vol. No.

IZVESTIYA FERROUS METALLURGY

Scientific and Technical Journal

Published since January 1958. Issued 6 times a year

IZVESTIYA FERROUS METALLURGY

www.fermet.misis.ru

ISSN 0368-0797 (Print) ISSN 2410-2091 (Online)

Alternative title:

Izvestiya vuzov. Chernaya metallurgiya

Founders:



Editor-in-Chief:

Leopol'd I. Leont'ev, Academician, Adviser of the Russian Academy of Sciences; Dr. Sci. (Eng.), Prof., NUST "MISIS"; Chief Researcher, Institute of Metallurgy UB RAS, Moscow
4 Leninskii Ave., Moscow 119049, Russian Federation
National University of Science and Technology "MISIS"

Deputy Editor-in-Chief:

Evgenii V. Protopopov, Dr. Sci. (Eng.), Prof., Siberian State Industrial University, Novokuznetsk

Publisher:

National University of Science and Technology "MISIS"

Editorial Office Address:

in Moscow

4 Leninskii Ave., Moscow 119049, Russian Federation
National University of Science and Technology "MISIS"
Tel.: +7 (495) 638-44-11
E-mail: fermet.misis@mail.ru, ferrous@sis.ru

in Novokuznetsk

42 Kirova Str., Novokuznetsk, Kemerovo Region – Kuzbass
654007, Russian Federation
Siberian State Industrial University
Tel.: +7 (3843) 74-86-28 E-mail: redjizvz@sibsiu.ru

Editorial Board:

Sailaubai O. Baisanov, Dr. Sci. (Eng.), Prof., Abishev Chemical-Metallurgical Institute, Karaganda, Republic of Kazakhstan
Vladimir D. Belov, Dr. Sci. (Eng.), Prof., NUST MISIS, Moscow
Anatolii A. Brodov, Cand. Sci. (Econ.), Bardin Central Research Institute for Ferrous Metallurgy, Moscow
Il'ya V. Chumanov, Dr. Sci. (Eng.), Prof., South Ural State Research University, Chelyabinsk
Andrei N. Dmitriev, Dr. Sci. (Eng.), Prof., Academician, RANS, A.M. Prokhorov Academy of Engineering Sciences, Institute of Metallurgy, Ural Branch of RAS, Ural Federal University, Yekaterinburg
Aleksei V. Dub, Dr. Sci. (Eng.), Prof., JSC "Science and Innovations", Moscow
Mikhail R. Filonov, Dr. Sci. (Eng.), Prof., NUST MISIS, Moscow
Sergei M. Gorbatyuk, Dr. Sci. (Eng.), Prof., NUST MISIS, Moscow
Konstantin V. Grigorovich, Academician of RAS, Dr. Sci. (Eng.), Baikov Institute of Metallurgy and Materials Science of RAS, Moscow
Victor E. Gromov, Dr. Sci. (Eng.), Prof., Siberian State Industrial University, Novokuznetsk
Aleksei G. Kolmakov, Dr. Sci. (Eng.), Corresponding Member of RAS, Baikov Institute of Metallurgy and Materials Science of RAS, Moscow
Valerii M. Kolokol'tsev, Dr. Sci. (Eng.), Prof., Magnitogorsk State Technical University, Magnitogorsk
Mariya V. Kostina, Dr. Sci. (Eng.), Baikov Institute of Metallurgy and Materials Science of RAS, Moscow
Konstantin L. Kosyrev, Dr. Sci. (Eng.), Academician of RANS, Electrosteel Heavy Engineering Works JSC, Moscow
Yuliya A. Kurganova, Dr. Sci. (Eng.), Prof., Bauman Moscow State Technical University, Moscow
Linn Horst, Linn High Therm GmbH, Hirschbach, Germany
Vladimir I. Lysak, Academician of RAS, Dr. Sci. (Eng.), Prof., Rector, Volgograd State Technical University, Volgograd
Valerii P. Meshalkin, Dr. Sci. (Eng.), Academician of RAS, Prof., D.I. Mendeleyev Russian Chemical-Technological University, Moscow
Radik R. Mulyukov, Dr. Sci. (Phys.-Chem.), Prof., Corresponding Member of RAS, Institute of Metals Superplasticity Problems of RAS, Ufa

Sergei A. Nikulin, Dr. Sci. (Eng.), Prof., Corresponding Member of RANS, NUST MISIS, Moscow
Asylbek Kh. Nurumgaliev, Dr. Sci. (Eng.), Prof., Karaganda State Industrial University, Karaganda, Republic of Kazakhstan
Oleg I. Ostrovski, Dr. Sci. (Eng.), Prof., University of New South Wales, Sydney, Australia
Loris Pietrelli, Dr., Scientist, Italian National Agency for New Technologies, Energy and Sustainable Economic Development, Rome, Italy
Igor' Yu. Pyshmintsev, Dr. Sci. (Eng.), Russian Research Institute of the Pipe Industry, Chelyabinsk
Andrei I. Rudskoi, Academician of RAS, Dr. Sci. (Eng.), Prof., Rector, Peter the Great Saint-Petersburg Polytechnic University, Saint-Petersburg
Oleg Yu. Sheshukov, Dr. Sci. (Eng.), Prof., Ural Federal University, Yekaterinburg
Laura M. Simonyan, Dr. Sci. (Eng.), Prof., NUST MISIS, Moscow
Robert F. Singer, Dr. Sci. (Eng.), Prof., Friedrich-Alexander University, Germany
Boris A. Sivak, Cand. Sci. (Eng.), Prof., VNIIMETMASH Holding Company, Moscow
Leonid A. Smirnov, Dr. Sci. (Eng.), Prof., Academician of RAS, OJSC "Ural Institute of Metals", Yekaterinburg
Sergei V. Solodov, Cand. Sci. (Eng.), NUST MISIS, Moscow
Marcus Speidel, Dr. Natur. Sci., Prof., Swiss Academy of Materials, Switzerland
Nikolai A. Spirin, Dr. Sci. (Eng.), Prof., Ural Federal University, Yekaterinburg
Guoi Tang, Institute of Advanced Materials of Tsinghua University, Shenzhen, China
Mikhail V. Temlyantsev, Dr. Sci. (Eng.), Prof., Siberian State Industrial University, Novokuznetsk
Ekaterina P. Volynkina, Dr. Sci. (Eng.), Advisor, ALE "Kuzbass Association of Waste Processors", Novokuznetsk
Aleksei B. Yur'ev, Dr. Sci. (Eng.), Rector, Siberian State Industrial University, Novokuznetsk
Vladimir S. Yusupov, Dr. Sci. (Eng.), Prof., Baikov Institute of Metallurgy and Materials Science of RAS, Moscow
Vladimir I. Zhuchkov, Dr. Sci. (Eng.), Prof., Institute of Metallurgy, Ural Branch of RAS, Ural Federal University, Yekaterinburg
Michael Zinigrad, Dr. Sci. (Physical Chemistry), Prof., Rector, Ariel University, Israel
Vladimir I. Zolotukhin, Dr. Sci. (Eng.), Prof., Tula State University, Tula

In accordance with paragraph 5 of the Rules for the formation of the Higher Attestation Commission list journal "Izvestiya. Ferrous metallurgy" is included in the list of leading peer-reviewed scientific journals, publication in which is taken into account in the defense of candidate and doctoral dissertations, as indexed in international data bases.

Indexed: Scopus, Russian Science Citation Index (RSCI), Research Bible, Chemical Abstracts, OCLC and Google Scholar
Registered in Federal Service for Supervision in the Sphere of Mass Communications **PI number FS77-35456.**



Articles are available under Creative Commons Attribution 4.0 License.

ИЗВЕСТИЯ ВЫСШИХ УЧЕБНЫХ ЗАВЕДЕНИЙ ЧЕРНАЯ МЕТАЛЛУРГИЯ

www.fermet.misis.ru

ISSN 0368-0797 (Print) ISSN 2410-2091 (Online)

Варианты названия:

Известия вузов. Черная металлургия

Izvestiya. Ferrous Metallurgy

Учредители:



Редакционная коллегия:

С. О. Байсанов, д.т.н., профессор, ХМИ им. Ж.Абишева, г. Караганда, Республика Казахстан

В. Д. Белов, д.т.н., профессор, НИТУ МИСИС, г. Москва

А. А. Бродов, к.экон.н., ФГУП «ЦНИИчермет им. И.П. Бардина», г. Москва

Е. П. Волынкина, д.т.н., советник, ОЮЛ «Кузбасская Ассоциация переработчиков отходов», г. Новокузнецк

С. М. Горбатько, д.т.н., профессор, НИТУ МИСИС, г. Москва

К. В. Григорович, академик РАН, д.т.н., ИМЕТ им. А.А. Байкова РАН, г. Москва

В. Е. Громов, д.ф.-м.н., профессор, СибГИУ, г. Новокузнецк

А. Н. Дмитриев, д.т.н., профессор, академик РАЕН, академик АИН РФ, г. Екатеринбург

А. В. Дуб, д.т.н., профессор, ЗАО «Наука и инновации», г. Москва

В. И. Жучков, д.т.н., профессор, ИМЕТ УрО РАН, г. Екатеринбург

Р. Ф. Зингер, д.т.н., профессор, Институт Фридриха-Александра, Германия

М. Зиниград, д.т.н., профессор, Институт Ариэля, Израиль

В. И. Золотухин, д.т.н., профессор, ТулГУ, г. Тула

А. Г. Колмаков, д.т.н., чл.-корр. РАН, ИМЕТ им. А.А. Байкова РАН, г. Москва

В. М. Колокольцев, д.т.н., профессор, МГТУ им. Г.И. Носова, г. Магнитогорск

М. В. Костина, д.т.н., ИМЕТ им. А.А. Байкова РАН, г. Москва

К. Л. Косырев, д.т.н., академик РАЕН, ОАО «Электростальский завод тяжелого машиностроения», г. Москва

Ю. А. Курганова, д.т.н., профессор, МГТУ им. Н.Э. Баумана, г. Москва

Х. Линн, ООО «Линн Хай Терм», Германия

В. И. Лысак, академик РАН, д.т.н., профессор, ВолгГТУ, г. Волгоград

В. П. Мешалкин, академик РАН, д.т.н., профессор, РХТУ им. Д.И. Менделеева, г. Москва

В соответствии п. 5 Правил формирования перечня ВАК журнал «Известия вузов. Черная металлургия» входит в перечень ведущих рецензируемых научных журналов и изданий, публикация в которых учитывается при защитах кандидатских и докторских диссертаций как индексируемый в МБД.

Главный редактор:

Леопольд Игоревич Леонтьев, академик РАН, советник, Президиум РАН; д.т.н., профессор, НИТУ «МИСИС»; главный научный сотрудник, Институт металлургии УрО РАН
Россия, 119049, Москва, Ленинский просп., д. 4, стр. 1, Национальный исследовательский технологический университет «МИСИС»

Заместитель главного редактора:

Евгений Валентинович Протопопов, д.т.н., профессор, Сибирский государственный индустриальный университет г. Новокузнецк

Издатель:

Национальный исследовательский технологический университет «МИСИС»

Адреса подразделений редакции:

в Москве

Россия, 119049, Москва, Ленинский просп., д. 4, стр. 1
Национальный исследовательский технологический университет «МИСИС»

Тел.: +7 (495) 638-44-11 E-mail: ferrous@sisis.ru

в Новокузнецке

Россия, 654007, Новокузнецк,
Кемеровская обл. – Кузбасс, ул. Кирова, зд. 42
Сибирский государственный индустриальный университет
Тел.: +7 (3843) 74-86-28 E-mail: redjizvz@sibsiu.ru

Р. Р. Мулюков, д.ф.м.-н., профессор, чл.-корр. ФГБУН ИПСМ РАН, г. Уфа
С. А. Никулин, д.т.н., профессор, чл.-корр. РАЕН, НИТУ МИСИС, г. Москва
А. Х. Нурумгалиев, д.т.н., профессор, КГИУ, г. Караганда, Республика Казахстан
О. И. Островский, д.т.н., профессор, Университет Нового Южного Уэльса, Сидней, Австралия
Л. Пиетрелли, д.т.н., Итальянское национальное агентство по новым технологиям, энергетике и устойчивому экономическому развитию, Рим, Италия
И. Ю. Пышминцев, д.т.н., РосНИТИ, г. Челябинск
А. И. Рудской, академик РАН, д.т.н., профессор, СПбПУ Петра Великого, г. Санкт-Петербург
Б. А. Сивак, к.т.н., профессор, АО АХК «ВНИИМЕТМАШ», г. Москва
Л. М. Симонян, д.т.н., профессор, НИТУ МИСИС, г. Москва
Л. А. Смирнов, академик РАН, д.т.н., профессор, ОАО «Уральский институт металлов», г. Екатеринбург
С. В. Солодов, к.т.н., НИТУ МИСИС, г. Москва
Н. А. Спирин, д.т.н., профессор, УрФУ, г. Екатеринбург
Г. Танг, Институт перспективных материалов университета Циньхуа, г. Шеньжень, Китай
М. В. Темлянецев, д.т.н., профессор, СибГИУ, г. Новокузнецк
М. Р. Филонов, д.т.н., профессор, НИТУ МИСИС, г. Москва
И. В. Чуманов, д.т.н., профессор, ЮУрГУ, г. Челябинск
О. Ю. Шешуков, д.т.н., профессор УрФУ, г. Екатеринбург
М. О. Шпайдель, д.ест.н., профессор, Швейцарская академия материаловедения, Швейцария
А. Б. Юрьев, д.т.н., ректор, СибГИУ, г. Новокузнецк
В. С. Юсупов, д.т.н., профессор, ИМЕТ им. А.А. Байкова РАН, г. Москва

Индексирование: Scopus, Russian Science Citation Index (RSCI), Research Bible, Chemical Abstracts, OCLC и Google Scholar

Зарегистрирован Федеральной службой по надзору в сфере связи и массовых коммуникаций ПИ № ФС77-35456.



Статьи доступны под лицензией Creative Commons Attribution 4.0 License.

CONTENTS

СОДЕРЖАНИЕ

METALLURGICAL TECHNOLOGIES

- Rybenko I.A., Nokhrina O.I., Rozhikhina I.D., Golodova M.A. Thermodynamic modeling of cobalt and nickel reduction using hydrometallurgical enrichment concentrates for steel alloying 384

MATERIALS SCIENCE

- Ivanov Yu.F., Petrikova E.A., Teresov A.D., Lopatin I.V., Tolkachev O.S. Complex electron-ion-plasma surface modification of high-alloy stainless steel 391
- Efimov M.O., Panchenko I.A., Shlyarova Yu.A. Gradient of microhardness in the contact zone coating (HEA CoCrFeNiMn) – substrate (alloy 5083) 398
- Astafurov S.V., Mel'nikov E.V., Astafurova E.G., Kolubaev E.A. Phase composition and microstructure of intermetallic alloys obtained using electron-beam additive manufacturing 401
- Galkin A.A., Kabaldin Yu.G., Mordovina Yu.S., Anosov M.S. Low-cycle fatigue of welded joint from steel of X70 strength class 409
- Pustovoyt V.N., Dolgachev Yu.V., Egorov M.S., Vernigorov Yu.M. Influence of inhomogeneities in chemical composition and porosity of sintered steel on development of martensitic transformation 417
- Popova N.A., Gromov V.E., Yur'ev A.B., Martusevich E.A., Porfir'ev M.A. Physics of hardening of the rolling surface of rail head from hypereutectoid steel after operation 424
- Shlyakhova G.V., Danilov V.I. Effect of electric arc surfacing on the structure and properties of coatings 433
- Zorya I.V., Poletaev G.M., Bebikhov Yu.V., Semenov A.S. Molecular dynamics study of the influence of carbon impurity on austenite nanoparticles crystallization during rapid cooling 440

PHYSICO-CHEMICAL BASICS
OF METALLURGICAL PROCESSES

- Bashchenko L.P., Bendre Yu.V., Kozyrev N.A., Mikhno A.R., Shurupov V.M., Zhukov A.V. Thermodynamic aspects of WO_3 tungsten oxide reduction by carbon, silicon, aluminum and titanium 449

МЕТАЛЛУРГИЧЕСКИЕ ТЕХНОЛОГИИ

- Рыбенко И.А., Нохрина О.И., Рожихина И.Д., Голодова М.А. Термодинамическое моделирование восстановления кобальта и никеля при использовании концентратов гидрометаллургического обогащения для легирования стали 384

МАТЕРИАЛОВЕДЕНИЕ

- Иванов Ю.Ф., Петрикова Е.А., Тересов А.Д., Лопатин И.В., Толкачев О.С. Комплексная электронно-ионно-плазменная модификация поверхности нержавеющей высоколегированной стали 391
- Ефимов М.О., Панченко И.А., Шлярова Ю.А. Градиент микротвердости в зоне контакта покрытия (ВЭС CoCrFeNiMn) – подложка (сплав 5083) 398
- Астафуров С.В., Мельников Е.В., Астафурова Е.Г., Колубаев Е.А. Фазовый состав и микроструктура интерметаллических сплавов, полученных методом проволочного электронно-лучевого аддитивного производства 401
- Галкин А.А., Кабалдин Ю.Г., Мордовина Ю.С., Аносов М.С. Исследование малоциклового усталости зон сварного соединения стали класса прочности X70 409
- Пустовойт В.Н., Долгачев Ю.В., Егоров М.С., Вернигорov Ю.М. Влияние неоднородностей химического состава и пористости спеченной стали на развитие мартенситного превращения 417
- Попова Н.А., Громов В.Е., Юрьев А.Б., Мартусевич Е.А., Порфирьев М.А. Физика упрочнения поверхности катания головки рельсов из заэвтектоидной стали после эксплуатации 424
- Шляхова Г.В., Данилов В.И. Исследование влияния электродуговой наплавки на структуру и свойства покрытий 433
- Зоря И.В., Полетаев Г.М., Бебихов Ю.В., Семенов А.С. Молекулярно-динамическое исследование влияния примеси углерода на процесс кристаллизации наночастиц аустенита при быстром охлаждении 440

ФИЗИКО-ХИМИЧЕСКИЕ ОСНОВЫ
МЕТАЛЛУРГИЧЕСКИХ ПРОЦЕССОВ

- Башенко Л.П., Бендре Ю.В., Козырев Н.А., Михно А.Р., Шурупов В.М., Жуков А.В. Термодинамические аспекты восстановления оксида вольфрама WO_3 углеродом, кремнием, алюминием и титаном 449

CONTENTS (Continuation)

СОДЕРЖАНИЕ (продолжение)

INNOVATIONS IN METALLURGICAL
INDUSTRIAL AND LABORATORY
EQUIPMENT, TECHNOLOGIES
AND MATERIALS

ИННОВАЦИИ В МЕТАЛЛУРГИЧЕСКОМ
ПРОМЫШЛЕННОМ И ЛАБОРАТОРНОМ
ОБОРУДОВАНИИ, ТЕХНОЛОГИЯХ
И МАТЕРИАЛАХ

Lekhov O.S., Mikhalev A.V., Nepryakhin S.O. Stress state of billet – mandrel system during production of hollow steel billet in a unit of continuous casting and deformation. Part 2 ... 457

Odinokov V.I., Evstigneev A.I., Dmitriev E.A., Namokov A.N., Evstigneeva A.A., Chernyshova D.V. Stress-strain state of ceramic shell mold during formation of spherical steel casting in it. Part 2 463

Morozov A.O., Komolova O.A., Em A.Yu., Zhemkov A.A., Grigorovich K.V., Yakubenko E.V., Cherkashina T.I., Dagman A.I. Development of a methodology for determining the content of non-metallic inclusions in steel 471

Лехов О.С., Михалев А.В., Непряхин С.О. Напряженное состояние системы заготовка – оправка при получении стальной поллой заготовки на установке непрерывного литья и деформации. Часть 2 457

Одинокров В.И., Евстигнеев А.И., Дмитриев Э.А., Намоконов А.Н., Евстигнеева А.А., Чернышова Д.В. Напряженно-деформированное состояние керамической оболочковой формы при формировании в ней стальной шарообразной отливки. Часть 2 463

Морозов А.О., Комолова О.А., Ем А.Ю., Жемков А.А., Григорович К.В., Якубенко Е.В., Черкашина Т.И., Дагман А.И. Разработка методики определения содержания неметаллических включений в стали 471

INFORMATION TECHNOLOGIES
AND AUTOMATIC CONTROL
IN FERROUS METALLURGY

ИНФОРМАЦИОННЫЕ ТЕХНОЛОГИИ
И АВТОМАТИЗАЦИЯ
В ЧЕРНОЙ МЕТАЛЛУРГИИ

Sivtsov A.V., Sheshukov O.Yu., Egiazar'yan D.K., Tsybalist M.M., Orlov P.P. Automated process control in electric arc furnaces in the aspect of digital twin technology 481

Сивцов А.В., Шешуков О.Ю., Егизарьян Д.К., Цымбалист М.М., Орлов П.П. Проблемы автоматизированного управления технологическим процессом в дуговых сталеплавильных печах в аспекте применения технологии цифровых двойников 481



UDC 669.168

DOI 10.17073/0368-0797-2024-4-384-390



Original article

Оригинальная статья

THERMODYNAMIC MODELING OF COBALT AND NICKEL REDUCTION USING HYDROMETALLURGICAL ENRICHMENT CONCENTRATES FOR STEEL ALLOYING

I. A. Rybenko , O. I. Nokhrina, I. D. Rozhikhina, M. A. Golodova

Siberian State Industrial University (42 Kirova Str., Novokuznetsk, Kemerovo Region – Kuzbass 654007, Russian Federation)

rybenkoi@mail.ru

Abstract. The article provides studies on reduction processes in model thermodynamic systems and processes of nickel reduction from nickel concentrate and cobalt and nickel from cobalt-nickel concentrate. Concentrates are obtained during hydrometallurgical enrichment of polymetallic manganese-containing ores of the Kemerovo region – Kuzbass. By thermodynamic modeling using TERRA software complex, it was determined that nickel can be completely reduced from oxide in the NiO–C system at a carbon consumption of 0.08 kg/kg NiO, and at a carbon consumption of 0.15 kg/kg NiO – in the NiO–Fe₂O₃–C system. It was found that cobalt reduction in the CoO–C system begins at a temperature of about 513 K at any carbon consumption. With a further increase in temperature, the reduction process depends only on consumption of the reducing agent. From the obtained thermodynamic modeling data, it follows that cobalt reduction from the cobalt-nickel concentrate begins at a temperature of about 513 K and subsequently depends slightly on temperature. The extraction of cobalt increases with the amount of reducing agent at temperatures up to 553 K, then remains constant up to 1473 K temperature. Nickel reduction takes place at a temperature above 473 K. The degree of nickel reduction slightly depends on the temperature and amount of reducing agent at consumption of the latter over 0.02 kg/kg of concentrate. Laboratory studies showed that during the melting period, nickel can be reduced from its oxide almost completely with solid carbon, since nickel has less sensitivity to oxygen than iron. Theoretical and experimental studies of steel direct alloying showed that it is advisable to use a solid phase process in reduction of nickel and cobalt. Nickel concentrate and cobalt-nickel concentrate during steel smelting in an electric furnace is advisable to be introduced into charge in the form of mixtures pelletized with a carbonaceous reducing agent.

Keywords: thermodynamic modeling, model system, nickel concentrate, cobalt-nickel concentrate

Acknowledgements: The research was supported by the Russian Foundation for Basic Research and the Subject of the Russian Federation (Kemerovo region – Kuzbass) in the framework of the scientific project No. 20-48-420001/22.

For citation: Rybenko I.A., Nokhrina O.I., Rozhikhina I.D., Golodova M.A. Thermodynamic modeling of cobalt and nickel reduction using hydrometallurgical enrichment concentrates for steel alloying. *Izvestiya. Ferrous Metallurgy*. 2024;67(4):384–390.

<https://doi.org/10.17073/0368-0797-2024-4-384-390>

ТЕРМОДИНАМИЧЕСКОЕ МОДЕЛИРОВАНИЕ ВОССТАНОВЛЕНИЯ КОБАЛЬТА И НИКЕЛЯ ПРИ ИСПОЛЬЗОВАНИИ КОНЦЕНТРАТОВ ГИДРОМЕТАЛЛУРГИЧЕСКОГО ОБОГАЩЕНИЯ ДЛЯ ЛЕГИРОВАНИЯ СТАЛИ

И. А. Рыбенко , О. И. Нохрина, И. Д. Рожихина, М. А. Голодова

Сибирский государственный индустриальный университет (Россия, 654007, Кемеровская обл. – Кузбасс, Новокузнецк, ул. Кирова, 42)

rybenkoi@mail.ru

Аннотация. В статье приведены исследования восстановительных процессов в модельных термодинамических системах и процессов восстановления никеля из никелевого концентрата и кобальта и никеля из кобальт-никелевого концентрата. Концентраты получены при гидрометаллургическом обогащении полиметаллических марганецсодержащих руд Кемеровской обл. – Кузбасса. Методом термодинамического моделирования с использованием программного комплекса Терра определено, что никель из оксида можно полностью восстановить в системе NiO–C при расходе углерода 0,08 кг/кг NiO и при расходе углерода 0,15 кг/кг NiO в системе NiO–Fe₂O₃–C. Восстановление кобальта в системе CoO–C начинается при температуре около 513 К при любых расходах углерода. С дальнейшим ростом температуры процесс восстановления зависит только от расхода восстановителя. Из полученных данных термодинамического моделирования следует, что восстановление кобальта из кобальт-никелевого концентрата начинается при температуре примерно 513 К

и в дальнейшем от температуры зависит незначительно. Степень извлечения кобальта возрастает с увеличением количества восстановителя при температурах до 553 К, затем остается постоянной до температуры 1473 К. Восстановление никеля протекает при температуре выше 473 К. Степень восстановления никеля слабо зависит от температуры и количества восстановителя при его расходе более 0,02 кг/кг концентрата. Проведенные лабораторные исследования показали, что в период плавления можно восстановить никель из его оксида твердым углеродом практически полностью, так как никель обладает меньшим сродством к кислороду, чем железо. Теоретические и экспериментальные исследования прямого легирования стали показали, что при восстановлении никеля и кобальта целесообразно использовать твердофазный процесс. Концентрат никеля и кобальт-никелевый концентрат при выплавке стали в электропечи желательно вводить в завалку в виде смесей, окомкованных с углеродистым восстановителем.

Ключевые слова: термодинамическое моделирование, модельная система, никелевый концентрат, кобальт-никелевый концентрат

Благодарности: Исследование выполнено при финансовой поддержке РФФИ и Субъекта РФ (Кемеровская обл. – Кузбасс) в рамках научного проекта № 20-48-420001/22.

Для цитирования: Рыбенко И.А., Нохрина О.И., Рожихина И.Д., Голодова М.А. Термодинамическое моделирование восстановления кобальта и никеля при использовании концентратов гидрометаллургического обогащения для легирования стали. *Известия вузов. Черная металлургия*. 2024;67(4):384–390. <https://doi.org/10.17073/0368-0797-2024-4-384-390>

INTRODUCTION

Modern technologies must meet certain requirements, the main ones being:

- rational use of material and energy resources;
- expansion of the product range;
- improvement of product quality;
- environmental safety.

These issues are particularly relevant in the production of ferrous metals. A significant focus is on obtaining ultra-pure steel with minimal undesirable impurities through more cost-effective methods and in larger quantities, as well as altering the structure and type of alloying elements and deoxidizers used, moving towards less stringent composition requirements and corresponding cost reductions.

An analysis of current steelmaking technologies reveals that the most significant cost factors in metal production are the expenses for deoxidation and alloying of steel, as well as the technological energy required. One way to increase the efficiency of steel production is to modify the technology for obtaining alloying elements by transitioning to direct alloying of steel in the furnace or ladle using ores and concentrates [1; 2].

In the past two decades, significant attention has been paid, both in Russia [3–5] and abroad [6–8], to the search for new chemical and hydrometallurgical methods for enriching low-grade ores (including manganese ores) as part of resource conservation efforts. When enriching polymetallic manganese-containing ores from Kuzbass using the technology proposed in [9], in addition to high-quality manganese and iron concentrates, non-ferrous metal concentrates (nickel concentrate, as well as nickel-cobalt concentrate) are obtained, which can be used for direct alloying.

Technological progress in mechanical engineering, construction, chemistry, and other industries drives the demand for high-quality steels and alloys. The most in-demand types are structural, heat-resistant, acid-resistant, and

stainless steels, which require non-ferrous metals in their production (with nickel being one of the primary ones).

Reserves of rich nickel ores with nickel content around 4 % are limited, leading to the use of low-grade silicate ores with nickel content up to 1.5 % [10–12]. Currently, there is considerable focus on finding new methods for enriching and utilizing nickel-containing ores [13–15]. As an alternative raw material, polymetallic manganese-containing ores and iron-manganese nodules, with nickel content up to 0.5 %, can be considered [16; 17].

Global nickel production remains steady at around 1 million tons annually. In the global economy, the demand for nickel continues to grow despite the constant rise in its price. The increasing demand for nickel is due to its wide range of applications, with the majority of produced nickel used for steel alloying.

The growing need for cobalt in various fields of science and technology, driven by the development of the aerospace industry and the production of specialty steels for oil extraction equipment, necessitates an increase in its production volume. Most cobalt produced is used to create various alloys. Cobalt is frequently used in alloys with iron, chromium, tungsten, and molybdenum. It enhances the cutting properties of high-speed steel, making it valuable in the tool industry.

Cobalt alloys possess excellent magnetic properties, corrosion resistance, wear resistance, and high thermal stability.

Adding cobalt to steel helps maintain magnetic properties at high temperatures and under vibrations, and increases resistance to demagnetization. For instance, Japanese steel containing up to 60 % Co has high coercivity and loses only 2.0–3.5 % of its magnetic properties under vibrations. Cobalt-based magnetic alloys are used in the production of electric motor cores, transformers, and other electrical devices [18; 19].

An analysis of the advantages and disadvantages of direct steel alloying shows that the feasibility of a particular technology is determined by technical and economic

indicators such as the duration of melting and the consumption of reducing agent. The goal of the research was to maximize the replacement of silicon, the primary reducing agent for alloying elements from concentrates, with the more cost-effective carbon, and to achieve consistent recovery of nickel and cobalt from the oxides present in concentrates obtained during the hydrometallurgical enrichment of polymetallic manganese-containing ores.

MATERIALS AND METHODS

In the context of steel production in electric arc furnaces, reducing agents such as carbon, carbon monoxide, and silicon dissolved in molten steel can be considered at different stages of melting. To determine the conditions for the reduction of alloying elements from concentrates, thermodynamic modeling methods based on the calculation of equilibrium states in model thermodynamic systems were used [20]. Thermodynamic modeling in this study was conducted using ready-made software products (TERRA software complex) developed at Moscow State Technical University, which allows the determination of the equilibrium composition of a multicomponent, heterogeneous thermodynamic system for high-temperature conditions based on the principle of maximum entropy.

An elementary system is formed by specifying the quantity of its constituent components and temperature. Condensed solution compositions are formed if necessary. For the selected two thermodynamic parameters, multi-variant calculations of equilibrium compositions are carried out depending on the thermodynamic parameters or the consumption of raw materials.

The set of substances that can form given the specified elemental composition of the mixture was determined through numerical modeling for the chosen temperature range and various thermodynamic states. From the complete list of possible substances, only those whose concentrations exceeded 10^{-4} mol/kg of the mixture were selected. Calculations were conducted in the temperature range from 573 to 1873 K, corresponding to steelmaking temperatures.

Thermodynamic modeling of nickel, cobalt, and combined nickel and cobalt reduction was performed for pure systems and concentrates obtained from the enrichment of polymetallic manganese raw materials: nickel concentrate (45.0 % Ni; 2.3 % Mn; 1.4 % Fe; 0.5 % Co; 0.1 % Cu; less than 0.015 % P; traces of SiO_2 and 2.82 % loss on ignition); cobalt-nickel concentrate (76.8 % CoO; 11.9 % NiO; 4.9 % Fe_2O_3 ; 1.2 % Mn_2O_3 ; 0.2 % SiO_2 ; 1.2 % CaCl_2 ; 3.8 % loss on ignition) and coke from EVRAZ United West Siberian Metallurgical Plant ($A^d = 13.6$ %; $V^{daf} = 2$ %; $W^p = 2$ %; 51.1 % SiO_2 ; 23.3 % Al_2O_3 ; 0.16 % MnO_2 ; 1.58 % MgO; 1.2 % CaO; 17.46 % Fe_2O_3 ; 0.5 % P_2O_5 ; 1.2 % K_2O ; 0.2 % Na_2O ; 74.4 % CO_2).

During laboratory studies, an optimal method for introducing nickel oxide into an electric arc furnace was experimentally determined and tested. Steel was smelted in a 10 kg capacity laboratory electric arc furnace. Pellets with a diameter of 20 – 30 mm were produced from nickel concentrate obtained from the enrichment of polymetallic manganese ores (with a fraction size less than 0.5 mm) and coke fines. The pellets were charged into the furnace in two ways: *I* – into the charge; *II* – during the reduction period, onto the metal bath before slag formation.

The number of pellets was calculated to achieve 1 % nickel content in the steel. Experimental heats were conducted using the classical two-slag technology. Scrap metal with the following composition, wt. %, was used: 0.275 C; 0.267 Si; 0.423 Mn; 0.175 Cr; 0.1 Ni; 0.027 S; 0.028 P; the remainder Fe. The mass of charge materials for experimental heat is provided in the Table. After smelting, samples of metal and slag were taken for chemical analysis. The metal and slag were tapped into a ladle. The resulting ingot was cut into three equal parts along its height for metal analysis.

RESULTS AND DISCUSSION

Nickel reduction from nickel concentrate oxides

The calculation of possible compositions resulting from nickel reduction processes in the thermodynamic

Initial charge materials for experimental heats

Исходные шихтовые материалы для опытных плавов

Indicator	Value for heat					
	1	2	3	4	5	6
Mass of briquettes, kg	0.757	0.756	0.758	0.677	0.678	0.676
Composition of briquettes, wt. %:						
Nickel concentrate	85	85	85	95	95	95
Coke	10	10	10	—	—	—
Binder	5	5	5	5	5	5
Mass of scrap metal, kg	9	9	9	9	9	9

system consisting of NiO–C was performed by varying the carbon content in the system, allowing the evaluation of the concentration limits for reduction processes. The model system NiO–C was formed by specifying the initial composition of the mixture: 1 kg of NiO and carbon in amounts ranging from 0.01 to 0.1 kg/kg of oxide. The studies were conducted in the temperature range from 1073 to 1873 K. The dependence of nickel recovery coefficients from the oxide on the amount of carbon at temperatures of 1073, 1473, and 1873 K are presented in Fig. 1. Thermodynamic calculations showed that maximum nickel reduction is achieved at a carbon consumption of 0.08 kg/kg NiO. Therefore, complete nickel reduction can be achieved during solid-phase reduction before the appearance of a liquid phase.

The results of equilibrium state calculations for the NiO–Fe₂O₃–C system within a carbon range of 0.01 – 0.50 kg/kg NiO and an initial amount of NiO (1 kg) and Fe₂O₃ (2 kg) are presented in Fig. 2. The significant condensed phase consists of Ni, NiO, C, FeO, and Fe₂O₃. The gas phase is represented by CO and CO₂ oxides.

The slag phase of the considered system is represented by FeO, Fe₂O₃, and NiO oxides. When the amount of reducing agent exceeds 0.2 kg/kg NiO, the slag phase consists only of FeO. Complete nickel reduction from

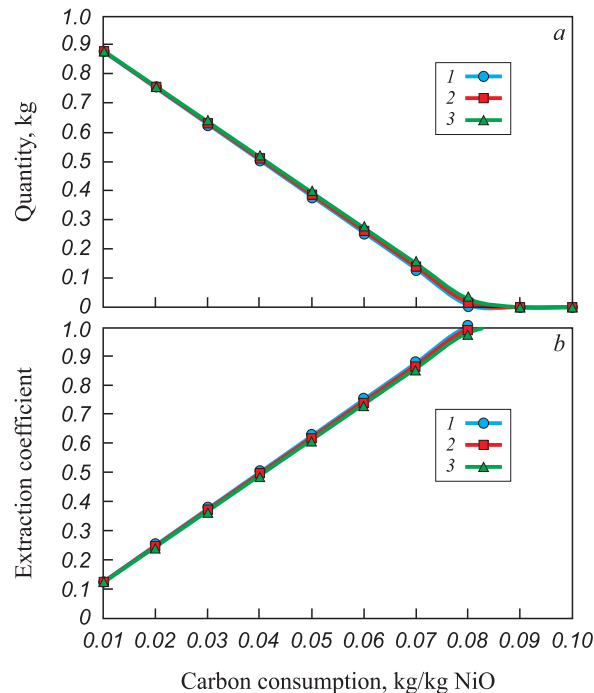


Fig. 1. Dependences of nickel reduction parameters on the amount of carbon in the NiO–C system at a temperature of 1073, 1473, 1873 K (1 – 3): a – amount of NiO; b – nickel extraction

Рис. 1. Зависимости параметров восстановления никеля от количества углерода в системе NiO–C при температурах 1073, 1473, 1873 К (1 – 3): а – количество NiO; б – извлечение никеля

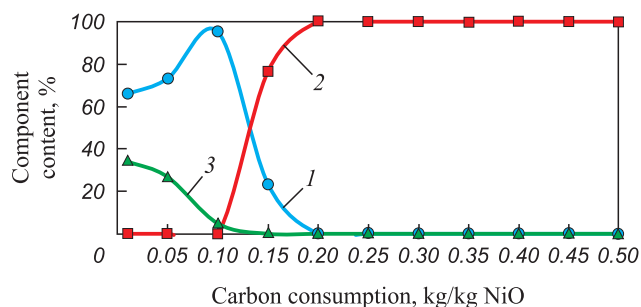


Fig. 2. Dependence of slag phase composition on carbon flow rate at constant temperature 1873 K in the NiO–Fe₂O₃–C system: 1 – Fe₂O₃, 2 – FeO, 3 – NiO

Рис. 2. Зависимость состава шлаковой фазы от расхода углерода при постоянной температуре 1873 К в системе NiO–Fe₂O₃–C: 1 – Fe₂O₃, 2 – FeO, 3 – NiO

oxide occurs at a carbon content of 0.15 kg/kg NiO in the NiO–Fe₂O₃–C system.

The results of thermodynamic modeling demonstrated that nickel can be fully reduced from its oxide in both the NiO–C system and the NiO–Fe₂O₃–C system at metallurgical process temperatures.

During laboratory experiments, the optimal method for introducing nickel oxide into the electric arc furnace was experimentally determined. In heats 1 to 3, pellets made from nickel concentrate were used, while in heats 4 to 6, a mixture of nickel concentrate and coke was used (see Table).

The results of experimental steel alloying heats using nickel-containing pellets showed that nickel recovery from the concentrate was 92 – 95 % (option I) and 75 – 78 % (option II).

The decrease in nickel recovery when it was added at the beginning of the reduction period is likely due to partial evaporation; as nickel is reduced in the arc zone, it may partially evaporate due to its relatively low boiling point.

Under steelmaking conditions in an electric arc furnace, within the temperature range of 1173 – 1873 K, nickel can be almost completely reduced from its oxide by solid carbon during the melting period, as nickel has a lower affinity for oxygen than iron.

Cobalt reduction in elementary systems

The study of cobalt oxide dissociation revealed that the highest oxide, Co₂O₃, is absent in the system at temperatures above 473 K. The cobalt oxide stable at room temperature is the complex oxide Co₃O₄, which has a spinel structure where one set of lattice sites is occupied by Co²⁺ ions and the other by Co³⁺ ions; it decomposes to form CoO at temperatures above 1173 K. The results of thermodynamic calculations are shown in Fig. 3. The dependencies indicate that Co₃O₄ remains stable up to 1173 K.

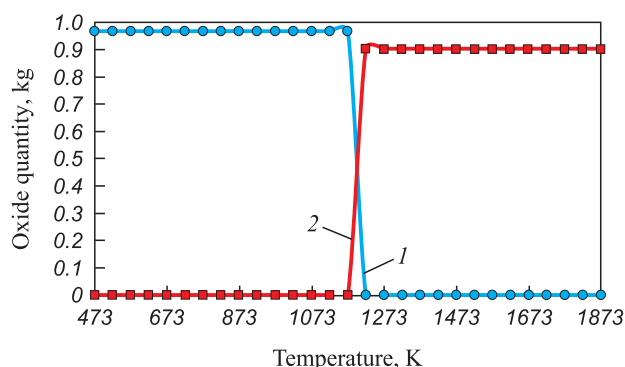


Fig. 3. Thermal dissociation of cobalt oxides:
1, 2 – Co_3O_4 , CoO

Рис. 3. Термическая диссоциация оксидов кобальта:
1, 2 – Co_3O_4 , CoO

In the temperature range of 1173 to 1223 K, the amount of Co_3O_4 decreases to zero, CoO appears at 1173 K, and its amount becomes maximal and stable to temperature changes at 1223 K.

In modeling cobalt reduction, the CoO-C system was considered. Calculations were performed in the temperature range of 273 to 1273 K, with reducing agent (carbon) consumption ranging from 0.02 to 0.10 kg/kg CoO . Thermodynamic modeling showed that cobalt reduction begins at approximately 513 K, regardless of carbon consumption. As the temperature increases, the reduction process depends solely on the amount of reducing agent (Fig. 4). Cobalt is fully reduced from its oxide at a carbon consumption of 0.1 kg/kg CoO at 1273 K.

Thermodynamic calculations of Co reduction in the Co-O-Si and Co-O-Al systems in the temperature range of 273 to 1273 K showed that cobalt is fully reduced at a silicon consumption of 0.1 kg/kg Co or at an aluminum consumption of 0.24 kg/kg CoO at 1273 K.

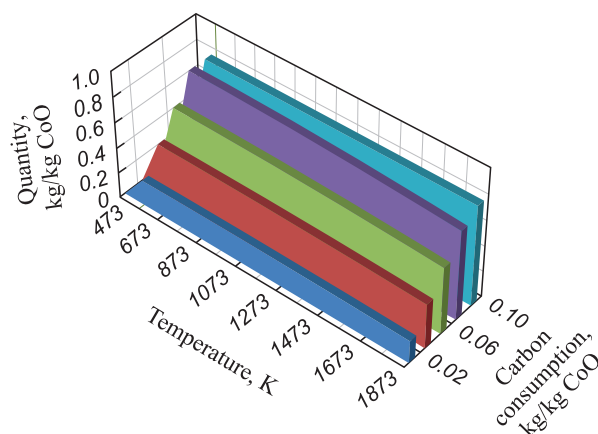


Fig. 4. Dependence of the amount of reduced cobalt on temperature and carbon consumption in the CoO-C system

Рис. 4. Зависимость количества восстановленного кобальта от температуры и расхода углерода в системе CoO-C

Nickel and cobalt reduction from cobalt-nickel concentrate

The reduction of cobalt and nickel from the oxides in the concentrate using coke was studied in the temperature range of 273 to 2073 K. Coke consumption varied from 0.02 to 0.10 kg/kg of concentrate.

The significant reduction products included:

- cobalt, nickel, cobalt oxides, nickel oxides, iron, manganese, calcium and magnesium silicates, and aluminates (condensed phase);
- water vapor, CO and CO_2 oxides, metal chlorides (gas phase); chlorides were detected at temperatures above 1513 K.

The dependencies of cobalt and nickel recovery coefficients from the cobalt-nickel concentrate on temperature and carbon consumption are shown in Fig. 5.

The thermodynamic data indicate that cobalt reduction begins at approximately 513 K and is minimally affected by further temperature increases. The degree of cobalt

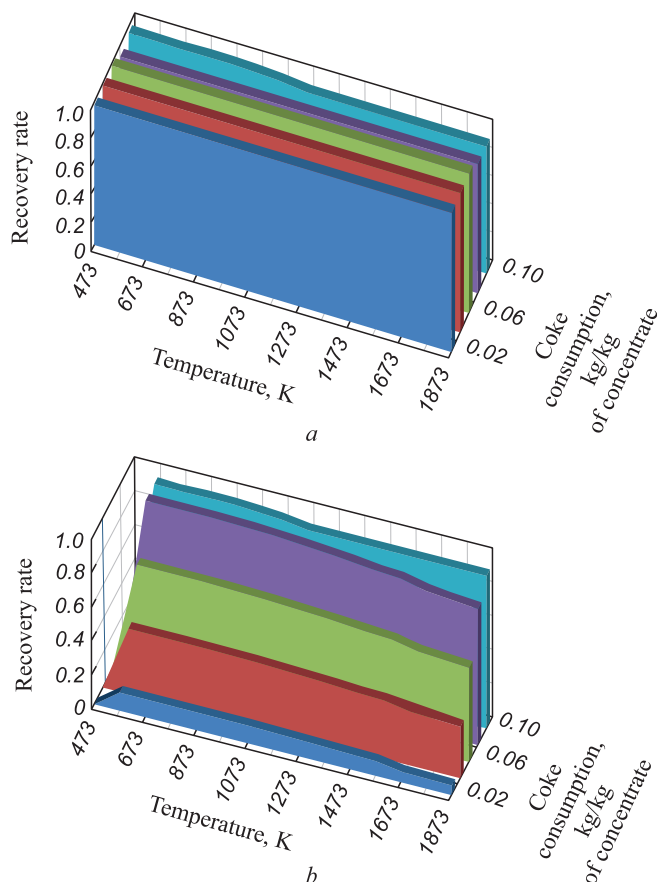


Fig. 5. Dependences of extraction coefficients of nickel (a) and cobalt (b) from cobalt-nickel concentrate on temperature and carbon consumption

Рис. 5. Зависимости коэффициентов извлечения никеля (a) и кобальта (b) из кобальт-никелевого концентрата от температуры и расхода углерода

recovery increases with the amount of reducing agent up to 553 K, after which it remains constant up to 1473 K. With further temperature increases, cobalt recovery decreases. When calculating the cobalt recovery coefficient, only cobalt present in the condensed phase was considered. The gas phase contained CoCl_2 , and its amount increased with rising temperature.

Nickel reduction occurs at temperatures above 473 K. The degree of nickel reduction is slightly dependent on temperature and amount of reducing agent when the latter exceeds 0.02 kg/kg of concentrate.

The study results showed that during the reduction of nickel and cobalt from concentrates, complete reduction of these elements is achieved at solid-phase reduction temperatures in the range of 573 to 1073 K. The data obtained are consistent with the results of previous studies [18; 19].

CONCLUSIONS

The results of theoretical and experimental studies suggest that solid-phase reduction is advisable for nickel and cobalt reduction. Nickel can be fully reduced from nickel concentrate by carbon at 1073 K, while cobalt and nickel reduction from cobalt-nickel concentrate begins at approximately 513 K and is minimally affected by further temperature increases. Therefore, it is advisable to introduce nickel and cobalt-nickel concentrates into the furnace charge during steelmaking in electric arc furnaces as mixtures pelletized with a carbonaceous reducing agent.

REFERENCES / СПИСОК ЛИТЕРАТУРЫ

1. Nokhrina O. I., Rozhikhina I.D., Dmitrienko V.I. Platonov M.A. Alloying and Modification of Steel using Natural and Man-Made Materials. Toms: Izd-vo Tomskogo politekhnicheskogo universiteta; 2013:320. (In Russ.).
Нохрина О.И., Рожихина И.Д., Дмитриенко В.И. Платонов М.А. Легирование и модифицирование стали с использованием природных и техногенных материалов. Томск: Изд-во Томского политехнического университета; 2013:320.
2. Nosov Yu.N., Kamshukov V.P., Sokolov V.V., etc. Direct alloying of steel with manganese agglomerate in a ladle at converter tapping. *Stal'*. 2004;(5):35–36. (In Russ.).
Носов Ю.Н., Камшуков В.П., Соколов В.В. и др. Прямое легирование стали марганцевым агломератом в ковше на выпуске из конвертера. *Сталь*. 2004;(5):35–36.
3. Nokhrina O.I., Rozhikhina I.D., Edil'baev A.I., Edil'baev B.A. Manganese ores of the Kemerovo region – Kuzbass and methods of their enrichment. *Izvestiya. Ferrous Metallurgy*. 2020;63(5):344–350. (In Russ.).
<https://doi.org/10.17073/0368-0797-2020-5-344-350>
Нохрина О.И., Рожихина И.Д., Едильбаев А.И., Едильбаев Б.А. Марганцевые руды Кемеровской области – Кузбасса и методы их обогащения. *Известия вузов. Черная металлургия*. 2020;63(5):344–350.
<https://doi.org/10.17073/0368-0797-2020-5-344-350>
4. Chernobrovin V.P., Mizin V.G., Sirina T.P., Dashevskii V.Ya. Complex Processing of Carbonate Manganese Raw Materials: Chemistry and Technology. Chelyabinsk: SUSU; 2009:294. (In Russ.).
Чернобровин В.П., Мизин В.Г., Сирина Т.П., Дашевский В.Я. Комплексная переработка карбонатного марганцевого сырья: химия и технология. Челябинск: ЮУрГУ; 2009:294.
5. Kurkov A.V., Mamoshin M.Yu., Rogozhin A.A. Breakthrough Hydrometallurgical Processes for the Sustainable Development of Mineral Processing Technologies. Moscow: VIMS; 2019:106. (In Russ.).
Курков А.В., Мамошин М.Ю., Рогожин А.А. Прорывные гидрометаллургические процессы для устойчивого развития технологий переработки минерального сырья. Москва: Научное издание ФГБУ «ВИМС»; 2019:106.
6. Pan M.C., Liu X.L., Zou R., Huang J., Han J.C. Study of heat treatment technology on medium-carbon-low-alloy-steel large hammer formation of gradient performance. *Advanced Materials Research*. 2014;881-883:1288–1292.
<http://dx.doi.org/10.4028/www.scientific.net/AMR.881-883.1288>
7. Sun D., Li M.L., Li C.H., Cul R., Zheng X.Y. A green enriching process of Mn from low grade ore of manganese carbonate. *Applied Mechanics and Materials*. 2014;644–650:5427–5430.
<http://dx.doi.org/10.4028/www.scientific.net/AMM.644-650.5427>
8. Ayala J., Fernandez B. Recovery of manganese from silico-manganese slag by means of a hydrometallurgical process. *Hydrometallurgy*. 2015;158:68–73.
<https://doi.org/10.1016/j.hydromet.2015.10.007>
9. Nokhrina O.I., Rozhikhina I.D., Rybenko I.A., Golodova M.A., Izrail'skii A.O. Hydrometallurgical enrichment of polymetallic and ferromanganese ore. *Izvestiya. Ferrous Metallurgy*. 2021;64(4):273–281. (In Russ.).
<https://doi.org/10.17073/0368-0797-2021-4-273-281>
Нохрина О.И., Рожихина И.Д., Рыбенко И.А., Голодова М.А., Израильский А.О. Гидрометаллургическое обогащение полиметаллических и железомарганцевых руд. *Известия вузов. Черная металлургия*. 2021;64(4):273–281. <https://doi.org/10.17073/0368-0797-2021-4-273-281>
10. Pat. 7125436 USA, IPC7 from 22 at 15/00, from 22 at 11/08. The method of autoclave leaching of nickel ores. Run L., Maurt T. No. 10/907324. Published on 10.24.2006. NPC 75/724.
11. Wang K., Li J., McDonald R.G., Browner R.E. The effect of iron precipitation upon nickel losses from synthetic atmospheric nickel laterite leach solutions: Statistical analysis and modeling. *Hydrometallurgy*. 2011;109(1-2):140–152.
<http://dx.doi.org/10.1016/j.hydromet.2011.06.009>
12. Anjum F., Shahid M., Akcil A. Biohydrometallurgy techniques of low grade ores: A review on black shale. *Hydrometallurgy*. 2012;117–118:1–12.
<http://dx.doi.org/10.1016/j.hydromet.2012.01.007>
13. Giannopoulou I., Panias D. Differential precipitation of copper and nickel from acidic polymetallic aqueous solutions. *Hydrometallurgy*. 2008;90(2–4):137–146.
<https://doi.org/10.1016/j.hydromet.2007.10.004>
14. 1731623 EVP, IPC from 22 to 23/00. Method for teaching and extraction of nickel and cobalt. H. Yakushiji, S. Ito, K. Jura, M. Shimamori. Published on 12.13.2006.

15. Coto O., Galizia F., Hernandez I., Marrero J., Donati E. Cobalt and nickel recoveries from laterite tailings by organic and inorganic bioacids. *Hydrometallurgy*. 2008; 94(1–4):18–22. <http://dx.doi.org/10.4028/www.scientific.net/AMR.20-21.107>
16. Ntuli F., Lewis A.E. Kinetic modelling of nickel powder precipitation by high-pressure hydrogen reduction. *Chemical Engineering Science*. 2009;64(9):2202–2215. <http://dx.doi.org/10.1016/j.ces.2009.01.026>
17. Proshunin I.E., Nokhrina O.I. Complex extraction of valuable components from ferromanganese nodules. *Izvestiya. Ferrous Metallurgy*. 2009;52(8):17–19. (In Russ.).
Прошунин И.Е., Нохрина О.И. Комплексное извлечение ценных компонентов из железомарганцевых конкреций. *Известия вузов. Черная металлургия*. 2009;52(8):17–19.
18. Kozlov P.A. Investigation of the effect of alloying on the composition of heat-resistant 9 % chromium steels for parts of thermal power equipment: Extended Abstract of Cand. Sci. Diss. 05.16.02. Moscow; 2011:25. (In Russ.).
Козлов П.А. Исследование влияния легирования на состав жаропрочных 9 %-ных хромистых сталей для элементов теплоэнергетического оборудования: автореф. дис... канд. техн. наук: 05.16.02. Москва; 2011:25.
19. Kniss V.A. Physico-chemical bases and technology of reduction melting of cobalt oxide in electric furnaces of direct current. Extended Abstract of Cand. Sci. Diss. 05.16.02. Yekaterinburg; 2008:31. (In Russ.).
Книсс В.А. Физико-химические основы и технология восстановительной плавки закиси-оксида кобальта в электропечах постоянного тока: автореф. дис... канд. техн. наук: 05.16.02. Екатеринбург; 2008:31.
20. Trusov B.G. TERRA software system for modeling phase and chemical equilibria at high temperatures. In: *III Int. Symp. "Combustion and Plasma Chemistry". August 24–26, 2005, Almaty, Kazakhstan*. Almaty: Kazak universiteti; 2005:52–57. (In Russ.).
Трусов Б.Г. Программная система ТЕРРА для моделирования фазовых и химических равновесий при высоких температурах. В кн.: *III междунар. симпозиум «Горение и плазмохимия». 24–26 августа 2005. Алматы, Казахстан*. Алматы: Казак университеті; 2005:52–57.

Information about the Authors

Сведения об авторах

Inna A. Rybenko, Dr. Sci. (Eng.), Prof., Head of the Chair of Applied Information Technologies and Programming, Siberian State Industrial University

ORCID: 0000-0003-1679-0839

E-mail: rybenkoi@mail.ru

Ol'ga I. Nokhrina, Dr. Sci. (Eng.), Prof. of the Chair of Ferrous Metallurgy and Chemical Technology, Siberian State Industrial University

ORCID: 0000-0001-9448-8948

E-mail: nvi52@mail.ru

Irina D. Rozhikhina, Dr. Sci. (Eng.), Prof. of the Chair of Ferrous Metallurgy and Chemical Technology, Siberian State Industrial University

ORCID: 0000-0002-3034-4539

E-mail: roghina_id@mail.ru

Marina A. Golodova, Cand. Sci. (Eng.), Assist. Prof. of the Chair of Architecture, Siberian State Industrial University

ORCID: 0000-0003-0105-9285

E-mail: m.irina1976@mail.ru

Инна Анатольевна Рыбенко, д.т.н., профессор, заведующий кафедрой прикладных информационных технологий и программирования, Сибирский государственный индустриальный университет

ORCID: 0000-0003-1679-0839

E-mail: rybenkoi@mail.ru

Ольга Ивановна Нохрина, д.т.н., профессор кафедры металлургии черных металлов и химической технологии, Сибирский государственный индустриальный университет

ORCID: 0000-0001-9448-8948

E-mail: nvi52@mail.ru

Ирина Дмитриевна Рожихина, д.т.н., профессор-консультант кафедры металлургии черных металлов и химической технологии, Сибирский государственный индустриальный университет

ORCID: 0000-0002-3034-4539

E-mail: roghina_id@mail.ru

Марина Анатольевна Голодова, к.т.н., доцент кафедры архитектуры, Сибирский государственный индустриальный университет

ORCID: 0000-0003-0105-9285

E-mail: m.irina1976@mail.ru

Contribution of the Authors

Вклад авторов

I. A. Rybenko – conducting thermodynamic calculations, processing calculation results.

O. I. Nokhrina – setting the task, analyzing literary sources, writing the main text of the article, conducting experiments and processing their results.

I. D. Rozhikhina – conducting experiments and processing their results, editing the article.

M. A. Golodova – processing thermodynamic calculations, plotting and describing of graphs, making drawings.

И. А. Рыбенко – проведение термодинамических расчетов, обработка результатов расчетов.

О. И. Нохрина – постановка задачи, анализ литературных источников, написание основного текста статьи, проведение экспериментов и обработка их результатов.

И. Д. Рожихина – проведение экспериментов и обработка их результатов, редактирование статьи.

М. А. Голодова – обработка термодинамических расчетов, построение графиков и их описание, выполнение рисунков.

Received 27.10.2023

Revised 12.01.2024

Accepted 14.03.2024

Поступила в редакцию 27.10.2023

После доработки 12.01.2024

Принята к публикации 14.03.2024



UDC 621.785.53; 539.25

DOI 10.17073/0368-0797-2024-4-391-397



Original article

Оригинальная статья

COMPLEX ELECTRON-ION-PLASMA SURFACE MODIFICATION OF HIGH-ALLOY STAINLESS STEEL

Yu. F. Ivanov[✉], E. A. Petrikova, A. D. Teresov,
I. V. Lopatin, O. S. Tolkachev

Institute of High Current Electronics, Siberian Branch of the Russian Academy of Sciences (2/3 Akademicheskii Ave., Tomsk 634055, Russian Federation)

✉ yufi55@mail.ru

Abstract. The work is devoted to identification and analysis of patterns of change in the elemental and phase composition, defective substructure, mechanical (microhardness) and tribological (wear resistance and friction coefficient) properties of stainless high-chromium steel subjected to complex processing, combining vacuum irradiation of the samples surface layer with an intense pulsed electron beam of submillisecond exposure duration and subsequent nitriding under electron-ionic heating conditions. High-chromium steel AISI 310S, which in the initial state is a polycrystalline aggregate based on γ -iron, was used as the research material. Pulsed electron beam treatment of steel was carried out on a “SOLO” installation equipped with an electron source with a plasma cathode based on a low-pressure pulsed arc discharge with grid stabilization of the cathode plasma boundary and an open anode plasma boundary. Steel nitriding was carried out on a “TRIO” installation with a chamber size of 600×600×600 mm, equipped with a switching unit to implement the electron-ionic processing mode. Nitriding was carried out at 723, 793, and 873 K temperatures for 1, 3 and 5 h. It was found that electron-ionic nitriding of the samples pre-irradiated with an electron beam (10 J/cm², 200 μ s, 3 pulses at 723 and 793 K for 3 h) is accompanied by the formation of a ceramic layer containing only iron and chromium nitrides. The highest values of steel wear resistance after electron-ionic nitriding, exceeding the wear resistance of the initial steel by more than 700 times, are observed at nitriding parameters of 793 K, 3 h.

Keywords: high-chromium steel, complex processing, pulsed electron beam treatment, nitriding, structure, phase composition, hardness, wear resistance, friction coefficient

Acknowledgements: The work was supported by the Ministry of Science and Higher Education of the Russian Federation (No. FWRM-2021-0006). The results of the TEM analysis were obtained on the basis of the Scientific and Educational Innovation Center “Nanomaterials and Nanotechnology” of the TPU Research Institute.

For citation: Ivanov Yu.F., Petrikova E.A., Teresov A.D., Lopatin I.V., Tolkachev O.S. Complex electron-ion-plasma surface modification of high-alloy stainless steel. *Izvestiya. Ferrous Metallurgy*. 2024;67(4):391–397. <https://doi.org/10.17073/0368-0797-2024-4-391-397>

КОМПЛЕКСНАЯ ЭЛЕКТРОННО-ИОННО-ПЛАЗМЕННАЯ МОДИФИКАЦИЯ ПОВЕРХНОСТИ НЕРЖАВЕЮЩЕЙ ВЫСОКОЛЕГИРОВАННОЙ СТАЛИ

Ю. Ф. Иванов[✉], Е. А. Петрикова, А. Д. Тересов,
И. В. Лопатин, О. С. Толкачев

Институт сильноточной электроники Сибирского отделения РАН (Россия, 634055, Томск, Академический пр., 2/3)

✉ yufi55@mail.ru

Аннотация. Работа посвящена выявлению и анализу закономерностей изменения элементного и фазового составов, дефектной субструктуры, механических (микротвердость) и трибологических (износостойкость и коэффициент трения) свойств нержавеющей высокохромистой стали, подвергнутой комплексной обработке, которая сочетает облучение в вакууме поверхностного слоя образцов интенсивным импульсным электронным пучком субмиллисекундной длительности воздействия и последующее азотирование в условиях элионного нагрева образцов. В качестве материала исследования используется высокохромистая сталь 20Х23Н18, являющаяся в исходном состоянии поликристаллическим агрегатом на основе γ -железа. Облучение стали импульсным электронным пучком авторы проводили на установке «СОЛО», оснащенной электронным источником с плазменным катодом на основе импульсного дугового разряда низкого давления с сеточной стабилизацией границы катодной плазмы и открытой границей анодной плазмы. Азотирование стали осуществлялось на

установке «ТРИО» с размерами камеры 600×600×600 мм, дооснащенной блоком коммутации для реализации элионного (электронного и ионного) режима обработки. Азотирование проводили при температурах 723, 793 и 873 К в течение 1, 3 и 5 ч. Элионное азотирование при температурах 723 и 793 К в течение 3 ч образцов, предварительно облученных электронным пучком (при режиме 10 Дж/см², 200 мкс, 3 имп.), сопровождается формированием керамического слоя, содержащего только нитриды железа и хрома. Наиболее высокие значения износостойкости стали после элионного азотирования, превышающие износостойкость исходной стали более чем в 700 раз, наблюдаются при параметрах азотирования 793 К, 3 ч.

Ключевые слова: высокохромистая сталь, комплексная обработка, облучение импульсным электронным пучком, азотирование, структура, фазовый состав, твердость, износостойкость, коэффициент трения

Благодарности: Работа выполнена в рамках государственного задания Министерства науки и высшего образования Российской Федерации (тема № FWRM-2021-0006). Результаты ПЭМ-анализа получены на базе Научно-образовательного инновационного центра «Наноматериалы и нанотехнологии» НИ ТПУ.

Для цитирования: Иванов Ю.Ф., Петрикова Е.А., Тересов А.Д., Лопатин И.В., Толкачев О.С. Комплексная электронно-ионно-плазменная модификация поверхности нержавеющей высоколегированной стали. *Известия вузов. Черная металлургия*. 2024;67(4):391–397. <https://doi.org/10.17073/0368-0797-2024-4-391-397>

INTRODUCTION

The recent studies have highlighted the increasing demand for surface modification of metals and alloys through complex processing. These processing combines various methods such as saturating the surface layer with gas atoms, depositing thin films of different metals followed by mixing under high-energy pulsed electron beams, applying hard and superhard wear-resistant coatings, and more [1; 2]. These processes result in a gradient structure in the near-surface layer, with a gradual change in the concentration of alloying elements with depth, significantly enhancing the surface's hardness, wear resistance, corrosion resistance, and electrical conductivity [3 – 5]. The most commonly used ion-plasma nitriding method in the industry is nitriding in an abnormal glow discharge [6 – 8]. However, this method has the main disadvantage of relatively high operating pressure, which hinders effective ion cleaning of the surface during nitriding. To overcome this drawback, the Institute of High Current Electronics of the Siberian Branch of the Russian Academy of Sciences developed the plasma generator “PINK,” which has been successfully used for a quarter of a century [9 – 11]. The necessary temperature for the nitriding process using the “PINK” plasma generator is maintained by a flow of ions from the discharge plasma, accelerated to an energy determined by the electric bias on the samples. This often leads to intensive ion etching of the treated surface and a significant increase in its roughness [12; 13]. To mitigate the impact of intense ion bombardment on the formation of the modified layer, studies [14; 15] proposed using the electronic component of the plasma for heating the samples, implementing an elion process. This process allows for adjusting the processing temperature without significantly altering the intensity of ion bombardment.

The aim of this work is to establish the patterns of evolution in the structure, mechanical, and tribological properties of high-chromium steel subjected to a comprehensive treatment that combines pulsed electron beam

irradiation and subsequent elion nitriding in a low-pressure gas discharge plasma.

MATERIALS AND METHODS

The material used for the study was high-chromium steel AISI 310S with the following composition (wt. %): C 0.2; Si 1.0; Mn 2.0; Ni 17 – 20; Cr 22 – 25; S 0.02; P 0.035; and the remainder Fe. The samples were in the form of plates measuring 10×10×5 mm. The steel was irradiated with a pulsed electron beam using the “SOLO” installation, equipped with an electron source featuring a plasma cathode based on a low-pressure pulsed arc discharge with grid stabilization of the cathode plasma boundary and an open anode plasma boundary [17; 18]. Based on thermal calculations, electron beam energy densities (E_s) of 10 and 30 J/cm² were selected (pulse duration 200 μs; number of pulses 3; frequency 0.3 s⁻¹). At an electron beam energy density of 10 J/cm² (200 μs, 3 pulses), a solid-phase mode is achieved, meaning transformations in the surface layer of AISI 310S steel occur within the temperature range where the surface layer remains in the solid state. At an electron beam energy density of 30 J/cm² (200 μs, 3 pulses), a liquid-phase mode is realized, meaning transformations in the surface layer of AISI 310S steel occur within the temperature range where the surface layer is in a molten state. The nitriding of the steel was performed using the “TRIO” installation, which has a chamber size of 600×600×600 mm and is equipped with a switching unit to implement the elion (electronic and ionic) processing mode [15]. This process was carried out at temperatures ranging from 723 to 873 K for 1 – 5 h. The temperature of the samples was regulated by the filling factor of the electronic phase. The samples were fixed on a stationary holder in the center of the chamber along the axis of the plasma sources, with the holder positioned at a 60° angle to each source and the samples on the front side of the holder. The process temperature was measured using a chromelalumel thermocouple fixed in the sample holder through a quartz cup.

The structure, elemental, and phase composition of the modified steel were investigated using *X*-ray diffraction analysis, optical microscopy, scanning electron microscopy (SEM), and transmission electron microscopy (TEM). The mechanical properties of the steel were characterized by microhardness (indenter load 0.5 N), and the tribological properties were characterized by wear resistance and the coefficient of friction. The parameters for the tribological tests under dry friction conditions at room temperature were as follows: counter body – a 6 mm diameter silicon carbide (SiC) ball, wear track diameter 4 mm, load 5 N, and friction path length 2000 m.

RESULTS AND DISCUSSION

Surface treatment of AISI 310S stainless steel with a pulsed electron beam at an energy density (E_s) of 10 J/cm² (200 μs, 3 pulses) results in the formation of slip traces on the irradiated surface (Fig. 1, *a*), indicating intense deformation of the surface layer due to the relaxation of elastic stresses formed in the surface layer of the samples during the rapid energy input and cooling process. The surface of the samples remains smooth, with no microcracks, microcraters, or micropores observed. This indicates that the irradiation did not lead to the melting of the surface layer of the samples.

Surface treatment of AISI 310S stainless steel with a pulsed electron beam at an energy density of 30 J/cm² (200 μs, 3 pulses) results in the formation of a highly relief structure on the irradiated surface, characterized by a large number of microcraters. A cellular structure is observed within the grains, indicating melting and subsequent high-speed crystallization of the surface layer (Fig. 1, *b*). Therefore, under this irradiation mode, the high-speed melting of the surface layer occurs, which aligns with the results of the temperature field calculations. The crystallization cell sizes range from 330 to 500 nm. Microcracks are present on the surface of the steel, located along the grain boundaries, indicating a high level of residual stresses formed in the surface layer due to rapid cooling.

It has been established that increasing the electron beam energy density leads to a rise in the wear coefficient (a decrease in wear resistance) of the steel from $1.9 \cdot 10^{-4}$ mm³/(N·m) at 10 J/cm² to $5.2 \cdot 10^{-4}$ mm³/(N·m) at 30 J/cm². The wear coefficient of the steel before pulsed electron beam irradiation is $4.9 \cdot 10^{-4}$ mm³/(N·m). Additionally, it was shown that the microhardness of the samples increases with the electron beam energy density, from 1.7 GPa in the initial state to 2.4 GPa after irradiation at 30 J/cm².

Subsequent nitriding of the steel resulted in a significant increase (4 to 9 times compared to the initial state) in

the hardness of the surface layer. The hardness of the steel decreases with increasing nitriding temperature and electron beam energy density. The maximum thickness of the hardened layer is 45 – 50 μm, achieved through a comprehensive treatment that combines irradiation at an electron beam energy density of 10 J/cm² and subsequent nitriding at a temperature of 793 K for 3 h. Nitriding at 793 K for 3 h yields the best results in tribological tests, with the wear resistance of steel samples irradiated with a pulsed electron beam at $E_s = 10$ J/cm² reaching $1.2 \cdot 10^{-6}$ mm³/(N·m), and at $E_s = 30$ J/cm² reaching $0.58 \cdot 10^{-6}$ mm³/(N·m), which is significantly higher than the wear resistance of the steel in both the initial and irradiated states.

X-ray phase analysis determined that the main phases of the modified samples are α-iron and γ-iron, as well as iron nitrides Fe₄N, Fe₂N, chromium nitrides CrN, and

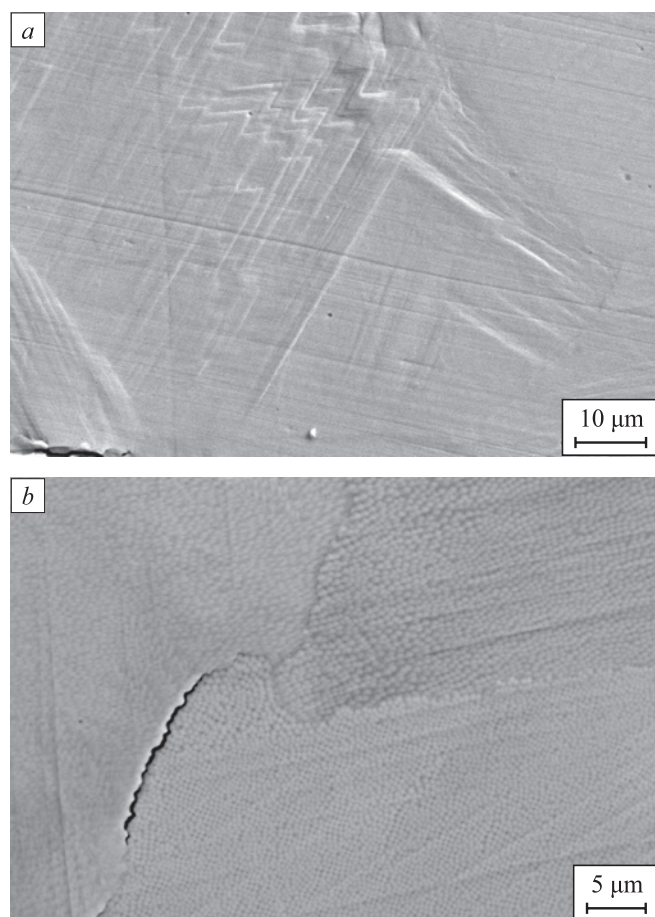


Fig. 1. Electron microscopic image of the surface structure of AISI 310S steel samples irradiated with a pulsed electron beam:

a – $E_s = 10$ J/cm² (200 μs, 3 pulses);

b – $E_s = 30$ J/cm² (200 μs, 3 pulses)

Рис. 1. Электронно-микроскопическое изображение структуры поверхности образцов стали 20Х23Н18, облученной импульсным электронным пучком:

a – $E_s = 10$ Дж/см² (200 мкс, 3 имп.);

b – $E_s = 30$ Дж/см² (200 мкс, 3 имп.)

the complex nitride Fe_3NiN . The highest microhardness values (15.8 and 15.6 GPa) were demonstrated by samples subjected to comprehensive treatment, which includes preliminary pulsed electron beam treatment (10 J/cm^2 , $200 \mu\text{s}$, 3 pulses) and subsequent nitriding at temperatures of 723 and 793 K for 3 h. The surface layer structure of these samples is characterized by the formation of a ceramic layer containing only iron and chromium nitrides.

Scanning electron microscopy first observed the phenomenon of blistering during electron-ion-plasma nitriding, resulting in the formation of bubbles on the material surface (Fig. 2, *a*).

It is noteworthy that the formation of bubbles is observed on the surface of metals and alloys, metal-ceramic, and ceramic materials subjected to intense corpuscular exposure (ions H^+ , B^+ , He^+ , etc.), and is most prominently manifested in nuclear and thermonuclear reactor technologies, as well as in space [19 – 21].

Studies of the fracture surface of samples pre-irradiated with a pulsed electron beam and subjected to elion nitriding revealed that the destruction of the surface layer of the steel predominantly follows a quasi-brittle mechanism (Fig. 2, *b*).

The defect structure of the modified layer was studied using transmission electron microscopy. It was found that nitriding is accompanied by the formation of a lamellar structure (Fig. 3).

Nitriding of samples subjected to preliminary treatment with a pulsed electron beam at an electron beam energy density of 10 J/cm^2 , pulse duration of $200 \mu\text{s}$, and three pulses, leads to the formation of a structure with alternating iron nitride and chromium nitride plates and results in a structure characterized by alternating γ -iron plates and predominantly iron nitrides.

CONCLUSIONS

Nitriding process was carried out on samples of AISI 310S steel, which had been pre-irradiated with a pulsed electron beam, in a low-pressure gas discharge plasma with sample heating by plasma electrons (elion nitriding method). The formation of blisters on the material surface was observed during elion nitriding. Nitriding resulted in the formation of a plate-like structure with alternating iron nitride and chromium nitride plates (for samples pre-irradiated with a pulsed electron beam at an energy density of 10 J/cm^2 , pulse duration of $200 \mu\text{s}$, and three pulses) or a structure with alternating γ -iron plates and predominantly iron nitrides (for samples pre-irradiated with a pulsed electron beam at an energy density of 30 J/cm^2 , pulse duration of $200 \mu\text{s}$, and three pulses). The highest microhardness values (15.8 and 15.6 GPa) were demonstrated by samples subjected to combined treatment, which included preliminary treatment with a pulsed electron beam (10 J/cm^2 , $200 \mu\text{s}$, three pulses) and subsequent nitriding at temperatures of 723 and

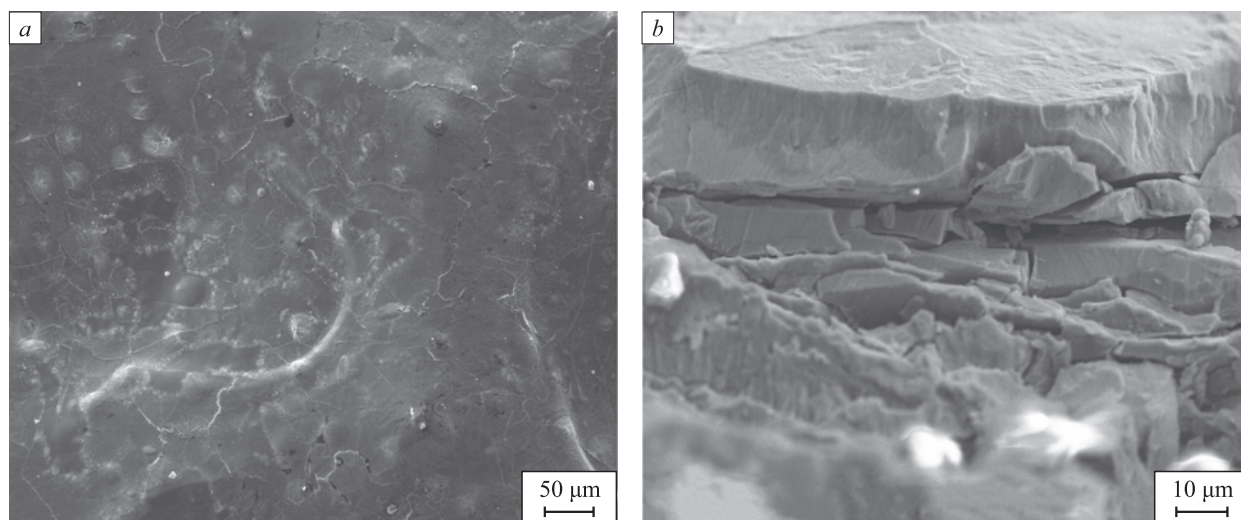


Fig. 2. Electron microscopic image of the AISI 310S steel structure subjected to complex modification, combining irradiation with a pulsed electron beam at 10 J/cm^2 , $200 \mu\text{s}$, 3 pulses (*a*) and 30 J/cm^2 , $200 \mu\text{s}$, 3 pulses (*b*) and subsequent nitriding at 793 K for 3 h:
a – modification surface; *b* – fracture surface

Рис. 2. Электронно-микроскопическое изображение структуры стали 20Х23Н18, подвергнутой комплексному модифицированию, сочетающему облучение импульсным электронным пучком при 10 Дж/см^2 , 200 мкс , 3 имп. (*a*) и при 30 Дж/см^2 , 200 мкс , 3 имп. (*b*) и последующее азотирование при 793 К, 3 ч:
a – поверхность модифицирования; *b* – поверхность излома

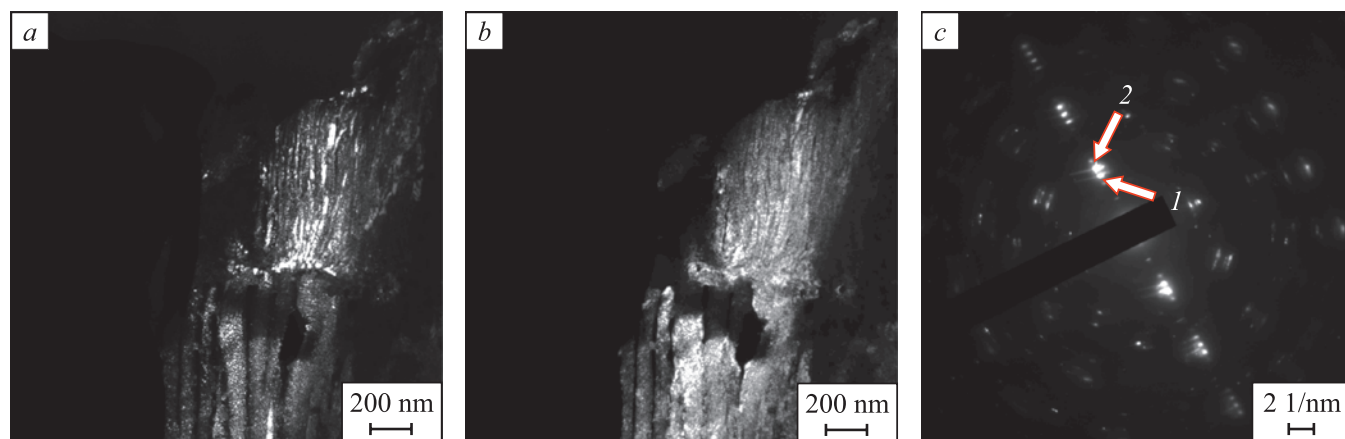


Fig. 3. Electron microscopic images of the AISI 310S steel surface layer structure subjected to complex modification (irradiation with a pulsed electron beam at 30 J/cm², 200 μs, 3 pulses and subsequent nitriding at 793 K for 3 h):
a and *b* – dark fields obtained in [111]γ-Fe and [002]γ-Fe + [002]Fe₄N reflections;
c – microelectron diffraction pattern (arrows indicate reflections in which dark fields 1 (*a*), 2 (*b*) were obtained)

Рис. 3. Электронно-микроскопическое изображение структуры поверхностного слоя стали 20Х23Н18, подвергнутой комплексной модификации (облучение импульсным электронным пучком при 30 Дж/см², 200 мкс, 3 имп. и последующее азотирование при 793 К, 3 ч.):
a и *b* – темное поле, полученное в рефlekсах [111]γ-Fe и [002]γ-Fe + [002]Fe₄N;
c – микроэлектроннограмма (стрелками указаны рефlekсы, в которых получены темные поля 1 (*a*), 2 (*b*))

793 K for 3 h. The highest wear resistance, significantly surpassing that of the steel in both its initial and irradiated states, was observed in samples pre-irradiated with a pulsed electron beam at $E_s = 30$ J/cm² and nitrided at a temperature of 793 K for 3 h.

REFERENCES / СПИСОК ЛИТЕРАТУРЫ

- Arzamasov B.N., Bratukhin A.G., Eliseev Y.S., Panayoti T.A. Ionic Chemical and Thermal Treatment of Alloys. Moscow: Bauman Moscow State Technical University; 1999:400. (In Russ.).
Ионная химико-термическая обработка сплавов / Б.Н. Арзамасов, А.Г. Братухин, Ю.С. Елисеев, Т.А. Панайоти. Москва: изд. МГТУ им Баумана; 1999:400.
- Berlin E.V., Koval N.N., Seidman L.A. Plasma Chemical-Thermal Surface Treatment of Steel Parts. Moscow: Technosfera; 2012:464. (In Russ.).
Берлин Е.В., Коваль Н.Н., Сейдман Л.А. Плазменная химико-термическая обработка поверхности стальных деталей. Москва: Техносфера; 2012:464.
- Budilov V.V., Agzamov R.D., Ramazanov K.N. Ion nitriding in glow discharge with hollow cathode effect. *Metal Science and Heat Treatment*. 2007;49(7):358–361.
<http://dx.doi.org/10.1007/s11041-007-0065-y>
- Koval N.N., Ryabchikov A.I., Sivin D.O., Lopatin I.V., Krysin O.V., Akhmadeev Yu.H., Ignatov D.Yu. Low-energy high-current plasma immersion implantation of nitrogen ions in plasma of non-self-sustained arc discharge with thermionic and hollow cathodes. *Surface and Coatings Technology*. 2018;340:152–158.
<https://doi.org/10.1016/j.surfcoat.2018.02.064>
- Lopatin I.V., Akhmadeev Yu.H., Koval N.N., Petrikova E.A. AISI 5140 steel nitriding in a plasma of a non-self-sustained arc discharge with a thermionic cathode under the pulse action of ions. *IOP Conference Series: Journal of Physics*. 2018;1115(3):032042.
<https://doi.org/10.1088/1742-6596/1115/3/032042>
- Shen L., Wang L., Wang Y., Wang C. Plasma nitriding of AISI 304 austenitic stainless steel with pre-shot peening. *Surface and Coatings Technology*. 2010;204(20):3222–3227.
<https://doi.org/10.1016/j.surfcoat.2010.03.018>
- Wang L., Ji S., Sun J. Effect of nitriding time on the nitrided layer of AISI 304 austenitic stainless steel. *Surface and Coatings Technology*. 2006;200(16-17):5067–5070.
<https://doi.org/10.1016/j.surfcoat.2005.05.036>
- Kaestner P., Michler Th., Weidner H., Rie K.-T., Bräuer G. Plasma nitrided austenitic stainless steels for automotive hydrogen applications. *Surface and Coatings Technology*. 2008;203(5-7):897–900.
<https://doi.org/10.1016/j.surfcoat.2008.08.024>
- Meletis E.I. Intensified plasma-assisted processing: science and engineering. *Surface and Coatings Technology*. 2002;149(2-3):95–113.
[https://doi.org/10.1016/S0257-8972\(01\)01441-4](https://doi.org/10.1016/S0257-8972(01)01441-4)
- Wei R., Benn C.R., Cooper C.V. High intensity plasma ion nitriding of airmet 100 martensitic steel. *Plasma Processes and Polymers*. 2007;4(S1):S700–S706.
<https://doi.org/10.1002/ppap.200731801>
- Shchanin P.M., Koval' N.N., Goncharenko I.M., Grigor'ev S.V. Nitriding of structural steels in low-pressure gas discharges. *Fizika i khimiya obrabotki materialov*. 2001;(3):16–19. (In Russ.).
Щанин П.М., Коваль Н.Н., Гончаренко И.М., Григорьев С.В. Азотирование конструкционных сталей в газовых разрядах низкого давления. *Физика и химия обработки материалов*. 2001;(3):16–19.
- Yeo S., Lee C.M., Yoon H.S., Kim J.H. Synthesis of plasma-nitrided Cr coatings on HT9 steel for advanced chemical

- barrier property in a nuclear cladding application. *Applied Surface Science*. 2022;579:152133.
<https://doi.org/10.1016/j.apsusc.2021.152133>
13. Godec M., Ruiz-Zepeda Fr., Podgornik B., Donik Čr., Kocijan Al., Skobir B., Danijela A. The influence of the plasma-nitriding temperature on the microstructure evolution and surface properties of additive-manufactured 18Ni300 maraging steel. *Surface and Coatings Technology*. 2022;433:128089.
<https://doi.org/10.1016/j.surfcoat.2022.128089>
 14. Akhmadeev Yu.H., Ivanov Yu.F., Krysin O.V., Lopatin I.V., Petrikova E.A., Rygina M.E. Electron-ion-plasma modification of carbon steel. *High Temperature Material Processes: An International Quarterly of High-Technology Plasma Processes*. 2021;25(1):47–55.
<https://doi.org/10.1615/HighTempMatProc.2021038031>
 15. Ivanov Y., Lopatin I., Denisova Y., Petrikova E., Tolkachev O. Elion method of nitriding of high-chromium stainless steel: Structure and properties. In: *Proceedings – 2020 7th Int. Congress on Energy Fluxes and Radiation Effects, EFRE 2020*. 2020:783–787.
<https://doi.org/10.1109/EFRE47760.2020.9241927>
 16. Ivanov Yu.F., Akhmadeev Yu.H., Lopatin I.V., Petrikova E.A., Denisova Yu.A., Teresov A.D., Krysin O.V. Complex beam-plasma surface treatment of high-chromium steel. *Journal of Physics: Conference Series*. 2018;1115(3):032031.
<https://doi.org/10.1088/1742-6596/1115/3/032031>
 17. Devyatkov B.N., Koval N.N., Shchanin P.M. Obtaining high-current low-energy electron beams in systems with a plasma emitter. *Izvestiya vuzov. Fizika*. 2001;44(9):36–43. (In Russ.).
 - Девятков В.Н., Коваль Н.Н., Щанин П.М. Получение сильноточных низкоэнергетических электронных пучков в системах с плазменным эмиттером. *Известия вузов. Физика*. 2001;44(9):36–43.
 18. Koval' N.N., Ivanov Yu.F. Nanostructuring of surfaces of metalloceramic and ceramic materials by electron-beams. *Russian Physics Journal*. 2008;51(5):505–516.
<https://doi.org/10.1007/s11182-008-9073-7>
 - Коваль Н.Н., Иванов Ю.Ф. Наноструктурирование поверхности металлокерамических и керамических материалов при импульсной электронно-пучковой обработке. *Известия вузов. Физика*. 2008;51(5):60–70.
 19. Shu W.M., Wakai E., Yamanishi T. Blister bursting and deuterium bursting release from tungsten exposed to high fluences of high flux and low energy deuterium plasma. *Nuclear Fusion*. 2007;47(3):201–209.
<https://doi.org/10.1088/0029-5515/47/3/006>
 20. Sznajder M., Geppert U., Dudek M. Degradation of metallic surfaces under space conditions, with particular emphasis on hydrogen recombination processes. *Advances in Space Research*. 2015;56(1):71–84.
<https://doi.org/10.48550/arXiv.1506.01790>
 21. Astrelin V.T., Burdakov A.V., Bykov P.V., Ivanov I.A., Ivanov A.A., Jongen Y., Konstantinov S.G., Kudryavtsev A.M., Kuklin K.N., Mekler K.I., Polosatkin S.V., Postupaev V.V., Rovenskikh A.F., Sinitskiy S.L., Zubairov E.R. Blistering of the selected materials irradiated by intense 200 keV proton beam. *Journal of Nuclear Materials*. 2010;396(1):43–48.
<https://doi.org/10.1016/j.jnucmat.2009.10.051>

Information about the Authors

Сведения об авторах

Yurii F. Ivanov, Dr. Sci. (Phys.-Math.), Prof., Chief Researcher of the Laboratory of Plasma Emission Electronics, Institute of High-Current Electronics, Siberian Branch of the Russian Academy of Sciences

ORCID: 0000-0001-8022-7958

E-mail: yufi55@mail.ru

Elizaveta A. Petrikova, Junior Researcher of the Laboratory of Plasma Emission Electronics, Institute of High Current Electronics, Siberian Branch of the Russian Academy of Sciences

ORCID: 0000-0002-1959-1459

E-mail: elizmarkova@yahoo.com

Anton D. Teresov, Research Associate of the Laboratory of Beam-Plasma Surface Engineering, Institute of High-Current Electronics, Siberian Branch of the Russian Academy of Sciences

ORCID: 0000-0002-5363-0108

E-mail: tad514@yandex.ru

Il'ya V. Lopatin, Cand. Sci. (Eng.), Senior Researcher of the Laboratory of Plasma Emission Electronics, Institute of High Current Electronics, Siberian Branch of the Russian Academy of Sciences

ORCID: 0000-0002-5192-871X

E-mail: lopatin@opee.hcei.tsc.ru

Oleg S. Tolkachev, Junior Researcher of the Laboratory of Plasma Emission Electronics, Institute of High Current Electronics, Siberian Branch of the Russian Academy of Sciences

ORCID: 0000-0001-7816-9920

E-mail: ole.ts@mail.ru

Юрий Федорович Иванов, д.ф.-м.н., профессор, главный научный сотрудник лаборатории плазменной эмиссионной электроники, Институт Сильноточной электроники Сибирского отделения РАН

ORCID: 0000-0001-8022-7958

E-mail: yufi55@mail.ru

Елизавета Алексеевна Петрикова, младший научный сотрудник лаборатории плазменной эмиссионной электроники, Институт сильноточной электроники Сибирского отделения РАН

ORCID: 0000-0002-1959-1459

E-mail: elizmarkova@yahoo.com

Антон Дмитриевич Тересов, научный сотрудник лаборатории пучково-плазменной инженерии поверхности, Институт сильноточной электроники Сибирского отделения РАН

ORCID: 0000-0002-5363-0108

E-mail: tad514@yandex.ru

Илья Викторович Лопатин, к.т.н., старший научный сотрудник лаборатории плазменной эмиссионной электроники, Институт сильноточной электроники Сибирского отделения РАН

ORCID: 0000-0002-5192-871X

E-mail: lopatin@opee.hcei.tsc.ru

Олег Сергеевич Толкачев, младший научный сотрудник лаборатории плазменной эмиссионной электроники, Институт сильноточной электроники Сибирского отделения РАН

ORCID: 0000-0001-7816-9920

E-mail: ole.ts@mail.ru

Contribution of the Authors

Вклад авторов

Yu. F. Ivanov – concept formulation, discussion of results, writing the text, conducting electron microscopic studies, analysis of results.

E. A. Petrikova – conducting tribological and mechanical studies, conducting scanning electron microscopic studies, discussion of results.

A. D. Teresov – selection of optimal electron beam treatment modes, conducting irradiation, discussion of results.

I. V. Lopatin – selection of optimum nitriding modes, conducting experiments on nitriding at different temperatures, discussion of results.

O. S. Tolkachev – conducting electron microscopic studies, analysis of results.

Ю. Ф. Иванов – формулирование концепции работы, обсуждение результатов, написание текста статьи, проведение электронно-микроскопических исследований, анализ результатов.

Е. А. Петрикова – проведение трибологических и механических испытаний, проведение исследований поверхности образцов методами сканирующей электронной микроскопии, обсуждение результатов.

А. Д. Тересов – подбор оптимальных режимов электронно-лучевой обработки образцов, проведение облучения, обсуждение результатов.

И. В. Лопатин – подбор оптимальных режимов азотирования, проведение экспериментов по азотированию образцов при различных температурах, обсуждение результатов.

О. С. Толкачев – проведение электронно-микроскопических исследований образцов, анализ результатов.

Received 21.12.2023

Revised 24.01.2024

Accepted 11.03.2024

Поступила в редакцию 21.12.2023

После доработки 24.01.2024

Принята к публикации 11.03.2024



UDC 536.625:539.25:539.651

DOI 10.17073/0368-0797-2024-4-398-400

Short report
Краткое сообщение

GRADIENT OF MICROHARDNESS IN THE CONTACT ZONE COATING (HEA CoCrFeNiMn) – SUBSTRATE (ALLOY 5083)

M. O. Efimov, I. A. Panchenko, Yu. A. Shlyarova

Siberian State Industrial University (42 Kirova Str., Novokuznetsk, Kemerovo Region – Kuzbass 654007, Russian Federation)

✉ rubannikova96@mail.ru

Abstract. In this work, a coating of a high-entropy alloy CoCrFeNiMn of non-atomic composition is formed on a substrate made of alloy 5083 by the method of wire-arc additive manufacturing (WAAM). The authors investigated the change in microhardness in the contact zone of the coating – substrate system. Using the methods of modern physical materials science, the structural and phase state, defect structure and elemental composition of the coating – substrate system were analyzed. The discovered physical mechanisms contribute to an increase in hardness in the contact zone.

Keywords: microhardness, contact zone, substrate, coating, high-entropy alloy, structure

Acknowledgements: The research was carried out within the framework of the state task of the Ministry of Science and Higher Education of the Russian Federation No. 0809-2021-0013. The authors express their gratitude to professors Yu.F. Ivanov and V.E. Gromov for discussing the results.

For citation: Efimov M.O., Panchenko I.A., Shlyarova Yu.A. Gradient of microhardness in the contact zone coating (HEA CoCrFeNiMn) – substrate (alloy 5083). *Izvestiya. Ferrous Metallurgy*. 2024;67(4):398–400. <https://doi.org/10.17073/0368-0797-2024-4-398-400>

ГРАДИЕНТ МИКРОТВЕРДОСТИ В ЗОНЕ КОНТАКТА ПОКРЫТИЕ (ВЭС CoCrFeNiMn) – ПОДЛОЖКА (СПЛАВ 5083)

М. О. Ефимов, И. А. Панченко, Ю. А. Шлярова

Сибирский государственный индустриальный университет (Россия, 654007, Кемеровская обл. – Кузбасс, Новокузнецк, ул. Кирова, 42)

✉ rubannikova96@mail.ru

Аннотация. В настоящей работе методом проволоочно-дугового аддитивного производства (WAAM) на подложке из сплава 5083 формируется покрытие из высокоэнтروпийного сплава CoCrFeNiMn неэквимономного состава. Авторы исследуют изменение микротвердости в зоне контакта системы покрытие – подложка. С помощью методов современного физического материаловедения проанализированы структурно-фазовое состояние, дефектная структура и элементный состав системы покрытие – подложка. Обнаружены физические механизмы, способствующие повышению твердости в зоне контакта.

Ключевые слова: микротвердость, зона контакта, подложка, покрытие, высокоэнтропийный сплав, структура

Благодарности: Работа выполнена в рамках государственного задания № 0809-2021-0013. Авторы выражают благодарность профессорам Ю.Ф. Иванову и В.Е. Громову за обсуждение результатов.

Для цитирования: Ефимов М.О., Панченко И.А., Шлярова Ю.А. Градиент микротвердости в зоне контакта покрытие (ВЭС CoCrFeNiMn) – подложка (сплав 5083). *Известия вузов. Черная металлургия*. 2024;67(4):398–400. <https://doi.org/10.17073/0368-0797-2024-4-398-400>

In recent years, researchers in physical materials science have focused on high-entropy alloys (HEAs) [1; 2], which exhibit abnormally high values of mixing entropy, surpassing those of complex alloys. The HEA concept involves achieving maximum mixing entropy from five or more elements in various atomic ratios. This results in single-phase structures with significant lattice distortion

and impeded diffusion, leading to enhanced strength properties and stability over a wide temperature range [3 – 5]. Developed HEAs show promise for applications in electronics, nuclear energy, transport engineering, aerospace, and other industries [6; 7]. The use of HEAs is expected to expand as new compositions are developed and their properties investigated. Currently, extensive information

is being gathered and understood about HEA synthesis methods, structural and phase states, defect substructures, and properties.

In this study, the change in microhardness within the contact zone of the HEA CoCrFeNiMn coating on the alloy 5083 substrate was analyzed.

The study used samples of the coating-substrate system, where the coating was a non-equiatomic composition of HEA CoCrFeNiMn, formed on a substrate of alloy 5083 using wire-arc additive manufacturing [3]. The hardness of the material was determined using the Vickers method on a PMT-3 microhardness tester with a load of 5 N. Studies of structural and phase states, defect substructure, and elemental composition were conducted using transmission electron diffraction microscopy on a JEM2100 instrument.

The microhardness of the coating – substrate system varies from 9.9 GPa at the coating – contact zone boundary to 1.5 GPa at the contact zone – substrate boundary. The microhardness of the coating and substrate is 3.0 and 1.0 GPa, respectively (Fig. 1).

The significant change in the microhardness of the contact zone is due to the structural and phase changes of the material when the coating is applied to the substrate. X-ray microanalysis confirmed the chemical homogeneity of the coating and the presence of aluminum atoms, indicating their diffusion from the substrate.

Electron microscope images of the contact zone revealed the formation of a grain-subgrain structure with crystallite sizes ranging from 0.5 to 1.1 μm (Fig. 2, *a*). Within the grains of such a structure, chaotic and cellular dislocation substructures with a scalar density of approximately 10^{10} cm^{-2} are present (Fig. 2, *b*).

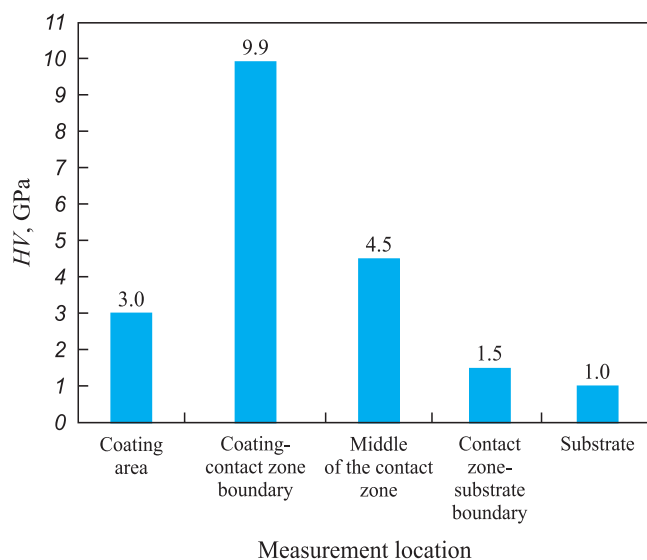


Fig. 1. Change in microhardness of the coating – substrate system

Рис. 1. Изменение микротвердости системы покрытие – подложка

Particles of the second phase were found within the volume of grains and subgrains, as well as at their boundaries. The sizes of these particles in the grain volume range from 15 to 17 nm, and at their boundaries from 30 to 35 nm. Analysis of X-ray diffraction patterns established that the chemical composition of the second-phase particles is Al_3Ni .

Plate-shaped formations were found in the contact zone on the substrate side. Analysis of dark-field images and indexing of the corresponding X-ray diffraction patterns allows us to conclude that these inclusions are iron aluminides of the composition Al_3Fe_4 .

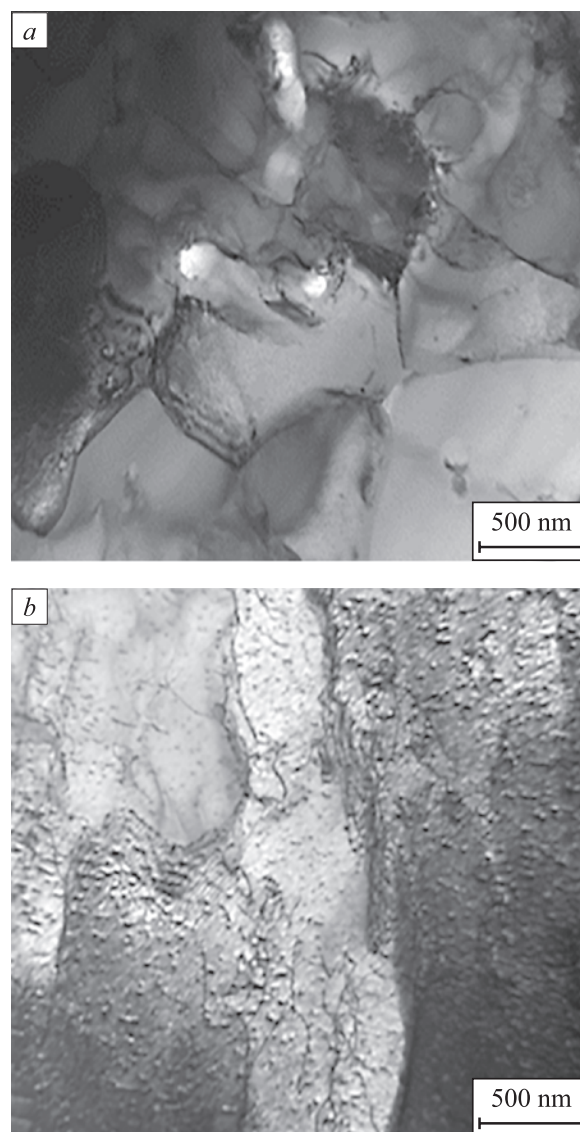


Fig. 2. Electron microscopic images of contact zone of the coating – substrate system:

a – grain-subgrain structure;
b – dislocation substructure

Рис. 2. Электронно-микроскопические изображения зоны контакта системы покрытие – подложка:
a – зеренно-субзеренная структура;
b – дислокационная субструктура

CONCLUSIONS

Analysis of the phase elemental composition and defect substructure suggests that the increase in microhardness in the contact zone of the coating-substrate system is due to several factors: the formation of a submicron grain-subgrain structure containing nanosized second-phase particles, solid-solution strengthening resulting from mutual alloying of the coating and substrate, and the formation of plate-shaped iron aluminides. Additionally, differences in thermophysical characteristics between the coating and the substrate may lead to the formation of internal stress fields in the contact zone.

REFERENCES / СПИСОК ЛИТЕРАТУРЫ

1. Zhang Y., Zuo T.T., Tang Z., Gao M.C., Dahmen K.A., Liaw P.K., Lu Z.P. Microstructures and properties of high-entropy alloys. *Progress in Materials Science*. 2014;61:1–93. <https://doi.org/10.1016/j.pmatsci.2013.10.001>
2. Rogachev A.S. Structure, stability and properties of high-entropy alloys. *Physics of Metals and Metallography*. 2020;121(8):733–764. <https://doi.org/10.1134/S0031918X20080098>
Рогачев А.С. Структура, стабильность и свойства высокоэнтропийных сплавов. *Физика металлов и металловедение*. 2020;121(8):807–841. <https://doi.org/10.31857/S0015323020080094>
3. Gromov V.E., Konovalov S.V., Ivanov Yu.F., Osintsev K.A. Structure and Properties of High-Entropy Alloys. Springer; 2021;107:110. <https://doi.org/10.1007/978-3-030-78364-8>
4. Cantor B. Multicomponent and high entropy alloys. *Entropy*. 2014;16(9):4749–4768. <https://doi.org/10.3390/e16094749>
5. Miracle D.B., Senkov O.N. A critical review of high entropy alloys and related concepts. *Acta Materialia*. 2017;122:448–511. <https://doi.org/10.1016/j.actamat.2016.08.081>
6. Yeh J.–W. Physical metallurgy of high-entropy alloys. *JOM*. 2015;67(10):2254–2261. <http://doi.org/10.1007/s11837-015-1583-5>
7. Tsai M.–H., Yeh J.–W. High-entropy alloys: A critical review. *Materials Research Letters*. 2014;2(3):107–123. <http://doi.org/10.1080/21663831.2014.912690>

Information about the Authors

Mikhail O. Efimov, Candidates for a degree of Cand. Sci.(Eng.) of the Chair of Science named after V.M. Finkel', Siberian State Industrial University

ORCID: 0000-0002-4890-3730

E-mail: moefimov@mail.ru

Irina A. Panchenko, Cand. Sci. (Eng.), Head of the Laboratory of Electron Microscopy and Image Processing, Siberian State Industrial University

ORCID: 0000-0002-1631-9644

E-mail: i.r.i.ss@yandex.ru

Yuliya A. Shlyarova, Postgraduate of the Chair of Science named after V.M. Finkel', Researcher of Laboratory of Electron Microscopy and Image Processing, Siberian State Industrial University

ORCID: 0000-0001-5677-1427

E-mail: rubannikova96@mail.ru

Сведения об авторах

Михаил Олегович Ефимов, соискатель кафедры естественно-научных дисциплин им. профессора В.М. Финкеля, Сибирский государственный индустриальный университет

ORCID: 0000-0002-4890-3730

E-mail: moefimov@mail.ru

Ирина Алексеевна Панченко, к.т.н., заведующий лабораторией электронной микроскопии и обработки изображений, Сибирский государственный индустриальный университет

ORCID: 0000-0002-1631-9644

E-mail: i.r.i.ss@yandex.ru

Юлия Андреевна Шлярова, аспирант кафедры естественно-научных дисциплин им. профессора В.М. Финкеля, научный сотрудник лаборатории электронной микроскопии и обработки изображений, Сибирский государственный индустриальный университет

ORCID: 0000-0001-5677-1427

E-mail: rubannikova96@mail.ru

Contribution of the Authors

M. O. Efimov – sample preparation, microhardness measurement, literary review.

I. A. Panchenko – TEM analysis, formulation of the work concept.

Yu. A. Shlyarova – discussion of results, writing the final version of the article.

Вклад авторов

М. О. Ефимов – подготовка образцов, измерение микротвердости, обзор литературы.

И. А. Панченко – ПЭМ анализ, формулирование концепции работы.

Ю. А. Шлярова – обсуждение результатов, подготовка окончательного варианта статьи.

Received 15.12.2023

Revised 10.01.2024

Accepted 12.02.2024

Поступила в редакцию 15.12.2023

После доработки 10.01.2024

Принята к публикации 12.02.2024



UDC 669.2/.8

DOI 10.17073/0368-0797-2024-4-401-408



Original article

Оригинальная статья

PHASE COMPOSITION AND MICROSTRUCTURE OF INTERMETALLIC ALLOYS OBTAINED USING ELECTRON-BEAM ADDITIVE MANUFACTURING

S. V. Astafurov, E. V. Mel'nikov, E. G. Astafurova[✉], E. A. Kolubaev

Institute of Strength Physics and Materials Science, Siberian Branch of the Russian Academy of Sciences (2/4 Akademicheskii Ave., Tomsk 634055, Russian Federation)

✉ elena.g.astafurova@ispm.su

Abstract. The paper investigates the microstructure and phase composition of nickel- and aluminum-based intermetallic alloys obtained using two-wire electron-beam additive manufacturing (EBAM). Relevance of the research is related to the widespread use of intermetallic alloys based on nickel and aluminum (mainly Ni_3Al) in various high-temperature applications and the need to use modern production methods when creating machine parts and mechanisms from these alloys. Using EBAM, the billets from intermetallic alloys with different ratios of the content of main components were obtained. Change in concentrations of the basic elements was carried out varying the ratio of feed rates of nickel and aluminum wires during additive manufacturing in the range from 1:1 to 3:1, respectively. The results of microscopic studies of the obtained alloys showed that, regardless of nickel content, the obtained alloys are characterized by a large-crystalline structure with grain sizes in the range of 100 – 300 μm for alloys with a component ratio of 1:1 and 150 – 400 μm for alloys with a component ratio of 2:1 and 3:1. At the same time, the alloy with an equal content of base components is characterized by more uniform grain and microstructure compared to those with high content of Ni. By changing the concentration ratio of the components, phase composition of the resulting billet can be purposefully controlled. In the case of an “equiatomic” content of the base components in the alloy, a NiAl -based compound with a small phase content based on the intermetallics Ni_3Al_5 and Ni_3Al is formed. At high concentrations of nickel, the intermetallic Ni_3Al phase is formed, and at a component ratio of 3:1, structure of the resulting billet consists mainly of Ni_3Al phase and the γ solid substitutional solution based on nickel. The paper demonstrates the possibility of direct production of intermetallic alloys with a given phase composition during electron-beam additive manufacturing.

Keywords: intermetallic alloy, additive manufacturing, microstructure, phase composition

Acknowledgements: The work was performed in accordance with the state assignment of the Institute of Strength Physics and Materials Science, Siberian Branch of the Russian Academy of Science, subject no. FWRW-2022-0005. The authors express their gratitude to Cand. Sci. (Phys.-Math.) V.E. Rubtsov and Cand. Sci. (Phys.-Math.) S.Y. Nikonov for their assistance in additive manufacturing of the alloys. The research was carried out using the equipment of the Nanotech Research Center (Institute of Strength Physics and Materials Science, Siberian Branch of Russian Academy of Sciences, Tomsk).

For citation: Astafurov S.V., Mel'nikov E.V., Astafurova E.G., Kolubaev E.A. Phase composition and microstructure of intermetallic alloys obtained using electron-beam additive manufacturing. *Izvestiya. Ferrous Metallurgy*. 2024;67(4):401–408.

<https://doi.org/10.17073/0368-0797-2024-4-401-408>

ФАЗОВЫЙ СОСТАВ И МИКРОСТРУКТУРА ИНТЕРМЕТАЛЛИЧЕСКИХ СПЛАВОВ, ПОЛУЧЕННЫХ МЕТОДОМ ПРОВОЛОЧНОГО ЭЛЕКТРОННО-ЛУЧЕВОГО АДДИТИВНОГО ПРОИЗВОДСТВА

С. В. Астафуров, Е. В. Мельников, Е. Г. Астафурова[✉], Е. А. Колубаев

Институт физики прочности и материаловедения Сибирского отделения РАН (Россия, 634055, Томск, пр. Академический, 2/4)

✉ elena.g.astafurova@ispm.su

Аннотация. В работе проведено исследование микроструктуры и фазового состава интерметаллических сплавов на основе никеля и алюминия, полученных с использованием двухпроволочного электронно-лучевого аддитивного производства (ЭЛАП). Актуальность проведенных исследований связана с широким использованием интерметаллических сплавов на основе никеля и алюминия (преимущественно Ni_3Al) в различных высокотемпературных приложениях и необходимостью использования современных методов производства

при создании деталей машин и механизмов из этих сплавов. С помощью ЭЛАП были получены заготовки интерметаллических сплавов с разным отношением содержания основных компонентов. Изменение концентрации базовых элементов осуществлялось путем изменения соотношения скоростей подачи никелевой и алюминиевой проволок в процессе аддитивного производства в диапазоне от 1:1 до 3:1 соответственно. Результаты микроскопических исследований полученных сплавов показали, что независимо от содержания никеля полученные сплавы характеризуются крупнокристаллической структурой с размерами зерен в диапазоне 100 – 300 мкм для сплавов с соотношением компонентов 1:1 и 150 – 400 мкм для сплавов с соотношением компонентов 2:1 и 3:1. При этом сплав с равным содержанием базовых компонентов характеризуется более однородной зеренной микроструктурой по сравнению со сплавами с высоким содержанием никеля. При изменении соотношения концентрации компонентов, подаваемых в процессе аддитивного производства, можно целенаправленно управлять фазовым составом получаемой заготовки. В случае «эквивалентного» содержания в сплаве базовых компонентов формируется соединение на основе NiAl с небольшим содержанием фаз на основе интерметаллидов Ni_3Al_5 и Ni_3Al . При больших концентрациях никеля формируется интерметаллидная фаза Ni_3Al , а при соотношении компонентов 3:1 структура получаемой заготовки состоит преимущественно из фазы Ni_3Al и γ твердого раствора замещения на основе никеля. В работе продемонстрирована возможность прямого получения интерметаллических сплавов с заданным фазовым составом в процессе электронно-лучевого аддитивного производства.

Ключевые слова: интерметаллический сплав, аддитивное производство, микроструктура, фазовый состав

Благодарности: Работа выполнена в рамках госзадания Института физики прочности и материаловедения Сибирского отделения РАН, тема номер FWRW-2022-0005. Авторы выражают благодарность к.ф.-м.н. В.Е. Рубцову и к.ф.-м.н. С.Ю. Никонову за помощь в аддитивном производстве сплавов. Исследования проведены с использованием оборудования ЦКП «Нанотех» (Институт физики прочности и материаловедения Сибирского отделения РАН, Томск).

Для цитирования: Астафуров С.В., Мельников Е.В., Астафурова Е.Г., Колубаев Е.А. Фазовый состав и микроструктура интерметаллических сплавов, полученных методом проволочного электронно-лучевого аддитивного производства. *Известия вузов. Черная металлургия*. 2024;67(4):401–408. <https://doi.org/10.17073/0368-0797-2024-4-401-408>

INTRODUCTION

Intermetallic alloys are solid materials composed of two or more metallic elements [1]. Unlike traditional alloys, intermetallics feature an ordered crystal structure with strong ionic or covalent bonds [1; 2]. These characteristics give intermetallic compounds a range of unique physical and mechanical properties, including high melting points and exceptional strength, even at extremely high temperatures [1; 2].

One of the most intriguing intermetallic compounds for industrial applications is the Ni_3Al alloy. It boasts high tensile and compressive strength across a broad temperature range, up to 1100 °C [3 – 5], a positive temperature dependence of yield strength between 0 and 800 – 900 °C [3 – 5], and excellent resistance to corrosion, fatigue, creep, and wear, even at elevated temperatures [6 – 8]. These unique properties make nickel and aluminum-based alloys highly valuable in various industries for high-temperature applications, particularly in the production of gas turbine engine blades, turbocharger rotors for diesel power plants, and structural components in the automotive, aerospace, metallurgical, and metal-working sectors [2; 3; 9].

However, these alloys have significant drawbacks, including low plasticity and a tendency toward brittle fracture, which complicates their processing during manufacturing [1; 4; 5]. Traditional powder metallurgy methods – such as casting, sintering, self-propagating high-temperature synthesis, and directional solidification [7; 9; 10] – are not suitable for producing finished products from intermetallic alloys [11 – 13]. As a result, additive manufacturing has emerged as a promising method for producing machine and mechanism parts from nickel aluminide. This process involves creating

a part with a specified shape by sequentially layering and melting powder raw materials or wire using a high-energy beam [10; 11; 14].

In [11], intermetallic alloys with a composite structure were produced using selective laser sintering (SLS) with various mass ratios of aluminum and nichrome alloy powders. The resulting matrix, based on nichrome, was filled with intermetallic particles of Ni_3Al and NiAl. In [15], layered intermetallic structures based on nickel and aluminum with various stoichiometric compositions were obtained using selective laser melting (SLM) technology. In [16], samples of Ni_3Al intermetallic alloy were produced using SLM and direct laser metal deposition (DLMD) methods, exhibiting slight microporosity and microcracks that formed during the cooling of the billets. Notably, the samples produced by SLS showed smaller grain sizes compared to those formed during DLMD additive manufacturing, which is attributed to the different heating and cooling regimes in the additive manufacturing process. The cracking of additive intermetallic billets can be avoided by preheating the powder mixture to 1100 °C [13]. In [17], selective electron-beam melting (SEBM) of the IC21 intermetallic alloy powder, based on nickel and aluminum, resulted in a material with a structure free of pores and predominantly consisting of the γ' phase of Ni_3Al . The alloy demonstrated high strength properties across a wide temperature range (25 – 1000 °C). When forming billets of the IC21 alloy using SLM technology, samples with a dendritic structure were obtained, consisting mainly of the γ' phase of Ni_3Al , with γ -phase and NiMo-phase grains in the dendrites and interdendritic spaces, respectively [18]. The significant cracking observed in the billets during their crystallization process was also highlighted in.

The primary drawbacks of using additive technologies based on dispersed powders as raw materials include the high cost of powders, their rapid oxidation, and low deposition rates, among other issues [12]. A solution to these problems is to use additive manufacturing methods that employ one or more metallic wires of a specified composition as the raw material. In [12], intermetallic alloys were produced using the wire and arc additive manufacturing (WAAM) method, utilizing nickel and aluminum wires. The refractory nickel wire was melted by an electric arc source, while the low-melting aluminum wire was added directly to the melt bath. It was shown that by adjusting the wire feed rates, the phase composition of the resulting compounds (Ni_3Al , NiAl , etc.) could be altered. In [14; 19], M. Zhang and co-authors demonstrated that when using a two-wire feed in WAAM, a dendritic $\gamma + \gamma'$ structure with γ' -phase layers in the interdendritic spaces of the Ni_3Al intermetallic alloy forms, and the strength of the resulting billets is comparable to commercial alloys.

Despite its high productivity and the absence of a need for complex and expensive equipment, a drawback of the WAAM method is that the additive manufacturing process occurs in an inert gas environment, which does not fully protect the product from harmful impurities and oxidation. From this perspective, the most effective approach is to use additive technologies where the billets are printed in a vacuum. Such methods include electron-beam additive manufacturing (EBAM) [20].

This study focuses on investigating the structure and phase composition of nickel- and aluminum-based intermetallic alloys produced using EBAM with aluminum and nickel wires.

EXPERIMENTAL METHODOLOGY

In this study, billets in the form of vertical walls with dimensions of $120 \times 24 \times 7$ mm and made of nickel and aluminum-based alloys, were produced using a laboratory electron-beam additive manufacturing (EBAM) setup developed in the Institute of Strength Physics and Materials Science SB RAS. To produce the billets, two wires with a diameter of 1.2 mm – nickel (NP-2 alloy, 99.5 wt. % Ni) and aluminum (ESAB OK Autrod 1070 alloy, 99.8 wt. % Al) – were fed into the melt bath. The additive manufacturing process was carried out under the following parameters: beam current (I) of $30 \div 35$ mA, beam scanning speed (V_b) of 2.5 mm/s along the deposited layer, accelerating voltage (U) of 30 kV, elliptical beam scan from the center, and a scan frequency of 100 Hz. The process was conducted in a vacuum at a pressure of 10^{-3} Pa. The billets were formed by sequential deposition of layers of uniform thickness onto a mild steel substrate. To obtain intermetallic alloys with varying volumetric contents of components, the feed rate ratios

of the nickel and aluminum wires were adjusted, resulting in billets with the following nickel-to-aluminum ratios: 1:1 (Ni + Al), 2:1 (2Ni + Al), and 3:1 (3Ni + Al).

Samples for structural and mechanical studies were cut from the cross-sections of the billets. For microstructural and phase analysis, the samples were mechanically polished, then electrolytically grinded in a solution of 25 g CrO_3 and 210 ml H_3PO_4 , and finally etched in a solution of 90 % CH_3COOH and 10 % HClO_4 . The microstructure was examined using optical microscopy (OM, Altami MET 1C) and scanning electron microscopy (SEM, Zeiss Leo Evo 50 with an energy-dispersive X-ray spectroscopy (EDS) attachment). X-ray structural and phase analyses were conducted using a Dron-3M diffractometer (Burevestnik) with CoK_α radiation. The lattice parameters of the phases were determined by extrapolating the dependence of the ($ahkl$), values, determined for each X-ray line with indices (hkl), on the function ($\cos\theta \cot\theta$) [21].

RESULTS AND DISCUSSION

Microstructure of alloys produced by EBAM

Fig. 1 presents OM and SEM images of the microstructure of nickel and aluminum-based intermetallic alloys produced using EBAM technology. Metallographic analysis revealed that the billets were free of macro- and microscopic pores or cracks. All three alloys exhibited a coarse-grained layered structure. Within the grains, a dendritic microstructure of different morphology often became visible during electrolytic polishing: depending on the grain orientation relative to the polished surface, either extended, wellformed dendritic branches or broken or partially dissolved dendritic lamellae could be observed. Additionally, homogeneous contrast areas (layers) were noted in the images, where no segregation was detected (Fig. 1).

The Ni + Al alloy demonstrated a fairly homogeneous structure with infrequent interlayers. On a macroscopic level, its structure was more uniform than that of the 2Ni + Al and 3Ni + Al alloys in terms of forming a layered structure. Meanwhile, the intragranular microstructure of the equiatomic alloy showed little variation along the height of the billet (Fig. 1, *a, b*). Most often, equiaxed grains ranging from 100 to 300 μm in size were observed (Fig. 1, *a, b*). The 2Ni + Al and 3Ni + Al alloys were characterized by a more heterogeneous structure, with relatively thick interlayers (up to 200 μm thick) and grains elongated in the direction of billet growth (Fig. 1, *c – e*), with grain sizes ranging from 150 to 400 μm . Notably, in alloys with higher nickel content, the dendrites were narrower, and their branches were often intact, indicating a significantly higher density of dendrite/interdendritic boundaries compared to the Ni + Al alloy.

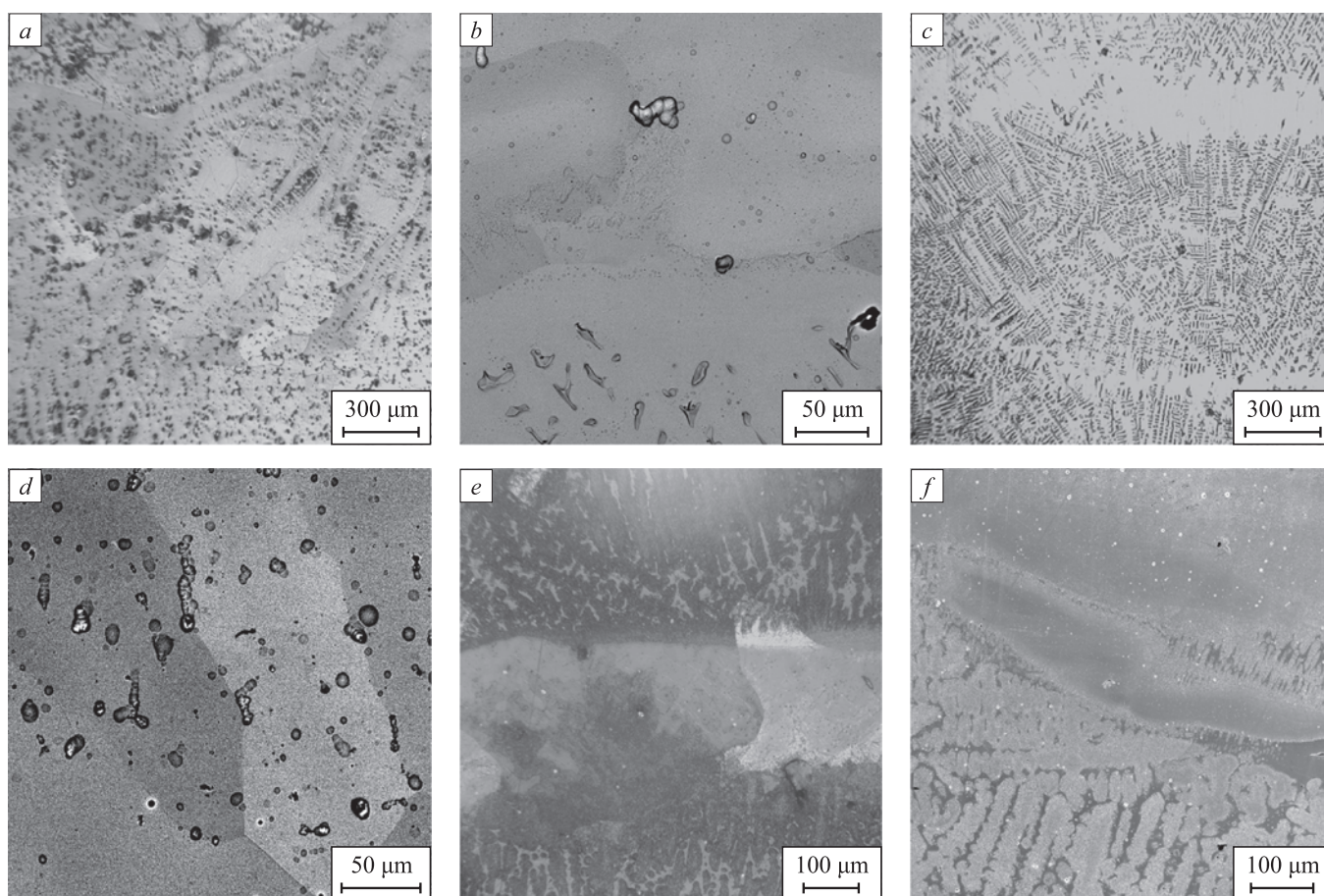


Fig. 1. Metallographic (a, c, e) and scanning electron microscopy (b, d, f) images of microstructure of Ni + Al (a, b), 2Ni + Al (c, d) and 3Ni + Al (e, f) intermetallic alloys

Рис. 1. ОМ (a, c, e) и СЭМ (b, d, f) изображения микроструктуры интерметаллических сплавов Ni + Al (a, b), 2Ni + Al (c, d) и 3Ni + Al (e, f)

Thus, using two-wire feed EBAM with an equal component ratio results in a homogeneous billet (in terms of microstructure) that is free of macro- and microscopic defects (pores, cracks, etc.) immediately after additive manufacturing.

Phase composition of alloys obtained by EBAM

According to the phase diagram of the nickel – aluminum system, alloys within this binary system can exist in the following phase states [22 – 24]:

- NiAl₃ (orthorhombic lattice, nickel content: 25 at. %);
- Ni₂Al₃ (trigonal crystal lattice, homogeneity range for nickel: 37 – 41 at. %);
- NiAl (BCC lattice, homogeneity range for nickel: 42 – 69 at. %);
- Ni₅Al₃ (orthorhombic crystal lattice, homogeneity range for nickel: 64 – 68 at. %);
- Ni₃Al (γ'-phase with FCC lattice (L1₂ superstructure), homogeneity range for nickel: 73 – 75 at. %);

– Ni₃Al (γ-phase, disordered solid solution with FCC lattice with homogeneity region for nickel: 73 – 75 at. %).

In this study of additive manufacturing of intermetallic alloys, the nickel content fed into the billet during EBAM is relatively high (according to the chemical composition of the NP-2 alloy, not less than 49.5 wt. % for the Ni + Al billet). Therefore, the expected phases in the resulting billets, based on the phase diagram, include NiAl, Ni₅Al₃, Ni₃Al, and a nickel-based alloy enriched with aluminum through a substitution mechanism (when the nickel content in the system exceeds 75 at. %).

X-ray phase and X-ray microanalyses revealed that the phase composition of the billets produced by EBAM is determined by the feed rate ratio of nickel and aluminum wires into the melt bath, or, in other words, by the mass ratio of the components of forming the intermetallic alloy. Figs. 2 and 3 show X-ray patterns and SEM images with marked EDS spectrum areas for the obtained billets. The table provides data on the chemical composition and corresponding phases in different areas of the examined samples (as per Fig. 3), obtained from EDS analysis for the three billets with different compo-

nent ratios of nickel and aluminum (phases were identified based on a comparison of the chemical composition in the EDS spectrum area with the “nickel – aluminum” phase diagram [22 – 24]).

Fig. 2, *a* shows that when the feed rate ratio of the two wires is Ni = 1:1, the resulting billet has a heterophase structure composed of NiAl, Ni₅Al₃, and Ni₃Al phases. However, according to X-ray phase analysis, the Ni₃Al intermetallic phase is not the predominant phase, and EDS analysis does not detect this phase at all (Fig. 3, *a*, see the Table). Consequently, in the EBAM process, when nickel and aluminum wires are fed into the melt bath at equal speeds, i.e., with a near-equal mass ratio of nickel and aluminum, the formed intermetallic alloy predominantly consists of NiAl and Ni₅Al₃ phases.

Increasing the wire feed rate ratio to Ni:Al = 2:1 in the EBAM process results in an intermetallic alloy with a more complex phase composition. According to the X-ray phase study (Fig. 2, *b*), the formed billet has a heterophase structure consisting of NiAl, Ni₅Al₃, Ni₃Al, and Ni phases. At the same time, EDS analysis indicates that the main phase in this case is Ni₃Al, with the content of the other three phases being relatively small (Fig. 2, *b*, see the Table).

Further increasing the wire feed rate ratio to Ni:Al = 3:1 leads to the formation of a two-phase alloy based on Ni and Ni₃Al (Fig. 2, *c*, Fig. 3, *c*, Table). In this case, the formed Ni₃Al intermetallic phase has a lattice parameter of $a = 0.3572$ nm. This value is lower than the typical value for the γ' -phase of $a = 0.3589$ nm (for the L1₂ superstructure [23]). Such differences may be due to the formation of a two-phase composition ($\gamma + \gamma'$) in the Ni₃Al grains during EBAM, i.e., the formation of regions of disordered γ' -solid solution based on Ni₃Al together with the ordered γ -phase. On the other hand, the lattice parameter of Ni in the formed alloy is higher than that of pure FCC nickel ($a = 0.3568$ nm vs. $a = 0.3526$ nm [25]). This may be due to the formation of a solid solution of aluminum in nickel via the substitution mechanism.

The results of X-ray phase analysis and energy-dispersive spectroscopy (EDS) of the intermetallic alloys produced by EBAM showed that their phase composition generally corresponds to the mass ratio of the initial materials (nickel and aluminum wires) fed into the melt bath during additive manufacturing. For instance, with a Ni ratio of 1:1, the primary phase is NiAl; at a ratio of 2:1, a significant portion of the Ni₃Al phase is formed, with the excess aluminum being redistributed to form Ni₅Al₃ grains. When the nickel content is three times that of aluminum, the primary phase is Ni₃Al. Moreover, X-ray phase and EDS analyses did not detect any unreacted aluminum in the resulting alloys, indicating that all the alu-

minum was fully incorporated into the formation of intermetallic compounds during the EBAM process.

Thus, the study results demonstrate that the EBAM process allows for the formation of nickel- and alumi-

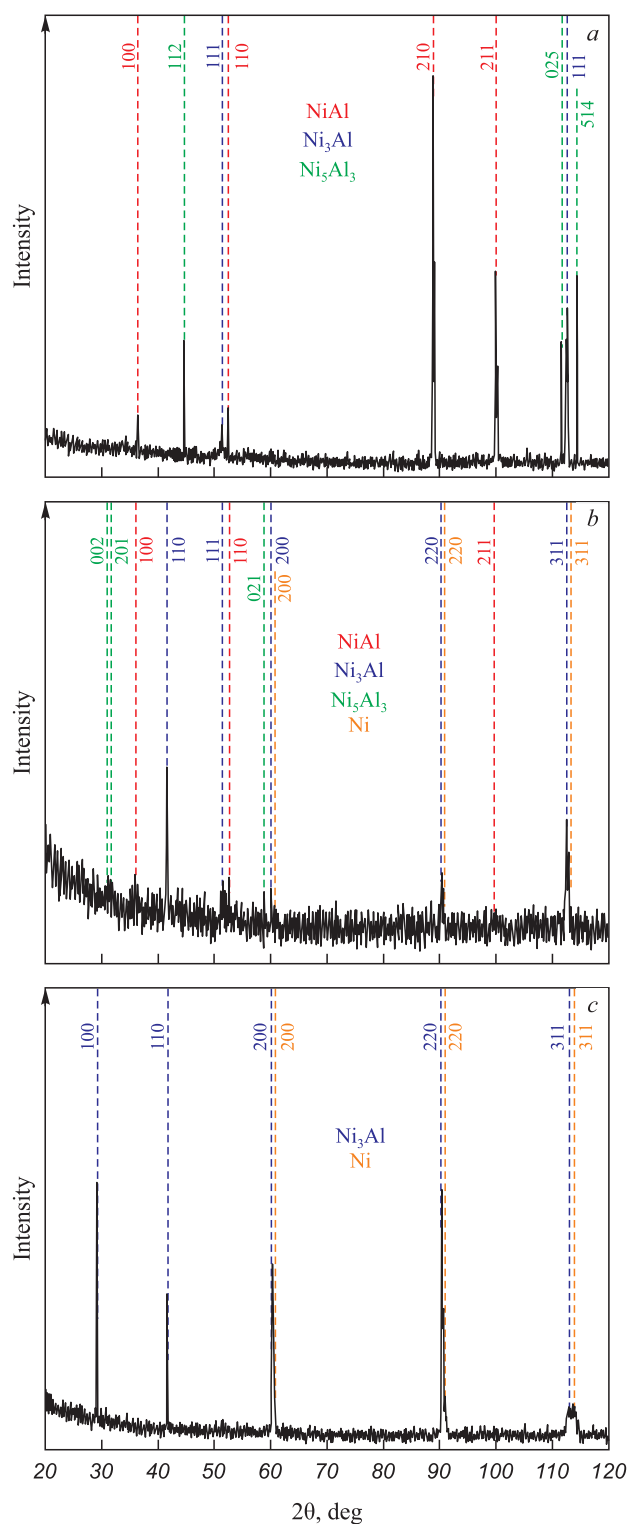


Fig. 2. XRD-patterns of intermetallic alloys Ni + Al, 2Ni + Al and 3Ni + Al (*a – c*)

Рис. 2. Рентгенограммы интерметаллических сплавов Ni + Al, 2Ni + Al и 3Ni + Al (*a – c*)

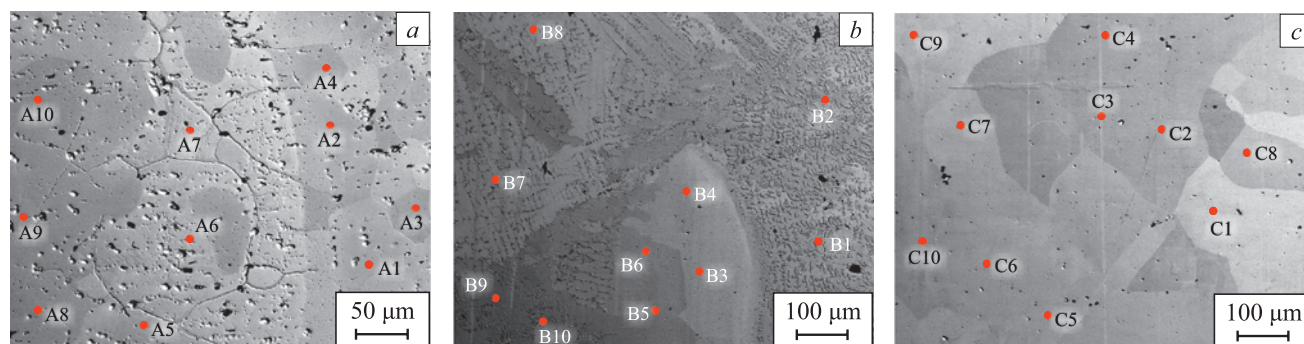


Fig. 3. SEM-images of microstructure of intermetallic alloys
Ni + Al, 2Ni + Al and 3Ni + Al (a – c) with EDS spectra positions (Table)

Рис. 3. СЭМ изображения микроструктуры интерметаллических сплавов
Ni + Al, 2Ni + Al и 3Ni + Al (a – c) с нанесенными областями определения ЭДС спектров (см. таблицу)

Chemical and phase composition of intermetallic alloys in the zones of EDS analysis shown in Fig. 3

Химический и фазовый составы интерметаллических сплавов в областях проведения ЭДС анализа, обозначенных на рис. 3

Ni:Al = 1:1			Ni:Al = 2:1			Ni:Al = 3:1		
Spectrum	Al/Ni, at. %	Phase	Spectrum	Al/Ni, at. %	Phase	Spectrum	Al/Ni, at. %	Phase
A1	42.5/57.5	NiAl	B1	40.6/59.4	NiAl	C1	18.2/81.8	Ni ₃ Al + Ni
A2	41.8/58.2	NiAl	B2	30.6/69.4	Ni ₅ Al + Ni ₃ Al	C2	16.1/83.9	Ni ₃ Al + Ni
A3	42.8/57.2	NiAl	B3	25.9/74.1	Ni ₃ Al	C3	15.4/84.6	Ni ₃ Al + Ni
A4	40.7/59.3	NiAl	B4	26.3/73.7	Ni ₃ Al	C4	15.1/84.9	Ni ₃ Al + Ni
A5	35.0/65.0	Ni ₅ Al ₃	B5	35.2/64.8	Ni ₅ Al ₃	C5	14.9/85.1	Ni ₃ Al + Ni
A6	36.1/63.9	Ni ₅ Al ₃	B6	22.7/77.3	Ni ₃ Al + Ni	C6	14.5/85.5	Ni ₃ Al + Ni
A7	36.2/63.8	Ni ₅ Al ₃	B7	27.4/72.6	Ni ₃ Al	C7	15.1/84.9	Ni ₃ Al + Ni
A8	36.3/63.7	Ni ₅ Al ₃	B8	26.9/73.1	Ni ₃ Al	C8	18.8/81.2	Ni ₃ Al + Ni
A9	37.6/62.4	NiAl	B9	26.6/73.4	Ni ₃ Al	C9	13.5/86.5	Ni ₃ Al + Ni
A10	37.1/62.9	NiAl	B10	46.0/54.0	NiAl	C10	15.3/84.7	Ni ₃ Al + Ni

num-based intermetallic alloys with a predetermined phase composition by varying the mass ratio of the components fed into the melt bath.

CONCLUSIONS

Using EBAM technology with a two-wire feed, billets of nickel- and aluminum-based intermetallic alloys with varying component contents were produced. The mass ratio of nickel to aluminum was adjusted by varying the feed rates of the two wires into the melt bath during the additive manufacturing process. The resulting billets were characterized by a coarse-grained, layered structure. The alloy with an equal content of nickel and aluminum exhibited a more homogeneous internal structure compared to the alloys with ratios of 2:1 and 3:1.

The phase composition of the resulting alloys was also determined by the mass ratio of the components used in the additive manufacturing process. When the wire

feed rate ratio was 1:1, a NiAl-based alloy was formed with a small content of Ni₃Al₅ and Ni₃Al phases. Increasing the nickel content alters the phase composition of the intermetallic alloy, and at a nickel-to-aluminum ratio of 3:1, the structure of the resulting billet predominantly consists of (γ + γ') Ni₃Al and a γ-substitutional solid solution based on nickel with a small amount of aluminum.

The results of this study demonstrated the fundamental possibility of producing nickel- and aluminum-based intermetallic alloys with a specified chemical composition using EBAM technology.

REFERENCES / СПИСОК ЛИТЕРАТУРЫ

- Jozwik P., Polkowski W., Bojar Z. Applications of Ni₃Al based intermetallic alloys – current stage and potential perspectives. *Materials*. 2015;8(5):2537–2568. <https://doi.org/10.3390/ma8052537>

2. Westbrook J.H., Fleischer R.L. Structural Applications of Intermetallic Compounds. Vol. 3. New York: John Wiley and Son Ltd.; 2000:292.
3. Bochenek K., Basista M. Advances in processing of NiAl intermetallic alloys and composites for high temperature aerospace applications. *Progress in Aerospace Sciences*. 2015;79: 136–146. <https://doi.org/10.1016/j.paerosci.2015.09.003>
4. Iwabuchi Y., Kobayashi I. Various properties of dual-phase intermetallic compound in Ni–Al system. *Materials Science*. 2010;638–642:1348–1352. <https://doi.org/10.4028/www.scientific.net/MSF.638-642.1348>
5. Lu Y., Gu J., Kim S., Hong H., Choi H., Lee J. Tensile behavior of directionally solidified Ni₃Al intermetallics with different Al contents and solidification rates. *Metals and Materials International*. 2014;20:221–227. <https://doi.org/10.1007/s12540-014-1021-1>
6. Sheng L.Y., Zhang W., Guo J.T., Wang Z.S., Ovcharenko V.E., Zhou L.Z., Ye H.Q. Microstructure and mechanical properties of Ni₃Al fabricated by thermal explosion and hot extrusion. *Intermetallics*. 2009;17(7):572–577. <https://doi.org/10.1016/j.intermet.2009.01.004>
7. Ovcharenko V.E., Boyangin E.N., Myshlyaev M.M., Ivanov Yu.F., Ivanov K.V. Formation of a multi-grain structure and its influence on strength and plasticity of the Ni₃Al intermetallic compound. *Fizika tverdogo tela*. 2015;57(7): 1270–1276. (In Russ.)
Овчаренко В.Е., Боянгин Е.Н., Мышляев М.М., Иванов Ю.Ф., Иванов К.В. Формирование мультigrанной структуры и ее влияние на прочность и пластичность интерметаллического соединения Ni₃Al. *Физика твердого тела*. 2015;57(7):1270–1276.
8. Guo J., Sheng L., Xie Y., Zhang Z., Ovcharenko V., Ye H. Microstructure and mechanical properties of Ni₃Al and Ni₃Al-B alloys fabricated by SHS/HE. *Intermetallics*. 2011;19(2):137–142. <https://doi.org/10.1016/j.intermet.2010.08.027>
9. Liu C.T., Sikka V.K. Nickel aluminides for structural use. *JOM*. 1986;38:19–21. <https://doi.org/10.1007/BF03257837>
10. Awotunde M.A., Ayodele O.O., Adegbenjo A.O., Okoro A.M., Shongwe M.B., Olubambi P.A. NiAl intermetallic composites – a review of processing methods, reinforcements and mechanical properties. *The International Journal of Advanced Manufacturing Technology*. 2019;104:1733–1747. <https://doi.org/10.1007/s00170-019-03984-9>
11. Shishkovsky I.V. Laser-controlled intermetallics synthesis during surface cladding. *Laser Surface Engineering*. 2015;237–286. <https://doi.org/10.1016/B978-1-78242-074-3.00011-8>
12. Meng Y., Li J., Gao M., Zeng X. Microstructure characteristics of wire arc additive manufactured Ni – Al intermetallic compounds. *Journal of Manufacturing Processes*. 2021;68(A):932–939. <https://doi.org/10.1016/j.jmapro.2021.06.022>
13. Müller M., Heinen B., Riede M., López E., Brückner F., Leyens C. Additive manufacturing of β -NiAl by means of laser metal deposition of pre-alloyed and elemental powders. *Materials*. 2021;14(9):2246. <https://doi.org/10.3390/ma14092246>
14. Zhang M., Wang Y., Yang Z., Ma Z., Wang Z., Wang D. Microstructure and mechanical properties of twin wire and arc additive manufactured Ni₃Al-based alloy. *Journal of Materials Processing Technology*. 2022;303:117529. <https://doi.org/10.1016/j.jmatprotec.2022.117529>
15. Nazarov A., Safronov V.A., Khmyrov R.S., Shishkovsky I. Fabrication of gradient structures in the Ni – Al system via SLM process. *Procedia IUTAM*. 2017;23:161–166. <https://doi.org/10.1016/j.piutam.2017.06.017>
16. Kotoban D., Nazarov A., Shishkovsky I. Comparative study of selective laser melting and direct laser metal deposition of Ni₃Al intermetallic alloy. *Procedia IUTAM*. 2017;23: 138–146. <https://doi.org/10.1016/j.piutam.2017.06.014>
17. Yao Y., Xing C., Peng H., Guo H., Chen B. Solidification microstructure and tensile deformation mechanisms of selective electron beam melted Ni₃Al-based alloy at room and elevated temperatures. *Materials Science and Engineering: A*. 2021;802:140629. <https://doi.org/10.1016/j.msea.2020.140629>
18. Chai H., Wang L., Lin X., Zhang S., Yang H., Huang W. Microstructure and cracking behavior of Ni₃Al-based IC21 alloy fabricated by selective laser melting. *Materials Characterization*. 2023;196:112592. <https://doi.org/10.1016/j.matchar.2022.112592>
19. Zhang M., Wang Y., Ma Z., Wang Z., Yang Z. Non-uniform high-temperature oxidation behavior of twin wire and arc additive manufactured Ni₃Al-based alloy. *Journal of Manufacturing Processes*. 2022;84:522–530. <https://doi.org/10.1016/j.jmapro.2022.10.035>
20. Kolubaev E.A., Rubtsov V.E., Chumaevsky A.V., Astafurova E.G. Micro-, meso- and macrostructural design of bulk metallic and polycrystalline materials by wire-feed electron-beam additive manufacturing. *Physical Mesomechanics*. 2022;25:479–491. <https://doi.org/10.1134/S1029959922060017>
21. Naidu S.V.N., Singh T. X-ray characterization of eroded 316 stainless steel. *Wear*. 1993;166(2):141–145. [https://doi.org/10.1016/0043-1648\(93\)90255-K](https://doi.org/10.1016/0043-1648(93)90255-K)
22. Lyakishev N.P. State Diagrams of Double Metal Systems; Handbook. Vol. 1. Moscow: Mashinostroenie; 1997:1024. (In Russ.)
Лякишев Н.П. Диаграммы состояния двойных металлических систем. Т. 1. Москва: Машиностроение; 1997:1024.
23. Kovtunov A.I., Myamin S.V. Intermetallic Alloys: An electronic textbook. Tolyatti: Izd-vo TSU; 2018:77. (In Russ.)
Ковтунов А.И., Мямин С.В. Интерметаллидные сплавы. Тольятти: Изд-во ТГУ; 2018:77.
24. Nash P., Singleton M.F., Murray J.L. Phase Diagrams of Binary Nickel Alloys. ASM International, Materials Park, OH; 1991:3–11.
25. Hermann K. Crystallography and Surface Structure: An Introduction for Surface Scientists and Nanoscientists. Weinheim: Wiley; 2011:298. <http://dx.doi.org/10.1002/9783527633296>

Information about the Authors

Сведения об авторах

Sergei V. Astafurov, Cand. Sci. (Phys.-Math.), Senior Researcher of the Laboratory of Physics of Hierarchical Structures in Metals and Alloys, Institute of Strength Physics and Materials Science, Siberian Branch of Russian Academy of Sciences

ORCID: 0000-0003-3532-3777

E-mail: svastafurov@gmail.com

Evgenii V. Mel'nikov, Junior Researcher of the Laboratory of Physics of Hierarchical Structures in Metals and Alloys, Institute of Strength Physics and Materials Science, Siberian Branch of Russian Academy of Sciences

ORCID: 0000-0001-8238-6055

E-mail: melnickow-jenya@yandex.ru

Elena G. Astafurova, Dr. Sci. (Phys.-Math.), Assist. Prof., Head of the Laboratory of Physics of Hierarchical Structures in Metals and Alloys, Institute of Strength Physics and Materials Science, Siberian Branch of Russian Academy of Sciences

ORCID: 0000-0002-1995-4205

E-mail: elena.g.astafurova@ispms.ru

Evgenii A. Kolubaev, Dr. Sci. (Eng.), Director, Institute of Strength Physics and Materials Science, Siberian Branch of the Russian Academy of Sciences

ORCID: 0000-0001-7288-3656

E-mail: eak@ispms.ru

Сергей Владимирович Астафуров, к.ф.-м.н., старший научный сотрудник лаборатории физики иерархических структур в металлах и сплавах, Институт физики прочности и материаловедения Сибирского отделения РАН

ORCID: 0000-0003-3532-3777

E-mail: svastafurov@gmail.com

Евгений Васильевич Мельников, младший научный сотрудник лаборатории физики иерархических структур в металлах и сплавах, Институт физики прочности и материаловедения Сибирского отделения РАН

ORCID: 0000-0001-8238-6055

E-mail: melnickow-jenya@yandex.ru

Елена Геннадьевна Астафурова, д.ф.-м.н., доцент, заведующий лабораторией физики иерархических структур в металлах и сплавах, Институт физики прочности и материаловедения Сибирского отделения РАН

ORCID: 0000-0002-1995-4205

E-mail: elena.g.astafurova@ispms.ru

Евгений Александрович Колубаев, д.т.н., директор, Институт физики прочности и материаловедения Сибирского отделения РАН

ORCID: 0000-0001-7288-3656

E-mail: eak@ispms.ru

Contribution of the Authors

Вклад авторов

S. V. Astafurov – literary review, microstructural studies, analysis of results, X-ray studies, writing the text, design of the article.

E. V. Mel'nikov – literary review, sample preparation, analysis and graphical representation of results.

E. G. Astafurova – scientific guidance, reviewing and editing of the final version of the article.

E. A. Kolubaev – scientific guidance, reviewing and editing of the final version of the article.

С. В. Астафуров – обзор литературы, проведение микроструктурных исследований, проведение рентгеновских исследований, анализ результатов, написание текста рукописи, оформление статьи.

Е. В. Мельников – обзор литературы, подготовка образцов, анализ и графическое представление полученных результатов.

Е. Г. Астафурова – научное руководство исследованиями, редактирование финальной версии статьи.

Е. А. Колубаев – научное руководство, редактирование финальной версии статьи.

Received 21.06.2023

Revised 10.01.2024

Accepted 20.05.2024

Поступила в редакцию 21.06.2023

После доработки 10.01.2024

Принята к публикации 20.05.2024



UDC 621.791.052:539.431

DOI 10.17073/0368-0797-2024-4-409-416



Original article

Оригинальная статья

LOW-CYCLE FATIGUE OF WELDED JOINT FROM STEEL OF X70 STRENGTH CLASS

A. A. Galkin, Yu. G. Kabaldin, Yu. S. Mordovina , M. S. Anosov

R.E. Alekseev Nizhny Novgorod State Technical University (24 Minina Str., Nizhny Novgorod 603022, Russian Federation)

 ips4@nntu.ru

Abstract. Steels of X70 strength class are particularly widely used in the field of heavy engineering. One of the most important issues when choosing steel for structures is its behavior under cyclic loads. It is difficult to find a description of the behavior of all zones of the welded joint under fatigue. The purpose of this study was to determine the fatigue characteristics of welded joints made of the Russian analogue of S690QL steel with fixation of acoustic and magnetic parameters for their use in the diagnosis. The objects of the study were the samples from domestic steel of X70 strength class. The chemical composition was determined using optical emission spectrometry. The grinds for microstructural analysis were prepared according to the standard technique with etching in the metal. The fatigue test was carried out on a specialized test bench. The authors used the acoustic system AIS NRK-3 for acoustic measurements and the acoustic parameter D – as an informative parameter. A MA-412MM coercitimeter was applied to evaluate the magnetic characteristics. The following were evaluated: residual magnetization B_r , coercive force H_c , H_c/B_r ratio. The smallest number of cycles corresponds to the deposited metal zone. The decrease in amplitude showed a significant variation in the behavior of the material depending on the junction zone. However, the curves for heat affected zone (HAZ) and the deposited metal are practically the same. HAZ differs to a lesser extent from the base metal than the deposited metal zone. The graph of the acoustic parameter in its form is the reverse of the magnetic characteristics graph. Thus, there is a minimum for the acoustic parameter, depending on the operating time, and a maximum for the magnetic characteristics. For both graphs, the extremum is the point corresponding to the operating time of 0.6.

Keywords: fatigue, low-cycle fatigue, welded joint, acoustic parameter, coercive force, residual magnetization, fatigue of welded joints, X70 strength class

For citation: Galkin A.A., Kabaldin Yu.G., Mordovina Yu.S., Anosov M.S. Low-cycle fatigue of welded joint from steel of X70 strength class. *Izvestiya. Ferrous Metallurgy*. 2024;67(4):409–416. <https://doi.org/10.17073/0368-0797-2024-4-409-416>

ИССЛЕДОВАНИЕ МАЛОЦИКЛОВОЙ УСТАЛОСТИ ЗОН СВАРНОГО СОЕДИНЕНИЯ СТАЛИ КЛАССА ПРОЧНОСТИ X70

А. А. Галкин, Ю. Г. Кабалдин, Ю. С. Мордовина , М. С. Аносов

Нижегородский государственный технический университет им. Р.Е. Алексеева (Россия, 603022, Нижний Новгород, ул. Минина, 24)

 ips4@nntu.ru

Аннотация. Широкое применение в области тяжелого машиностроения получили стали класса прочности X70. Одним из наиболее важных вопросов при выборе стали для конструкций является ее поведение при циклических нагрузках. В научной литературе трудно найти описание поведения всех зон сварного соединения при усталости. Поэтому целью данного исследования является определение характеристик усталостной прочности сварных соединений из российского аналога стали S690QL с фиксацией параметров акустической и магнитной дефектоскопии для их применения при диагностике конструкций во время эксплуатации. В качестве объекта исследования были взяты образцы из отечественной стали класса прочности X70. Химический состав определялся с помощью оптико-эмиссионной спектроскопии. Подготовка шлифов для микроструктурного анализа проводилась по стандартной методике с травлением в нитале. Испытание на усталость проводилось на специализированном стенде. Для акустических измерений применяли акустический комплекс АИС НРК-3, в качестве информативного параметра использовался акустический параметр D . Для оценки магнитных характеристик использовался коэрцитиметр МА-412ММ. Оценивались остаточная намагниченность B_r , коэрцитивная сила H_c , отношение H_c/B_r . Наименьшее количество циклов соответствует зоне наплавленного металла. Снижение амплитуды показало значительный разбег в поведении материала в зависимости от зоны соединения. Однако кривые для зоны термического влияния (ЗТВ) и для наплавленного металла практически совпадают. При этом ЗТВ в меньшей степени отличается от основного металла, чем зона наплавленного металла. График акустического параметра по своему виду является обратным по отношению к графику магнитных характеристик. Так, для акустического

параметра в зависимости от наработки имеется минимум, а для магнитных характеристик – максимум. Но для обоих графиков экстремумом является точка, соответствующая наработке 0,6.

Ключевые слова: усталость, малоцикловая усталость, сварные соединения, акустический параметр, коэрцитивная сила, остаточная намагниченность, усталость сварных соединений, класс прочности X70

Для цитирования: Галкин А.А., Кабалдин Ю.Г., Мордовина Ю.С., Аносов М.С. Исследование малоциклового усталости зон сварного соединения стали класса прочности X70. *Известия вузов. Черная металлургия*. 2024;67(4):409–416.
<https://doi.org/10.17073/0368-0797-2024-4-409-416>

INTRODUCTION

High-strength steel with a yield strength of 690 MPa (X70 strength class) is widely used in the production of earth-moving machinery, lifting machines, and cranes [1]. These high-strength steels are often defined as having a tensile strength of 1800 – 2000 MPa [2; 3]. However, in the same industries, steels referred to as High Strength Steel (HSS) in foreign literature are also used, with tensile strength starting from as low as 490 MPa [4; 5].

This class of steel was developed by combining alloying with controlled rolling technologies. It includes: S700MC (standard EN 10149-2); S690Q, S690QL, S690QL1 (standard EN 10025-6); QStE 690 TM (Germany); Strenx 700MC (SSAB); E 690 D (France); A514 (AISI, USA). In Russia, analogous steels have been developed under import substitution conditions.

One of the most important questions when choosing steel for structures is its behavior under cyclic loads, which lead to fatigue failure. Traditionally, low-cycle and high-cycle fatigue are distinguished [6]. Recently, the concepts of gigacycle and even teracycle fatigue (hyperfatigue failure) have been introduced. These are differentiated by the number of working cycles (N) preceding failure:

- low-cycle fatigue: $N \leq 5 \cdot 10^4$ cycles;
- high-cycle fatigue: $5 \cdot 10^4 < N \leq 10^8$ cycles;
- gigacycle fatigue: $N > 10^8$ cycles [7; 8];
- teracycle fatigue: $N = 10^{10} \dots 10^{12}$ cycles [9].

This study examines low-cycle fatigue (LCF) – the fatigue of material where damage occurs under elastoplastic deformation in a microvolume. The maximum durability before failure is approximately $N_k = 5 \cdot 10^4$ cycles [10]. Low-cycle failure in mechanical engineering is most often associated with comparatively rare but repetitive overloads. This type can be encountered in any branches of mechanical engineering but is particularly frequent in aircraft engines, aerospace industry, powertrains in the automotive industry, and power plants [11; 12].

Mainly, fatigue resistance characteristics are determined for metal not subjected to welding, or only

the behavior of a single joint zone is described [13 – 15]. Therefore, the issue of material behavior under fatigue is more acute for welded joint zones, as such studies are much less represented. It is even more challenging to find information on new grades of materials due to difficulties in obtaining metal for research.

It is well known that the least durable area of a welded joint is either the heat-affected zone (HAZ) [16; 17] or the deposited metal zone, which can differ significantly in chemical composition from the base metal. Considering that welding is a source of defects resulting from physical and structural changes, the fatigue strength of welded joints is lower than that of the base material [18; 19]. It is noted that the weld seam under standard testing methods is the most reliable part of the welded structure, but it becomes the most vulnerable during fatigue testing: characteristics decrease by up to 60 % compared to unwelded metal [20].

Thus, the aim of this study is to determine the fatigue strength characteristics of welded joints made of new domestic steel (analogous to S690QL) while simultaneously recording the parameters of acoustic and magnetic flaw detection for the application of the obtained values in further diagnostics of structures made from the studied steel during operation.

MATERIALS AND METHODS

The study focuses on welded samples made from domestic steel with of X70 strength class. The investigated steel is an analogue of the European S690QL steel. Its chemical composition and mechanical properties, specified in the Technical Standard (TS), are presented in Tables 1 and 2, respectively. For the butt weld, a filler material of 1.2 mm ESAB ArisroRod 69 welding wire was chosen (chemical composition), wt. %: C 0.089; Cr 0.26; Mn 1.54; Mo 0.24; Ni 1.23; Si 0.53).

The actual chemical composition of the investigated steel was determined using optical emission spectrometry on an ARL 3460 spectrometer.

Preparation of samples for microstructural analysis followed standard procedures (grinding with sandpaper followed by polishing with felt) with etching in nital. Microstructure images were captured using an Altami MET 1C microscope.

Table 1. Chemical composition of the studied steel (maximum content)

Таблица 1. Марочный химический состав исследуемой стали (указано максимальное содержание)

Element	C	Si	Mn	P	S	Cr	Mo	Ni	Cu	Nb	V	Al
Content, %	0.20	0.86	1.80	0.018	0.01	1.00	0.50	1.10	0.30	0.07	0.14	0.05

Table 2. Mechanical properties of the studied rolled steel

Таблица 2. Механические свойства проката исследуемых сталей

Plate thickness	Yield strength, MPa	Tensile strength, MPa	Elongation, %	Impact toughness, KCV_{-40} , J/cm ²
<40 mm	690	770 – 940	14	80.0
≥40 mm				37.5

Fatigue testing was conducted on a specialized test bench, shown in Fig. 1, *a*. The test bench includes a fatigue strength testing setup, signal registration, and processing equipment. Acoustic emission sensors were mounted on the sample. The fatigue test sample configuration is shown in Fig. 1, *b*.

Loading during testing followed a cantilever bending scheme (cycle asymmetry coefficient $R = -1$) at a temperature of 20 °C, considering the requirements of GOST 25.502–79. The frequency of elastoplastic cyclic loading was set at 25 Hz. The loading amplitude (σ_{\max}) was calculated based on the loading scheme, sample dimensions, and material mechanical characteristics.

For acoustic measurements, the AIS NRK-3 acoustic system was used. The dimensionless parameter D , referred to as the acoustic parameter, was employed as an informative parameter in acoustic emission and is defined by the formula

$$D = \frac{c_1 + c_2}{c_3},$$

where c_1 and c_2 are the propagation speeds of shear elastic waves with polarization (direction of particle oscillation) along and across the sample axis, respectively; c_3 is the propagation speed (delay) of the longitudinal elastic wave [21; 22].

Magnetic characteristics were assessed using a magnetic metal analyzer – coercimeter MA-412MM. The magnetic characteristics evaluated were residual magnetization B_r , coercive force H_c , and H_c/B_r ratio.

RESULTS AND DISCUSSION

The chemical analysis showed that the obtained result generally corresponds to the grade composition of the steel (Table 3).

Fig. 2 shows the microstructures of the weld zones of the investigated steel. The base metal consists of fine

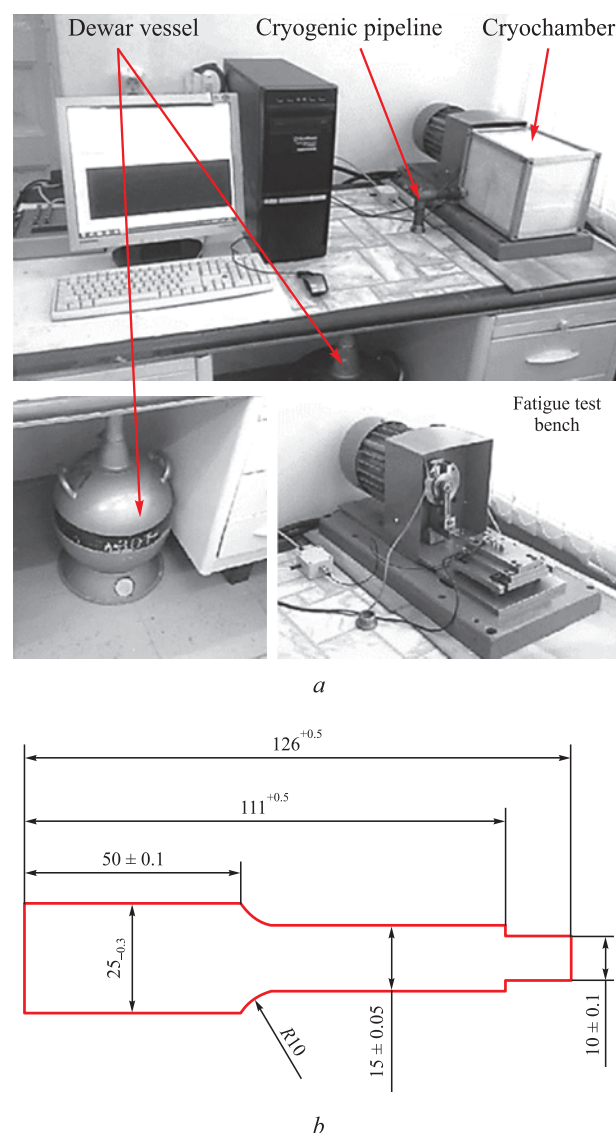


Fig. 1. Fatigue test:
a – fatigue test bench;
b – diagram of a sample for fatigue test

Рис. 1. Испытание на усталость:
a – стенд для испытаний образцов;
b – схема образца для испытаний

Table 3. Actual chemical composition of the steel of X70 strength class

Таблица 3. Фактический химический состав стали класса прочности X70

Element	C	Si	Mn	P	S	Cr	Mo	Ni	Cu	Nb	V	Al
Content, %	0.160	0.340	1.250	0.010	0.0006	0.280	0.220	0.030	0.050	0.020	0.003	0.040

grains of acicular ferrite with tempered sorbite inclusions. The heat-affected zone contains well-defined grains of ferrite with troostite-sorbite inclusions. The average grain size was 35 μm . The microstructure of the deposited metal consists of spheroidized ferrite and pearlite

with sorbitic structures, and traces of bainite. The crystals are oriented parallel to the heat flow.

LCF tests were also conducted on welded samples in all three zones of the weld joint. The obtained data are presented in Table 4 and shown in graphs in Fig. 3. Most samples of S690QL steel (Russia) failed in the weld zone during LCF testing. This could be due to the deposited metal differing in chemical composition from the investigated steel, resulting in different mechanical properties

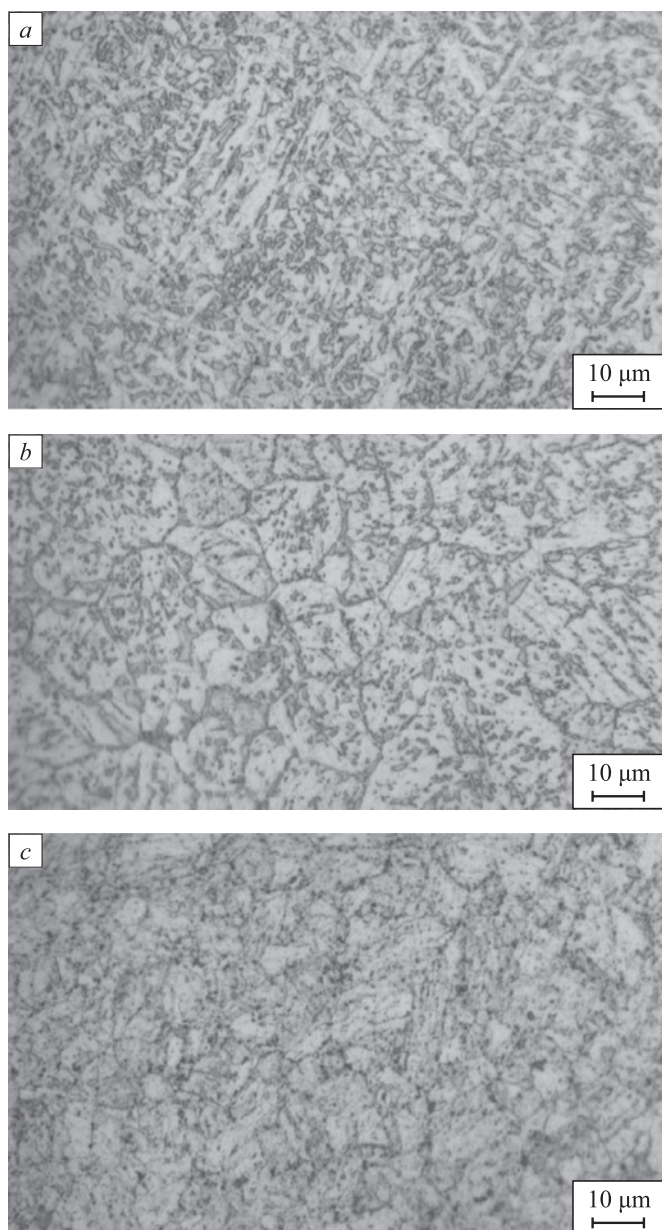


Fig. 2. Microstructure of butt welded joints:

a – deposited metal; *b* – heat affected zone; *c* – base metal

Рис. 2. Микроструктура стыковых сварных соединений:

a – наплавленный металл; *b* – зона термического влияния; *c* – основной металл

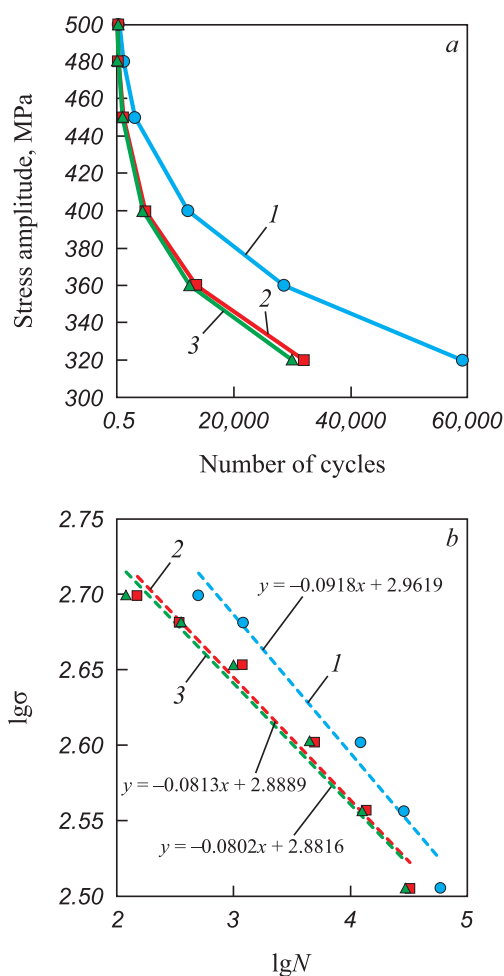


Fig. 3. Wehler curves for S690QL steel (Russia)

depending on the tested welded joint zone:

a – absolute coordinates; *b* – logarithmic coordinates;

1 – base metal; *2* – HAZ; *3* – deposited metal

Рис. 3. Кривые Велера для стали S690QL (Россия)

в зависимости от испытанной зоны сварного соединения:

a – абсолютные координаты;

b – логарифмические координаты;

1 – основной металл; *2* – ЗТВ; *3* – наплавленный металл

Table 4. Results of low-cycle fatigue tests of S690QL steel (Russia)**Таблица 4. Результаты испытаний на МЦУ стали S690QL (Россия)**

Weld zone	Stress, MPa					
	320	360	400	450	480	500
	Number of cycles					
Base metal	59,000	28,560	12,200	3150	1200	500
HAZ	32,000	13,600	4900	1200	340	150
Deposited metal	30,000	12,500	4500	1000	350	120

compared to the base metal. Microstructural heterogeneity also contributes to this: the deposited metal shows signs of a quenched structure, with oriented structural components that reduce ductility and consequently lower the energy threshold for fatigue crack propagation.

The tangent of the slope of the lines in Fig. 3, b (-0.0918 , -0.0813 , -0.0802) corresponds to low-carbon, low-alloy ferrite-pearlite class steels (e.g., 09G2S).

The comparison of fatigue resistance in the weld zones of S690QL steel (Russia) shows the following results.

- The fatigue curves for all weld zones intersect only in the high-stress region (around 500 MPa). However, this appears so only due to the scale. In reality, at 500 MPa, the number of cycles for the base metal is 230 % higher than that for the HAZ and 320 % higher than that for the deposited metal.

- Further reduction in amplitude shows a significant divergence in material behavior depending on the weld

zone. However, the curves for the HAZ and deposited metal almost coincide (both in absolute and logarithmic coordinates). If the percentage difference between the fatigue characteristics for the pairs “base metal – deposited metal” and “base metal – heat-affected zone” is plotted, the resulting graph is shown in Fig. 4. It is evident that the HAZ differs less from the base metal compared to the deposited metal. Additionally, the percentage difference for the deposited metal shows a nearly linear trend compared to the HAZ. Clearly, the greater the stress amplitude, the larger the percentage difference for both zones.

For the study of ultrasonic parameter changes, additional fatigue tests were conducted with stress amplitudes of 300, 350, and 450 MPa. It was established that the most informative is the pattern of changes in the acoustic parameter D . The study of this parameter was conducted up to the point of main crack formation. The obtained dependencies of the acoustic parameter D on the sample's operating time N/N^* (the ratio of the number of cycles corresponding to a given point to the number of cycles recorded during tensile testing) at the investigated stress amplitudes are shown in Fig. 5.

To determine changes in the magnetic characteristics of the steel based on its operating time, one stress amplitude – 350 MPa – was selected. The corresponding dependencies are shown in Fig. 6.

The analysis of acoustic parameter changes (Fig. 5) shows that for S690QL steel (Russia), a monotonous decrease in parameter D is observed up to an operating time of 0.6 (except for the curve with an amplitude of 450 MPa), followed by a slight increase before the formation of the main crack.

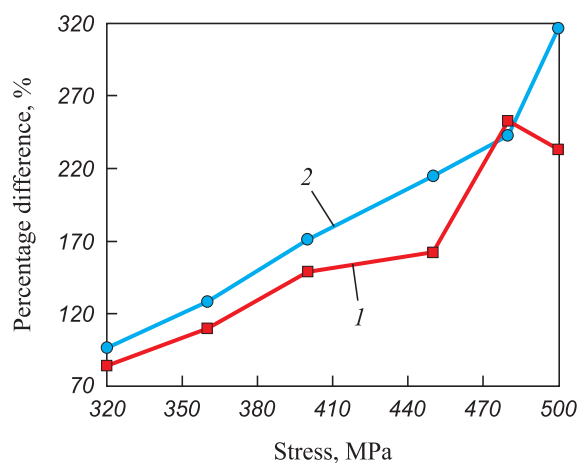


Fig. 4. Percentage difference for welded joint zones in comparison with the base metal:
1 – HAZ; 2 – deposited metal

Рис. 4. Процентная разность для зон сварного соединения в сравнении с основным металлом:
1 – ЗТВ; 2 – наплавленный металл

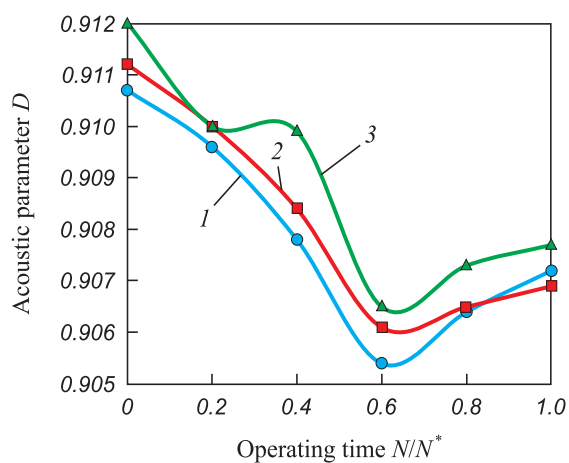


Fig. 5. Dependence of acoustic parameter D on operating time (N/N^*) for steel S690QL (Russia) at MPa:
1 – 300; 2 – 350; 3 – 450

Рис. 5. Зависимость акустического параметра D от наработки (N/N^*) для стали S690QL (Россия), МПа:
1 – 300; 2 – 350; 3 – 450

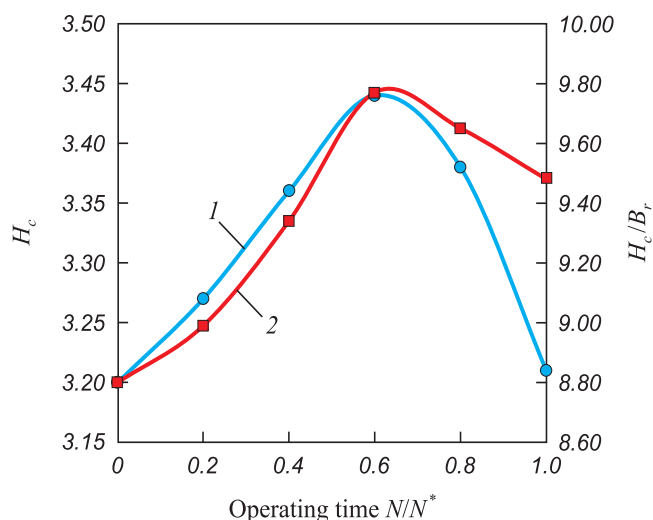


Fig. 6. Dependence of magnetic characteristics on operating time (N/N^*) for steel S690QL (Russia): 1 – H_c ; 2 – H_c/B_r

Рис. 6. Зависимость магнитных характеристик от наработки (N/N^*) для стали S690QL (Россия): 1 – H_c ; 2 – H_c/B_r

Fig. 6 shows the dependencies of magnetic characteristics during fatigue loading. Overall, the dependencies of the coercive force H_c and its ratio to residual magnetization (H_c/B_r) correlate with each other and with changes in the acoustic parameter. This dependency remains practically unchanged with varying stress amplitudes. For example, up to an operating time of 0.6, a monotonous increase in magnetic characteristics is observed, followed by a decrease to initial values in the stage before the formation of the main crack.

A similar pattern of changes in acoustic and magnetic parameters with comparable values was obtained for 09G2S steel [21], which can be explained by the chemical composition of the steels (both are low-carbon, low-alloyed) and their structural class (ferrite-pearlite when cooled in air).

CONCLUSIONS

The conducted studies have shown that the weakest point under fatigue for the steel of X70 strength class is the deposited metal, due to the difference in chemical composition between the welding wire and the base metal (particularly in carbon content: up to 0.2 % for the steel, and up to 0.089 % for the wire).

The behavior of the weld zones of the investigated steel shows a consistent pattern; however, the fatigue resistance of the deposited metal and the heat-affected zone is significantly lower than that of the base metal. Notably, the number of cycles during fatigue testing decreases more significantly for the deposited metal. It is observed that the greater the amplitude stresses, the higher the per-

centage difference between the considered weld zone and the base metal.

The dependencies of the acoustic parameter and magnetic characteristics (coercive force, and its ratio to residual magnetization) exhibited extremums at the point corresponding to 0.6 of the operating time on the respective graphs, indicating the formation of a main crack. Thus, the main stage of failure for the steel of X70 strength class occurs when 60 % of the resource is expended.

REFERENCES / СПИСОК ЛИТЕРАТУРЫ

- Nikolić R., Arsic D., Lazić V. Application of the S690QL class steel in responsible welded structures. *Materials Engineering-Materialove Inzinierstvo*. 2013;20(4):174–183.
- Якушева Н.А. Высокопрочные конструкционные стали для деталей шасси перспективных изделий авиационной техники. *Авиационные материалы и технологии*. 2020;(2(59)):3–9. <https://doi.org/10.18577/2071-9140-2020-0-2-3-9>
- Yakusheva N.A. High-strength constructional steels for landing gears of perspective products of aircraft equipment. *Aviation Materials and Technologies*. 2020;(2(59)):3–9. (In Russ.). <https://doi.org/10.18577/2071-9140-2020-0-2-3-9>
- Каблов Е.Н., Бакрадзе М.М., Громов В.И., Вознесенская Н.М., Якушева Н.А. Новые высокопрочные конструкционные и коррозионностойкие стали для аэрокосмической техники разработки ФГУП «ВИАМ» (обзор). *Авиационные материалы и технологии*. 2020;(1(58)):3–11. <https://doi.org/10.18577/2071-9140-2020-0-1-3-11>
- Kablov E.N., Bakradze M.M., Gromov V.I., Voznesenskaya N.M., Yakusheva N.A. New high strength structural and corrosion-resistant steels for aerospace equipment developed by FSUE “VIAM” (review). *Aviation Materials and Technologies*. 2020;(1(58)):3–11. (In Russ.). <https://doi.org/10.18577/2071-9140-2020-0-1-3-11>
- Ivković D., Adamović D., Arsic D., Ratković N., Mitrović A., Nikolić R. Review of the advanced high-strength steels used in the automotive industry review of advanced high-strength steels and their manufacturing procedures. *Mobility and Vehicle Mechanics*. 2023;49(3):47–64.
- Cadoni E. High and very-high strength steels under harsh conditions of temperature and loading. *Procedia Structural Integrity*. 2023;47:348–353. <https://doi.org/10.1016/j.prostr.2023.07.090>
- Murakami Y., Nomoto T., Ueda T. Factors influencing the mechanism of superlong fatigue failure in steels. *Fatigue & Fracture of Engineering Materials & Structures*. 1999;22(7):581–590. <https://doi.org/10.1046/j.1460-2695.1999.00187.x>
- Тотай А.В., Федонин О.Н., Хандожко А.В., Петрешин Д.И. Технологическое обеспечение гигацикловой усталости деталей класса валов. *Транспортное машиностроение*. 2023;2023(11):15–24. <https://doi.org/10.30987/2782-5957-2023-11-15-24>
- Totay A.V., Fedonin O.N., Khandozhko A.V., Petreshin D.I. Technological support of gigacycle fatigue of shaft parts. *Transport Engineering*. 2023;(11(23)):15–24. (In Russ.). <https://doi.org/10.30987/2782-5957-2023-11-15-24>

8. Ботвина Л.Р. Гигацикловая усталость – новая проблема физики и механики разрушения. *Заводская лаборатория*. 2004;70(4):41–51.
Botvina L.R. Gigacycle fatigue - a new problem of physics and mechanics of destruction. *Zavodskaya laboratoriya*. 2004;70(4):41–51. (In Russ.).
9. Селезнев М.Н., Мерсон Е.Д. Выявление зон усталостной трещины при гигацикловой усталости стали 42CrMo4 с применением количественной фрактографии. *Вектор науки Тольяттинского государственного университета*. 2019;(3):33–39.
<https://doi.org/10.18323/2073-5073-2019-3-33-39>
Seleznev M.N., Merson E.D. Identification of fatigue crack zones in very high cycle fatigued 42CrMo4 steel with the use of quantitative fractography. *Vektor nauki Tol'yatinskogo gosudarstvennogo universiteta*. 2019;(3):33–39. (In Russ.).
<https://doi.org/10.18323/2073-5073-2019-3-33-39>
10. Ерасов В.С., Орешко Е.И. Испытания на усталость металлических материалов (обзор). Часть 1. Основные определения, параметры нагружения, представление результатов испытаний. *Авиационные материалы и технологии*. 2020;(4(61)):59–70.
<https://doi.org/10.18577/2071-9140-2020-0-4-59-70>
Erasov V.S., Oreshko E.I. Fatigue tests of metal materials (review). Part 1. Main definitions, loading parameters, representation of results of tests. *Aviation Materials and Technologies*. 2020;(4(61)):59–70. (In Russ.).
<https://doi.org/10.18577/2071-9140-2020-0-4-59-70>
11. Rémy L. Low cycle fatigue of alloys in hot section components: progress in life assessment. *Procedia Structural Integrity*. 2023;14:3–10.
<https://doi.org/10.1016/j.prostr.2019.05.002>
12. Salehnasab B., Hashem-Sharifi S. Low cycle fatigue behavior and life prediction of a directionally solidified alloy. *Journal of Design Against Fatigue*. 2024;2(1):1–10.
<https://doi.org/10.62676/ygye8n63>
13. Zhu Z., Qianshuo F., Wang B., Zheng W., Yu Y. High-cycle fatigue performance of the heat-affected zone of Q370qENH weathering bridge steel. *Journal of Materials in Civil Engineering*. 2024;36(4):17056.
<https://doi.org/10.1061/JMCEE7.MTENG-17056>
14. Grönlund K., Ahola A., Riski J., Pesonen T., Lipiäinen K., Björk T. Overload and variable amplitude load effects on the fatigue strength of welded joints. *Welding in the World*. 2023;68:411–425.
<https://doi.org/10.1007/s40194-023-01642-z>
15. Tang Z., Cai Z., Wu J. Influence of element segregation at grain boundary of heat affected zone on low-cycle fatigue property of weldment. *Journal of Mechanical Engineering*. 2015;51(14):78–85.
<https://doi.org/10.3901/JME.2015.14.078>
16. Васечкин М.А., Егоров С.В., Коломенский А.Б., Чертов Е.Д. Временное сопротивление разрыву сварных конструкций, изготовленных из отечественных и импортных материалов. *Вестник ВГУИТ*. 2015;(4(66)):61–65.
Vasechkin M.A., Egorov S.V., Kolomenskii A.B., Chertov E.D. Temporary tensile strength of welded structures made from domestic and foreign materials. *Proceedings of the Voronezh State University of Engineering Technologies*. 2015;(4(66)):61–65. (In Russ.).
17. Лещик С.Д., Жуковский В.Е., Ношчик Р.А. Влияние принудительного охлаждения сварного шва и зоны термического влияния в процессе сварки на характеристики сварного соединения. *Вестник Гродзенскага дзяржаўнага ўніверсітэта імя Янкі Купалы. Серыя 6. Тэхніка*. 2023;13(1):45–55.
Leshchik S.D., Zhukovski V.E., Noshchik R.A. Influence of forced cooling of the weld and heat-affected zone during welding on the welded joint characteristics. *Vesnik Hrodzenskaha Dziarzhaunaha Universiteta Imia Ianki Kupaly. Seriya 6. Tekhnika*. 2023;13(1):45–55. (In Russ.).
18. Song W., Liu X., Razavi N. Fatigue assessment of steel load-carrying cruciform welded joints by means of local approaches. *Fatigue & Fracture of Engineering Materials & Structures*. 2018;41(12):2598–2613.
<https://doi.org/10.1111/ffe.12870>
19. Płaczek D., Maćkowiak P., Boroński D. fatigue analysis of welded joints using a thin-walled Al/Fe explosive welded transition joints. *Materials*. 2023;16(18):6259.
<https://doi.org/10.3390/ma16186259>
20. Гридасова Е.А., Веретковский А.В., Сафарьянц А.А., Леонтьев Л.Б. Исследования усталостных свойств сварных соединений в условиях высокочастотного нагружения. *Вестник Инженерной школы Дальневосточного федерального университета*. 2019;(2(39)):3–11.
<https://dx.doi.org/10.24866/2227-6858/2019-2-1>
Gridasova E., Veretkovskiy A., Safariants A. Review of research of fatigue properties of welded joints under high-frequency loading. *FEFU: School of Engineering Bulletin*. 2019;(2(39)):3–11. (In Russ.).
<https://dx.doi.org/10.24866/2227-6858/2019-2-1>
21. Аносов М.С., Рябов Д.А., Чернигин М.А., Соловьев А.А. Неразрушающий контроль накопления усталостных повреждений в стали Св-09Г2С, полученной 3D-печатью электродуговой наплавкой. *Вестник Магнитогорского государственного технического университета им. Г.И. Носова*. 2023;21(2):47–53.
<https://doi.org/10.18503/1995-2732-2023-21-2-47-53>
Anosov M.S., Ryabov D.A., Chernigin M.A., Solovyov A.A. Non-destructive testing of the accumulation of fatigue damage in steel Sv-09G2S produced by wire arc additive manufacturing. *Vestnik of Nosov Magnitogorsk State Technical University*. 2023;21(2):47–53. (In Russ.).
<https://doi.org/10.18503/1995-2732-2023-21-2-47-53>
22. Хлыбов А.А., Рябов Д.А., Соловьев А.А., Аносов М.С., Матвеев Ю.И. Влияние пластической деформации на структуру и свойства стали 20ХГСА, полученной методом аддитивного электродугового выращивания. *Научные проблемы водного транспорта*. 2023;(75):95–107. (In Russ.). <https://doi.org/10.37890/jwt.vi75.382>
Khlybov A.A., Ryabov D.A., Solovyov A.A., Anosov M.S., Matveev Yu.I. The effect of plastic deformation on the structure and properties of 20CrMnSi steel obtained by additive electric arc cultivation. *Russian Journal of Water Transport*. 2023;(75):95–107. (In Russ.).
<https://doi.org/10.37890/jwt.vi75.382>

Information about the Authors

Andrei A. Galkin, Postgraduate of the Chair “Technology and Equipment Engineering”, R.E. Alekseev Nizhny Novgorod State Technical University

E-mail: galkinnnov@mail.ru

Yurii G. Kabaldin, Dr. Sci. (Eng.), Prof. of the Chair “Technology and Equipment Engineering”, R.E. Alekseev Nizhny Novgorod State Technical University

ORCID: 0000-0003-4300-6659

E-mail: uru.40@mail.ru

Yuliya S. Mordovina, Engineer of the Chair “Technology and Equipment Engineering”, Postgraduate, R.E. Alekseev Nizhny Novgorod State Technical University

E-mail: ips4@nntu.ru

Maksim S. Anosov, Cand. Sci. (Eng.), Assist. Prof. of the Chair “Technology and Equipment Engineering”, R.E. Alekseev Nizhny Novgorod State Technical University

E-mail: anosov-maksim@list.ru

Сведения об авторах

Андрей Александрович Галкин, аспирант кафедры «Технология и оборудование машиностроения», Нижегородский государственный технический университет им. Р.Е. Алексеева

E-mail: galkinnnov@mail.ru

Юрий Георгиевич Кабалдин, д.т.н., профессор кафедры «Технология и оборудование машиностроения», Нижегородский государственный технический университет им. Р.Е. Алексеева

ORCID: 0000-0003-4300-6659

E-mail: uru.40@mail.ru

Юлия Сергеевна Мордовина, инженер кафедры «Технология и оборудование машиностроения», аспирант, Нижегородский государственный технический университет им. Р.Е. Алексеева

E-mail: ips4@nntu.ru

Максим Сергеевич Аносов, к.т.н., доцент кафедры «Технология и оборудование машиностроения», Нижегородский государственный технический университет им. Р.Е. Алексеева

E-mail: anosov-maksim@list.ru

Contribution of the Authors

A. A. Galkin – preparation of all samples, conducting fatigue tests, summarizing data.

Yu. G. Kabaldin – drawing up an experimental research plan, scientific guidance.

Yu. S. Mordovina – metallographic analysis, design and editing of the article.

M. S. Anosov – setting research goals, conducting flaw detection.

Вклад авторов

А. А. Галкин – подготовка всех образцов, проведение испытаний на усталость, обобщение данных.

Ю. Г. Кабалдин – составление плана экспериментального исследования, научное руководство.

Ю. С. Мордовина – металлографический анализ, оформление и редактирование статьи.

М. С. Аносов – постановка задач исследования, проведение дефектоскопии.

Received 27.02.2024

Revised 11.03.2024

Accepted 19.06.2024

Поступила в редакцию 27.02.2024

После доработки 11.03.2024

Принята к публикации 19.06.2024



UDC 669.1:66.04

DOI 10.17073/0368-0797-2024-4-417-423



Original article

Оригинальная статья

INFLUENCE OF INHOMOGENEITIES IN CHEMICAL COMPOSITION AND POROSITY OF SINTERED STEEL ON DEVELOPMENT OF MARTENSITIC TRANSFORMATION

V. N. Pustovoit, Yu. V. Dolgachev[✉], M. S. Egorov, Yu. M. Vernigorov

■ Don State Technical University (1 Gagarina Sqr., Rostov-on-Don 344002, Russian Federation)

✉ yuridol@mail.ru

Abstract. The article is devoted to the study of martensitic transformation in porous sintered steels. When analyzing the process of development of martensitic transformation in porous sintered steel, the influence of two factors was assessed: depletion of carbon in the near-surface layers of pores and a change in the energy balance due to relaxation of transformation stresses on free surfaces of the pores. The martensitic transformation was studied in porous steel with a carbon content of 1.56 wt. % obtained after pressing and sintering of a mixture of PZhRV iron powders and GK-3 graphite in hydrogen atmosphere at 1200 °C. Gas carburizing at 1100 °C and homogenization helped to achieve the specified carbon content. The samples were quenched in a sodium chloride solution at a temperature of 27 °C. Pre-cooling was used from temperatures A_{st} to 800 °C at a rate of 62 °C/s. X-ray microanalysis of carbon distribution was carried out using the installation CAMECA Microsonde M.S. 46 with a probe diameter of two microns. The martensite plates predominantly formed on the pores' surfaces and their cross section had shape close to rhomboidal. The data obtained on the morphology of α' -phase crystals growing from pores and the study by X-ray spectral microanalysis of carbon distribution along the largest martensite plates convince us of the absence of any significant changes in carbon content and, as a consequence, their influence on development of martensitic transformation in the area of pores is not the leader. For sintered porous steels, an irremovable factor in the increase in temperature is the presence of porosity, in contrast to a removable factor – inhomogeneity of the chemical composition, which is caused by incompleteness of the alloy homogenization processes, both during sintering and during the austenitization process that precedes quenching.

Keywords: martensite, sintered steel, pores, free surface, quenching, stress relaxation

For citation: Pustovoit V.N., Dolgachev Yu.V., Egorov M.S., Vernigorov Yu.M. Influence of inhomogeneities in chemical composition and porosity of sintered steel on development of martensitic transformation. *Izvestiya. Ferrous Metallurgy*. 2024;67(4):417–423.

<https://doi.org/10.17073/0368-0797-2024-4-417-423>

ВЛИЯНИЕ НЕОДНОРОДНОСТЕЙ ХИМИЧЕСКОГО СОСТАВА И ПОРИСТОСТИ СПЕЧЕННОЙ СТАЛИ НА РАЗВИТИЕ МАРТЕНСИТНОГО ПРЕВРАЩЕНИЯ

В. Н. Пустовойт, Ю. В. Долгачев[✉], М. С. Егоров, Ю. М. Вернигоров

■ Донской государственный технический университет (Россия, 344003, Ростов-на-Дону, пл. Гагарина, 1)

✉ yuridol@mail.ru

Аннотация. Авторы исследовали мартенситное превращение в пористых спеченных сталях. При анализе процесса развития мартенситного превращения учтено влияние двух факторов: обеднение углеродом приповерхностных слоев пор; изменение энергетического баланса за счет релаксации напряжений превращения на свободных поверхностях пор. Исследования проводились на образцах пористых сталей с содержанием углерода 1,56 мас. %, полученных после прессования и спекания в атмосфере водорода при температуре 1200 °C смеси порошков железа ПЖРВ и графита ГК-3. Проводилась также газовая цементация при температуре 1100 °C и гомогенизация, позволяющая достигнуть указанного содержания углерода. Закалка образцов проходила в растворе поваренной соли при температуре 27 °C. Применялось предварительное подстуживание с температур A_{st} до 800 °C со скоростью 62 °C/s. Рентгеноспектральный микроанализ распределения углерода выполнялся на установке CAMECA. Microsonde M.S. 46 при диаметре зонда 2 мкм. Обнаружено преимущественное образование пластин мартенсита на поверхностях пор, а также близкая к ромбоидальной форма их поперечного сечения. Полученные данные о морфологии кристаллов α' -фазы, растущих от пор, и исследования методом рентгеноспектрального микроанализа распределения углерода вдоль наиболее крупных пластин мартенсита подтверждают отсутствие каких-либо

существенных изменений концентрации углерода. Как следствие, их влияние на развитие мартенситного превращения в районе пор не является ведущим. Для спеченных пористых сталей неустраняемым фактором повышения температуры является наличие пористости в отличие от устранимого фактора неоднородности химического состава, которая обусловлена неполнотой процессов гомогенизации сплава как при спекании, так и в процессе аустенитизации, предшествующей закалке.

Ключевые слова: мартенсит, спеченная сталь, поры, свободная поверхность, закалка, релаксация напряжений

Для цитирования: Пустовойт В.Н., Долгачев Ю.В., Егоров М.С., Вернигоров Ю.М. Влияние неоднородностей химического состава и пористости спеченной стали на развитие мартенситного превращения. *Известия вузов. Черная металлургия*. 2024;67(4):417–423.

<https://doi.org/10.17073/0368-0797-2024-4-417-423>

INTRODUCTION

The characteristics of martensitic transformation in porous sintered steels have been studied in considerable detail [1 – 3]. For sintered steels, an increase in the M_s point (martensite start temperature) is characteristic as porosity (the ratio of pore volume to the total volume of the product) increases. This phenomenon is generally explained by the reduction in resistance to plastic deformation in the γ -phase, which is characteristic of martensitic transformation [1; 4; 5]. However, the nucleation of martensite occurs in regions with significantly smaller diameters than those of the pores and the distances between them, so considering the properties of steels with normal density allows for a more precise understanding of nucleation processes. Additionally, the influence of the free surface on the nucleation of martensite needs to be studied. Thus, elastic interactions between martensite crystals and the free surfaces of pores can play a decisive role in the development of the martensitic reaction in sintered steels. Another potential reason for the increase in the M_s point could be segregation factors, which often occur in sintered steel due to segregation processes and incomplete solubility between components [1; 6 – 8]. The factor of decarburization, leading to a shift in the M_s point due to the formation of carbides along pore boundaries (near the surface) during quenching, cannot be excluded. A similar effect has been observed during the precipitation of cementite and other carbides at grain boundaries. In studies [9; 10], carbide precipitation was associated with grain boundary segregation processes of sulfur, which induces carbon mobility. In porous sintered steel, concentrations of S and P are $\leq 0.05\%$ and O_2 is $\leq 0.25\%$, so segregation processes at various types of boundaries are also possible. The studies [11; 12] considered martensitic transformation that can be initiated by carbide precipitates during the aging of high-alloy austenitic steels. These processes also need to be examined for porous sintered steels.

In this study, we examined the martensitic transformation in sintered steels, considering the potential for carbon depletion in areas near the surface of the porous material and alterations in the energy balance resulting from relaxation processes occurring at the pores.

RESEARCH METHODOLOGY

The potential influence of chemical composition inhomogeneities near the pores on the $\gamma \rightarrow \alpha$ transformation was evaluated in experiments with samples obtained by sintering PZhRV iron and GK-3 graphite powders. The pressing and sintering were conducted in a hydrogen atmosphere at a temperature of 1200 °C for half an hour, resulting in a carbon concentration of 1.25 %, which was subsequently increased to 1.56 % during the carburizing process at 1100 °C and homogenization annealing.

Quenching was performed in an aqueous NaCl solution at a temperature of 27 °C. Pre-cooling was also applied before quenching, reducing the temperature from above the SE line to 800 °C at a rate of approximately 62 °C/s.

The carbon distribution was analyzed using X-ray microanalysis with a CAMECA Microsonde M.S. 46 system with a probe radius of 2 μm .

RESULTS AND DISCUSSION

Microstructural analysis revealed that martensite crystals predominantly formed at the surfaces of pores, with the crystals exhibiting a near-rhomboidal shape (Fig. 1, *a, b*). Twinned crystals ranging in size from 40 to 60 μm were also observed (Fig. 1, *c*).

Cooling down induced the precipitation of Fe_3C at grain boundaries, as well as within the γ -matrix. Consequently, the subsequent quenching led to the formation of martensite in carbon-depleted austenitic regions adjacent to cementite plates, characterized by a mixed crystal morphology with a predominant lath structure (Fig. 2, *a, b*). In microvolumes of austenite free from cementite precipitates, twinned martensite was observed (Fig. 2, *b*). Near the carbide formations, regions of low-carbon α' -phase with various morphological types, approximately 3 μm in size, were found (Fig. 2, *b*). Decarburization near the Fe_3C plates was detected, as confirmed by X-ray microanalysis (Fig. 3). The thicknesses of the decarburized layer near Fe_3C , determined by both X-ray microanalysis and microstructural analysis, were consistent.

In cases where the $\gamma \rightarrow \alpha'$ transition at the pore edge is initiated by decarburization, this should be distinctly

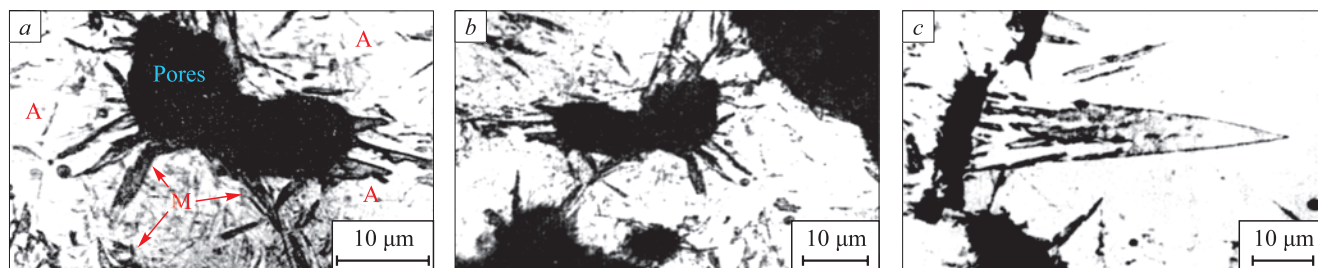


Fig. 1. Microstructure of sintered Fe – 1.56 % C steel after quenching:
a – c – various sections of the microsection

Рис. 1. Микроструктура спеченной Fe – 1,56 % С стали после закалки:
a – c – различные участки микрошлифа

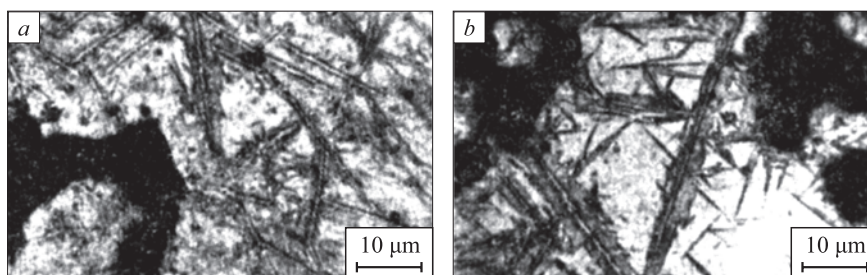


Fig. 2. Structure of porous Fe – 1.57 % C steel with carbides released during cooling-down:
a, b – various sections of the microsection

Рис. 2. Структура пористой Fe – 1,57 % С стали с выделениями карбидов при подстуживании:
a, b – различные участки микрошлифа

observable in microstructural analysis. However, the morphological analysis of martensite crystals formed from the pore, along with the results from *X*-ray microanalysis of carbon concentration near the largest α' -phase crystals

(Fig. 1, c), did not reveal significant differences in carbon content. Consequently, their influence on the $\gamma \rightarrow \alpha'$ transition process in the pore region appears to be negligible.

The influence of porosity on the transformation during quenching was theoretically analyzed, taking into account the potential for stress relaxation at the free surface of the pores, which occurs during transformation. It was assumed that, in the case of heterogeneous nucleation, part of the free energy associated with interactions between martensite and defects remains unchanged in the pore region and between the pores. It was considered that nucleation from the pore edge would occur if the other components of free energy necessary for homogeneous nucleation at the pores and between them were identical. Additionally, it was assumed that the form of the energy function for both cases remains constant. Thus, the free energy values were equated for homogeneous nucleation at the pores and between them when the nucleus reached the critical radius r^* .

The martensite crystal was modeled as a flat nucleus with elliptical, rectangular, and rhomboidal shapes (Fig. 4). Shear deformation was modeled using continuously distributed dislocations [13 – 15]. The elastic shear energy during nucleation can be determined as follows [16]:

$$E_1 = \frac{1}{2} \sum_i \int_{S_i} b_i \bar{\sigma}_{x,y}^0(x, Y_i) dS_i, \quad (1)$$

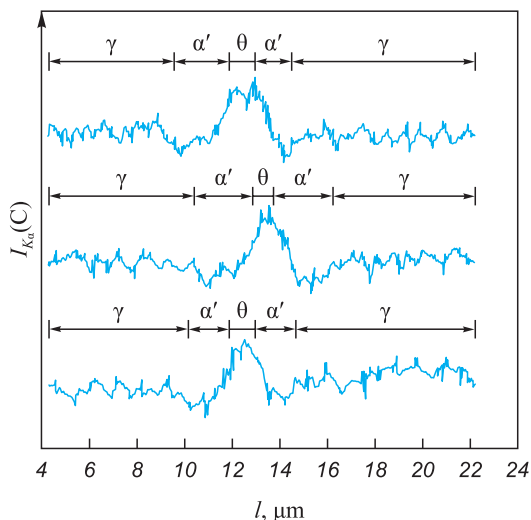


Fig. 3. Results of microanalysis (intensity of K_α -radiation C) in the perpendicular direction from Fe_3C precipitates:
 γ – austenite regions; α' – martensite edges; θ – cementite regions

Рис. 3. Результаты микроанализа (интенсивности K_α -излучения C) в перпендикулярном направлении от выделений Fe_3C :
 γ – участки аустенита; α' – оторочки мартенсита;
 θ – участки цемента

where b_i is the Burgers vector of the i -th dislocation loop; $\bar{\sigma}_{x,y}^{-0i}$ is the shear stress induced by the dislocation ensemble; Y_i is the ordinate of the i -th loop plane; S_i is the cross-sectional area of the plate in the i -th loop plane.

Then,

$$\bar{\sigma}_{x,y}^{-0} = \sum \bar{\sigma}_{x,y}^{-j}; \quad (2)$$

$$\bar{\sigma}_{x,y}^{-j}(x,y) = \frac{\mu b_j}{2\pi(1-\nu)} \times \left\{ \frac{(x+l_j) \left[(x+l_j)^2 - (y-Y_j)^2 \right]}{\left[(x+l_j)^2 + (y-Y_j)^2 \right]^2} - \frac{(x-l_j) \left[(x-l_j)^2 - (y-Y_j)^2 \right]}{\left[(x-l_j)^2 + (y-Y_j)^2 \right]^2} \right\}, \quad (3)$$

where μ is the shear modulus; ν is Poisson's ratio; l_j is the absolute value of the j -th loop abscissa; $b_j = |Y_j - Y_{j+1}|$; γ_x is the macroscopic shear along the x -axis (assuming $\gamma_y^2 \ll \gamma_x^2$, dilation is not considered).

In the case of growth from a pore (Fig. 4, b) of a nucleus with the same cross-sectional area, the elastic energy is determined by similar dependencies:

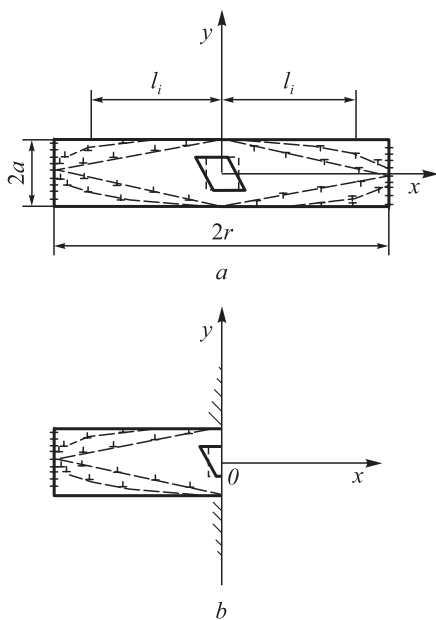


Fig. 4. Representation of the cross-section of martensite nuclei of ellipsoidal, rectangular and rhomboidal shapes:

a – continuously located dislocations in a continuous medium; b – in the case of formation from a free surface

Рис. 4. Представление поперечного сечения зародышей мартенсита эллиптической, прямоугольной и ромбовидной форм:

a – непрерывно расположенные дислокации в сплошной среде; b – в случае образования от свободной поверхности

$$E_2 = \frac{1}{2} \sum_i \int_{S_i} b_i \bar{\sigma}_{x,y}(x, Y_i) dS_i; \quad (4)$$

$$\bar{\sigma}_{x,y} = \sum \bar{\sigma}_{x,y}^j + \bar{\sigma}_{x,y}^+. \quad (5)$$

Based on the data from [17], it is possible to calculate the value $\bar{\sigma}_{x,y}^+$, which determines the relaxation of transformation stresses at the pore edge, and subsequently compute the values of $E_1(c)$ and $E_2(c)$, where $c = a/r$ (with a and r being the half-thickness and radius of the martensite crystal, as shown in Fig. 4). The resulting dependencies, recalculated per unit volume as $\frac{E_1(c)}{V}$ and $\frac{E_2(c)}{V}$, are illustrated in Fig. 5. It becomes evident that the shape of the nucleus does not significantly impact the obtained data, although the elastic energy during nucleation from a pore decreases more markedly in the case of a rhomboidal cross-section (Fig. 5, curve $1'$). Experimentally, such rhomboidal-shaped plates growing from pores have been observed (Fig. 1). Therefore, all subsequent relationships refer to a plate with a rhomboidal cross-section.

Within the range of $0.1 \leq c \leq 0.4$ the curves $\frac{E_1(c)}{V}$ and $\frac{E_2(c)}{V}$ assuming $c_2 \ll 1$ with an accuracy of $\varepsilon < 5\%$, are described by linear equations of the form

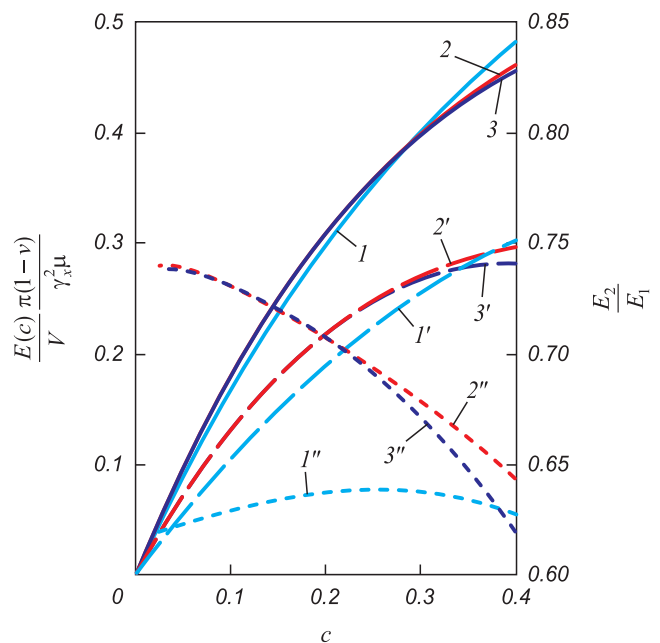


Fig. 5. Dependencies $\frac{E_1(c)}{V}$, $\frac{E_2(c)}{V}$ and $\frac{E_1(c)}{E_2(c)}$ for plates with a rhomboidal (curves $1, 1', 1''$); rectangle (curves $2, 2', 2''$); ellipse (curves $3, 3', 3''$) cross sections

Рис. 5. Зависимости $\frac{E_1(c)}{V}$, $\frac{E_2(c)}{V}$ и $\frac{E_1(c)}{E_2(c)}$ для пластин с поперечным сечением в форме ромба (кривые $1, 1', 1''$); прямоугольника (кривые $2, 2', 2''$); эллипса (кривые $3, 3', 3''$)

$$\frac{E_1(c)}{V} = \frac{\mu\gamma_x^2}{\pi(1-\nu)} (1.188c + 0.03) \text{ 1/m, J/m}^3; \quad (6)$$

$$\frac{E_2(c)}{V} = \frac{\mu\gamma_x^2}{\pi(1-\nu)} (0.746c + 0.019) \text{ 1/m, J/m}^3. \quad (7)$$

Using the traditional approach [18], the value of the “classical” nucleation barrier can be determined as follows:

$$F^* = \frac{32}{27} \frac{\sigma^2 A'}{(\Delta f^{\alpha \rightarrow \gamma} - A^*)^2};$$

$$A' = \frac{dE(c)/V}{dc}; \quad (8)$$

$$A^* = \left(\frac{E(c)}{V} \right) - A'.$$

From equation (8), the M_s point for nucleation at the pore surface (denoted as T_2 in this context) can be derived if T_1 is known – the M_s temperature during martensite formation within the austenite volume between pores:

$$\Delta f^{\alpha \rightarrow \gamma}(T_2) = \sqrt{\frac{A'_1}{A'_2}} (\Delta f^{\alpha \rightarrow \gamma}(T_1) - A_1^*) + A_2^*, \quad (9)$$

where A'_1 and A'_2 correspond A'_1 and A'_2 , respectively, in the case of nucleation within the austenite volume between the pores (index 1) and at the free surface of the pores (index 2).

For the values $\mu = 8 \cdot 10^{10} \text{ N/m}^2$; $\nu = 0.23$; $\gamma_x = 0.18$; $\sigma = 0.2 \text{ N/m}^2$; $\Delta f^{\alpha \rightarrow \gamma}(T_1) = 1.75 \cdot 10^8 \text{ J/m}^3$ [18] for steels with a carbon concentration of 0.4 – 1.2 %, the increase in T_2 over T_1 is approximately 75 K.

The following conclusions can be drawn from these results:

1. Stress relaxation at the pore surface (Fig. 5) is minimal compared to the scenario where the crystal is

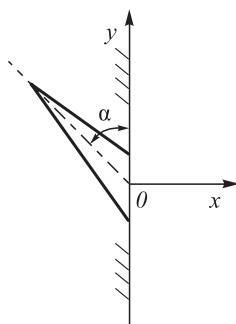


Fig. 6. Arrangement of two-dimensional plate at angle α to the pores' free surface

Рис. 6. Расположение двумерной пластины под углом α к свободной поверхности пор

inclined relative to the surface (Fig. 6), where the martensite start temperature would be even higher. The potential increase in the M_s point depends on the angle α (Fig. 6), with the maximum being the equilibrium temperature of the transforming phases. As the angle varies from 90 to 0°, the number of habit planes changes by a factor of $\sin \alpha$. In the case of a spherical pore, any angle may be equally probable; thus, as α decreases, the probability of nucleation from the pore diminishes according to the $\sin \alpha$ function. The modeling results show good agreement with experimental data: in steels with a carbon concentration of 0.4 – 1.2 % and a porosity of approximately 30 %, the M_s point increases by about 100 °C [2; 19].

2. As observed from equation (9), the increase in T_2 over T_1 for Fe – 0.4 ÷ 1.2 % C steels is independent of alloy composition, which is also experimentally confirmed [2; 20].

3. The well-known linear dependence of the M_s temperature of sintered steels on porosity can be attributed to the approximately linear increase in the specific free surface area of the material. The accuracy of experimental determination of the M_s temperature allows it to be fixed only when more than 1 % of the α' -phase volume fraction appears, thereby clearly illustrating the dependence of M_s on porosity.

4. Experimental data indicate that for crystals formed at an angle of 90° from the pore, the maximum ratio of half-thickness to radius was $c \leq 0.23$. Theoretically, the maximum value is 0.25.

CONCLUSIONS

The calculation results indicate that martensite crystals oriented at a 90° angle to the pore have the highest probability of nucleation, with the ratio of their half-thickness to radius approaching the maximum possible value. It has been demonstrated that the difference in the martensite start temperature between nucleation at the pore surface and nucleation between pores is independent of the alloy composition. The well-known linear dependence of the martensite start temperature on porosity is determined by the increase in the specific free surface area. Therefore, in sintered porous steels, porosity is an unavoidable factor that raises the M_s temperature. Segregation effects, which arise due to incomplete homogenization during sintering or during austenitization prior to quenching, can be excluded.

REFERENCES / СПИСОК ЛИТЕРАТУРЫ

- Gurevich Yu.G., Rakhmanov V.I. Heat Treatment of Powder Steels. Moscow: Metallurgiya; 1985:81.
Гуревич Ю.Г., Рахманов В.И. Термическая обработка порошковых сталей. Москва: Metallurgiya; 1985:81.

2. Ermakov S.S. Heat Treatment of Powder Steel Parts. Leningrad: LDNTP; 1981:24.
Ермаков С.С. Термическая обработка порошковых стальных деталей. Ленинград: ЛДНТП; 1981:24.
3. Egorov M.S., Egorova R.V., Tsordanidi G.G. Formation of structural features of powder materials during cooling after heat treatment. *Safety of Technogenic and Natural Systems*. 2022;(2):69–75. (In Russ.).
<https://doi.org/10.23947/2541-9129-2022-2-69-75>
Егоров М.С., Егорова Р.В., Цорданиди Г.Г. Формирование структурных особенностей порошковых материалов при охлаждении после термической обработки. *Безопасность техногенных и природных систем*. 2022;(2):69–75.
<https://doi.org/10.23947/2541-9129-2022-2-69-75>
4. Pustovoyt V.N., Dolgachev Yu.V., Kornilov Yu.A., Sorochkina O.Yu. Unstable of the crystalline lattice before martensite transformation and the influence of the external magnetic field under these conditions. *Vestnik Donskogo gosudarstvennogo tekhnicheskogo universiteta*. 2009;9(2(41)):238–248. (In Russ.).
Пустовойт В.Н., Долгачев Ю.В., Корнилов Ю.А., Сорочкина О.Ю. Неустойчивость кристаллической решетки перед мартенситным превращением и влияние внешнего магнитного поля в этих условиях. *Вестник Донского государственного технического университета*. 2009;9(2(41)):238–248.
5. Egorov M.S., Egorova R.V. Determination of mechanical properties of sintered dispersion-strengthened iron-based alloys depending on sintering conditions. *Safety of Technogenic and Natural Systems*. 2022;(2):76–83. (In Russ.).
<https://doi.org/10.23947/2541-9129-2022-2-76-83>
Егоров М.С., Егорова Р.В. Определение зависимости механических свойств спеченных дисперсно-упрочненных сплавов на основе железа от условий спекания. *Безопасность техногенных и природных систем*. 2022;(2):76–83.
<https://doi.org/10.23947/2541-9129-2022-2-76-83>
6. Antsiferov V.N., Gilev V.G. Studies of the structure of martensite in sintered carbon steels. *Izvestiya. Ferrous Metallurgy*. 1982;25(5):99–102. (In Russ.).
Анциферов В.Н., Гилев В.Г. Исследования структуры мартенсита в спеченных углеродистых сталях. *Известия вузов. Черная металлургия*. 1982;25(5):99–102.
7. Antsiferov V.N., Grevnov L.M. Structure of Powder Steels. Ekaterinburg: UB RAS; 2011:219.
Анциферов В.Н., Гревнов Л.М. Структура порошковых сталей. Екатеринбург: УрО РАН; 2011:219.
8. Antsiferov V.N. Formation of fulleren-content structure in process of powders iron-graphite compound sintering. *Perspektivnye materialy*. 2009;(6):77–82. (In Russ.).
Анциферов В.Н. Формирование фуллеренсодержащей структуры в процессе спекания порошковых железо-графитовых композиций. *Перспективные материалы*. 2009;(6):77–82.
9. Umemoto M., Furuhashi T., Tamura I. Effects of austenitizing temperature on the kinetics of bainite reaction at constant austenite grain size in Fe–C and Fe–Ni–C alloys. *Acta Metallurgica*. 1986;34(11):2235–2245.
[https://doi.org/10.1016/0001-6160\(86\)90169-0](https://doi.org/10.1016/0001-6160(86)90169-0)
10. Morsdorf L., Kashiwar A., Kübel C., Tasan C.C. Carbon segregation and cementite precipitation at grain boundaries in quenched and tempered lath martensite. *Materials Science and Engineering: A*. 2023;862:144369.
<https://doi.org/10.1016/j.msea.2022.144369>
11. Butler E.P., Burke M.G. Chromium depletion and martensite formation at grain boundaries in sensitised austenitic stainless steel. *Acta Metallurgica*. 1986;34(3):557–570.
[https://doi.org/10.1016/0001-6160\(86\)90091-X](https://doi.org/10.1016/0001-6160(86)90091-X)
12. Zhang Y., Zhan D., Qi X., Jiang Z. Austenite and precipitation in secondary-hardening ultra-high-strength stainless steel. *Materials Characterization*. 2018;144:393–399.
<https://doi.org/10.1016/j.matchar.2018.07.038>
13. Roitburd A.L. Theory of heterophase structure formation during phase transformations in solid state. *Uspekhi fizicheskikh nauk*. 1974;113:69–104. (In Russ.).
Ройтбурд А.Л. Теория формирования гетерофазной структуры при фазовых превращениях в твердом состоянии. *Успехи физических наук*. 1974;113:69–104.
14. Olson G.B., Cohen M. Interphase-boundary dislocations and the concept of coherency. *Acta Metallurgica*. 1979;27(12):1907–1918.
[https://doi.org/10.1016/0001-6160\(79\)90081-6](https://doi.org/10.1016/0001-6160(79)90081-6)
15. Khachaturyan A.G. Theory of Structural Transformations in Solids. Courier Corporation; 2008:576.
16. Rabotnov Yu.N. Mechanics of Deformable Solids. Moscow: Nauka; 1988:712.
Работнов Ю.Н. Механика деформируемого твердого тела. Москва: Наука; 1988:712.
17. Anderson P.M., Hirth J.P., Lothe J. Theory of Dislocations. Cambridge University Press; 2017:699.
18. Kaufman L., Cohen M. Thermodynamics and kinetics of martensitic transformations. *Progress in Metal Physics*. 1958;7:165–246.
[https://doi.org/10.1016/0502-8205\(58\)90005-4](https://doi.org/10.1016/0502-8205(58)90005-4)
19. Danninger H., Gierl C., Mühlbauer G., Gonzalez M.S., Schmidt J., Specht E. Thermophysical properties of sintered steels – Effect of porosity. *International Journal of Powder Metallurgy*. 2011;47(3):31–42.
20. Ternero F., Rosa L.G., Urban P., Montes J.M., Cuevas F.G. Influence of the total porosity on the properties of sintered materials – A review. *Metals*. 2021;11(5):730.
<https://doi.org/10.3390/met11050730>

Information about the Authors

Сведения об авторах

Viktor N. Pustovoyt, Dr. Sci. (Eng.), Prof. of the Chair of Materials Science and Metals Technology, Don State Technical University

ORCID: 0000-0001-6999-3520

E-mail: pustovoyt45@gmail.com

Yurii V. Dolgachev, Cand. Sci. (Eng.), Assist. Prof. of the Chair of Materials Science and Metals Technology, Don State Technical University

ORCID: 0000-0002-8558-1136

E-mail: yuridol@mail.ru

Maksim S. Egorov, Cand. Sci. (Eng.), Assist. Prof., Head of the Chair of Materials Science and Metals Technology, Don State Technical University

E-mail: aquavdonsk@mail.ru

Yurii M. Vernigorov, Dr. Sci. (Eng.), Prof. of the Chair of Physics, Don State Technical University

E-mail: jvernigorov@donstu.ru

Виктор Николаевич Пустовойт, д.т.н., профессор кафедры «Материаловедение и технологии металлов», Донской государственной технической университет

ORCID: 0000-0001-6999-3520

E-mail: pustovoyt45@gmail.com

Юрий Вячеславович Долгачев, к.т.н., доцент кафедры «Материаловедение и технологии металлов», Донской государственной технической университет

ORCID: 0000-0002-8558-1136

E-mail: yuridol@mail.ru

Максим Сергеевич Егоров, к.т.н., доцент, заведующий кафедрой «Материаловедение и технологии металлов», Донской государственной технической университет

E-mail: aquavdonsk@mail.ru

Юрий Михайлович Вернигорov, д.т.н., профессор кафедры «Физика», Донской государственной технической университет

E-mail: jvernigorov@donstu.ru

Contribution of the Authors

Вклад авторов

V. N. Pustovoyt – formation of the basic concept, goals and objectives of the study; scientific guidance, editing of the text and conclusions.

Yu. V. Dolgachev – conducting experimental studies, microstructural and X-ray spectral analysis, writing the text, formulation of conclusions.

M. S. Egorov – obtaining sintered samples, their hardening and preparation for subsequent analyses; participation in theoretical parts of the study.

Yu. M. Vernigorov – participation in the creation of a martensitic crystal model; processing, analysis and discussion of the results.

В. Н. Пустовойт – формирование основной концепции, цели и задач исследования; научное руководство, редактирование текста и выводов.

Ю. В. Долгачев – проведение экспериментальных исследований, микроструктурный и рентгеноспектральный анализ, подготовка текста, формулирование выводов.

М. С. Егоров – получение спеченных образцов, их закалка и подготовка для последующих анализов; участие в теоретической части исследования.

Ю. М. Вернигорov – участие в создании модели мартенситного кристалла; обработка, анализ и обсуждение результатов исследования.

Received 15.01.2024

Revised 05.02.2024

Accepted 06.02.2024

Поступила в редакцию 15.01.2024

После доработки 05.02.2024

Принята к публикации 06.02.2024



UDC 669.539.382:669.17:6251

DOI 10.17073/0368-0797-2024-4-424-432



Original article

Оригинальная статья

PHYSICS OF HARDENING OF THE ROLLING SURFACE OF RAIL HEAD FROM HYPEREUTECTOID STEEL AFTER OPERATION

N. A. Popova¹, V. E. Gromov² , A. B. Yur'ev²,
E. A. Martusevich², M. A. Porfir'ev²

¹ Tomsk State University of Architecture and Building (2 Solyanaya Sqr., Tomsk 634003, Russian Federation)

² Siberian State Industrial University (42 Kirova Str., Novokuznetsk, Kemerovo Region – Kuzbass 654007, Russian Federation)

gromov@physics.sibsiu.ru

Abstract. In Russia, with its extensive railway system, for more than 5 years, special-purpose rails of increased wear resistance and contact endurance of the DH400RK category were produced from steel with a carbon content $>0.8\%$. On the head rolling surface of differentially hardened long rails made of hypereutectoid steel after long-term operation, transmission electron microscopy methods revealed the morphological components of the structure: lamellar pearlite, fragmented pearlite, destroyed lamellar pearlite, globular pearlite, completely destroyed pearlite, subgrain structure. The contribution of hardening due to: lattice friction, solid solution hardening, pearlite hardening, incoherent cementite particles, grain boundaries and subboundaries, dislocation substructure and internal stress fields were quantified. A hierarchy of these mechanisms was made and it was noted that for the fillet surface of the rail head, the main hardening mechanism is hardening by incoherent particles, as well as mechanisms caused by internal long-range (local) stresses, internal shear stresses (“forests” of dislocations) and substructural hardening. For the rolling surface along the central axis of the rail head, the main role in hardening belongs to long-range stress fields (especially its elastic component), hardening by incoherent particles and substructural hardening. Taking into account the volume fractions of the morphological components and their yield strength, the additive yield strength on the head rolling surface in the center and on the fillet was determined: 7950 and 2218 MPa, respectively. The paper presents a physical interpretation of the difference in values of the additive yield strength on the rolling surface of the rail head in the center and on the fillet.

Keywords: rolling surface, rails, fillet, hardening mechanisms, additive yield strength, hypereutectoid steel

Acknowledgements: The work was performed within the framework of the state task of the Ministry of Science and Higher Education of the Russian Federation (subject No. FEMN-2023-0003). The authors express their gratitude to E.V. Polevoi for the samples provided and to I.Y. Litovchenko for assistance in conducting TEM studies.

For citation: Popova N.A., Gromov V.E., Yur'ev A.B., Martusevich E.A., Porfir'ev M.A. Physics of hardening of the rolling surface of rail head from hypereutectoid steel after operation. *Izvestiya. Ferrous Metallurgy*. 2024;67(4):424–432. <https://doi.org/10.17073/0368-0797-2024-4-424-432>

ФИЗИКА УПРОЧНЕНИЯ ПОВЕРХНОСТИ КАТАНИЯ ГОЛОВКИ РЕЛЬСОВ ИЗ ЗАЭВТЕКТОИДНОЙ СТАЛИ ПОСЛЕ ЭКСПЛУАТАЦИИ

Н. А. Попова¹, В. Е. Громов² , А. Б. Юрьев²,
Е. А. Мартусевич², М. А. Порфирьев²

¹ Томский государственный архитектурно-строительный университет (Россия, 634003, Томск, пл. Соляная, 2)

² Сибирский государственный индустриальный университет (Россия, 654007, Кемеровская обл. – Кузбасс, Новокузнецк, ул. Кирова, 42)

gromov@physics.sibsiu.ru

Аннотация. В России с ее протяженной сетью железных дорог более пяти лет производится рельсы специального назначения повышенной износостойкости и контактной выносливости категории ДТ400ИК из стали с содержанием углерода более $0,8\%$. На поверхности катания головки дифференцированно закаленных длинномерных рельсов из заэвтектоидной стали после длительной эксплуатации (пропущенный тоннаж 187 млн т брутто на экспериментальном кольце) методами просвечивающей электронной микроскопии выявлены морфологические составляющие структуры: пластинчатый перлит, фрагментированный перлит, разрушенный пластинчатый перлит, глобулярный перлит, полностью разрушенный перлит, субзеренная структура. Проведена количественная оценка вкладов упрочнения, обусловленных трением кристаллической решетки, твердорастворным упрочнением, упрочнением за счет перлита, упрочнением некогерентными частицами цементита, границами зерен и субграницами, дислокационной субструктурой и внутренними полями напряжений. Установлена

иерархия этих механизмов и отмечено, что для поверхности скругления (выкружки) головки рельсов основным механизмом упрочнения является упрочнение некогерентными частицами, а также механизмы, обусловленные внутренними дальнедействующими (локальными) напряжениями, внутренними напряжениями сдвига («лес» дислокаций) и субструктурным упрочнением. Для поверхности катания по центральной оси головки рельсов основная роль в упрочнении принадлежит упрочнению дальнедействующими полями напряжений (особенно ее упругой компонентой), упрочнению некогерентными частицами и субструктурному упрочнению. С учетом объемных долей морфологических составляющих и их предела текучести определен аддитивный предел текучести на поверхности катания по центру головки и выкружке. Он составил 7950 и 2218 МПа для центра головки и выкружки. Представлена физическая интерпретация различия значений аддитивного предела текучести на поверхности катания головки рельсов в центре и на выкружке.

Ключевые слова: поверхность катания, рельсы, выкружка, механизмы упрочнения, аддитивный предел текучести, заэвтектоидная сталь

Благодарности: Работа выполнена в рамках государственного задания Министерства науки и высшего образования Российской Федерации (тема № FEMN-2023-0003). Авторы выражают благодарность Е.В. Полевому за предоставленные образцы, И.Ю. Литовченко за помощь в проведении ПЭМ-исследований.

Для цитирования: Попова Н.А., Громов В.Е., Юрьев А.Б., Мартусевич Е.А., Порфирьев М.А. Физика упрочнения поверхности катания головки рельсов из заэвтектоидной стали после эксплуатации. *Известия вузов. Черная металлургия*. 2024;67(4):424–432.

<https://doi.org/10.17073/0368-0797-2024-4-424-432>

INTRODUCTION

Rails are predominantly removed from service due to contact fatigue damage and surface wear [1; 2]. In recent years, with increasing railway traffic speeds and axle loads, the operational durability requirements for rails have become more demanding [3 – 5]. From both practical and fundamental perspectives, the development of special-purpose rails with enhanced performance characteristics is of significant importance [6 – 8]. In Russia, home to one of the world's longest railway networks, this challenge has been addressed since 2018 through the production of long, differentially hardened rails with improved wear resistance and contact fatigue strength, classified as DT400IK [9]. These rails are manufactured from steel containing more than 0.8 wt. % carbon, which ensures the formation of a subgrain structure with a high density of low-angle boundaries in the surface layer. Modern physical materials science techniques, particularly transmission electron microscopy [10 – 12], are employed to monitor changes in structure, phase composition, and defect substructure that lead to the degradation of mechanical properties [13 – 15]. Improving the technology for special-purpose rail production and ensuring high-performance properties requires a deep understanding of the physical nature and evolution trends of the structural-phase states and fine substructure in the surface layers of rails [16 – 18]. Such data are crucial for reliably achieving the target of transporting up to 2 billion tons [19 – 21]. Analysis conducted on rails made of hypoeutectoid steel with carbon content below 0.8 wt. % – as presented in [22 – 25] – has enabled the quantification of physical hardening mechanisms, the establishment of their hierarchy, and the determination of overall yield strength. However, there is a notable lack of studies focused on rails made of hypereutectoid steel.

The objective of this study is to compare the deformation hardening mechanisms of the rolling surface and

fillet of special-purpose DH400RK rails after they have been in operation on the Russian Railways (RZD) test circuit at Scherbinka, following a tonnage of 187 million tons (gross).

MATERIALS AND METHODS

The internal structure and phase composition were studied on samples of differentially hardened DH400RK category rails, made from E0.9C–Cr–N–V–Fe grade steel produced by EVRAZ ZSMK, after they had undergone a tonnage of 187 million tons (gross) at the Russian Railways (RZD) test circuit. The chemical composition of E90HAF rail steel, according to GOST 5185 – 2013 and TS 24.10.75111-298-057576.2017, included the following main elements, wt. %: 0.92 C, 0.4 Si, 1.0 Mn, 0.3 Cr, 0.14 V, with iron as the base. The mechanical properties are as follows: yield strength – over 900 MPa, tensile strength – 1350 MPa, relative elongation – 9.0 %, relative reduction – 18 %, impact toughness – 15 J/cm², and hardness on the rolling surface of the rail head – 400 – 450 HB.

The rolling surface and fillet of the rail head were investigated (Fig. 1) using transmission electron microscopy (TEM) on thin foils with a JEM-2100 electron microscope (Jeol, Japan) [26 – 28].

To evaluate the hardening mechanisms that contribute to the yield strength in the studied steel, each sample was analyzed for structural morphological features, phase composition, and fine structure parameters, including the volume fractions of morphological constituents P_v . The localization of the carbide phase (cementite) was identified, and for each specific location, the shape, size (d), particle spacing (r), and volume fraction (δ) of the particles were determined. In each morphological component, as well as in the material as a whole, the scalar ρ and excessive ρ_{\pm} dislocation densities were calculated, along with the amplitudes of internal stresses generated by them – namely, shear stresses (σ_f , or “forests”

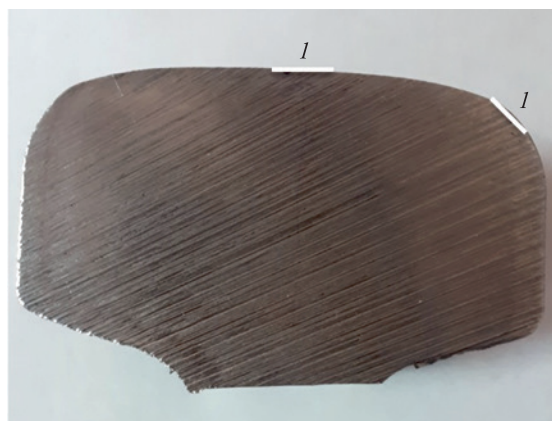


Fig. 1. Schematic representation of a rail sample after passing a tonnage of 187 million tons, indicating the places used to study the structure:

I – rolling surfaces and rounding of the rail head (fillet)

Рис. 1. Схематическое изображение образца рельса после пропущенного тоннажа 187 млн т с указанием мест, использованных для исследования структуры:

I – поверхности катания и скругления головки рельса (выкружки)

of dislocations) and long-range stresses (σ_l), which arise in regions with an excess dislocation density. All quantitative parameters of the fine structure were measured within each morphological component and statistically processed, with the mean values presented in Table 1 (where D_1 represents the fragment or subgrain size;

χ , χ_{pl} and χ_{el} represent the curvature-torsion amplitude of the crystal lattice and its plastic and elastic components, respectively; σ_l^{pl} and σ_l^{el} are the amplitudes of internal long-range stresses and their plastic and elastic components.

The technique for determining these quantitative parameters is detailed in [9; 29].

RESULTS AND DISCUSSION

The studies have shown that regardless of the location on the rail head surface (Fig. 1) the following morphological components are observed in the structure: lamellar (ideal) pearlite with parallel alternating lamellae of ferrite and cementite; fragmented lamellar pearlite, in which dislocation walls across the di-rection of α -phase plates are formed; destroyed lamellar pearlite with bent, cut and crushed Fe_3C lamellae; globular pearlite in the form of grains with globular Fe_3C particles, subgrain structure – small equiaxed fragments with cementite particles along the boundaries and in the junctions. The images of these morphological components are consistent with those observed for rails made of hypoeutectoid steel, as shown in [1].

A different type of structure was identified on the fillet surface – a completely destroyed structure. This structure, characterized by completely destroyed pearlite colonies,

Table 1. Quantitative parameters of the structure of hypereutectoid rail steel on the rounding surface of the rail head (fillet)

Таблица 1. Количественные параметры структуры заэвтектоидной рельсовой стали на поверхности скругления головки рельса (выкружки)

Parameters		Pearlite				Destroyed structure	Subgrain structure
		ideal	fragmented	destroyed	globular		
P_v , %		5	20	10	3	60	2
D_1 , nm		–	80×125	–	–	–	90
$\rho \cdot 10^{-10}$, cm ⁻²		6.5	4.3	4.5	3.0	6.6	1.4
σ_f , MPa		510	415	425	345	515	235
$\chi = \chi_{pl} + \chi_{el}$, cm ⁻¹		765 + 0	1075 + 75	805 + 0	740 + 0	1650 + 95	350 + 390
$\rho_{\pm} \cdot 10^{-10}$, cm ⁻²		3.1	4.3	3.2	3.0	6.6	1.4
$\sigma_l = \sigma_l^{pl} + \sigma_l^{el}$, MPa		350 + 0	415 + 120	355 + 0	345 + 0	515 + 150	235 + 625
Fe_3C (at the boundaries)	d , nm	–	15×95	–	–	–	5×35
	r , nm	–	105	–	–	–	85
	δ , %	–	0.7	–	–	–	0.05
Fe_3C (inside)	d , nm	15	5×15	20×110	45	8×30	–
	r , nm	80	40	120	100	40	–
	δ , %	12.0	0.1	1.2	2.3	0.4	0
Fe_3C (at subgrain junctions)	d , nm	–	–	–	–	–	20
	r , nm	–	–	–	–	–	115
	δ , %	–	–	–	–	–	0.15

contains small, chaotically arranged carbide particles (Fe_3C) with an acicular shape and a high scalar dislocation density (Fig. 2, *a*).

The material on the rolling surface in the head center predominantly consists of a subgrain structure (90 %) (Fig. 2, *b*), while this structure accounts for only 2 % of the fillet surface. The research demonstrated that, in all morphological components, the dislocation structure type remains consistent: the dislocation substructure is represented by dense dislocation arrays. In all morphological components, there are bend extinction contours, originating from interfaces of pearlite grains and colonies, cementite plates in pearlite grains, fragment and subgrain boundaries, carbide particles (cementite) of lamellar and rounded shapes located on the boundaries and within the dislocation fragments and subgrains, junctions of subgrains, and the dislocation substructure.

Calculations presented in [9] indicate that, in the fillet surface layer, within the ideal, destroyed, and globular pearlite, the scalar density of dislocations ρ is higher than the excess density of dislocations ρ_{\pm} , as determined from the width of the bend extinction contours (Table 1), meaning that $\rho > \rho_{\pm}$ and, accordingly, $\sigma_l < \sigma_f$. This indicates that the curvature-twist of the crystal lattice in these morphological components is purely plastic in nature. In fragmented pearlite, as well as in completely destroyed and subgrain structures, the value ρ is smaller than the calculated value of ρ_{\pm} , meaning $\rho < \rho_{\pm}$ and, $\sigma_f < \sigma_l$, which implies that the curvature-twist of the crystal lattice in these components is elastic-plastic in nature. However, in fragmented pearlite and completely destroyed structures $\chi_{pl} \gg \chi_{el}$, whereas in the subgrain structure $\chi_{pl} \approx \chi_{el}$ (Table 1).

In the surface layer of the rail head center, the value ρ in all morphological components was found to be smaller than the value of ρ_{\pm} calculated based on the width of extinction contours [9] (Table 2). This indicates that the curvature-twist of the crystal lattice in all morphological components is elastic-plastic, with $\chi = \chi_{pl} + \chi_{el}$.

In the subgrain structure, which occupies the majority of the material, χ_{el} is nearly three times greater than χ_{pl} .

In the surface layer of the rail head, elastic-plastic curvature-twist of the crystal lattice is observed across all morphological components. Notably, in the subgrain structure, which makes up 90 % of the material, the values of χ and σ_l are the highest, while the value of σ_{pl} is more than an order of magnitude smaller than that of σ_{el} (Table 2). This explains the presence of microcracks in these areas.

The quantitative results presented in Tables 1 and 2 served as the basis for calculating the additive (total) yield strength in each morphological component and for the material as a whole. It is important to note that individual mechanisms contribute differently to overall strengthening, as these are influenced by various factors in each case [30 – 32]. Therefore, when estimating the additive yield strength σ_{ad} , it is crucial to consider the volume fractions P_v of each morphological component σ_i

$$\sigma = \sum P_i \sigma_i,$$

where P_i and σ_i are volume fractions and yield strength of each morphological component of the structure.

Previously, it was assumed that the additive yield strength could be determined by simply summing the contributions of individual hardening mechanisms [30]. However, it has now been demonstrated that, in some cases, these values should be summed using a quadratic approximation [31; 32]. This approach is particularly relevant for the mechanisms $\Delta\sigma_f$ and $\Delta\sigma_g$, which act locally and inhomogeneously within the grains. Thus,

$$\sigma_{ad} = \Delta\sigma_p + \Delta\sigma_s + \Delta\sigma_g + \Delta\sigma_{or} + \Delta\sigma_{perl} + \Delta\sigma_{ss} + \sqrt{\Delta\sigma_f^2 + \Delta\sigma_l^2},$$

where $\Delta\sigma_n = 35 \text{ MPa}$ [9] represents the friction stress of dislocations in the crystal lattice of α -iron; $\Delta\sigma_s$ refers

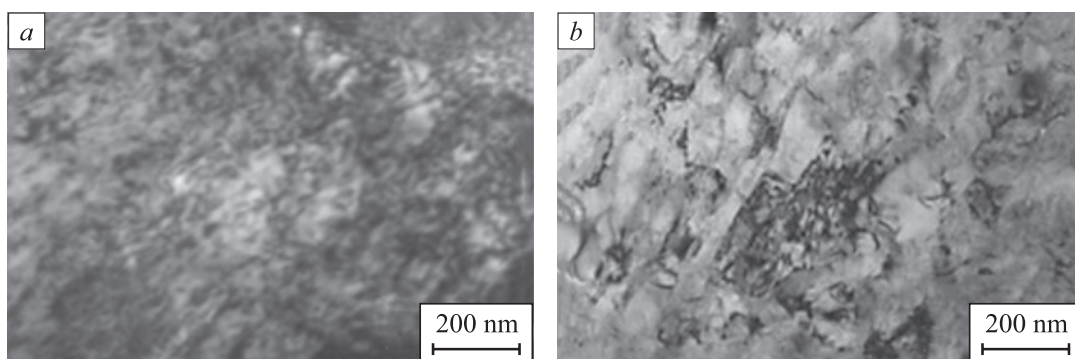


Fig. 2. TEM images of a completely destroyed (*a*) and subgrain structure (*b*)

Рис. 2. ПЭМ-изображения полностью разрушенной (*a*) и субзеренной структуры (*b*)

Table 2. Parameters of the fine structure of pearlite in the rolling surface center

Таблица 2. Параметры тонкой структуры перлита в центре поверхности катания

Parameters		Pearlite				Subgrain structure
		ideal	fragmented	destroyed	globular	
P_v , %		~1	10	0	0	90
D_1 , nm		–	50×160	–	–	80
$\rho \cdot 10^{-10}$, cm ⁻²		8.3	5.0	–	–	3.6
σ_f , MPa		575	445	–	–	380
$\chi = \chi_{pl} + \chi_{el}$, cm ⁻¹		2075 + 25	1250 + 1430	–	–	900 + 2660
$\rho_{\pm} \cdot 10^{-10}$, cm ⁻²		8.3	5.0	–	–	3.6
$\sigma_1 = \sigma_1^{pl} + \sigma_1^{el}$, MPa		575 + 40	445 + 2280	–	–	380 + 4255
Fe ₃ C (at the boundaries)	d , nm	–	15	–	–	15
	r , nm	–	40	–	–	30
	δ , %	–	0.6	–	–	1.0
Fe ₃ C (inside)	d , nm	15×20	15	–	–	10
	r , nm	40	35	–	–	35
	δ , %	1.1	0.7	–	–	0.2
Fe ₃ C (at subgrain junctions)	d , nm	–	–	–	–	20
	r , nm	–	–	–	–	100
	δ , %	–	–	–	–	0.01

to solid solution hardening (the hardening of ferrite solid solution by dissolved alloying elements); $\Delta\sigma_g$ denotes grain boundary hardening (due to grain boundaries); $\Delta\sigma_{or}$ is the hardening of material by incoherent particles as dislocations bypass them via the Orowan mechanism; $\Delta\sigma_{perl}$ represents hardening due to pearlitic component (barrier inhibition within pearlitic colonies); $\Delta\sigma_{ss}$ refers to substructural hardening (due to intraphase boundaries) the formula contains no such values); $\Delta\sigma_f$ is the hardening by the “forest” of dislocations that cut glide dislocations (internal shear stress); and $\Delta\sigma_1$ represents hardening by long-range stress fields (internal moment or local stresses), with $\Delta\sigma_1 = \Delta\sigma_{el} + \Delta\sigma_{pl}$, where $\Delta\sigma_{el}$ is the elastic component and $\Delta\sigma_{pl}$ is the plastic component of long-range stresses.

The contributions of these hardening mechanisms were qualitatively assessed using the formulas given in [29; 31; 32], and the results are presented in Tables 3 and 4.

The analysis of data from Tables 3 and 4 shows that the strength of the steel is multifactorial, with physical mechanisms that are cumulative in nature. For the fillet surface, the primary hardening mechanism is Orowan strengthening ($\Delta\sigma_{or}$). This is primarily because the completely destroyed structure occupies the majority (60 %) of the fillet surface. The contributions from long-range stress fields ($\Delta\sigma_g$) and the stresses from the “forest” of dislocations ($\Delta\sigma_f$) are also significant. The emerging subgrain structure forms numerous grain junctions,

leading to an increase in the sources of extinction contours and, consequently, a growth in $\Delta\sigma_g$. However, since the volume fraction of the subgrain structure (P_v) is low (2 %), its contribution to the strengthening of the fillet surface is minimal. The strengthening is primarily due to the fragmented substructure and the completely destroyed structure. The additive yield strength at the fillet surface is 2218 MPa.

For the central part of the rolling surface of the rail head, the additive yield strength is much higher, reaching 7950 MPa. The main hardening mechanisms (Table 4) include strengthening by internal elastic local stresses, substructural strengthening, and strengthening by incoherent particles.

The significant difference in the values of additive yield strength ($\sigma_{ad}^{fillet} < \sigma_{ad}^{centr}$) can be explained by the fact that, in the head center’s rolling surface, the volume fraction of the subgrain structure is 45 times higher than that in the fillet. The subgrains form in the nanometer size range, leading to a high density of sub-boundaries and junctions (primarily triple junctions) of subgrains, which are the sources of extinction contours (mainly elastic). These contours result in high values of internal long-range stresses, with the elastic component being more than an order of magnitude higher than the plastic one. This combination determines the final effect. On the fillet surface, the main morphological components are destroyed pearlite and a completely destroyed structure with low-density boundaries.

Table 3. Contribution of various mechanisms to hardening of hypereutectoid rail steel in various morphological components and in general according to the material of the rounding surface of the rail head (fillet)

Таблица 3. Величины вкладов различных механизмов в упрочнение заэвтектоидной рельсовой стали в различных морфологических составляющих и в целом по материалу поверхности скругления головки рельса (выкружки)

Contributions	Pearlite				Destroyed structure	Subgrain structure	In the material
	ideal	fragmented	destroyed	globular			
$P_v, \%$	5	20	10	3	60	2	100
$\Delta\sigma_p, \text{MPa}$	35	35	35	35	35	35	35
$\Delta\sigma_s, \text{MPa}$	80	180	80	80	150	90	142
$\Delta\sigma_g, \text{MPa}$	–	–	205	360	195	–	148
$\Delta\sigma_{perl}, \text{MPa}$	965	–	–	–	–	–	48
$\Delta\sigma_{ss}, \text{MPa}$	–	1465	–	–	–	1665	326
$\Delta\sigma_{or}, \text{MPa}$	–	1125	340	200	805	580	760
$\Delta\sigma_f, \text{MPa}$	510	415	425	345	515	235	475
$\Delta\sigma_{pl}, \text{MPa}$	350	415	355	345	515	235	467
$\Delta\sigma_{cl}, \text{MPa}$	0	120	0	0	150	625	127
$\Delta\sigma_l, \text{MPa}$	350	535	355	345	665	860	587
$\Sigma\Delta\sigma_i, \text{MPa}$	1699	3482	1214	1163	2026	3261	2218
$\Sigma\Delta\sigma_i P_i, \text{MPa}$	85	696	121	35	1216	65	2218

Table 4. Contribution of various mechanisms to hardening of rail steel in various morphological components and in general for the material in the rail head center

Таблица 4. Величины вкладов различных механизмов в упрочнение рельсовой стали в различных морфологических составляющих и в целом по материалу в центре головки рельса

Contributions	Pearlite				Subgrain structure	In the material
	ideal	fragmented	destroyed	globular		
$P_v, \%$	~1	10	0	0	90	100
$\Delta\sigma_p, \text{MPa}$	35	35	–	–	35	35
$\Delta\sigma_s, \text{MPa}$	80	210	–	–	210	210
$\Delta\sigma_g, \text{MPa}$	–	–	–	–	–	0
$\Delta\sigma_{perl}, \text{MPa}$	1120	–	–	–	–	10
$\Delta\sigma_{ss}, \text{MPa}$	–	1430	–	–	1875	1830
$\Delta\sigma_{or}, \text{MPa}$	–	1070	–	–	1435	1400
$\Delta\sigma_f, \text{MPa}$	575	445	–	–	380	390
$\Delta\sigma_{pl}, \text{MPa}$	575	445	–	–	380	390
$\Delta\sigma_{cl}, \text{MPa}$	40	2280	–	–	4255	4060
$\Delta\sigma_l, \text{MPa}$	615	2725	–	–	4635	4450
$\Sigma\Delta\sigma_i, \text{MPa}$	2077	5506	–	–	8206	7957
$\Sigma\Delta\sigma_i P_i, \text{MPa}$	21	551	–	–	7385	7957

CONCLUSIONS

Transmission electron microscopy was used to reveal the morphological components of the rolling surface of the rail head made of hypereutectoid steel, both

at the center and in the fillet. The identified components include lamellar pearlite, fragmented pearlite, destroyed lamellar pearlite, globular pearlite, completely destroyed pearlite, and subgrain structure. We conducted a quantitative analysis of hardening mechanisms and assessed

the contributions from lattice friction, solid solution hardening, pearlite hardening, incoherent cementite particles, grain boundaries and sub-boundaries, dislocation substructure, and internal stress fields. For the fillet surface, we established that the main hardening mechanism is due to incoherent particles, along with mechanisms based on internal long-range (local) stresses, internal shear stresses (“forests” of dislocations), and substructural hardening.

For the central part of the rolling surface, the primary hardening mechanisms are long-range stress fields, incoherent particles, and substructural hardening. We determined the additive yield strength at the rolling surface and explained the difference in its values between the head center and the fillet.

REFERENCES / СПИСОК ЛИТЕРАТУРЫ

- Yur'ev A.A., Kuznetsov R.V., Gromov V.E., Ivanov Yu.F., Shlyarova Yu.A. Long Rails: Structure and Properties after Long-Term Operation. Novokuznetsk: Poligrafist; 2022:311. (In Russ.).
Юрьев А.А., Кузнецов Р.В., Громов В.Е., Иванов Ю.Ф., Шлярова Ю.А. Длинномерные рельсы: структура и свойства после сверхдлительной эксплуатации. Новокузнецк: «Полиграфист»; 2022:311.
- Shur E.A. Rails Damage. Moscow: Intekst; 2012:153. (In Russ.).
Шур Е.А. Повреждения рельсов. Москва: Интекст; 2012:153.
- Steenbergen M. Rolling contact fatigue: Spalling versus transverse fracture of rails. *Wear*. 2017;380-381:96–105. <http://doi.org/10.1016/j.wear.2017.03.003>
- Skrypnik R., Ekh M., Nielsen J.C.O., Palsson B.A. Prediction of plastic deformation and wear in railway crossings – Comparing the performance of two rail steel grades. *Wear*. 2019;428-429:302–314. <http://doi.org/10.1016/j.wear.2019.03.019>
- Miranda R.S., Rezende A.B., Fonseca S.T., Fernandes F.M., Sinatora A., Mei P.R. Fatigue and wear behavior of pearlitic and bainitic microstructures with the same chemical composition and hardness using twin-disc tests. *Wear*. 2022; 494-495:204253. <http://doi.org/10.1016/j.wear.2022.204253>
- Pereira H.B., Alves L.H.D., Rezende A.B., Mei P.R., Goldenstein H. Influence of the microstructure on the rolling contact fatigue of rail steel: Spheroidized pearlite and fully pearlitic microstructure analysis. *Wear*. 2022;498-499:204299. <http://doi.org/10.1016/j.wear.2022.204299>
- Ivanov Yu.F., Porfir'ev M.A., Gromov V.E., Kryukov R.E., Shlyarova Yu.A. Structural and phase states in the head of special-purpose rails after prolonged operation. *Metally*. 2023;(6):53–58. (In Russ.). <http://doi.org/10.31857/S086957332306006X>
Иванов Ю.Ф., Порфирьев М.А., Громов В.Е., Крюков Р.Е., Шлярова Ю.А. Структурно-фазовые состояния в головке рельсов специального назначения после длительной эксплуатации. *Металлы*. 2023;(6):53–58. <http://doi.org/10.31857/S086957332306006X>
- Ivanisenko Yu., Fecht H.J. Microstructure modification in the surface layers of railway rails and wheels: Effect of high strain rate deformation. *Steel Tech*. 2008;3(1):19–23.
- Porfir'ev M.A., Gromov V.E., Ivanov Yu.F., Popova N.A., Shlyarov V.V. Thin structure of long-length rails made of hypereutectoid steel after long-term operation. Novokuznetsk: Poligrafist; 2023:285. (In Russ.).
Порфирьев М.А., Громов В.Е., Иванов Ю.Ф., Попова Н.А., Шляров В.В. Тонкая структура длинномерных рельсов из заэвтектоидной стали после длительной эксплуатации. Новокузнецк: Полиграфист; 2023:285.
- Nikas D., Zhang X., Ahlstrom J. Evaluation of local strength via microstructural quantification in a pearlitic rail steel deformed by simultaneous compression and torsion. *Materials Science and Engineering: A*. 2018;737:341–347. <https://doi.org/10.1016/j.msea.2018.09.067>
- Masoumi M., Sinatora A., Sietsma H.G. Role of microstructure and crystallographic orientation in fatigue crack failure analysis of a heavy haul railway rail. *Engineering Failure Analysis*. 2019;96:320–329. <http://doi.org/10.1016/j.engfailanal.2018.10.022>
- Turan M.E., Aydin F., Sun Y., Cetin M. Residual stress measurement by strain gauge and X-ray diffraction method in different shaped rails. *Engineering Failure Analysis*. 2019;96: 525–529. <https://doi.org/10.1016/j.engfailanal.2018.10.016>
- Li X.C., Ding H.H., Wang W.J., Guo J., Liu Q.Y., Zhou Z.R. Investigation on the relationship between microstructure and wear characteristic of rail materials. *Tribology International*. 2021; 163:107152. <http://doi.org/10.1016/j.triboint.2021.107152>
- Kanematsu Y., Uehigashi N., Matsui M., Noguchi S. Influence of a decarburized layer on the formation of microcracks in railway rails: On-site investigation and twindisc study. *Wear*. 2022;504–505:204427. <https://doi.org/10.1016/j.wear.2022.204427>
- Rong K.-J., Xiao Y.-L., Shen M.-X., Zhao H.-P., Wang W.-J., Xiong G.-Y. Influence of ambient humidity on the adhesion and damage behavior of wheel-rail interface under hot weather condition. *Wear*. 2021;486-487:204091. <https://doi.org/10.1016/j.wear.2021.204091>
- Improvement of rail steels. *Zheleznnye dorogi mira*. 2016;(1):74–76. (In Russ.).
Совершенствование рельсовых сталей. *Железные дороги мира*. 2016;(1):74–76.
- Dobuzhskaya A.B., Galitsyn G.A., Yunin G.N., Polevoi E.V., Yunusov A.M. Effect of chemical composition, microstructure and mechanical properties on the wear resistance of rail steel. *Steel in Translation*. 2020;50(12):906–910. <https://doi.org/10.3103/S0967091220120037>
Добужская А.Б., Галицын Г.А., Юнин Г.Н., Полевой Е.В., Юнусов А.М. Влияние химического состава, микроструктуры и механических свойств на износостойкость рельсовой стали. *Сталь*. 2020;(12):52–55.
- Wen J., Marteau J., Bouvier S., Risbet M., Cristofari F., Secorde P. Comparison of microstructure changes induced in two pearlitic rail steels subjected to a full-scale wheel/rail contact rig test. *Wear*. 2020;456-457:203354. <http://doi.org/10.1016/j.wear.2020.203354>
- Hu Y., Guo L.C., Maiorino M., Liu J.P., Ding H.H., Lewis R., Meli E., Rindi A., Liu Q.Y., Wang W.J. Comparison of wear and rolling contact fatigue behaviours of bainitic and pearlitic rails under various rolling-sliding conditions. *Wear*.

- 2020;460-461:203455.
<http://doi.org/10.1016/j.wear.2020.203455>
20. Hu Y., Zhou L., Ding H.H., Lewis R., Liu Q.Y., Guo J., Wang W.J. Microstructure evolution of railway pearlitic wheel steels under rolling-sliding contact loading. *Tribology International*. 2021;154:106685.
<http://doi.org/10.1016/j.triboint.2020.106685>
 21. Zhou L., Bai W., Han Z., Wang W., Hu Yu., Ding H., Lewis R., Meli E., Liu Q., Guo J. Comparison of the damage and microstructure evolution of eutectoid and hypereutectoid rail steels under a rolling-sliding contact. *Wear*. 2022;492-493:204233.
<http://doi.org/10.1016/j.wear.2021.204233>
 22. Bai W., Zhou L., Wang P., Hu Y., Wang W., Ding H., Han Z., Xu X., Zhu M. Damage behavior of heavy-haul rail steels used from the mild conditions to harsh conditions. *Wear*. 2022;496-497:204290.
<http://doi.org/10.1016/j.wear.2022.204290>
 23. Alwahdi F.A.M., Kapoor A., Franklin F.J. Subsurface microstructural analysis and mechanical properties of pearlitic rail steels in service. *Wear*. 2013;302(1-2):1453–1460.
<http://doi.org/10.1016/j.wear.2012.12.058>
 24. Wang W.J., Lewis R., Yang B., Guo L.C., Liu Q.Y., Zhu M.H. Wear and damage transitions of wheel and rail materials under various contact conditions. *Wear*. 2016;362-363:146–152.
<http://doi.org/10.1016/j.wear.2016.05.021>
 25. Pan R., Ren R., Zhao X., Chen C. Influence of microstructure evolution during the sliding wear of CL65 steel. *Wear*. 2018;400-401:169–176.
<http://doi.org/10.1016/j.wear.2018.01.005>
 26. Egerton F.R. Physical Principles of Electron Microscopy. Basel: Springer International Publishing; 2016:196.
<https://doi.org/10.1007/978-3-319-39877-8>
 27. Kumar C.S.S.R. Transmission Electron Microscopy. Characterization of Nanomaterials. New York: Springer; 2014:717.
 28. Carter C.B., Williams D.B. Transmission Electron Microscopy: Diffraction, Imaging, and Spectrometry. Berlin: Springer International Publishing; 2016:518.
<https://doi.org/10.1017/S1431927618000296>
 29. Popova N.A., Gromov V.E., Ivanov Yu.F., Porfir'ev M.A., Nikonenko E.L., Shlyarova Yu.A. Effect of long-term operation on the structural-phase state of hypereutectoid rail steel. *Materialovedenie*. 2023;(10):17–28. (In Russ.).
<https://doi.org/10.31044/1684-579X-2023-0-10-17-28>
Попова Н.А., Громов В.Е., Иванов Ю.Ф., Порфирьев М.А., Никоненко Е.Л., Шлярова Ю.А. Влияние длительной эксплуатации на структурно-фазовое состояние заэвтектоидной рельсовой стали. *Материаловедение*. 2023;(10):17–28. <https://doi.org/10.31044/1684-579X-2023-0-10-17-28>
 30. Gol'dshtein M.I., Farber V.M. Dispersion Hardening of Steel. Moscow: Metallurgiya; 1979:208. (In Russ.).
Гольдштейн М.И., Фарбер В.М. Дисперсионное упрочнение стали. Москва: Металлургия; 1979:208.
 31. Kozlov E.V., Koneva N.A. The nature of metal materials hardening. *Izvestiya vuzov. Fizika*. 2002;45(3):52–71. (In Russ.).
Козлов Э.В., Конева Н.А. Природа упрочнения металлических материалов. *Известия вузов. Физика*. 2002; 45(3):52–71.
 32. Kozlov E.V., Malinovskaya V.A., Popova N.A. Quantitative assessment of hardening of nitrocedmented steel 20Kh2N4A after low tempering. *Izvestiya. Ferrous Metallurgy*. 2006; 49(6):37–39. (In Russ.).
Козлов Э.В., Малиновская В.А., Попова Н.А. Количественная оценка упрочнения нитроцементованной стали 20Х2Н4А после низкого отпуска. *Известия вузов. Черная металлургия*. 2006;49(6):37–39.

Information about the Authors

Сведения об авторах

Natal'ya A. Popova, Cand. Sci. (Eng.), Research Associate of the Scientific and Educational Laboratory "Nanomaterials and Nanotechnologies", Tomsk State University of Architecture and Building
ORCID: 0000-0001-8823-4562
E-mail: natalya-popova-44@mail.ru

Viktor E. Gromov, Dr. Sci. (Phys.-Math.), Prof., Head of the Chair of Science named after V.M. Finkel; Siberian State Industrial University
ORCID: 0000-0002-5147-5343
E-mail: gromov@physics.sibsiu.ru

Aleksei B. Yur'ev, Dr. Sci. (Eng.), Prof., Rector, Siberian State Industrial University
ORCID: 0000-0002-9932-4755
E-mail: rector@sibsiu.ru

Efim A. Martusevich, Cand. Sci. (Eng.), Research Associate of the Laboratory of Electron Microscopy and Image Processing, Siberian State Industrial University
ORCID: 0000-0002-2335-7788
E-mail: program.pro666@gmail.com

Mikhail A. Porfir'ev, Research Associate of Department of Scientific Researches, Siberian State Industrial University
ORCID: 0000-0003-3602-5739
E-mail: mporf372@gmail.com

Наталья Анатольевна Попова, к.т.н., научный сотрудник научно-учебной лаборатории «Наноматериалы и нанотехнологии», Томский государственный архитектурно-строительный университет
ORCID: 0000-0001-8823-4562
E-mail: natalya-popova-44@mail.ru

Виктор Евгеньевич Громов, д.ф.-м.н., профессор, заведующий кафедрой естественнонаучных дисциплин им. проф. В.М. Финкеля, Сибирский государственный индустриальный университет
ORCID: 0000-0002-5147-5343
E-mail: gromov@physics.sibsiu.ru

Алексей Борисович Юрьев, д.т.н., профессор, ректор, Сибирский государственный индустриальный университет
ORCID: 0000-0002-9932-4755
E-mail: rector@sibsiu.ru

Ефим Александрович Мартусевич, к.т.н., научный сотрудник лаборатории электронной микроскопии и обработки изображений, Сибирский государственный индустриальный университет
ORCID: 0000-0002-2335-7788
E-mail: program.pro666@gmail.com

Михаил Анатольевич Порфирьев, научный сотрудник Управления научных исследований, Сибирский государственный индустриальный университет
ORCID: 0000-0003-3602-5739
E-mail: mporf372@gmail.com

Contribution of the Authors

Вклад авторов

N. A. Popova – quantitative calculation of hardening mechanisms.

V. E. Gromov – formation of the article concept, discussion of the results, writing the article final version.

A. B. Yur'ev – discussion of the results, writing the article draft.

E. A. Martusevich – preparation of samples for TEM studies, processing of measurement results.

M. A. Porfir'ev – production of foils, participation in TEM studies, literary review.

Н. А. Попова – количественный расчет механизмов упрочнения.

В. Е. Громов – формирование концепции статьи, обсуждение результатов, написание окончательного варианта статьи.

А. Б. Юрьев – обсуждение результатов, написание чернового варианта статьи.

Е. А. Мартусевич – подготовка образцов для ПЭМ-исследований, обработка результатов измерений.

М. А. Порфирьев – изготовление фольг, участие в ПЭМ-исследованиях, обзор литературы.

Received 02.02.2024

Revised 19.02.2024

Accepted 29.03.2024

Поступила в редакцию 02.02.2024

После доработки 19.02.2024

Принята к публикации 29.03.2024



UDC 621.791.927.5:620.178

DOI 10.17073/0368-0797-2024-4-433-439



Original article

Оригинальная статья

EFFECT OF ELECTRIC ARC SURFACING ON THE STRUCTURE AND PROPERTIES OF COATINGS

G. V. Shlyakhova[✉], V. I. Danilov

Institute of Strength Physics and Materials Science, Siberian Branch of the Russian Academy of Sciences (2/4 Akademicheskii Ave., Tomsk 634055, Russian Federation)

✉ shgv@ispms.ru

Abstract. Surfacing, like welding, is associated with heating metals in a wide range of temperatures and subsequent cooling of heated zones at different rates. This leads to complex structural and phase changes that are crucial for operational properties of the “protected material – coating” joint. The structure and properties of the alloyage zone of these two materials depend on the degree of penetration, nature of the intermediate layers that arise, and carbon diffusion in the boundary areas. When surfacing on low-carbon steel, depending on the composition of the deposited metal, the structures with a predominant amount of martensite or austenite can be obtained in the alloyage zone, depending on carbon content. The structure and mechanical properties of the bimetallic joint between carbon steel and stainless steel were studied depending on the modes of electric arc surfacing (submerged arc surfacing in one pass, in argon for one and two passes). It was established that the structural and phase composition of the deposited metal is austenite, finely dispersed carbides and a needle component. The structure of the layer deposited in argon in one pass is more homogeneous and does not contain defects. The microhardness increases smoothly along the depth of the deposited layer. As a result of surfacing in argon in two passes, the joint has a homogeneous microstructure, but a large number of microdefects are formed in the layer, which can further lead to the formation of a crack near the alloyage boundary. In submerged surfacing, the heating rate and specific heat input are insufficient, therefore, the surfacing bath is poorly mixed, which leads to a suboptimal structure and the formation of thermal stresses at the alloyage boundary and to the formation of a coating that is heterogeneous in structure and microhardness.

Keywords: electric arc welding, wire, structure, microhardness, defects, martensite, widmanstatten structure, scanned images

Acknowledgements: The work was performed in accordance with the state assignment of the Institute of Strength Physics and Materials Science, Siberian Branch of the Russian Academy of Science, subject no. FWRW-2021-0011.

For citation: Shlyakhova G.V., Danilov V.I. Effect of electric arc surfacing on the structure and properties of coatings. *Izvestiya. Ferrous Metallurgy*. 2024;67(4):433–439. <https://doi.org/10.17073/0368-0797-2024-4-433-439>

ИССЛЕДОВАНИЕ ВЛИЯНИЯ ЭЛЕКТРОДУГОВОЙ НАПЛАВКИ НА СТРУКТУРУ И СВОЙСТВА ПОКРЫТИЙ

Г. В. Шляхова[✉], В. И. Данилов

Институт физики прочности и материаловедения Сибирского отделения РАН (Россия, 634055, Томск, пр. Академический, 2/4)

✉ shgv@ispms.ru

Аннотация. Наплавка, как и сварка, связана с нагревом металлов в широком интервале температур и последующим охлаждением нагретых зон с разными скоростями. Это приводит к сложным структурным и фазовым изменениям, имеющим определяющее значение для эксплуатационных свойств соединения защищаемый материал – покрытие. Строение и свойства зоны сплавления этих двух материалов зависят от степени проплавления, характера возникающих промежуточных слоев и диффузии углерода в приграничных участках. При наплавке на низкоуглеродистую сталь, в зависимости от состава наплавляемого металла, в зоне сплавления могут получаться структуры с преобладающим количеством мартенсита или аустенита в зависимости от содержания углерода. В работе исследовали структуру и механические свойства биметаллического соединения углеродистая сталь – нержавеющая сталь в зависимости от режимов электродуговой наплавки (под флюсом за один проход, в аргоне за один и два прохода). Установлено, что структурно-фазовый состав наплавленного металла – аустенит, мелкодисперсные карбиды и игольчатая составляющая. Структура наплавленного в аргоне за один проход слоя является более однородной и не содержит макродефектов. Микротвердость плавно увеличивается по глубине наплавленного слоя. В результате наплавки в аргоне за два прохода соединение имеет однородную микроструктуру, но в слое образуется большое количество микродефектов, которые в дальнейшем могут привести к образованию трещины вблизи границы сплавления. При наплавке под флюсом скорость нагрева и удельное тепловложение недостаточны, поэтому наплавочная ванна плохо перемешивается, что приводит к неопти-

мальной структуре и формированию термических напряжений на границе сплавления и к формированию неоднородного по структуре и микротвердости покрытия.

Ключевые слова: электродуговая наплавка, проволока, структура, микротвердость, дефекты, мартенсит, видманштетт, скан-изображения

Благодарности: Работа выполнена в соответствии с государственным заданием Института физики прочности и материаловедения Сибирского отделения РАН, тема номер FWRW-2021-0011.

Для цитирования: Шляхова Г.В., Данилов В.И. Исследование влияния электродуговой наплавки на структуру и свойства покрытий. *Известия вузов. Черная металлургия*. 2024;67(4):433–439. <https://doi.org/10.17073/0368-0797-2024-4-433-439>

INTRODUCTION

In many industries, such as chemical, nuclear, aerospace, and others, the structural strength of components is often determined by the materials' resistance to aggressive environments. Technically, this challenge can be fully addressed by using corrosion-resistant materials [1 – 3]. However, from an economic stand-point, such a solution may not always be rational, particularly in applications like the secondary coolant circuits in nuclear power plants. While corrosion-resistant steel is essential for manufacturing pipelines, high-quality carbon steels can be used for valves and some pump components, provided that anticorrosion coatings are applied to the surfaces exposed to the coolant [4]. One of the most widespread and effective methods for applying such coatings is electric arc surfacing [5 – 7]. Currently, the scientific principles of electric arc surfacing are well established, and numerous modifications of this method exist. Electric arc surfacing is easily mechanized, ensuring high productivity. It allows for the uniform application of metal layers with the desired physical and mechanical properties, thus fulfilling the required technological objectives [8 – 12]. In the present study, the goal was to protect valves made of low-carbon steel from aggressive liquids. Challenges arose when transitioning from previously used surfacing materials to new ones.

Surfacing, like welding, involves heating metals over a wide temperature range and subsequently cooling the heated zones at different rates. This leads to complex structural and phase changes, which play a critical role in determining the operational properties of the “protected material – coating” joint [15]. The coating is formed during the crystallization of the molten electrode metal and the fused base metal, acquiring a cast structure. The characteristics of the aloyage zone between the deposited layer and the base material are particularly important for the properties and performance of the coating, especially when they differ in composition and structural class. The aloyage zone determines the reliability of the bond between the deposited metal and the base material [14 – 16]. The base material is low-carbon steel, while the deposited metal is stainless steel. The structure and properties of the aloyage zone between these two materials will depend on the degree of penetration, the nature of the intermediate layers that

form, and carbon diffusion in the boundary areas [17; 18]. When surfacing low-carbon steel, depending on the composition of the deposited metal, the aloyage zone may develop structures with a predominant amount of martensite or austenite, depending on the carbon content. The deposited metal, depending on the chromium and nickel content, may exhibit an austenitic or austenitic-ferritic structure. If the nickel and chromium content is insufficient, the deposited metal may develop a secondary austenitic-martensitic structure [4; 8; 19]. The properties of the deposited metal and the resulting structure of the surfacing layer are significantly influenced by the mixing of the base metal and the electrode material. Generally, minimal mixing of the deposited metal with the base metal is desired. When stainless steels are deposited onto unalloyed steel, a sharply defined transition zone often forms between the deposited and base metals, with a relatively wide width [20; 21].

This study investigates the influence of various electric arc surfacing methods on the structure and mechanical properties of the bimetallic joint between carbon steel and stainless steel.

MATERIALS AND METHODS

The study investigated the structure and properties of coatings obtained through mechanized surfacing using consumable electrodes made of solid stainless steel wire with an Fe–C–Cr–Ni–Si–Mn alloying system. The wire had a diameter of 1.8 mm, and various numbers of layers were applied using the following methods: submerged arc surfacing (1 pass), argon arc surfacing (1 pass), and argon arc surfacing (2 passes). The chemical composition of the Fe–C–Cr–Ni–Si–Mn wire was as follows, in wt. %: ≤ 0.12 C; ~ 15.0 Cr; ~ 0.8 Mn; ~ 4.5 Si; ~ 8.5 Ni; < 0.04 S; < 0.04 P; with the remainder being iron.

Surfacing was performed on specimens of high-quality carbon steel 20 with dimensions of $50 \times 15 \times 10$ mm (length \times width \times height).

To study the microstructure, cross-sectional samples were prepared from each specimen after each surfacing mode. The preparation of the samples involved mechanical grinding, mechanical polishing on a synthetic diamond material, transitioning from coarse to fine diamond powder, and chemical etching [8; 10; 22]. The study of the structure and the measurement of the microhard-

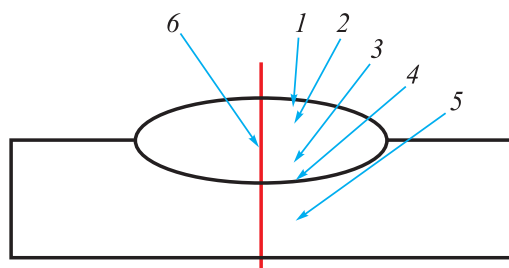


Fig. 1. Diagram of typical connection zones for metallographic studies:

1 – deposited roller; 2 – the upper part of deposited metal;
3 – the lower part of deposited metal; 4 – alloyage zone of roller and base metal; 5 – base metal; 6 – microhardness measuring line

Рис. 1. Схема характерных участков соединения для проведения металлографических исследований:

1 – наплавленный валик; 2 – верхняя часть наплавленного металла;
3 – нижняя часть наплавленного металла;
4 – зона сплавления валика и основного металла;
5 – основной металл; 6 – линия измерения микротвердости

ness of the “coating – base metal” joint were performed on polished samples according to the scheme presented in Fig. 1.

Structural investigations were conducted using optical microscopy (OM) and atomic force microscopy (AFM) with Neophot-21 and Solver PH47-PRO microscopes, respectively [22]. Microhardness measurements were carried out using a PMT-3 microhardness tester under a load of 0.1 N.

RESULTS AND DISCUSSION

A visual inspection of the unetched crosssections from the three variants showed no macrodefects, such as pores or cracks, in the surfaced layers. However, scan images of the etched crosssections obtained with an atomic force microscope (AFM) revealed that, in all surfacing modes, rare isolated microdefects in the form of spherical pores were predominantly present at the alloyage boundary between the stainless steel and steel 20 (Fig. 2). Profilograms constructed using the sectioning method allowed for determining their morphology and size. The maximum dimensions of the micropores in the longitudinal and transverse directions were 10 and 15 μm , respectively. However, due to their small size, they are not classified as surfacing defects.

The structure of the base metal (region 5) in all cases corresponds to the structure of low-carbon steel 20 (Fig. 3), characterized by polyhedral grains of ferrite and pearlite, with an average grain size of approximately 52 μm , corresponding to a grain number of 5 to 6. The microhardness was $HV_{0.1} = 1320 \text{ MPa}$.

The deposited metal formed in all three surfacing variants can be conventionally divided into four regions, with the thickness of these regions varying depending on the surfacing mode. Point 4 corresponds to the alloyage

boundary (the dark layer in Fig. 4) and the heat-affected zone (HAZ). In the HAZ, a Widmanstatten structure is observed adjacent to the alloyage boundary. Directly at the alloyage line, a decarburized layer with the lowest hardness ($HV_{0.1} = 1000 \text{ MPa}$) was detected. The thick-

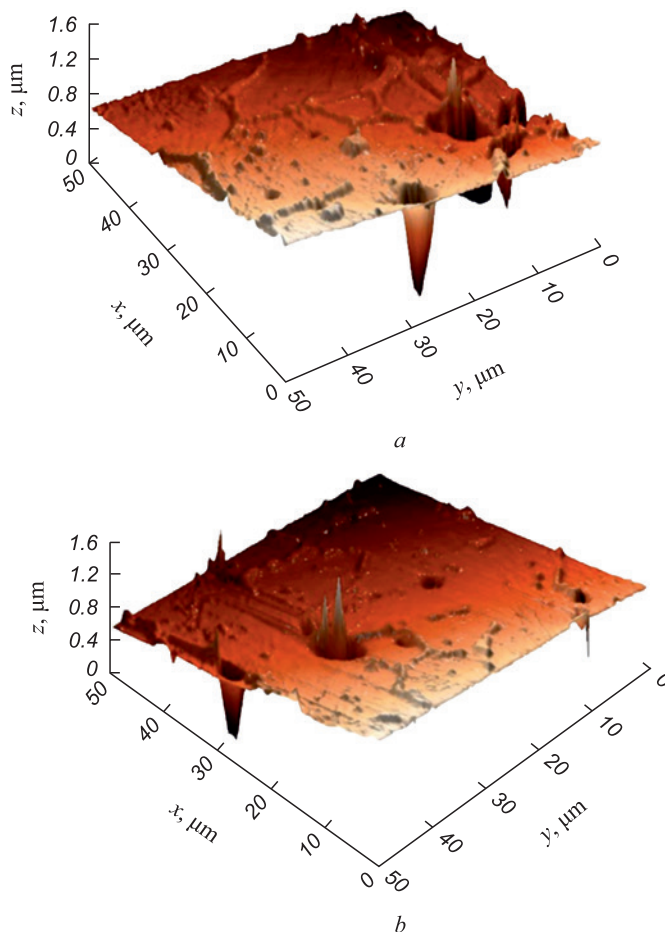


Fig. 2. Topography of defects near the alloyage boundary (AFM) (3D images)

Рис. 2. Топография дефектов вблизи границы сплавления (АСМ) (3D изображения)

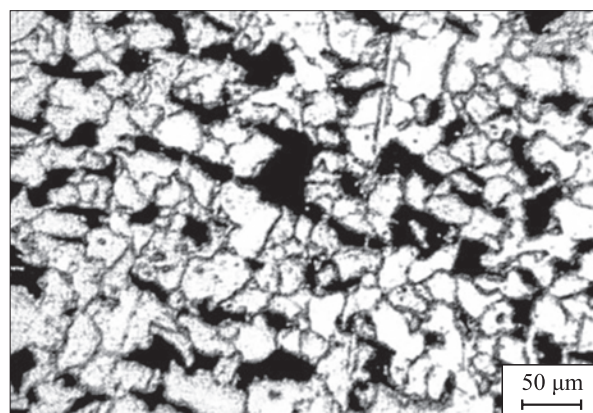


Fig. 3. Structure of 20 steel

Рис. 3. Структура стали 20

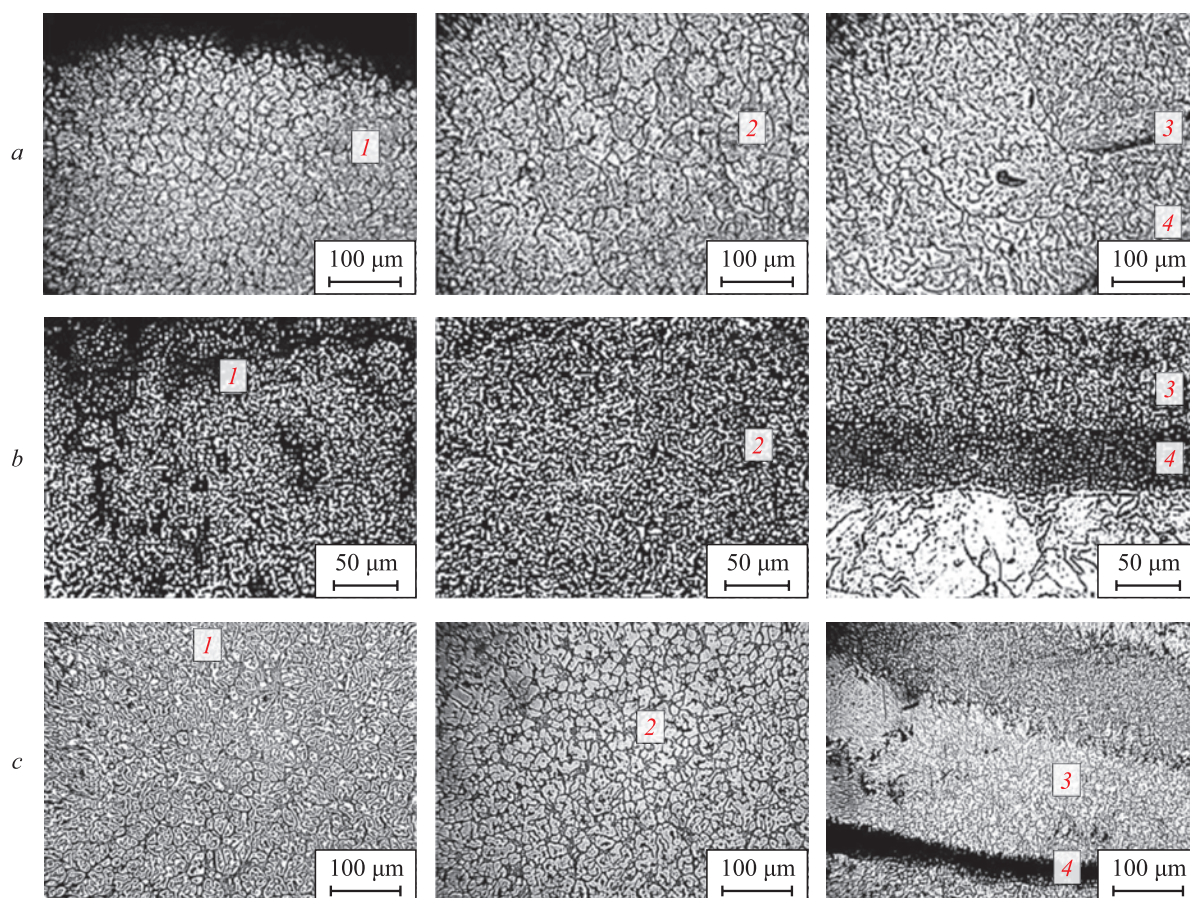


Fig. 4. Structure of deposited layer (Fig. 1), made according to option 1 – 3 (a – c):

1 – deposited roller; 2 – the upper part of deposited metal; 3 – the lower part of deposited metal; 4 – alloyage zone of roller and base metal

Рис. 4. Структура наплавленного слоя (см. рис. 1), выполненного по варианту 1 – 3 (a – c):

1 – наплавленный валик; 2 – верхняя часть наплавленного металла; 3 – нижняя часть наплавленного металла;
4 – зона сплавления валика и основного металла

ness of this layer in the sample processed according to variant 1 was approximately 100 μm , and in variant 2, it reached a maximum of 120 μm . In the sample surfaced using mode 3, the decarburized layer was not detected, with only small, very rare areas up to a maximum depth of 15 μm observed.

In the surfacing conducted according to variant 1, the phase composition is primarily austenite, with varying morphology and size of structural elements (Fig. 4, a). The extent of characteristic regions of the joint (ΔL)

and the corresponding microhardness values are indicated in the table (measured from the upper, or free, surface of the surfacing; see the diagram in Fig. 1). In region 3, the austenite grains contain a acicular component that could not be precisely identified. Most likely, these are martensitic needles, as evidenced by the high micro-hardness values (Fig. 5): the microhardness in region 3 is nearly twice that of regions 1 and 2, reaching $HV_{0.1} \approx 6500$ MPa. Isolated micropores were found near the boundary.

Values of microhardness in deposited layer

Значения микротвердости в наплавленном слое

Region	HV _{0.1} , MPa	ΔL , μm	HV _{0.1} , MPa	ΔL , μm	HV _{0.1} , MPa	ΔL , μm
	Variant 1		Variant 2		Variant 3	
1	3300	1680	2060	1000	2800	4200
2	3550	1400	2500	3500	3000	3900
3	5100	2100	3100	1050	3500	2100
4	6500	8	4200	60	4600	50

The microstructure of the deposited metal in the joint obtained using variant 2 is more homogeneous than that of the sample from variant 1 (Fig. 4, b). The microhardness changes relatively smoothly with depth, reaching its maximum only at the aloyage boundary (Fig. 5, Table). The aloyage zone (heavily etched region 4) is approximately 60 μm thick, with a hardness 1.5 times higher than the average hardness of the deposited metal, though significantly lower than in the sample surfaced using variant 1 (6500 MPa). The phase composition of the deposited metal includes austenite and fine-dispersed carbides, with a acicular component appearing near the aloyage boundary. Overall, the joint obtained using variant 2 is the most refined, free of defects such as microcracks in the deposited metal and at the aloyage boundary.

The structure of the deposited metal surfaced using variant 3 is more homogeneous than that of the sample from variant 1 and is similar to the structure of the sample from variant 2, despite the use of two-pass surfacing here (Fig. 4, c). The microhardness in the main part of the surfacing (more than 80 %) does not significantly change with depth. In the remaining 20 % of the surfacing thickness, it increases by approximately 15 %, reaching a maximum in the boundary area (see Table). The aloyage boundary itself (heavily etched region) is about 50 μm thick, with a hardness 1.5 times higher than the average hardness of the deposited metal (Fig. 5). Overall, the joint from variant 3 has a good homogeneous microstructure, but the largest number of micropores formed in the deposited metal near the boundary.

Submerged arc surfacing (variant 1) results in a coating with a heterogeneous structure and microhard-

ness. Isolated micropores were found in the coating near the aloyage line with the base metal. In this part of the coating, there is an increased content of quenched (acicular) structures.

Based on the macro- and microstructural analysis of the surfaced layers, it was established that the most refined structure is found in the sample processed using variant 2 – argon arc surfacing in one pass. The structure of the deposited metal consists of austenite, fine-dispersed carbides, and a acicular component near the aloyage boundary. The microhardness of the surfaced layer changes smoothly with depth, reaching maximum values only at the aloyage boundary. No microdefects were found.

The analysis of the structural-phase composition of the metal surfaced using variant 3 – argon arc surfacing in two passes – showed that the joint has a good homogeneous microstructure; however, the largest number of micropores was found in the layer surfaced during the first pass near the aloyage boundary. An increased content of acicular structures and, consequently, higher microhardness were also observed in this area.

CONCLUSIONS

The study established that during surfacing, carbon diffuses into the deposited metal, leading to the formation of carbides and the development of hardened structures, such as an acicular structure. In the heat-affected zone, a Widmanstatten structure forms, characterized by fine needles extending from ferritic plates. The base metal structure remains ferrite-pearlite.

In submerged arc surfacing, the heating rate and specific heat input are insufficient, resulting in poor mixing of the weld bath. This leads to a suboptimal structure and the formation of thermal stresses at the aloyage boundary. A similar issue arises in two-pass surfacing, where the lower layer is not fully penetrated.

REFERENCES / СПИСОК ЛИТЕРАТУРЫ

1. Sidorov V.P., Mel'zitdinova A.V. The methodology for determining the requirements for the accuracy of welding parameters. *Svarka i diagnostika*. 2014;(3):10–13. (In Russ.).
Сидоров В.П., Мельзитдинова А.В. Методика определения требований к точности параметров сварки. *Сварка и диагностика*. 2014;(3):10–13.
2. Borisova A.L., Mits I.V., Kaida T.V., Dzykovich I.Ya., Korzhik V.N. Structure and properties of ferrobrium-based electric arc coatings obtained from powder wires. *Avtomaticheskaya svarka*. 1991;(9(462)):66–68. (In Russ.).
Борисова А.Л., Миц И.В., Кайда Т.В., Дзыкович И.Я., Коржик В.Н. Структура и свойства электродуговых покрытий на основе ферробора, полученных из порошковых проволок. *Автоматическая сварка*. 1991;(9(462)):66–68.

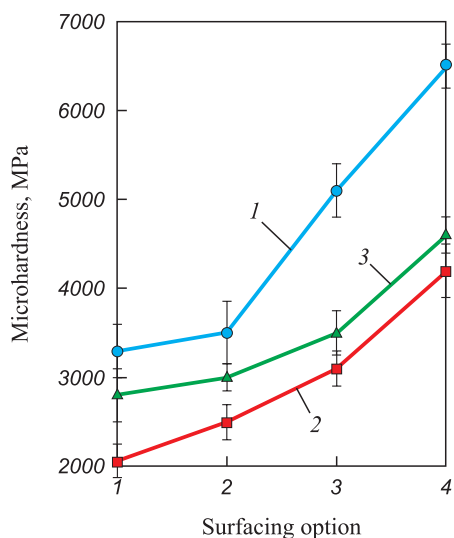


Fig. 5. Dependence of microhardness of deposited layer on surfacing method

Рис. 5. Зависимость микротвердости наплавленного слоя от способа наплавки

3. Skoblo T.S., Tikhonov A.V., Rybalko I.N. New method for parts restoration. *Avtomobil'nyi transport*. 2012;(31):124–128. (In Russ.).
Скобло Т.С., Тихонов А.В., Рыбалко И.Н. Новый способ восстановления деталей. *Автомобильный транспорт*. 2012;(31):124–128.
4. Ivashko V.S., Kurash V.V., Kudina A.V. Formation of high-quality wear-resistant metal coatings by electric arc surfacing in an ultrasonic field with introduction of a carbide powder additive into the melt. *Teoriya i praktika mashinostroeniya*. 2003;(2):77–81. (In Russ.).
Ивашко В.С., Кураш В.В., Кудина А.В. Формирование качественных износостойких металлопокрытий способом электродуговой наплавки в ультразвуковом поле с введением в расплав твердосплавной порошковой присадки. *Теория и практика машиностроения*. 2003;(2):77–81.
5. Kozyrev N.A., Kibko N.V., Umanskii A.A., Titov D.A., Sokolov P.D. Improving the quality of deposited layer of rolling rolls by optimizing the composition of powder wires. *Svarochnoe proizvodstvo*. 2017;(7):29–34. (In Russ.).
Козырев Н.А., Кибко Н.В., Уманский А.А., Титов Д.А., Соколов П.Д. Повышение качества наплавленного слоя прокатных валков за счет оптимизации состава порошковых проволок. *Сварочное производство*. 2017;(7):29–34.
6. Kuznetsov M.A., Zernin E.A., Kolmogorov D.E., Shlyakhova G.V., Danilov V.I. Structure, morphology and dispersion of metal deposited by arc welding with a melting electrode in argon in the presence of nanostructured modifiers. *Svarka i diagnostika*. 2012;(6):8–10. (In Russ.).
Кузнецов М.А., Зернин Е.А., Колмогоров Д.Е., Шляхова Г.В., Данилов В.И. Строение, морфология и дисперсность металла, наплавленного дуговой сваркой плавящимся электродом в аргоне в присутствии наноструктурированных модификаторов. *Сварка и диагностика*. 2012;(6):8–10.
7. Il'yaschenko D.P., Chinakhov D.A., Danilov V.I., Schlyakhova G.V., Gotovshchik Yu.M. Physical nature of the processes in forming structures, phase and chemical compositions of medium-carbon steel welds. *IOP Conference Series: Materials Science and Engineering*. 2015;91:012006. <http://dx.doi.org/10.1088/1757-899X/91/1/012006>
8. Kuznetsov M.A., Zernin E.A., Kartsev D.S., Shlyakhova G.V., Danilov V.I. Microstructure of welded joints obtained using aluminum oxyhydroxide. *Svarka i diagnostika*. 2016;(4):24–26. (In Russ.).
Кузнецов М.А., Зернин Е.А., Карцев Д.С., Шляхова Г.В., Данилов В.И. Микроструктура сварных соединений, полученных с применением оксигидроксида алюминия. *Сварка и диагностика*. 2016;(4):24–26.
9. Gusev A.I., Kibko N.V., Popova M.V., Kozyrev N.A., Osetkovskii I.V. Surfacing of details of mining equipment by powder wires of C – Si – Mn – Mo – V – B and C – Si – Mn – Cr – Mo – V systems. *Izvestiya. Ferrous Metallurgy*. 2017;60(4):318–323. (In Russ.). <https://doi.org/10.17073/0368-0797-2017-4-318-323>
Гусев А.И., Кибко Н.В., Попова М.В., Козырев Н.А., Осетковский И.В. Наплавка порошковыми проволоками систем C – Si – Mn – Mo – V – B и C – Si – Mn – Cr – Mo – V деталей горнорудного оборудования. *Известия вузов. Черная металлургия*. 2017;60(4):318–323. <https://doi.org/10.17073/0368-0797-2017-4-318-323>
10. Gusev A.I., Usoltsev A.A., Kozyrev N.A., Kibko N.V., Bashchenko L.P. Development of flux-cored wire for surfacing of parts operating under conditions of wear. *Izvestiya. Ferrous Metallurgy*. 2018;61(11):898–906. (In Russ.). <https://doi.org/10.17073/0368-0797-2018-11-898-906>
Гусев А.И., Усольцев А.А., Козырев Н.А., Кибко Н.В., Башченко Л.П. Разработка порошковой проволоки для наплавки деталей, работающих в условиях износа. *Известия вузов. Черная металлургия*. 2018;61(11):898–906. <https://doi.org/10.17073/0368-0797-2018-11-898-906>
11. Świerczyńska A., Varbai B., Pandey Ch., Fydrich D. Exploring the trends in flux-cored arc welding: scientometric analysis approach. *The International Journal of Advanced Manufacturing Technology*. 2024;130:87–110. <https://doi.org/10.1007/s00170-023-12682-6>
12. Gusev A.I., Kozyrev N.A., Usoltsev A.A., Kryukov R.E., Mikhno A.R. Development of a flux-cored wire for surfacing mining equipment operating in the conditions of shock-abrasive wear. *IOP Conf. Series: Earth and Environmental Science*. 2018;206:012034. <https://doi.org/10.1088/1755-1315/206/1/012034>
13. Pańcikiewicz K. Preliminary process and microstructure examination of flux-cored wire arc additive manufactured 18Ni–12Co–4Mo–Ti maraging steel. *Materials*. 2021;14(21):6725. <https://doi.org/10.3390/ma14216725>
14. Moreno J.S., Conde F.F., Correa C.A., Barbosa L.H., da Silva E.P., Avila J., Pinto H.C. Pulsed FCAW of martensitic stainless clads onto mild steel: microstructure, hardness, and residual stresses. *Materials*. 2022;15(8):2715. <https://doi.org/10.3390/ma15082715>
15. Parshin S., Levchenko A., Wang P., Maystro A. Mathematical analysis of the influence of the flux-cored wire chemical composition on the electrical parameters and quality in the underwater wet cutting. *Advances in Materials Science*. 2021;21(1):77–89. <https://doi.org/10.2478/adms-2021-0006>
16. Cheilyakh Ya.A., Chigarev V.V. Structure and properties of deposited wear-resistant Fe–Cr–Mn steel with a controlled content of metastable austenite. *Avtomaticheskaya svarka*. 2011;(8):20–24. (In Russ.).
Чейлях Я.А., Чигарев В.В. Структура и свойства наплавленной износостойкой Fe–Cr–Mn стали с регулируемым содержанием метастабильного аустенита. *Автоматическая сварка*. 2011;(8):20–24.
17. Mutaşcu D., Karancı O., Mitelea I., Crăciunescu C.M., Buzdugan D., Uțu I.D. Pulsed TIG cladding of a highly carbon-, chromium-, molybdenum-, niobium-, tungsten- and vanadium-alloyed flux-cored wire electrode on duplex stainless steel X2CrNiMoN 22-5-3. *Materials*. 2023;16(13):4557. <https://doi.org/10.3390/ma16134557>
18. Metlitskii V.A. Flux-cored wires for arc welding and surfacing of cast iron. *Welding International*. 2008;22(11):796–800. <http://dx.doi.org/10.1080/09507110802593646>
19. Kejžar R., Grum J. Hardfacing of wear-resistant deposits by MAG welding with a flux-cored wire having graphite in its filling. *Welding International*. 2005;20(6):961–976. <http://dx.doi.org/10.1081/AMP-200060424>
20. Deng X.T., Fu T.L., Wang Z.D., Misra R.D.K., Wang G.D. Epsilon carbide precipitation and wear behaviour of low alloy wear resistant steels. *Materials Science and Techno-*

logy. 2016;32(4):320–327.

<http://dx.doi.org/10.1080/02670836.2015.1137410>

21. Filippov M.A., Shumyakov V.I., Balin S.A., Zhilin A.S., Lehchilo V.V., Rimer G.A. Structure and wear resistance of deposited alloys based on metastable chromium – carbon austenite. *Welding International*. 2015;29(10):819–822. <https://doi.org/10.1080/09507116.2014.986891>
22. Shlyakhova G.V., Barannikova S.A., Li Yu.V., Bochkareva A.V., Zuev L.B. Study of the structure of bimetal const-

ruction carbon steel – stainless steel. *Izvestiya. Ferrous Metallurgy*. 2018;61(4):300–305. (In Russ.).

<https://doi.org/10.17073/0368-0797-2018-4-300-305>

Шляхова Г.В., Баранникова С.А., Бочкарёва А.В., Ли Ю.В., Зуев Л.Б. Исследование структуры биметалла конструкционная углеродистая сталь – нержавеющая сталь. *Известия вузов. Черная металлургия*. 2018; 61(4):300–305.

<https://doi.org/10.17073/0368-0797-2018-4-300-305>

Information about the Authors

Galina V. Shlyakhova, Cand. Sci. (Eng.), Research Associate of the Laboratory of Strength Physics, Institute of Strength Physics and Materials Science, Siberian Branch of Russian Academy of Sciences

ORCID: 0000-0001-9578-2989

E-mail: shgv@ispms.ru

Vladimir I. Danilov, Dr. Sci. (Phys.-Math.), Prof., Chief Researcher of the Laboratory of Strength Physics, Institute of Strength Physics and Materials Science, Siberian Branch of the Russian Academy of Sciences

ORCID: 0000-0002-5741-7574

E-mail: dvi@ispms.ru

Сведения об авторах

Галина Витальевна Шляхова, к.т.н., научный сотрудник лаборатории физики прочности, Институт физики прочности и материаловедения Сибирского отделения РАН

ORCID: 0000-0001-9578-2989

E-mail: shgv@ispms.ru

Владимир Иванович Данилов, д.ф.-м.н., профессор, главный научный сотрудник лаборатории физики прочности, Институт физики прочности и материаловедения Сибирского отделения РАН

ORCID: 0000-0002-5741-7574

E-mail: dvi@ispms.ru

Contribution of the Authors

G. V. Shlyakhova – preparing the samples, conducting the research, analyzing the results, writing the text.

V. I. Danilov – formulating the article concept, discussing the results, preparing an outline for the article.

Вклад авторов

Г. В. Шляхова – подготовка образцов, проведение исследований, анализ результатов, написание текста статьи.

В. И. Данилов – формулирование концепции работы, обсуждение результатов, подготовка плана статьи.

Received 27.02.2024

Revised 15.03.2024

Accepted 25.03.2024

Поступила в редакцию 27.02.2024

После доработки 15.03.2024

Принята к публикации 25.03.2024



UDC 538.953

DOI 10.17073/0368-0797-2024-4-440-448



Original article

Оригинальная статья

MOLECULAR DYNAMICS STUDY OF THE INFLUENCE OF CARBON IMPURITY ON AUSTENITE NANOPARTICLES CRYSTALLIZATION DURING RAPID COOLING

I. V. Zorya¹, G. M. Poletaev^{2,3}, Yu. V. Bebikhov⁴, A. S. Semenov⁴

¹ Siberian State Industrial University (42 Kirova Str., Novokuznetsk, Kemerovo Region – Kuzbass 654007, Russian Federation)

² Katanov Khakassian State University (90 Lenina Ave., Abakan, Republic of Khakassia 655012, Russian Federation)

³ Polzunov Altai State Technical University (46 Lenina Ave., Barnaul, Altai Territory 656038, Russian Federation)

⁴ Mirny Polytechnic Institute (branch) of North-Eastern Federal University (5 Tikhonova Str., Mirny, Republic of Sakha (Yakutia) 678170, Russian Federation)

✉ zorya.i@mail.ru

Abstract. The molecular dynamics method was used to study the structure formation during austenite nanoparticles crystallization in the presence of carbon impurities. The paper describes the dependence of the melt cooling rate, particle size, concentration of carbon atoms in the particle on the resulting structure features during crystallization and temperature of the crystallization onset. Formation of the nanocrystalline structure of nanoparticles can be controlled by varying the cooling rate and introducing a carbon impurity: at a cooling rate above 10^{13} K/s in the model used, crystallization did not have time to occur; at a rate below $5 \cdot 10^{12}$ K/s, the austenite particle crystallized to form a nanocrystalline structure. At the same time, with a decrease in the cooling rate, a decrease in the density of defects in the final structure was observed. At a rate of $5 \cdot 10^{11}$ K/s or less, crystallization of carbon-free particles took place with the formation of low-energy grain boundaries (with a high density of conjugate nodes: special boundaries, twins). The crystallization temperature during cooling at a rate below 10^{12} K/s is inversely proportional to the particle diameter: as the particle size decreases, the proportion of free surface increases, which leads to a decrease in the probability of crystalline nuclei formation. In addition, the crystallization temperature increases with a decrease in the cooling rate. The introduction of a carbon impurity led to a decrease in the crystallization temperature of nanoparticles: in the presence of 10 at. %. As a percentage of carbon, it decreased by about 200 K for particles of different sizes. Carbon atoms often formed clusters consisting of several carbon atoms. Such clusters distorted the resulting crystal lattice of metal around them, preventing crystallization. In the presence of a carbon impurity, the final structure of the crystallized particles contained a higher density of grain boundaries and other defects. Carbon atoms, especially clusters of them, were fixed mainly at grain boundaries and triple joints.

Keywords: molecular dynamics, nanoparticle, crystallization, nanocrystal, austenite

Acknowledgements: The research was supported by the Russian Science Foundation (grant No. 23-12-20003, <https://rscf.ru/project/23-12-20003/>) and the Government of the Republic of Khakassia.

For citation: Zorya I.V., Poletaev G.M., Bebikhov Yu.V., Semenov A.S. Molecular dynamics study of the influence of carbon impurity on austenite nanoparticles crystallization during rapid cooling. *Izvestiya. Ferrous Metallurgy*. 2024;67(4):440–448. <https://doi.org/10.17073/0368-0797-2024-4-440-448>

МОЛЕКУЛЯРНО-ДИНАМИЧЕСКОЕ ИССЛЕДОВАНИЕ ВЛИЯНИЯ ПРИМЕСИ УГЛЕРОДА НА ПРОЦЕСС КРИСТАЛЛИЗАЦИИ НАНОЧАСТИЦ АУСТЕНИТА ПРИ БЫСТРОМ ОХЛАЖДЕНИИ

И. В. Зоря¹, Г. М. Полетаев^{2,3}, Ю. В. Бебихов⁴, А. С. Семенов⁴

¹ Сибирский государственный индустриальный университет (Россия, 654007, Кемеровская обл. – Кузбасс, Новокузнецк, ул. Кирова, 42)

² Хакасский государственный университет им. Н.Ф. Катанова (Россия, 655012, Республика Хакасия, Абакан, пр. Ленина, 90)

³ Алтайский государственный технический университет им. И.И. Ползунова (Россия, 656038, Алтайский край, Барнаул, пр. Ленина, 46)

⁴ Политехнический институт Северо-Восточного федерального университета им. М.К. Аммосова (Россия, 678170, Республика Саха (Якутия), Мирный, ул. Тихонова, 5)

✉ zorya.i@mail.ru

Аннотация. Методом молекулярной динамики проведено исследование формирования структуры при кристаллизации наночастиц аустенита в условиях наличия примеси углерода. Рассматривалось влияние скорости охлаждения расплава, размера частиц, концентрации атомов углерода в частице на особенности образующейся структуры при кристаллизации и температуру начала кристаллизации. Показано, что формированием нанокристаллической структуры наночастиц можно управлять путем варьирования скорости охлаждения и введения примеси углерода: при скорости охлаждения выше 10^{13} К/с в используемой модели кристаллизация не успевала произойти, при скорости ниже $5 \cdot 10^{12}$ К/с частица аустенита кристаллизовалась с образованием нанокристаллической структуры. При этом при снижении скорости охлаждения наблюдалось уменьшение плотности дефектов в конечной структуре. При скорости $5 \cdot 10^{11}$ К/с и менее кристаллизация частиц без углерода проходила с образованием низкоэнергетических границ зерен (с высокой плотностью сопряженных узлов: специальных границ, двойников). Температура кристаллизации при охлаждении со скоростью ниже 10^{12} К/с обратно пропорциональна диаметру частицы: по мере уменьшения размера частицы увеличивается доля свободной поверхности, что приводит к уменьшению вероятности образования кристаллических зародышей. Кроме того, температура кристаллизации увеличивается при уменьшении скорости охлаждения. Введение примеси углерода приводило к снижению температуры кристаллизации наночастиц: при наличии 10 ат. % углерода она уменьшалась примерно на 200 К для частиц разного размера. Атомы углерода часто образовывали скопления, состоящие из нескольких атомов углерода. Такие скопления искажали образующуюся кристаллическую решетку металла вокруг себя, препятствуя кристаллизации. В условиях наличия примеси углерода конечная структура кристаллизовавшихся частиц имела более высокую плотность границ зерен и других дефектов. Атомы углерода, особенно скопления из них, закреплялись преимущественно на границах зерен и тройных стыках.

Ключевые слова: молекулярная динамика, наночастица, кристаллизация, нанокристалл, аустенит

Благодарности: Исследование выполнено за счет гранта Российского научного фонда (проект № 23-12-20003, <https://rscf.ru/project/23-12-20003/>) при паритетной финансовой поддержке Правительства Республики Хакасия.

Для цитирования: Зоря И.В., Полетаев Г.М., Бебихов Ю.В., Семенов А.С. Молекулярно-динамическое исследование влияния примеси углерода на процесс кристаллизации наночастиц аустенита при быстром охлаждении. *Известия вузов. Черная металлургия*. 2024;67(4):440–448. <https://doi.org/10.17073/0368-0797-2024-4-440-448>

INTRODUCTION

Metallic nanoparticles exhibit a unique set of physical, chemical, and optical properties. These properties make nanoparticles highly promising for applications in areas such as microelectronics, optoelectronics, plasmonics [1; 2], medicine and biology [3; 4], chemical catalysis, and the production of gas sensors [5; 6]. In the manufacturing of nanoparticles, significant attention is given to controlling the phase state, size, and shape of the particles due to their critical impact on beneficial properties [7 – 10]. Consequently, investigating the factors influencing the mechanisms and kinetics of phase transitions, as well as the final structure of the particles, is of great importance. Recently, particles with a high level of atomic structure disorder, such as amorphous or nanocrystalline structures, have garnered significant inter-

est [11 – 14]. These particles possess high stored energy and a unique electronic structure, making them promising for use in catalysis, biomedicine, optics, and electronics [15 – 17].

A nanocrystalline structure, which is a polycrystalline structure with relatively small grain sizes (ranging from a few nanometers to several tens of nanometers) and a high density of non-equilibrium grain boundaries, can be obtained not only through intense deformation but also through sufficiently rapid cooling, where the recrystallization process is suppressed during grain growth, leading to the formation of numerous small grains [18; 19]. Through computer modeling in studies [20 – 23], it has been shown, for example, that nanoparticles of pure metals crystallize with a nanocrystalline structure with high grain boundary density and an average grain size of only

a few nanometers when cooled at a rate of approximately 10^{12} K/s from the molten state. In studies [20; 22; 23], it was demonstrated that at a cooling rate exceeding 10^{13} K/s, homogeneous crystallization does not have time to occur, and the cooled particles in the molecular dynamics model exhibit an amorphous structure.

The interaction of impurity atoms of light elements with metals is of significant scientific and technological interest. Even at low concentrations, atoms of carbon, nitrogen, and oxygen significantly affect the properties of metals. Despite the importance of understanding the mechanisms and processes underlying the influence of alloying with light element impurities on the properties of metals, many questions regarding the behavior of impurities at the atomic level in the metallic matrix remain unresolved. One such question is the determination of the impact of impurities on phase transitions, particularly the exploration of ways to control the temperature intervals of phase existence in metallic nanomaterials by varying impurities. This study is devoted to investigating, at the atomic level using molecular dynamics, the crystallization process of austenite nanoparticles and the effect of carbon impurity on these processes.

MODEL DESCRIPTION

For describing Fe–Fe interactions in austenite, the Lau EAM potential [24] was used, which accurately reproduces the structural, energetic, and elastic characteristics of austenite [24; 25]. To describe the interactions of iron atoms with carbon atoms and carbon atoms with each other in the metal matrix, Morse potentials [26] were used, determined based on experimental data on the dissolution energy and migration energy of carbon impurity atoms in the austenite crystal, atomic radii, their electronegativity, binding energy, and other characteristics.

In the model, a spherical austenite particle was initially created by cutting out a sphere of the appropriate size from an ideal FCC crystal. Particles with diameters ranging from 1.5 to 12.0 nm were considered. The particle was placed in a rectangular parallelepiped calculation cell with periodic boundary conditions. Although free conditions (i.e., the absence of any boundary conditions) can be used for this model, periodic boundary conditions were employed in this study to ensure that atoms evaporating from the particle surface at high temperatures do not escape far from the particle but remain within the calculation cell. The distance between the walls of the calculation cell was sufficiently large to prevent interaction between the particle and its virtual duplicate [27; 28].

Carbon impurity atoms were introduced randomly throughout the entire volume of the metallic particle. The impurity concentration varied from 0 to 10 at. %. After creating the initial spherical particle, structural relaxation was performed to establish the equilibrium

atomic structure. Temperature control was carried out using the Nose-Hoover thermostat. The temperature in the model was set by adjusting the atomic velocities. The time integration step in the molecular dynamics method was 1 fs.

The resulting particles were used as starting points for simulating the gradual heating and subsequent cooling of the particles. For particles of each size, simulations were conducted with constant heating rates from the monocrystalline state to temperatures significantly exceeding the melting point (from 600 to 2000 K for larger particles and generally up to 1800 K for relatively small particles) and reverse cooling from the molten state to 600 K (for crystallization simulation). The temperature change during heating and cooling was carried out at a constant rate by correspondingly adjusting the velocity magnitudes of all atoms in the model. It is known that when cooling melts at rates above 10^{13} – 10^{14} K/s, homogeneous crystallization does not have time to occur even in pure metals, resulting in metallic glasses [29; 30]. At the same time, as shown in studies [20–23] and will be demonstrated below, cooling rate of 10^{12} K/s is sufficient for crystallization to occur.

RESULTS AND DISCUSSION

The average potential energy of an atom was chosen as the primary characteristic of the state of the nanoparticle structure. Fig. 1 shows the dependence of the average atomic energy on temperature for particles with diameters of 8.0 and 2.5 nm during heating from the monocrystalline state and reverse cooling from the melt at different temperature change rates: $5 \cdot 10^{11}$, 10^{12} and $5 \cdot 10^{12}$ K/s. The sharp changes in the average atomic energy on the graphs apparently correspond to phase transitions: during the increase – melting, and during the decrease – crystallization. As is well known, the melting – crystallization phase transitions do not occur instantaneously; the crystal – liquid front moves at a finite speed, depending on the temperature, and usually ranges from several tens of meters per second [31; 32]. No stationary crystal – liquid front was observed; once formed, this front typically moved until the entire particle melted or crystallized. In light of the above, the phase transition temperatures were determined by the moment of their onset (indicated by arrows in Fig. 1).

Crystallization during gradual cooling from the melt occurred at a temperature significantly lower than the melting point. This substantial difference between the melting temperature (T_m) and the crystallization temperature (T_c) in nanoparticles is a well-known phenomenon in modeling [20; 22; 33]. As shown, the crystallization process is more sensitive to the rate of temperature change than melting: for all three rates, the onset of melting is roughly the same, while the crystallization

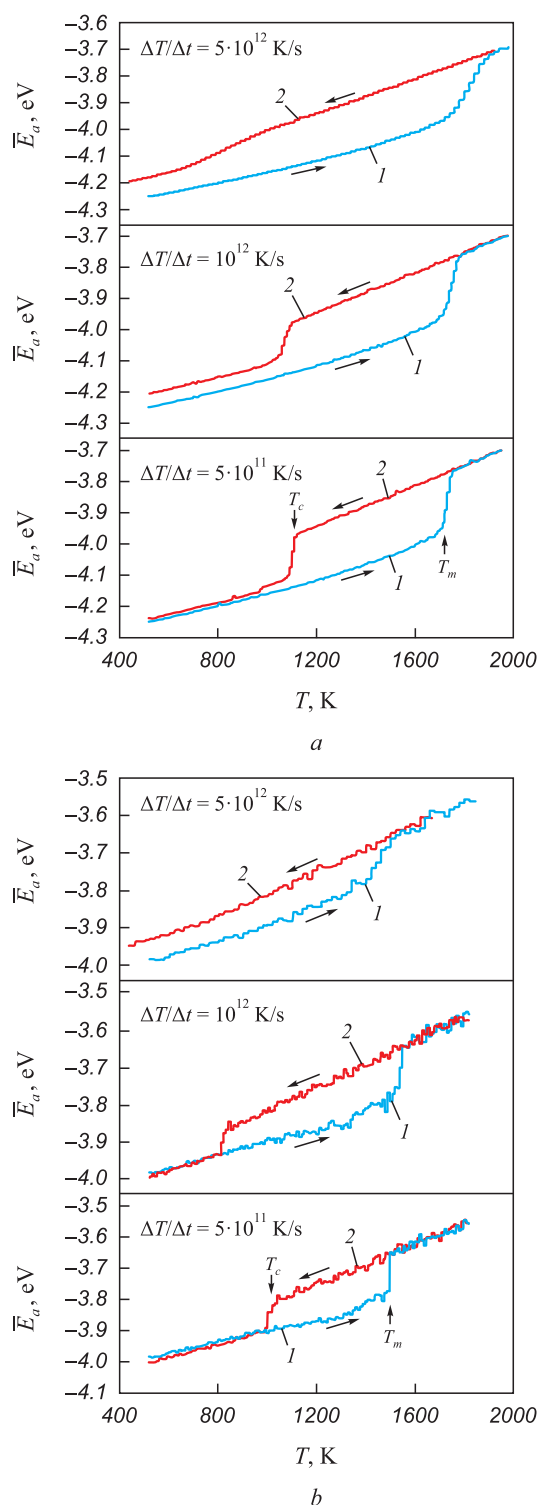


Fig. 1. Dependences of the average potential energy of an atom on temperature at different heating/cooling rates of austenite nanoparticles with a diameter of 8.0 (a) and 2.5 nm (b):

1 – heating of a single crystal particle;
2 – cooling of a particle from the molten state;
 T_m – melting point; T_c – crystallization temperature

Рис. 1. Зависимости средней потенциальной энергии атома от температуры при разной скорости нагревания/охлаждения наночастиц аустенита диаметром 8,0 (a) и 2,5 нм (b):

1 – нагрев монокристаллической частицы;
2 – охлаждение частицы из расплавленного состояния;
 T_m – температура плавления; T_c – температура кристаллизации

onset temperatures vary considerably. At a cooling rate of $5 \cdot 10^{12}$ K/s, crystallization only partially occurred for the 8.0 nm particle (as indicated by the relatively small drop in average atomic energy) and did not occur at all for the 2.5 nm particle (Fig. 1, a). As is well known, homogeneous crystallization involves two stages: nucleation of crystalline nuclei followed by their growth, i.e., the advancement of the crystallization front. These stages occur sequentially, and once stable nuclei are formed, the front moves at approximately the same speed as during melting, as evidenced by the similar slopes of the graphs during melting and crystallization in most cases.

It should be noted that for the 8.0 nm particle, after crystallization, the average atomic energy is higher than in the initial monocrystalline particle (Fig. 1, a, curve 2), and the higher the cooling rate, the greater this difference. This is explained by the formation of a nanocrystalline structure after crystallization, characterized by higher average atomic energy values compared to the monocrystalline particle due to the presence of grain boundaries and other defects. The higher the cooling rate, the less time is spent on structural relaxation, and the higher the defect density in the cooled particle.

As the particle diameter decreased, the dependence of the average atomic energy on temperature underwent qualitative changes. Firstly, the energy difference between the crystalline and amorphous states was noticeably smaller compared to larger particles (Fig. 1, b). This is likely due to the relatively higher proportion of surface atoms in this case. Moreover, for smaller particles, the energy value fluctuations were higher, and the error in determining phase transition temperatures was greater, due to the relatively smaller number of atoms in them.

Another important change in the graphs with decreasing particle size was the decrease in melting and crystallization temperatures, as well as the stronger influence of the cooling rate on the crystallization temperature. This is obviously a consequence of the higher proportion of surface atoms as the particle diameter decreases. At a cooling rate of $5 \cdot 10^{12}$ K/s, crystallization did not occur at all for particles with diameters smaller than 3 nm, as evidenced by the absence of a downward energy jump corresponding to crystallization (e.g., Fig. 1, b, curve 2).

Fig. 2 shows the atomic structure in a cross-section of particles with an 8.0 nm diameter, obtained using a crystalline phase visualizer. This visualizer determines the affiliation of each atom to a particular crystalline structure by analyzing the arrangement of neighboring atoms [34]. As seen in Fig. 2, with increasing cooling rate, grain sizes decrease, and the number of structural imperfections, including grain boundaries, increases. At a cooling rate of $5 \cdot 10^{11}$ K/s, judging by the very close positioning of curves 1 and 2 in Fig. 1, i.e., the slight dif-

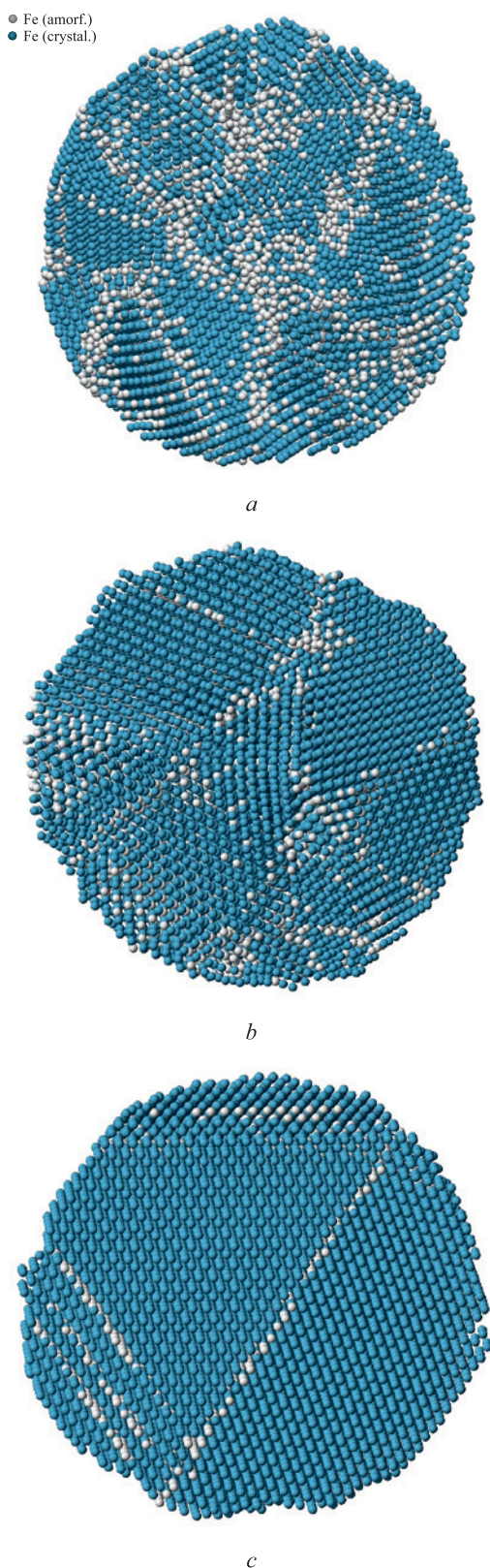


Fig. 2. Atomic structure of austenite particles with a diameter of 8.0 nm, free of carbon impurities, in a section obtained as a result of crystallization at a cooling rate of $5 \cdot 10^{12}$ (a), 10^{12} (b) and $5 \cdot 10^{11}$ K/s (c)

Рис. 2. Атомная структура частиц аустенита диаметром 8,0 нм, не содержащих примеси углерода, в срезе, полученная в результате кристаллизации при скорости охлаждения $5 \cdot 10^{12}$ (a), 10^{12} (b) и $5 \cdot 10^{11}$ К/с (c)

ference between the average energy of monocrystalline and crystallized particles, crystallization likely occurred often with the formation of low-energy grain boundaries (with a high density of coincident sites: special boundaries, twins).

To mathematically describe the influence of the free surface of nanoparticles on their melting temperature, a formula based on the assumption that the phase transition temperature change is proportional to the surface area-to-volume ratio of the particle is often used [35 – 37], i.e., for a spherical particle, this change should be proportional to $N^{-1/3}$ or d^{-1} (where N is the number of atoms in the particle; d is the particle diameter). In this study, the assumption for the crystallization temperature was used, with an added correction δ accounting for the finite thickness of the particle's surface layer:

$$T_c(d) = T_c^0 \left(1 - \frac{\alpha_c}{d - \delta} \right), \quad (1)$$

where T_c and T_c^0 are the crystallization temperatures of the particle and bulk material, respectively; α_c is a parameter that accounts for the extent of the particle surface's influence on its crystallization.

Formula (1) was used to construct an approximation curve for the dependence of the crystallization temperature of nanoparticles on their diameter (dashed lines in Fig. 3). As can be seen, for cooling rates of 10^{12} K/s and $5 \cdot 10^{11}$ K/s, the values obtained in the model (shown by markers in Fig. 4) closely match the approximation curves, confirming the leading role of the free surface not only in the melting process but also in the crystallization of nanoparticles. The parameter values for calculation by formula (1) were as follows (1): $T_c^0 = 1190$ K, $\alpha_c = 0.38$ K·nm, $\delta = 0.4$ nm for a cooling rate of $5 \cdot 10^{11}$ K/s

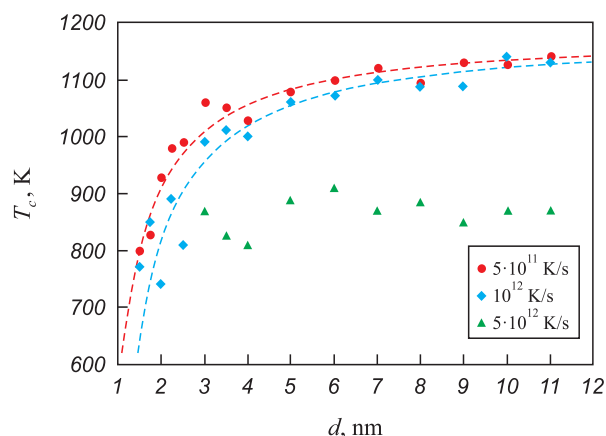


Fig. 3. Crystallization temperature of an austenite particle depending on its diameter at different melt cooling rates

Рис. 3. Температура кристаллизации частицы аустенита в зависимости от ее диаметра при разной скорости охлаждения расплава

and $T_c^0 = 1190$ K, $\alpha_c = 0.49$ K·nm, $\delta = 0.4$ nm for a cooling rate of 10^{12} K/s.

As shown in the dependencies in Fig. 3, the crystallization temperature increases as the cooling rate decreases. This fact confirms that the formation of nucleation sites is a probabilistic process requiring a relatively long time for the formation of stable nuclei. At a cooling rate of $5 \cdot 10^{12}$ K/s, particles with diameters smaller than 3 nm did not crystallize (triangular markers in Fig. 3). The error in determining the onset of crystallization at this rate was higher than at the other rates considered. Nevertheless, it is clear that at the highest of the rates considered, $5 \cdot 10^{12}$ K/s, crystallization occurs at lower temperatures than at lower rates.

The introduction of carbon impurity led to a decrease in the crystallization temperature. Fig. 4 shows the dependence of the crystallization temperature on particle diameter (Fig. 4, *a*) and carbon impurity concentration (Fig. 4, *b*). The following parameter values were obtained for calculation using formula (1): $T_c^0 = 1155$ K,

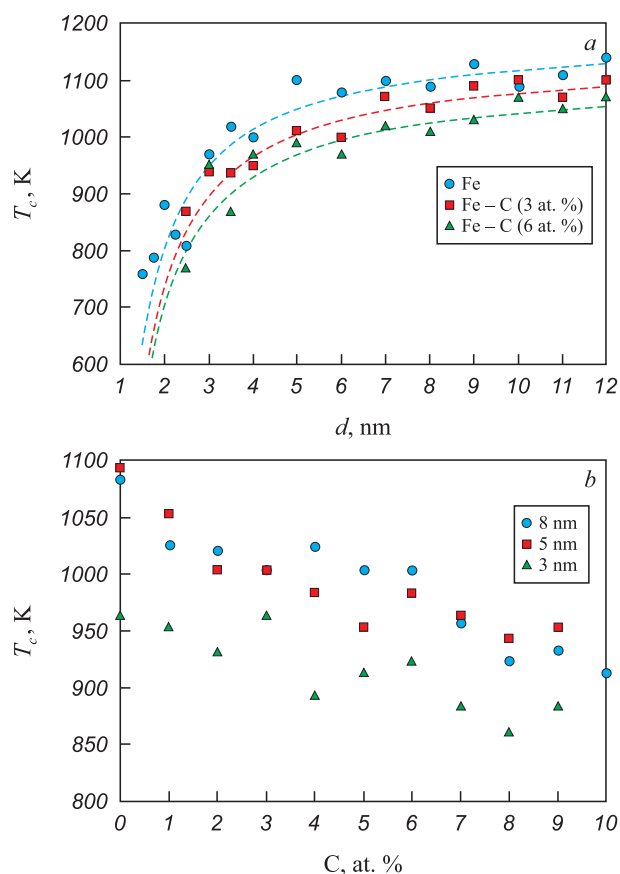


Fig. 4. Dependences of crystallization temperature of an austenite particle during cooling at a rate of 10^{12} K/s on the particle diameter at different concentrations of carbon impurity (*a*) and on carbon concentration at different particle sizes (*b*)

Рис. 4. Зависимости температуры кристаллизации частицы аустенита при охлаждении со скоростью 10^{12} К/с от диаметра частицы при разных концентрациях примеси углерода (*a*) и от концентрации углерода при разных размерах частиц (*b*)

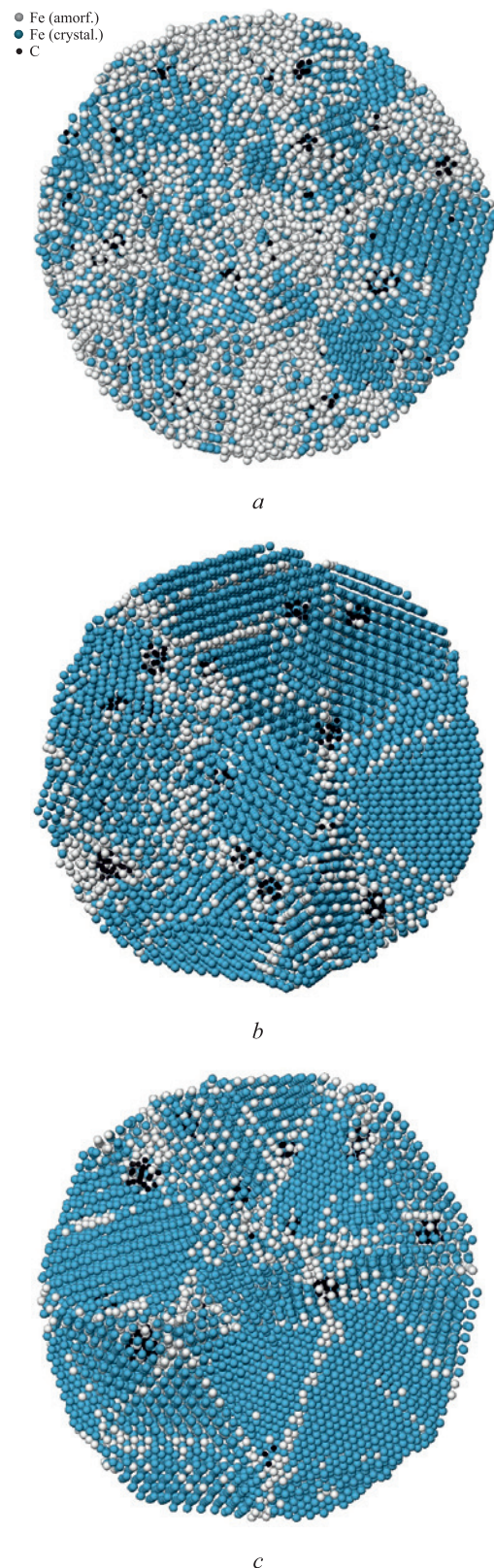


Fig. 5. Atomic structure of austenite particles with a diameter of 8.0 nm containing 3 at. % carbon, in the section obtained as a result of crystallization at a cooling rate of $5 \cdot 10^{12}$ (*a*), 10^{12} (*b*) and $5 \cdot 10^{11}$ K/s (*c*)

Рис. 5. Атомная структура частиц аустенита диаметром 8,0 нм, содержащих 3 ат. % углерода, в срезе, полученная в результате кристаллизации при скорости охлаждения $5 \cdot 10^{12}$ (*a*), 10^{12} (*b*) и $5 \cdot 10^{11}$ К/с (*c*)

$\alpha_c = 0.57 \text{ K} \cdot \text{nm}$ for a concentration of 3 at. %; $T_c^0 = 1120 \text{ K}$, $\alpha_c = 0.59 \text{ K} \cdot \text{nm}$ for a concentration of 6 at. %. The δ value, which reflects the width of the surface layer, was found to be the same in all cases – 0.4 nm.

As the carbon concentration increased within the considered impurity atom concentration range, the crystallization temperature of the austenite particle decreased significantly: by nearly 200 K at a concentration of 10 at. % (Fig. 4, b). Carbon atoms, diffusing in the metal lattice, often formed clusters consisting of several carbon atoms (Fig. 5). These clusters distorted the emerging metal crystal lattice around them, hindering crystallization. Crystallization nuclei formed predominantly in the particle volume, followed by the intensive growth of crystals and the formation of a polycrystalline structure.

Fig. 5 shows the atomic structure of particles with a diameter of 8.0 nm, containing 3 at. % carbon, crystallized at different cooling rates. Comparing the structures shown in Fig. 2 for particles without carbon impurity, it is evident that the number of structural imperfections, grain boundaries, and other defects is significantly higher in the presence of carbon. The most notable difference was observed at the lowest cooling rate considered: $5 \cdot 10^{11} \text{ K/s}$. Without carbon impurity, the particle crystallized with a much lower defect density (Fig. 2, c) than in the presence of carbon (Fig. 5, c). In the latter case, the structure was almost indistinguishable from the structure obtained during cooling at a rate of 10^{12} K/s (Fig. 5, b). Carbon impurity atoms, especially clusters of them, predominantly settled at grain boundaries and triple junctions.

CONCLUSIONS

A study using molecular dynamics was conducted to investigate the structural formation during the crystallization of austenite nanoparticles in the presence of carbon impurity. The effects of melt cooling rate, particle size, and carbon atom concentration on the crystallization process, resulting structural features, and crystallization onset temperature were examined. It was shown that the formation of a nanocrystalline structure in nanoparticles can be controlled by varying the cooling rate and introducing carbon impurity. In the model used, at a cooling rate above 10^{13} K/s , crystallization did not occur; at a rate below $5 \cdot 10^{12} \text{ K/s}$, the austenite particles crystallized, forming a nanocrystalline structure. Additionally, as the cooling rate decreased, the defect density in the final structure also decreased. At a cooling rate of $5 \cdot 10^{11} \text{ K/s}$ or less, crystallization of carbon-free particles resulted in the formation of low-energy grain boundaries (with a high density of coincident sites: special boundaries, twins).

The crystallization temperature at a cooling rate below 10^{12} K/s is inversely proportional to the particle diameter: as the particle size decreases, the proportion of the free

surface increases, which reduces the probability of crystalline nuclei formation. Additionally, the crystallization temperature increases as the cooling rate decreases.

The introduction of carbon impurity led to a decrease in the crystallization temperature of nanoparticles: in the presence of 10 at. % carbon, the temperature decreased by approximately 200 K for particles of different sizes. Carbon atoms often formed clusters consisting of several atoms. These clusters distorted the forming metal crystal lattice around them, hindering crystallization. In the presence of carbon impurity, the final structure of the crystallized particles contained a higher density of grain boundaries and other defects. Carbon atoms, especially in clusters, predominantly settled at grain boundaries and triple junctions.

REFERENCES / СПИСОК ЛИТЕРАТУРЫ

- Humbert C., Noblet T., Dalstein L., Busson B., Barbillon G. Sum-frequency generation spectroscopy of plasmonic nano-materials: A review. *Materials*. 2019;12(5):836. <https://doi.org/10.3390/ma12050836>
- Mantri Y., Jokerst J.V. Engineering plasmonic nanoparticles for enhanced photoacoustic imaging. *ACS Nano*. 2020;14(8): 9408–9422. <https://doi.org/10.1021/acsnano.0c05215>
- Jain T.K., Morales M.A., Sahoo S.K., Leslie-Pelecky D.L., Labhasetwar V. Iron oxide nanoparticles for sustained delivery of anticancer agents. *Molecular Pharmaceutics*. 2005; 2(3):194–205. <https://doi.org/10.1021/mp0500014>
- Shim S.Y., Lim D.K., Nam J.M. Ultrasensitive optical bio-diagnostic methods using metallic nanoparticles. *Nanomedicine*. 2008;3(2):215–232. <https://doi.org/10.2217/17435889.3.2.215>
- Kodama K., Nagai T., Kuwaki A., Jinnouchi R., Morimoto Y. Challenges in applying highly active Pt-based nanostructured catalysts for oxygen reduction reactions to fuel cell vehicles. *Nature Nanotechnology*. 2021;16:140–147. <https://doi.org/10.1038/s41565-020-00824-w>
- Mitchell S., Qin R., Zheng N., Perez-Ramirez J. Nanoscale engineering of catalytic materials for sustainable technologies. *Nature Nanotechnology*. 2021;16:129–139. <https://doi.org/10.1038/s41565-020-00799-8>
- Wagener P., Jakobi J., Rehbock C., Chakravadhanula V.S.K., Thede C., Wiedwald U., Bartsch M., Kienleand L., Barcikowski S. Solvent-surface interactions control the phase structure in laser-generated iron-gold core-shell nanoparticles. *Scientific Reports*. 2016;6:23352. <https://doi.org/10.1038/srep23352>
- Ziefub A.R., Reichenberger S., Rehbock C., Chakraborty I., Gharib M., Parak W.J., Barcikowski S. Laser fragmentation of colloidal gold nanoparticles with high-intensity nanosecond pulses is driven by a single-step fragmentation mechanism with a defined educt particle-size threshold. *The Journal of Physical Chemistry C*. 2018;122(38):22125–22136. <https://doi.org/10.1021/acs.jpcc.8b04374>
- Amikura K., Kimura T., Hamada M., Yokoyama N., Miyazaki J., Yamada Y. Copper oxide particles produced by laser ablation in water. *Applied Surface Science*. 2008;254(21): 6976–6982. <https://doi.org/10.1016/j.apsusc.2008.05.091>

10. Barcikowski S., Compagnini G. Advanced nanoparticle generation and excitation by lasers in liquids. *Physical Chemistry Chemical Physics*. 2013;15(9):3022–3026. <https://doi.org/10.1039/C2CP90132C>
11. Liang S.-X., Zhang L.-C., Reichenberger S., Barcikowski S. Design and perspective of amorphous metal nanoparticles from laser synthesis and processing. *Physical Chemistry Chemical Physics*. 2021;23(19):11121–11154. <https://doi.org/10.1039/D1CP00701G>
12. Sun J., Sinha S.K., Khammari A., Picher M., Terrones M., Banhart F. The amorphization of metal nanoparticles in graphitic shells under laser pulses. *Carbon*. 2020;161:495–501. <https://doi.org/10.1016/j.carbon.2020.01.067>
13. He D.S., Huang Y., Myers B.D., Isheim D., Fan X., Xia G.-J., Deng Y., Xie L., Han S., Qiu Y., Wang Y.-G., Luan J., Jiao Z., Huang L., Dravid V.P., He J. Single-element amorphous palladium nanoparticles formed via phase separation. *Nano Research*. 2022;15:5575–5580. <https://doi.org/10.1007/s12274-022-4173-1>
14. Qian Y., Silva A., Yu E., Anderson C.L., Liu Y., Theis W., Ercius P., Xu T. Crystallization of nanoparticles induced by precipitation of trace polymeric additives. *Nature Communications*. 2021;12(1):2767. <https://doi.org/10.1038/s41467-021-22950-2>
15. Pei Y., Zhou G., Luan N., Zong B., Qiao M., Tao F. Synthesis and catalysis of chemically reduced metal-metalloid amorphous alloys. *Chemical Society Reviews*. 2012;41(24):8140–8162. <https://doi.org/10.1039/c2cs35182j>
16. Jia Z., Wang Q., Sun L., Wang Q., Zhang L.C., Wu G., Luan J.H., Jiao Z.B., Wang A., Liang S.X., Gu M., Lu J. Metallic glass catalysts: attractive in situ self-reconstructed hierarchical gradient structure of metallic glass for high efficiency and remarkable stability in catalytic performance. *Advanced Functional Materials*. 2019;29(19):1970131. <https://doi.org/10.1002/adfm.201970131>
17. Chen Q., Yan Z., Guo L., Zhang H., Zhang L.-C., Wang W. Role of maze like structure and Y_2O_3 on Al-based amorphous ribbon surface in MO solution degradation. *Journal of Molecular Liquids*. 2020;318:114318. <https://doi.org/10.1016/j.molliq.2020.114318>
18. Kumar K.S., Van Swygenhoven H., Suresh S. Mechanical behavior of nanocrystalline metals and alloys. *Acta Materialia*. 2003;51(19):5743–5774. <https://doi.org/10.1016/j.actamat.2003.08.032>
19. Meyers M.A., Mishra A., Benson D.J. Mechanical properties of nanocrystalline materials. *Progress in Materials Science*. 2006;51(4):427–556. <https://doi.org/10.1016/j.pmatsci.2005.08.003>
20. Nguyen T.D., Nguyen C.C., Tran V.H. Molecular dynamics study of microscopic structures, phase transitions and dynamic crystallization in Ni nanoparticles. *RSC Advances*. 2017;7(41):25406–25413. <https://doi.org/10.1039/C6RA27841H>
21. Trang G.T.T., Kien P.H., Hung P.K., Ha N.T.T. Molecular dynamics simulation of microstructure and atom-level mechanism of crystallization pathway in iron nanoparticle. *Journal of Physics: Conference Series*. 2020;1506:012020. <https://doi.org/10.1088/1742-6596/1506/1/012020>
22. Poletaev G.M., Gafner Y.Y., Gafner S.L. Molecular dynamics study of melting, crystallization and devitrification of nickel nanoparticles. *Letters on Materials*. 2023;13(4):298–303. <https://doi.org/10.22226/2410-3535-2023-4-298-303>
23. Poletaev G.M., Bebikhov Y.V., Semenov A.S. Molecular dynamics study of the formation of the nanocrystalline structure in nickel nanoparticles during rapid cooling from the melt. *Materials Chemistry and Physics*. 2023;309:128358. <https://doi.org/10.1016/j.matchemphys.2023.128358>
24. Lau T.T., Forst C.J., Lin X., Gale J.D., Yip S., Van Vliet K.J. Many-body potential for point defect clusters in Fe–C alloys. *Physical Review Letters*. 2007;98(21):215501. <https://doi.org/10.1103/PhysRevLett.98.215501>
25. Oila A., Bull S.J. Atomistic simulation of Fe–C austenite. *Computational Materials Science*. 2009;45(2):235–239. <https://doi.org/10.1016/j.commatsci.2008.09.013>
26. Lv B., Chen C., Zhang F., Poletaev G.M., Rakitin R.Y. Potentials for describing interatomic interactions in γ Fe–Mn–C–N system. *Metals*. 2022;12(6):982. <https://doi.org/10.3390/met12060982>
27. Poletaev G., Gafner Y., Gafner S., Bebikhov Y., Semenov A. Molecular dynamics study of the devitrification of amorphous copper nanoparticles in vacuum and in a silver shell. *Metals*. 2023;13(10):1664. <https://doi.org/10.3390/met13101664>
28. Gafner Y., Gafner S., Redel L., Poletaev G. Estimation of the structure of binary Ag–Cu nanoparticles during their crystallization by computer simulation. *Journal of Nanoparticle Research*. 2023;25:205. <https://doi.org/10.1007/s11051-023-05850-y>
29. Liang S.-X., Zhang L.-C., Reichenberger S., Barcikowski S. Design and perspective of amorphous metal nanoparticles from laser synthesis and processing. *Physical Chemistry Chemical Physics*. 2021;23(19):11121–11154. <https://doi.org/10.1039/D1CP00701G>
30. Zhong L., Wang J., Sheng H., Zhang Z., Mao S.X. Formation of monatomic metallic glasses through ultrafast liquid quenching. *Nature*. 2014;512:177–180. <https://doi.org/10.1038/nature13617>
31. Chan W.-L., Averback R.S., Cahill D.G., Ashkenazy Y. Solidification velocities in deeply undercooled silver. *Physical Review Letters*. 2009;102(9):095701. <https://doi.org/10.1103/PhysRevLett.102.095701>
32. Zhang H.Y., Liu F., Yang Y., Sun D.Y. The molecular dynamics study of vacancy formation during solidification of pure metals. *Scientific Reports*. 2017;7:10241. <https://doi.org/10.1038/s41598-017-10662-x>
33. Qi Y., Cagin T., Johnson W.L., Goddard III W.A. Melting and crystallization in Ni nanoclusters: the mesoscale regime. *The Journal of Chemical Physics*. 2001;115(1):385–394. <https://doi.org/10.1063/1.1373664>
34. Tsuzuki H., Branicio P.S., Rino J.P. Structural characterization of deformed crystals by analysis of common atomic neighborhood. *Computer Physics Communications*. 2007;177(6):518–523. <https://doi.org/10.1016/j.cpc.2007.05.018>
35. Xiong S., Qi W., Cheng Y., Huang B., Wang M., Li Y. Universal relation for size dependent thermodynamic properties of metallic nanoparticles. *Physical Chemistry Chemical Physics*. 2011;13(22):10652–10660. <https://doi.org/10.1039/C0CP90161J>
36. Nanda K.K. Liquid-drop model for the surface energy of nanoparticles. *Physics Letters A*. 2012;376(19):1647–1649. <https://doi.org/10.1016/j.physleta.2012.03.055>
37. Safaei A., Attarian Shandiz M., Sanjabi S., Barber Z.H. Modeling the melting temperature of nanoparticles by an analytical approach. *The Journal of Physical Chemistry C*. 2008;112(1):99–105. <https://doi.org/10.1021/jp0744681>

Information about the Authors

Сведения об авторах

Irina V. Zorya, Dr. Sci. (Phys.-Math.), Prof., Head of the Chair of Heat-Gas-Water Supply, Water Disposal and Ventilation, Siberian State Industrial University

ORCID: 0000-0001-5748-813X

E-mail: zorya.i@mail.ru

Gennadii M. Poletaev, Dr. Sci. (Phys.-Math.), Prof., Head of the Chair of Advanced Mathematics, Polzunov Altai State Technical University; Prof., Katanov Khakassian State University

ORCID: 0000-0002-5252-2455

E-mail: gmpoletaev@mail.ru

Yurii V. Bebikhov, Cand. Sci. (Phys.-Math.), Assist. Prof., Mirny Polytechnic Institute (branch) of North-Eastern Federal University

ORCID: 0000-0002-8366-4819

E-mail: bebikhov.yura@mail.ru

Aleksandr S. Semenov, Dr. Sci. (Phys.-Math.), Director, Mirny Polytechnic Institute (branch) of North-Eastern Federal University

ORCID: 0000-0001-9940-3915

E-mail: as.semenov@s-vfu.ru

Ирина Васильевна Зоря, д.ф.-м.н., профессор, заведующий кафедрой теплогазоводоснабжения, водоотведения и вентиляции, Сибирский государственный индустриальный университет

ORCID: 0000-0001-5748-813X

E-mail: zorya.i@mail.ru

Геннадий Михайлович Полетаев, д.ф.-м.н., профессор, заведующий кафедрой высшей математики, Алтайский государственный технический университет им. И.И. Ползунова; профессор, Хакасский государственный университет им. Н.Ф. Катанова

ORCID: 0000-0002-5252-2455

E-mail: gmpoletaev@mail.ru

Юрий Владимирович Бебихов, к.ф.-м.н., доцент, Политехнический институт Северо-Восточного федерального университета им. М. К. Аммосова

ORCID: 0000-0002-8366-4819

E-mail: bebikhov.yura@mail.ru

Александр Сергеевич Семенов, д.ф.-м.н., директор, Политехнический институт Северо-Восточного федерального университета им. М. К. Аммосова

ORCID: 0000-0001-9940-3915

E-mail: as.semenov@s-vfu.ru

Contribution of the Authors

Вклад авторов

I. V. Zorya – problem statement, literary analysis, processing of results, writing the main text.

G. M. Poletaev – problem statement, development of a computer model, literary analysis, processing of results, editing the article final version.

Yu. V. Bebikhov – performing calculations and obtaining results, creating drawings and graphs.

A. S. Semenov – performing calculations and obtaining results, creating drawings and graphs.

И. В. Зоря – постановка задачи, анализ литературных источников, обработка результатов, написание основного текста статьи.

Г. М. Полетаев – постановка задачи, разработка компьютерной модели, анализ литературных источников, обработка результатов, редактирование финальной версии статьи.

Ю. В. Бебихов – проведение расчетов и получение результатов, создание рисунков и графиков для статьи.

А. С. Семенов – проведение расчетов и получение результатов, создание рисунков и графиков для статьи.

Поступила в редакцию 18.03.2024

После доработки 05.04.2024

Принята к публикации 10.04.2024

Received 18.03.2024

Revised 05.04.2024

Accepted 10.04.2024



UDC 621.791:624

DOI 10.17073/0368-0797-2024-4-449-456



Original article

Оригинальная статья

THERMODYNAMIC ASPECTS OF WO₃ TUNGSTEN OXIDE REDUCTION
BY CARBON, SILICON, ALUMINUM AND TITANIUML. P. Bashchenko¹, Yu. V. Bendre¹, N. A. Kozyrev²,
A. R. Mikhno¹✉, V. M. Shurupov¹, A. V. Zhukov¹¹ Siberian State Industrial University (42 Kirova Str., Novokuznetsk, Kemerovo Region – Kuzbass 654007, Russian Federation)² I.P. Bardin Central Research Institute of Ferrous Metallurgy (23/9 Radio Str., Moscow 105005, Russian Federation)

✉ mikno-mm131@mail.ru

Abstract. The development and research of new materials for machine parts of the mining and metallurgical complex by the method of surfacing with flux cored wire has a lot of attention nowadays. Flux cored wires are widely used for surfacing of steels with high wear resistance, in which reduced tungsten in the form of ferroalloys, ligatures and metal powder of various degrees of purity are used as fillers. However, due to the scarcity and high cost of tungsten, its rational use is an urgent task. For practical application, the technology of surfacing with tungsten-containing flux cored wire is of interest; using it the maximum extraction of tungsten into the deposited layer is achieved due to reduction processes in the arc. In order to increase the beneficial use of tungsten, the technologies of indirect alloying with tungsten during surfacing under the flux of flux cored wires, in which tungsten oxide is used as a filler on the one hand, and reducing agent – on the other, deserve consideration. It can be expected that during arc discharge, tungsten and (or) chemical compounds of tungsten with reducing agents can be formed during the surfacing process. This paper presents the results of a comparative analysis of the thermodynamic processes of tungsten oxide reduction by carbon, silicon, aluminum and titanium during arc discharge occurring during surfacing with flux cored wires under a layer of flux. The thermodynamic analysis of 41 reactions in standard states showed that the presence of reducing agents (carbon, silicon, aluminum, titanium) in the flux cored wire used for surfacing will contribute to the formation of silicides and tungsten carbides, and, possibly, tungsten itself. It was determined that the best state for the participation of tungsten oxide in reactions in the arc is WO₃(g) gaseous state.

Keywords: reduction, tungsten oxide, thermodynamics, standard Gibbs energy of reaction, carbon, silicon, aluminum, titanium, non-metallic inclusions, thermodynamic probability of reaction

For citation: Bashchenko L.P., Bendre Yu.V., Kozyrev N.A., Mikhno A.R., Shurupov V.M., Zhukov A.V. Thermodynamic aspects of WO₃ tungsten oxide reduction by carbon, silicon, aluminum and titanium. *Izvestiya. Ferrous Metallurgy*. 2024;67(4):449–456.

<https://doi.org/10.17073/0368-0797-2024-4-449-456>

ТЕРМОДИНАМИЧЕСКИЕ АСПЕКТЫ
ВОССТАНОВЛЕНИЯ ОКСИДА ВОЛЬФРАМА WO₃
УГЛЕРОДОМ, КРЕМНИЕМ, АЛЮМИНИЕМ И ТИТАНОМЛ. П. Бащенко¹, Ю. В. Бендре¹, Н. А. Козырев²,
А. Р. Михно¹✉, В. М. Шурупов¹, А. В. Жуков¹¹ Сибирский государственный индустриальный университет (Россия, 654007, Кемеровская обл. – Кузбасс, Новокузнецк, ул. Кирова, 42)² Центральный научно-исследовательский институт черной металлургии им. И.П. Бардина (Россия, 105005, Москва, ул. Радио, 23/9)

✉ mikno-mm131@mail.ru

Аннотация. В настоящее время разработке и исследованию новых материалов для деталей машин горно-металлургического комплекса методом наплавки порошковой проволокой уделяется большое внимание. Широкое распространение для наплавки сталей с высокой износостойкостью получили порошковые проволоки, в которых в качестве наполнителей используется восстановленный вольфрам в виде ферросплавов, лигатур и металлического порошка различной степени чистоты. Однако в связи с дефицитностью и высокой стои-

мостью вольфрама актуальной задачей является его рациональное использование. Для практического применения представляет интерес технология наплавки вольфрамсодержащей порошковой проволокой, при использовании которой достигается максимальное извлечение вольфрама в наплавленный слой за счет восстановительных процессов в дуге. С целью повышения полезного использования вольфрама заслуживают рассмотрения технологии косвенного легирования вольфрамом при наплавке под флюсом из порошковых проволок, в которых в качестве наполнителя используются, с одной стороны – оксид вольфрама, а с другой – восстановители. Можно ожидать, что при дуговом разряде в процессе наплавки могут образовываться вольфрам и (или) химические соединения вольфрама с восстановителями. В настоящей работе представлены результаты сравнительного анализа протекания термодинамических процессов восстановления оксида вольфрама углеродом, кремнием, алюминием и титаном при дуговом разряде, возникающем во время наплавки порошковыми проволоками под слоем флюса. Проведенный термодинамический анализ 41 реакции в стандартных состояниях показал, что наличие в используемой для наплавки порошковой проволоке восстановителей (углерода, кремния, алюминия, титана) будет способствовать образованию силицидов и карбидов вольфрама, а, возможно, и самого вольфрама. Определено, что лучшим состоянием для участия оксида вольфрама в реакциях в дуге является газообразное состояние WO₃(г).

Ключевые слова: восстановление, оксид вольфрама, термодинамика, стандартная энергия Гиббса реакции, углерод, кремний, алюминий, титан, неметаллические включения, термодинамическая вероятность протекания реакции

Для цитирования: Башенко Л.П., Бендре Ю.В., Козырев Н.А., Михно А.Р., Шурупов В.М., Жуков А.В. Термодинамические аспекты восстановления оксида вольфрама WO₃ углеродом, кремнием, алюминием и титаном. *Известия вузов. Черная металлургия*. 2024;67(4):449–456. <https://doi.org/10.17073/0368-0797-2024-4-449-456>

INTRODUCTION

For over 40 years, the use of surfacing with welding flux cored wire has been widely adopted. Combining this with advanced surfacing methods allows for solving complex technological challenges at a fundamentally new level [1 – 3].

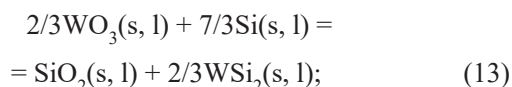
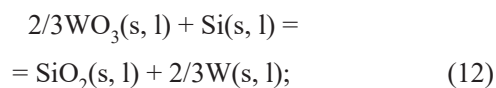
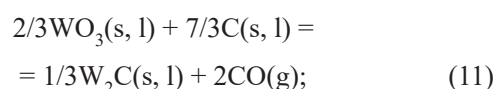
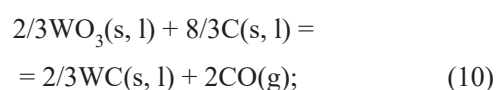
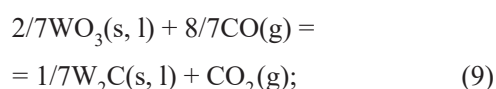
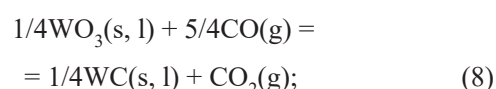
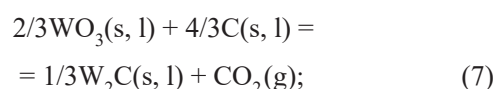
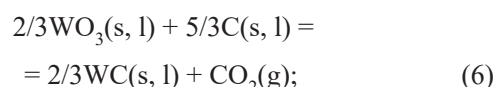
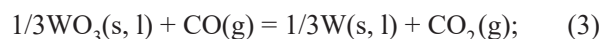
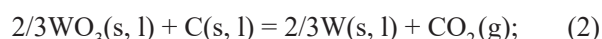
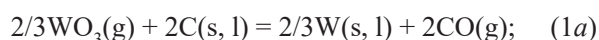
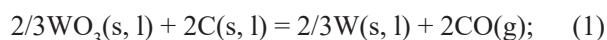
Developing technology for applying wear-resistant surfacing involves several key stages: analyzing the nature of the part's wear; assessing the weldability of the structural material and the permissible changes in the part's geometry due to the thermal effects of surfacing; selecting a wear-resistant alloy; choosing a surfacing method; and developing surfacing regimes [4 – 8].

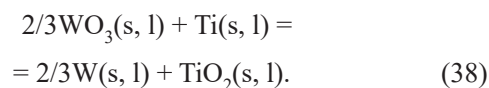
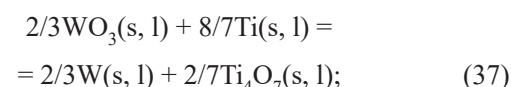
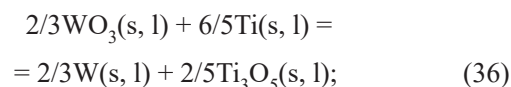
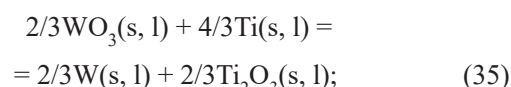
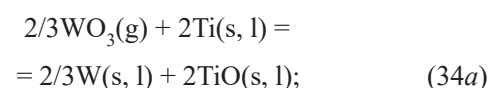
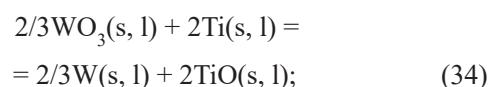
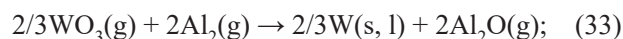
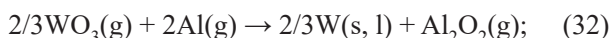
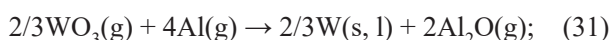
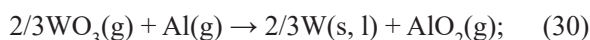
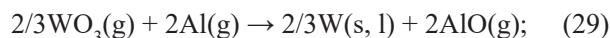
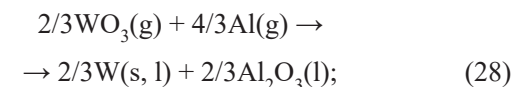
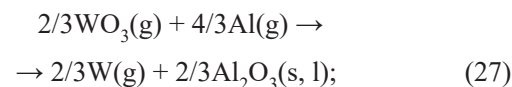
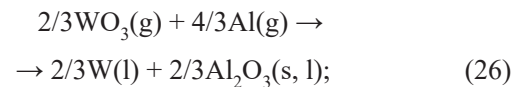
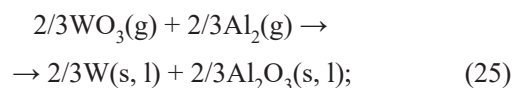
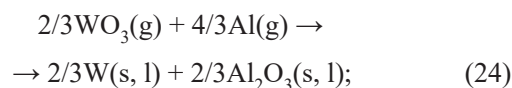
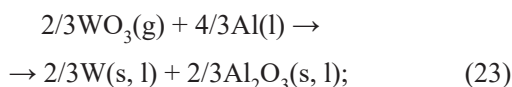
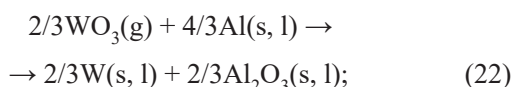
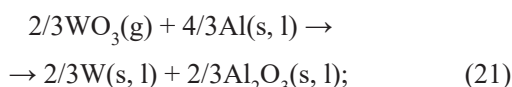
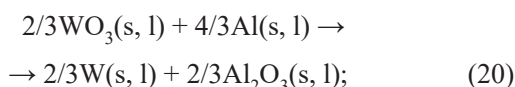
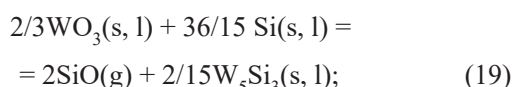
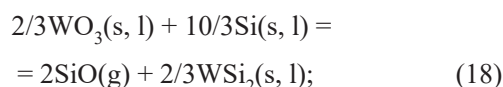
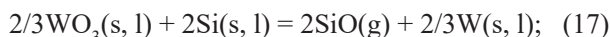
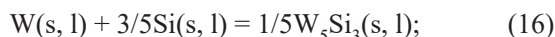
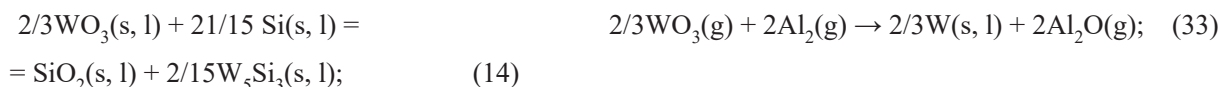
Recently, particular attention in manufacturing flux cored wire has been given to selecting charge materials [9 – 11]. One component of these charge materials is tungsten powder. Tungsten coatings are noted for their high wear resistance under “metal-to-metal” friction at elevated temperatures, as well as good heat and thermal resistance. They are mainly used in metallurgy and mechanical engineering for surfacing hot rolling rolls, hot cutting knives for metal, hot rolling stamps, and similar applications [12 – 15]. However, due to the high cost of pure powder and the absence of domestic manufacturers of this component within the Russian Federation, proposals have arisen to replace “pure” tungsten powder with tungsten oxide [16 – 18].

This work aims to conduct a comparative thermodynamic assessment of the likelihood of the reduction processes of tungsten oxide (WO₃) by carbon, silicon, aluminum, and titanium during the arc discharge that occurs when surfacing with flux-cored wires under a layer of flux.

MATERIALS AND METHODS

A thermodynamic assessment was conducted to evaluate the likelihood of the following reactions:





The necessary thermodynamic characteristics of reactions (1) – (38) for the comparative assessment of the reductive properties of carbon, silicon, aluminum, and titanium with respect to tungsten oxide WO₃ in standard conditions [$H^\circ(T)$, $\Delta_r S^\circ(T)$, $\Delta_r G^\circ(T)$] for reactants in solid crystalline (s), liquid (l), and gaseous (g) states, depending on temperature, were calculated using well-known methods [19]. These calculations were performed over the temperature range of the welding arc (1500 – 3500 K) based on the thermodynamic properties [$H^\circ(T) - H^\circ(298.15 \text{ K})$, $S^\circ(T)$, $\Delta_f H^\circ(298.15 \text{ K})$] of the WO₃, W, C, CO, CO₂, Si, SiO, SiO₂, WSi₂, W₅Si₃, Al, Al₂, Al₂O₃, AlO, AlO₂, Al₂O, Al₂O₂, Ti, TiO, Ti₂O₃, Ti₃O₅, Ti₄O₇, TiO₂. The calculations used data from reference books [19; 20], and all reactions were written for 1 mole of oxygen.

In the temperature range of 1500 – 3500 K, the following phase transitions (melting, boiling) occur: WO₃ (1745 K), W₂C (3008 K), WC (3058 K), W₅Si₃ (2623 K), Si (1685 K), SiO₂ (1696 K), Al (2791 K), Al₂O₃ (2327 K), Ti (1939 K), TiO (2023 K), Ti₂O₃ (2115 K), Ti₃O₅ (2050 K), Ti₄O₇ (1950 K), TiO₂ (2130 K).

RESULTS AND DISCUSSION

Among the solid crystalline reductants considered, aluminum has the lowest melting point. After melting, it is also expected to vaporize most easily.

To evaluate the potential impact of tungsten oxide (WO₃) evaporation in the arc on the thermodynamic properties of the reactions, we calculated the thermodynamic characteristics of 15 reactions. In these reactions,

tungsten oxide was considered to be in its gaseous state (WO₃(g)) (reactions 1a, 17a, 22 – 33, 34a).

Reactions (4), (5), and (15), (16) are not reactions that reduce tungsten oxide. Comparing their thermodynamics with those of reactions (6), (7) and (13), (14) respectively, shows a lower likelihood of forming tungsten carbides and silicides from the direct interaction of tungsten with carbon (4), (5) and silicon (15), (16) than from the reduction of tungsten oxide by carbon (6), (7) or silicon (13), (14).

The standard Gibbs energies of all 41 reactions, grouped by the type of reductant and temperature, are presented in the Table. The results and specific conclusions regarding the effectiveness of each reductant (carbon, silicon, aluminum, titanium) are discussed in studies [21 – 23]. Compared to the work [23], the reactions (34) – (38) for the reduction of WO₃ by titanium in this study are written for 1 mole of oxygen (O₂), not for 1 mole of Ti.

The next step was to select the most effective reductants and the optimal conditions for these reactions.

It is known that the partial derivative of the standard Gibbs energy of a reaction with respect to temperature at constant pressure equals the standard entropy of the reaction with an opposite sign:

$$\left(\frac{\partial \Delta_r G^\circ(T)}{\partial T} \right)_p = -\Delta_r S^\circ(T). \quad (39)$$

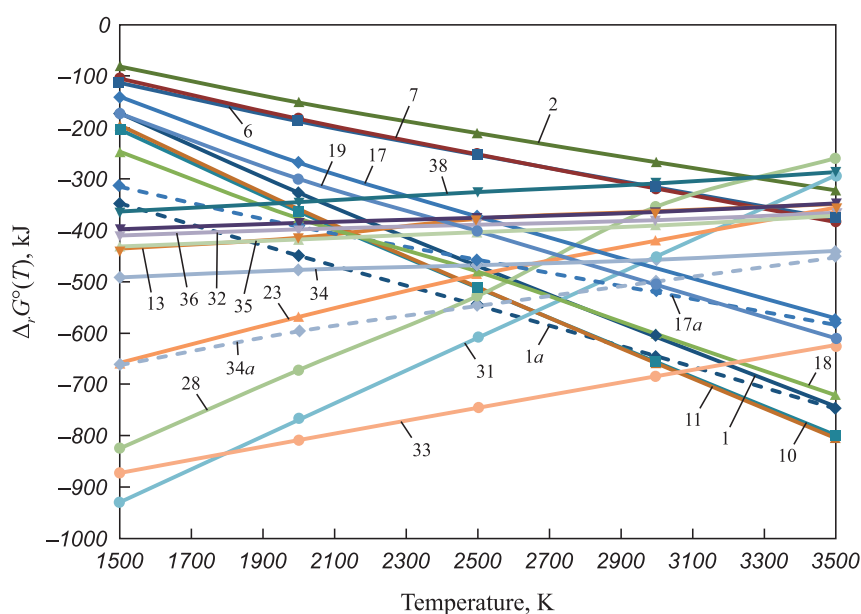
From this equation, it follows that the nature of the change in the standard Gibbs energy of a reaction with temperature is determined by the sign of the reac-

tion's standard entropy. In this context, $S_g^\circ > S_l^\circ > S_s^\circ$ for the same substance. Since the reactions (1) – (38) involve substances in all three physical states, many reactions exhibit significant changes in $\Delta_r G^\circ(T)$ depending on the temperature, both decreasing and increasing.

An analysis of the Table data shows that at 1500 K $\Delta_r G^\circ(T)$ changes from +58.44 kJ for reaction (32) to –929.12 kJ for reaction (31), and at 3500 K, it changes from +1389.31 kJ for reaction (32) to –803.92 kJ for reaction (11). Given such significant differences in $\Delta_r G^\circ(T)$ values, it makes sense to focus on the most thermodynamically probable reactions. These reactions are marked with asterisks in the table, and the dependencies of $\Delta_r G^\circ(T)$ on temperature are shown in the Figure.

Clearly, the graphs in the figure visually separate into three groups. The first group consists of the most probable reactions in the 1500 – 2500 K temperature range. These are reactions (31), (33), (28), (23) between gaseous WO₃ and aluminum, forming liquid or gaseous aluminum oxides. In the gas phase, the formation of aluminum dimer (Al₂) has a high probability of yielding tungsten with AlO₂(g) up to 3000 K (reaction (33)).

The second and larger group includes reactions (1), (1a), (11), (17), (17a), (18), and (19), which have a high probability of occurring in the temperature range of 2500 – 3500 K. In these reactions, the reductants are carbon and silicon, known for their increasing reductive properties as temperatures rise. Carbon and silicon also tend to disproportionate when reacting with metal oxides, especially those of active metals. This results in high thermodynamic probabilities for reactions (11), (18), and (19), where, alongside the oxides CO(g) and SiO(g)



Standard Gibbs energies of reactions (1) – (38) depending on temperature

Стандартные энергии Гиббса реакций (1) – (38) в зависимости от температуры

Standard Gibbs energies of reactions (1) – (38) depending on temperature

Стандартные энергии Гиббса реакций (1) – (38) в зависимости от температуры

Reductant	Reaction	$\Delta_r G^\circ(T)$, kJ, for T , K				
		1500	2000	2500	3000	3500
Carbon (C)	(1)*	–172.23	–326.83	–469.26	–607.39	–742.27
	(1a)*	–347.58	–449.50	–545.97	–644.87	–746.81
	(2)	–81.04	–151.09	–210.61	–267.20	–321.74
	(3)	5.08	12.32	24.02	36.49	49.40
	(4)	–47.76	–54.97	–63.57	–73.34	–83.87
	(5)	–35.11	–47.77	–61.80	–76.87	–92.47
	(6)*	–112.88	–187.74	–252.99	–316.10	–377.65
	(7)*	–104.45	–182.94	–251.81	–318.45	–383.38
	(8)	14.66	39.43	66.79	94.08	121.21
	(9)	7.35	22.02	39.88	57.92	76.00
	(10)*	–204.07	–363.48	–511.64	–656.29	–798.18
	(11)*	–195.64	–358.68	–510.46	–658.64	–803.92
Silicon (Si)	(12)	–328.43	–305.67	–270.56	–234.84	–198.98
	(13)*	–435.49	–414.30	–377.62	–362.83	–348.71
	(14)	–361.28	–337.12	–298.79	–267.13	–237.75
	(15)	–160.59	–162.95	–160.59	–191.99	–224.60
	(16)	–49.27	–47.17	–42.35	–48.44	–58.16
	(17)*	–139.95	–268.31	–373.17	–473.62	–570.77
	(17a)*	–315.29	–392.63	–457.24	–520.75	–583.70
	(18)*	–247.01	–376.94	–480.23	–601.61	–720.50
Aluminum (Al)	(19)*	–172.80	–299.76	–401.40	–505.91	–609.54
	(20)	–487.08	–456.23	–430.31	–387.47	–302.46
	(21)	–493.67	–448.82	–407.37	–348.34	–246.88
	(22)	–657.76	–568.48	–486.78	–390.80	–259.87
	(23)*	–657.75	–568.48	–486.78	–420.08	–356.00
	(24)	–844.31	–681.37	–527.86	–390.80	–259.87
	(25)	–825.37	–694.55	–573.26	–468.49	–369.83
	(26)	–826.07	–667.47	–518.28	–385.57	–258.64
	(27)	–418.44	–303.12	–197.12	–107.41	–23.50
	(28)*	–824.33	–671.84	–527.86	–354.05	–259.87
	(29)	–232.62	–200.33	–169.51	–140.93	–114.48
	(30)	–103.20	–66.548	–30.876	3.831	37.348
	(31)*	–929.12	–768.84	–609.48	–451.04	–293.75
	(32)	58.44	385.76	717.33	1052.17	1389.32
	(33)*	–872.28	–808.38	–745.69	–684.09	–623.66
Titanium (Ti)	(34)*	–491.61	–476.89	–467.84	–457.20	–440.10
	(34a)*	–662.29	–596.54	–547.24	–499.67	–453.08
	(35)*	–431.27	–417.72	–403.45	–390.66	–371.58
	(36)*	–409.99	–398.06	–388.98	–380.15	–365.78
	(37)*	–397.80	–385.35	–375.47	–364.24	–347.54
	(38)*	–363.22	–344.96	–325.39	–308.68	–286.65

(positive oxidation states of carbon and silicon), carbides and silicides of various compositions (negative oxidation states of carbon and silicon) are formed.

The third group includes reactions (34), (34a), (35), (36), (37), (38). These involve titanium, which does not readily vaporize or form gaseous oxides. Thus, the graphs show a slight upward slope, indicating less negative values $\Delta_r G^\circ(T)$ with increasing temperature. As with other reductants, the evaporation of WO_3 enhances the thermodynamic likelihood of its reduction by titanium (reaction (34a)). It can be concluded that titanium is an effective reductant that performs well across the entire temperature range of the welding arc.

The analysis of the thermodynamic properties of the reactions showed that the presence of reductants (carbon, silicon, aluminum, titanium) alongside tungsten oxide (WO_3) in the flux-cored wire used for surfacing, either separately or together, will promote the formation of tungsten silicides and carbides, and possibly elemental tungsten. Tungsten oxide exhibits the highest reactivity in its gaseous state $WO_3(g)$, which aligns perfectly with the physical properties of WO_3 . In the literature, WO_3 is described as “volatile upon calcination”.

Aluminum has the highest chemical affinity for gaseous tungsten oxide $WO_3(g)$ in the form of $Al(g)$ and the dimer $Al_2(g)$ in the temperature range of 1500 – 3000 K. The most likely oxidation product of aluminum is $Al_2O(g)$, which suggests the absence of non-metallic inclusions of $Al_2O_3(s)$ in the deposited metal. Thus, aluminum is the most effective reductant at relatively low temperatures in the arc.

Using silicon and carbon as reductants promotes the formation of both tungsten and its silicides and carbides in the metal melt due to disproportionation reactions, which are characteristic of these elements. Carbon and silicon are the most effective reductants at the highest temperatures in the arc.

Titanium is a quality reductant that performs its reductive functions across the entire temperature range of the welding arc. When titanium is used in the flux-cored wire, it is likely to produce $TiO_2(s)$ and $Ti_4O_7(s)$ oxides as non-metallic inclusions in the deposited metal.

CONCLUSIONS

Based on the available thermodynamic data for the reactants, calculations were performed to determine the properties $[\Delta_r H^\circ(T), \Delta_r S^\circ(T), \Delta_r G^\circ(T)]$ of the reactions involving the reduction of tungsten oxide (WO_3) by carbon, silicon, aluminum, and titanium (41 reactions) in their standard states within the temperature range of 1500 – 3500 K.

The presence of reductants (carbon, silicon, aluminum, titanium) alongside tungsten oxide (WO_3) in

the flux cored wire used for surfacing, either individually or together, will promote the formation of tungsten silicides and carbides, and possibly elemental tungsten.

Aluminum has the highest chemical affinity for gaseous tungsten oxide $WO_3(g)$ in the forms of $Al(g)$ and the dimer $Al_2(g)$ in the temperature range of 1500 – 3000 K. The most likely oxidation product of aluminum is $Al_2O(g)$, which suggests the absence of non-metallic inclusions of $Al_2O_3(s)$ in the deposited metal. Thus, aluminum is the most effective reductant at relatively low temperatures in the arc. Using silicon and carbon as reductants promotes the formation of both tungsten and its silicides and carbides in the metal melt. Titanium is an effective reductant across the entire temperature range of the welding arc, and its use is likely to result in the formation of TiO_2 and Ti_4O_7 oxides as non-metallic inclusions in the deposited metal.

The obtained data on the reduction of WO_3 provide a basis for conducting practical experiments on incorporating tungsten oxide and reductants into the composition of the flux cored wire charge.

REFERENCES / СПИСОК ЛИТЕРАТУРЫ

1. Li W., Wang H., Yu R., Wang J., Wang J., Wi M., Maksimov S.Yu. High-speed photography analysis for underwater flux-cored wire arc cutting process. *Transactions on Intelligent Welding Manufacturing*. 2020;141–151. https://doi.org/10.1007/978-981-13-8192-8_7
2. Eremin E.N., Losev A.S., Ponomarev I.A., Borodikhin S.A., Volochayev M.N. Wear resistance of steel obtained by surfacing a flux-cored wire 30N8Kh6M3STYu. *Journal of Physics: Conference Series*. 2020;1546:012060. <https://doi.org/10.1088/1742-6596/1546/1/012060>
3. Moreno J.R.S., Guimarães J.B., Lizzi E.A. da S., Correa C.A. Analyze and optimize the welding parameters of the process by pulsed tubular wire (FCAW – Flux Cored Arc Welding) based on the geometry of the weld beads resulting from each test. *Journal of Material Science and Technology Research*. 2022;9(1):11–23. <https://doi.org/10.31875/2410-4701.2022.09.02>
4. Il'yaschenko D.P., Zernin E.A., Sapozhkov S.B., Loskutov L.G. Method for predicting the composition of the protective coating in MMA. *IOP Conference Series: Materials Science and Engineering*. 2020;939:012029. <https://doi.org/10.1088/1757-899X/939/1/012029>
5. Kobernik N.V., Pankratov A.S., Sorokin S.S., Petrova V.V., Galinovskii A.L., Orlik A.G., Stroitelev D.V. Effect of chromium carbide introduced into a flux cored wire charge on the structure and properties of the hardfacing deposit. *Russian Metallurgy (Metally)*. 2020;2020(13):1485–1490. <https://doi.org/10.1134/S0036029520130145>
6. Wu W., Zhang T., Chen H., Peng J., Yang K., Lin S., Wen P., Li Z., Yang S., Kou S. Effect of heat input on microstructure and mechanical properties of deposited metal of E120C-K4 high strength steel flux-cored wire. *Materials*. 2023;16(8):3239. <https://doi.org/10.3390/ma16083239>

7. Smolentsev A.S., Votina E.B., Veselova V.E., Balin A.N. Study of microstructure and properties of high-strength alloy steel welded joints made with austenitic flux-cored wire with nitrogen. *Metallurgist*. 2023;67(7-8):928–937. <https://doi.org/10.1007/s11015-023-01582-5>
8. Liu H.-Yu., Song Zh.-L., Cao Q., Chen S.-P., Meng Q.-S. Microstructure and properties of Fe-Cr-C hardfacing alloys reinforced with TiC-NbC. *Journal of Iron and Steel Research, International*. 2016;23(3):276–280. [https://doi.org/10.1016/s1006-706x\(16\)30045-0](https://doi.org/10.1016/s1006-706x(16)30045-0)
9. Malushin N.N., Gromov V.E., Romanov D.A., Bashchenko L.P., Kovalev A.P. Development of complex hardening technology of cold rolling rolls by plasma surfacing. *Zagotovitel'nye proizvodstva v mashinostroenii*. 2023;21(7):296–302. (In Russ.). <https://doi.org/10.36652/1684-1107-2023-21-7-296-302>
Малушин Н.Н., Громов В.Е., Романов Д.А., Башченко Л.П., Ковалев А.П. Разработка комплексной технологии упрочнения валков холодной прокатки плазменной наплавкой. *Заготовительные производства в машиностроении*. 2023;21(7):296–302. <https://doi.org/10.36652/1684-1107-2023-21-7-296-302>
10. Ryabtsev I.A., Lentuygov I.P., Bezushko O.N., Goncharova O.N., Ryabtsev I.I., Lukyanenko A.A. Influence of methods of preparation of a charge of flux-cored wires on the structure of the deposited metal and the environmental safety of the working area during arc surfacing. *Welding Production*. 2022;(8):47–53. (In Russ.).
Рябцев И.А., Лентюгов И.П., Безушко О.Н., Гончарова О.Н., Рябцев И.И., Лукьяненко А.А. Влияние способов подготовки шихты порошковых проволок на структуру наплавленного металла и экологическую безопасность рабочей зоны при дуговой наплавке. *Сварочное производство*. 2022;(8):47–53.
11. Malushin N.N., Martyushev N.V., Valuev D.V., Karlina A.I., Kovalev A.P., Gizatulina R.A. Strengthening of metallurgical equipment parts by plasma surfacing in nitrogen atmosphere. *Metallurgist*. 2022;65(11-12):1468–1475. <https://doi.org/10.1007/s11015-022-01292-4>
12. Vinokurov G.G., Vasil'eva M.I., Kychkin A.K., Moskvitina L.V. Structure and tribological properties of the wear-resistant coatings deposited using flux-cored wires modified by tantalum and tungsten. *Russian Metallurgy (Metally)*. 2019;2019(13):1357–1362. <https://doi.org/10.1134/S0036029519130391>
13. Ma Q., Li H., Liu S., Liu D., Wang P., Zhu Q., Lei Y. Comparative evaluation of self-shielded flux-cored wires designed for high strength low alloy steel in underwater wet welding: Arc stability, slag characteristics, and joints' quality. *Journal of Materials Engineering and Performance*. 2022;31(4):5231–5244. <https://doi.org/10.1007/s11665-022-06683-x>
14. Zou Z., Liu Z., Han X. Effect of W on microstructure and properties of Fe-Cr-C-W-B surfacing alloy. *Transactions of the China Welding Institution*. 2021;42(7):91–96. <https://doi.org/10.12073/j.hjxb.20210208001>
15. Smolentsev A.S., Veselova V.E., Berezovsky A.V., Usoltsev E.A., Shak A.V. Structure and properties of welded joints of high-strength steels made by metal-core wire with nitrogen. *Metallurg*. 2023;(9):71–77. (In Russ.).
Смоленцев А.С., Веселова В.Е., Березовский А.В., Усольцев Е.А., Шак А.В. Структура и свойства сварных соединений из высокопрочных сталей, выполненных металлопорошковой проволокой с азотом. *Металлург*. 2023;(9):71–77.
16. Malushin N.N., Romanov D.A., Kovalev A.P., Bashchenko L.P., Semin A.P. Stress state in deposited steel cast rolls with high surface hardness after argon plasma-jet hard-facing. *Russian Physics Journal*. 2022;64(12):2185–2192. <https://doi.org/10.1007/s11182-022-02575-8>
17. Pandova I., Makarenko V., Mitrofanov P., Dyadyura K., Hrebnyk L. Influence of non-metallic inclusions on the corrosion resistance of stainless steels in arc surfacing. *MM Science Journal*. 2021;2021(6):4775–4780. https://doi.org/10.17973/MMSJ.2021_10_2021032
18. Malushin N.N., Kovalev A.P., Smagin D.A. The choice of a surfacing method for hardening parts of mining and metallurgical equipment. *Bulletin of Scientific Conferences*. 2015; (2-1(2)):105–106. (In Russ.).
Малушин Н.Н., Ковалев А.П., Смагин Д.А. Выбор способа наплавки для упрочнения деталей горно-металлургического оборудования. *Вестник научных конференций*. 2015;(2-1(2)):105–106.
19. Thermodynamic Properties of Individual Substances: Reference. Vol. 1. Book 1. Glushko V.P., Gurvich L.V., etc. eds. Moscow: Nauka; 1978:440. (In Russ.).
Термодинамические свойства индивидуальных веществ: Справ. Т. 1. Кн. 1 / Под ред. В.П. Глушко, Л.В. Гурвича и др. Москва: Наука; 1978:440.
20. Barin I., Knacke O., Kubaschewski O. Thermochemical Properties of Inorganic Substances. Berlin: Springer-Verlag; 1977.
21. Kryukov R.E., Goryushkin V.F., Bendre Yu.V., Bashchenko L.P., Kozyrev N.A. Thermodynamic aspects of Cr₂O₃ reduction by carbon. *Izvestiya. Ferrous Metallurgy*. 2019; 62(12):950–956. (In Russ.). <https://doi.org/10.17073/0368-0797-2019-12-950-956>
Крюков Р.Е., Горюшкин В.Ф., Бендре Ю.В., Башченко Л.П., Козырев Н.А. Некоторые термодинамические аспекты восстановления Cr₂O₃ углеродом. *Известия вузов. Черная металлургия*. 2019;62(12):950–956. <https://doi.org/10.17073/0368-0797-2019-12-950-956>
22. Bendre Yu.V., Goryushkin V.F., Kryukov R.E., Kozyrev N.A., Shurupov V.M. Some thermodynamic aspects of WO₃ recovery by silicon. *Izvestiya. Ferrous Metallurgy*. 2017;60(6):481–485. (In Russ.). <https://doi.org/10.17073/0368-0797-2017-6-481-485>
Бендре Ю.В., Горюшкин В.Ф., Крюков Р.Е., Козырев Н.А., Шурупов В.М. Некоторые термодинамические аспекты восстановления вольфрама из оксида WO₃ кремнием. *Известия вузов. Черная металлургия*. 2017;60(6):481–485. <https://doi.org/10.17073/0368-0797-2017-6-481-485>
23. Bendre Yu.V., Goryushkin V.F., Kozyrev N.A., Shevchenko R.A., Oznobikhina N.V. Thermodynamic aspects of metal oxides reduction by aluminum and titanium during thermite welding of rails. *Bulletin of the Siberian State Industrial University*. 2021;3(37):13–19. (In Russ.).
Бендре Ю.В., Горюшкин В.Ф., Козырев Н.А., Шевченко Р.А., Оздобихина Н.В. Термодинамические аспекты восстановления оксидов металлов алюминием и титаном при термитной сварке рельсов. *Вестник Сибирского государственного индустриального университета*. 2021;3(37):13–19.

Information about the Authors

Сведения об авторах

Lyudmila P. Bashchenko, Cand. Sci. (Eng.), Assist. Prof. of the Chair "Thermal Power and Ecology", Siberian State Industrial University
ORCID: 0000-0003-1878-909X
E-mail: luda.baschenko@gmail.com

Yuliya V. Bendre, Cand. Sci. (Chem.), Assist. Prof. of the Chair of Ferrous Metallurgy and Chemical Technology, Siberian State Industrial University
E-mail: bendre@list.ru

Nikolai A. Kozyrev, Dr. Sci. (Eng.), Deputy Director of the Scientific Center for High-Quality Steels, I.P. Bardin Central Research Institute of Ferrous Metallurgy
ORCID: 0000-0002-7391-6816
E-mail: n.kozyrev@chermet.net

Aleksei R. Mikhno, Director of the Scientific and Production Center "Welding Processes and Technologies", Siberian State Industrial University
ORCID: 0000-0002-7305-6692
E-mail: mikno-mm131@mail.ru

Vadim M. Shurupov, Postgraduate of the Chair of Ferrous Metallurgy and Chemical Technology, Siberian State Industrial University
E-mail: shurupovvm@sgaz.pro

Andrei V. Zhukov, Postgraduate of the Chair of Ferrous Metallurgy and Chemical Technology, Siberian State Industrial University
E-mail: Svarka42@mail.ru

Людмила Петровна Бащенко, к.т.н., доцент кафедры теплоэнергетики и экологии, Сибирский государственный индустриальный университет
ORCID: 0000-0003-1878-909X
E-mail: luda.baschenko@gmail.com

Юлия Владимировна Бендре, к.х.н., доцент кафедры металлургии черных металлов и химической технологии, Сибирский государственный индустриальный университет
E-mail: bendre@list.ru

Николай Анатольевич Козырев, д.т.н., заместитель директора научного центра качественных сталей, Центральный научно-исследовательский институт черной металлургии им. И.П. Бардина
ORCID: 0000-0002-7391-6816
E-mail: n.kozyrev@chermet.net

Алексей Романович Мухно, директор НПЦ «Сварочные процессы и технологии», Сибирский государственный индустриальный университет
ORCID: 0000-0002-7305-6692
E-mail: mikno-mm131@mail.ru

Вадим Михайлович Шурупов, аспирант кафедры металлургии черных металлов и химической технологии, Сибирский государственный индустриальный университет
E-mail: shurupovvm@sgaz.pro

Андрей Владимирович Жуков, аспирант кафедры металлургии черных металлов и химической технологии, Сибирский государственный индустриальный университет
E-mail: Svarka42@mail.ru

Contribution of the Authors

Вклад авторов

L. P. Bashchenko – collecting research data, analysis of results, preparing materials for the article.

Yu. V. Bendre – conducting thermodynamic calculations, analytical evaluation of results.

N. A. Kozyrev – forming the research main idea, developing a research plan, setting tasks, analysis of results.

A. R. Mikhno – processing of results, design of the article.

V. M. Shurupov – conducting practical experiments on the results obtained, design of the article.

A. V. Zhukov – organization of sample testing, analysis of results.

Л. П. Бащенко – сбор данных исследований, анализ результатов исследований, подготовка материалов для статьи.

Ю. В. Бендре – проведение термодинамических расчетов, аналитическая оценка полученных результатов.

Н. А. Козырев – формирование основной идеи исследований, разработка плана исследований, постановка задач, анализ результатов исследований.

А. Р. Мухно – обработка полученных результатов, оформление статьи.

В. М. Шурупов – проведение практических экспериментов по полученным результатам, оформление статьи.

А. В. Жуков – организация испытаний образцов, анализ результатов исследований.

Received 06.02.2024
 Revised 25.03.2024
 Accepted 29.03.2024

Поступила в редакцию 06.02.2024
 После доработки 25.03.2024
 Принята к публикации 29.03.2024

ИННОВАЦИИ В МЕТАЛЛУРГИЧЕСКОМ
ПРОМЫШЛЕННОМ И ЛАБОРАТОРНОМ
ОБОРУДОВАНИИ, ТЕХНОЛОГИЯХ И МАТЕРИАЛАХINNOVATION IN METALLURGICAL
INDUSTRIAL AND LABORATORY EQUIPMENT,
TECHNOLOGIES AND MATERIALS

UDC 621.746+621.771

DOI 10.17073/0368-0797-2024-4-457-462



Original article

Оригинальная статья

STRESS STATE OF BILLET – MANDREL SYSTEM DURING PRODUCTION OF HOLLOW STEEL BILLET IN A UNIT OF CONTINUOUS CASTING AND DEFORMATION. PART 2

O. S. Lekhov¹, A. V. Mikhalev², S. O. Nepryakhin³¹ Russian State Vocational Pedagogical University (11 Mashinostroitelei Str., Yekaterinburg 620012, Russian Federation)² JSC “Ural Pipe Plant” (28 Sakko i Vantsetti Str., Pervouralsk, Sverdlovsk Region 623107, Russian Federation)³ Ural Federal University named after the First President of Russia B.N. Yeltsin (28 Mira Str., Yekaterinburg 620002, Russian Federation)

✉ MXLehov@yandex.ru

Abstract. The paper presents the results of theoretical research of stress-strain state of a billet – mandrel system when producing steel hollow billets in a unit of combined continuous casting and deformation, in which the working surface of the calibrated anvils are made with a variable radius. The necessity of making the working surface of the calibrated anvils with a variable radius is substantiated and initial data for the calculations is given. The calculation results are considered along the lines of the volumetric model passing through the characteristic points of deformation centers. The authors determined the forces when the anvils compress the wall of a hollow billet and the force of pulling the hollow billet from the mold. The laws of metal axial displacements and stresses in the deformation centers during compressing the wall of a hollow billet was established at the combined process of continuous casting and deformation in the unit. Nature of the stressed state of the metal wall of a hollow billet is considered from the perspective of improving its quality. The technique studied allows to determine the stress-strain state of a mandrel when producing a hollow steel billet using such a unit. The authors provided the recommendations for reliable gripping and compression with calibrated anvils of a hollow steel billet coming from a water-cooled copper mold of the unit of combined continuous casting and deformation.

Keywords: unit, continuous casting, anvil, deformation, hollow billet, stress, finite element

For citation: Lekhov O.S., Mikhalev A.V., Nepryakhin S.O. Stress state of billet – mandrel system during production of hollow steel billet in a unit of continuous casting and deformation. Part 2. *Izvestiya. Ferrous Metallurgy*. 2024;67(4):457–462.

<https://doi.org/10.17073/0368-0797-2024-4-457-462>

НАПРЯЖЕННОЕ СОСТОЯНИЕ СИСТЕМЫ ЗАГОТОВКА – ОПРАВКА ПРИ ПОЛУЧЕНИИ СТАЛЬНОЙ ПОЛОЙ ЗАГОТОВКИ НА УСТАНОВКЕ НЕПРЕРЫВНОГО ЛИТЬЯ И ДЕФОРМАЦИИ. ЧАСТЬ 2

О. С. Лехов¹, А. В. Михалев², С. О. Непряхин³¹ Российский государственный профессионально-педагогический университет (Россия, 620012, Екатеринбург, ул. Машиностроителей, 11)² ОАО «Уральский трубный завод» (Россия, 623107, Свердловская обл., Первоуральск, ул. Сакко и Ванцетти, 28)³ Уральский федеральный университет имени первого Президента России Б.Н. Ельцина (Россия, 620002, Екатеринбург, ул. Мира, 19)

✉ MXLehov@yandex.ru

Аннотация. В статье представлены результаты теоретического исследования напряженно-деформированного состояния системы заготовка – оправка при производстве стальных полых заготовок на установке совмещенного непрерывного литья и деформации, в которой рабочие поверхности калиброванных бойков выполнены с переменным радиусом. Обоснована необходимость выполнения рабочей поверхности калиброванных бойков с переменным радиусом и приведены исходные данные для расчетов. Результаты рассматриваются по линиям объемной модели, проходящим через характерные точки очагов деформации. Авторы определили усилия при обжатии бойками

стенки полой заготовки и силу вытягивания полой заготовки из кристаллизатора установки. Исследованы закономерности осевых перемещений металла и напряжений в очагах деформации при сжатии стенки полой заготовки при совмещенном процессе непрерывного литья и деформирования. Характер напряженного состояния металлической стенки полой заготовки рассматривается с точки зрения повышения ее качества. Изученная методика позволяет определить напряженно-деформированное состояние оправки при изготовлении полой стальной заготовки с использованием установки непрерывного литья и деформации. Авторами представлены рекомендации для осуществления надежного захвата и обжатия калиброванными бойками полой стальной заготовки, поступающей из водоохлаждаемого медного кристаллизатора установки совмещенного процесса непрерывного литья и деформации.

Ключевые слова: установка, непрерывное литье, боек, деформация, полая заготовка, напряжение, конечный элемент

Для цитирования: Лехов О.С., Михалев А.В., Непряхин С.О. Напряженное состояние системы заготовка – оправка при получении стальной полой заготовки на установке непрерывного литья и деформации. Часть 2. *Известия вузов. Черная металлургия*. 2024;67(4):457–462. <https://doi.org/10.17073/0368-0797-2024-4-457-462>

INTRODUCTION

The study [1] presents the results of calculating the stress-strain state of the metal in the deformation centers during the production of steel hollow billets in a unit of continuous casting and deformation, where the working surfaces of the anvils are made with a constant radius. This paper presents the results of calculating the bending zone and the deformation center of the tube during the compression of the billet by 5 mm with simultaneous lowering of the anvil by 5 mm, where the anvil's working surface is made with a variable radius. This configuration allows for reliable gripping and compression of the hollow billet by the anvils as it exits the unit's mold.

CALCULATION RESULTS

The simulation involved compressing billet by 5 mm (anvil movement of –5 mm along the X -axis) with simultaneously lowering the anvil by 5 mm (anvil movement of –5 mm along the Z -axis).

The results are presented through points along lines in the $Y = 0$ plane (Fig. 1).

The nature of the displacements and stresses is illustrated in Figs. 1 and 2.

In the Cartesian coordinate system, the displacement and stress lines align with those in the cylindrical coordinate system [2 – 4].

During compression of the hollow billet wall by the anvils, the force along the X -axis is 694 kN, and along the Y -axis, it is 384 kN. The pulling force of the billet from the crystallizer along the Z -axis is 41 kN.

In addition to the graphs (Fig. 2), Table 1 provides specific values of displacements and stresses at points 1 – 15. Since the maximum and minimum values of the parameters are not always located at these points, the maximum and minimum displacements and stresses along these three lines are also provided.

From the data, it is evident that along the length of the deformation center (line 2 – 3 – 4), at point 3, the billet wall is compressed by 5 mm with simultaneous movement of the billet by 5 mm in the casting direction

(Table 1, Fig. 2, *a*). Notably, when the hollow billet wall is compressed by the calibrated anvils, the metal displacement along the X -axis decreases to 3 mm (point 8), while along the Z -axis, it increases to 6.6 mm (Fig. 2, *b*, point 9).

When compressing the hollow billet with anvils designed with a variable radius working surface, the nature of the metal's stressed state in the deformation center changes [5 – 7]. In this case, the highest compressive stresses arise in the billet wall along the X -axis and line 3 – 8 – 13, with values of –152.0, –187.5, and –190.0 MPa, respectively (Table 1, Figs. 2, *c*, *d*, 3). The maximum compressive stress (–190 MPa) occurs at the contact surface between the hollow billet wall and the mandrel (Table 1, point 13).

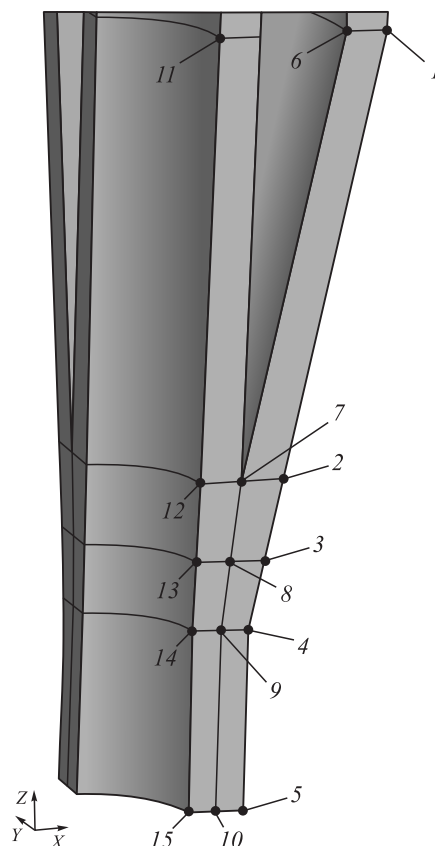


Fig. 1. Location of points for representing the calculation results

Рис. 1. Положение точек для представления результатов расчета

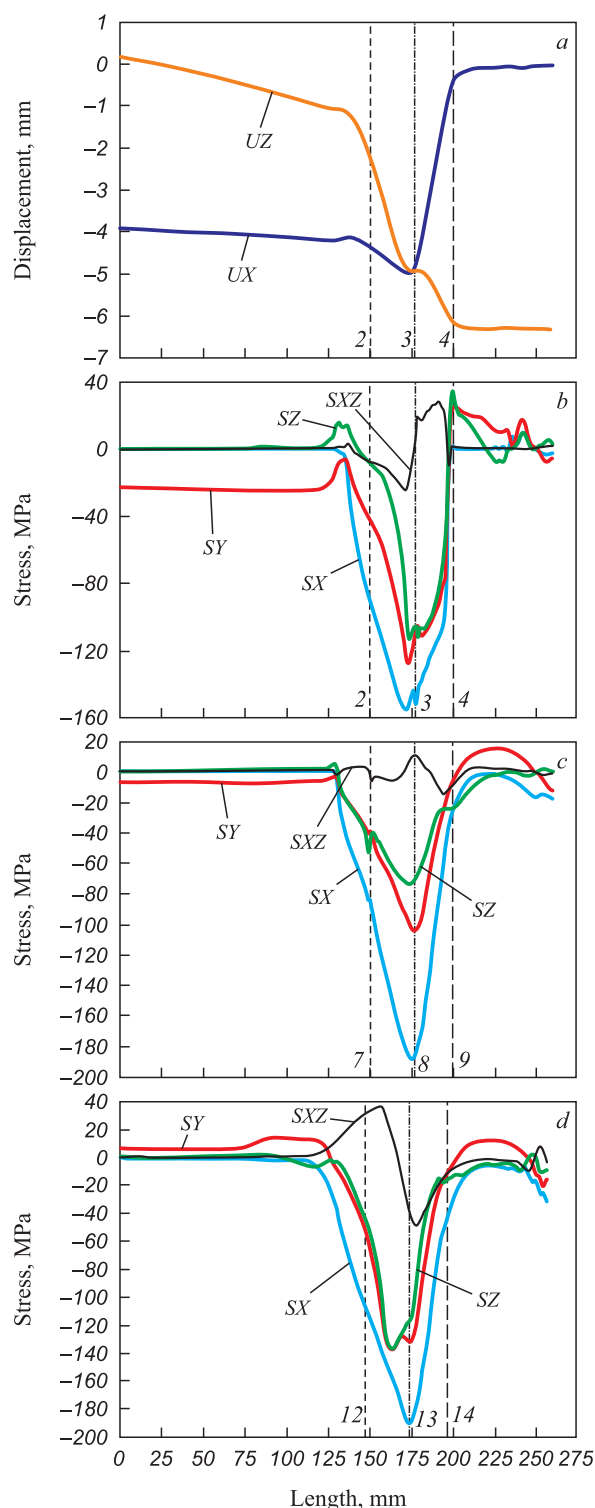


Fig. 2. Patterns of displacements (a) and stresses (b, c, d) along the lines passing through points 1 – 2 – 3 – 4 – 5 (a, b), 6 – 7 – 8 – 9 – 10 (c) and 11 – 12 – 13 – 14 – 15 (d) (billet compression with the anvil by 5 mm while simultaneous lowering by 5 mm, working surface of the anvil is made with a variable radius)

Рис. 2. Характер перемещений (a) и напряжений (b, c, d) по линиям, проведенным через точки 1 – 2 – 3 – 4 – 5 (a, b), 6 – 7 – 8 – 9 – 10 (c) и 11 – 12 – 13 – 14 – 15 (d) (обжатие заготовки бойком на 5 мм с одновременным опусканием последнего на 5 мм, рабочая поверхность бойка выполнена по переменному радиусу)

CALCULATION OF THE STRESS-STRAIN STATE

OF THE MANDREL

The stress-strain state of a mandrel with a diameter of 60 mm and a channel diameter of 10 mm was calculated. This was done by solving an elastoplastic problem using the finite element method within the ANSYS software package [8 – 10].

Table 1. Results of calculation of displacements and stresses at the points 1 – 5, 6 – 10 and 11 – 15 (billet compression with the anvil by 5 mm with simultaneous lowering of it by 5 mm; working surface of the anvil is made with a variable radius)

Таблица 1. Результаты расчета перемещений и напряжений в точках 1 – 5, 6 – 10 и 11 – 15 (обжатие заготовки бойком на 5 мм с одновременным опусканием последнего на 5 мм; рабочая поверхность бойка выполнена по переменному радиусу)

Point	Displacement, mm		Stress, MPa			
	UX	UZ	SX	SY	SZ	SXZ
Results along the line passing through points 1 – 5						
1	–3.9	0.2	0	–22.7	0.5	0
2	–4.4	–2.3	–91.0	–43.4	–8.7	–7.7
3	–5.0	–5.0	–152.0	–106.7	–105.7	5.2
4	–0.4	–6.2	0.2	24.4	29.4	1.5
5	–0.1	–6.3	–2.1	–5.2	0.9	1.2
Min along line 1 – 5	0	0.2	9.3	24.4	33.9	28.0
Max along line 1 – 5	–5.0	–6.3	–155.0	–127.0	–112.8	–24.3
Results along the line passing through points 6 – 10						
6	–4.1	0.2	0	–7.1	0.5	0
7	–2.3	–1.6	–84.7	–39.4	–44.7	–5.9
8	–3.0	–5.2	–186.5	–104.1	–71.0	10.8
9	–0.3	–6.6	–24.9	–5.4	–23.5	–9.1
10	0	–6.3	–17.6	–12.3	–0.2	–1.2
Min along line 6 – 10	0	0.2	0	15.1	5.2	10.8
Max along line 6 – 10	–4.4	–6.7	–188.4	–104.1	–73.7	–14.5
Results along the line passing through points 11 – 15						
11	0	–1.6	–0.2	6.0	1.6	–0.6
12	–0.1	–2.5	–106.4	–52.4	–43.0	31.3
13	–0.1	–3.7	–190.0	–131.2	–117.6	–39.1
14	0	–6.4	–42.0	–11.3	–15.5	–12.3
15	0	–6.3	–30.9	–16.1	–9.1	–2.5
Min along line 11 – 15	0	–1.4	–0.2	13.8	2.1	36.4
Max along line 11 – 15	–0.1	–6.5	–190.0	–137.0	–137.2	–48.6

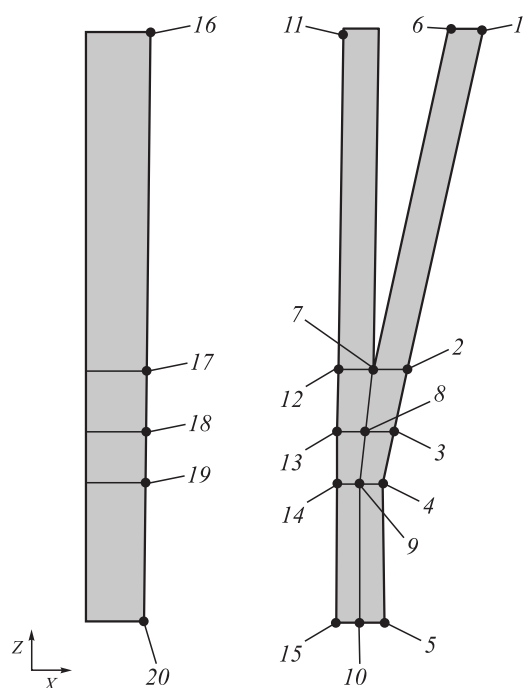


Fig. 3. Location of points for representing the calculation results of the mandrel

Рис. 3. Положение точек для представления результатов расчета оправки

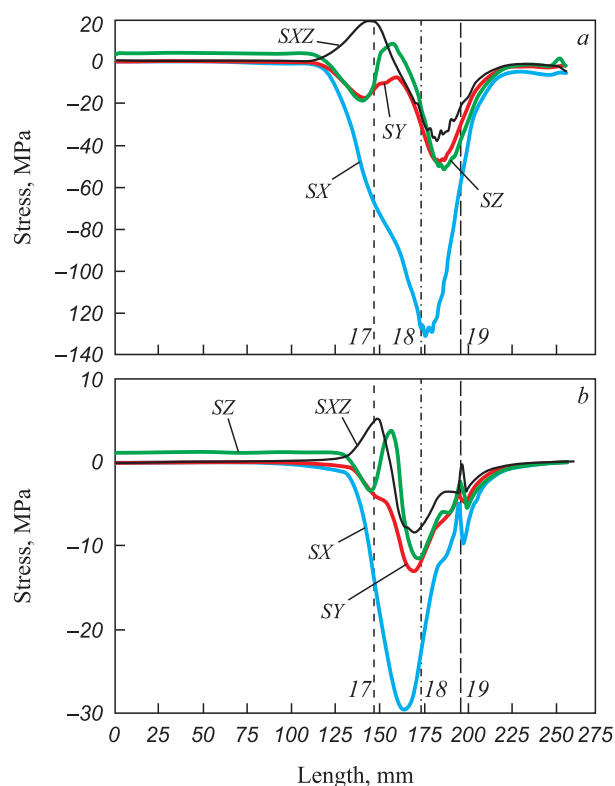


Fig. 4. Stress patterns along the lines passing through the points 16 – 17 – 18 – 19 – 20: a and b – compression by 5 and 11 mm

Рис. 4. Характер напряжений по линиям, проведенным через точки 16 – 17 – 18 – 19 – 20: а и б – обжатие 5 и 11 мм

Table 2. Results of calculation at the lines' points, maximum and minimum values of the studied parameters along the line passing through the points 16 – 20 (working surface of the anvil is made with a variable radius)

Таблица 2. Результаты расчета в точках линий, а также максимальные и минимальные значения исследуемых параметров по линии, проходящей через точки 16 – 20 (рабочая поверхность бойка по переменному радиусу)

Point	Displacement, mm		Stress, MPa			
	UX	UZ	SX	SY	SZ	SXZ
16	–0.01	–0.08	0	0	3.90	0
17	–0.07	–0.15	–66.90	–13.20	–10.00	19.60
18	–0.12	–0.27	–127.20	–29.20	–20.20	–25.60
19	–0.06	–0.27	–56.80	–30.10	–37.00	–22.10
20	0	–0.25	–5.30	–2.10	–4.00	–3.80
Min along line 16 – 20	0	–0.08	0	0	8.60	19.60
Max along line 16 – 20	–0.12	–0.29	–130.80	–47.50	–51.20	–37.40

The simulation involved compressing the billet by 5 mm (anvil movement of –5 mm along the X-axis) while simultaneously lowering the anvil by 5 mm (anvil movement of –5 mm along the Z-axis).

The calculation results are provided along the line passing through points 16 – 20 (Fig. 3). The stress distribution is shown in Fig. 4. In addition to the graphs, Table 2 provides specific values of displacements and stresses at points 16 – 20. Since the maximum and minimum values of the parameters are not always located at these points, the maximum and minimum displacements and stresses along this line are also provided [14 – 16].

The data indicate that at the contact surface between the mandrel and the billet wall in the deformation center (along line 17 – 18 – 19), the mandrel experiences maximum compressive stresses (–130.8 MPa) in the direction of the X-axis. This should be considered when selecting the structural parameters and material for the mandrel [17 – 20].

CONCLUSION

The regularities of metal displacement and axial stress distribution in the deformation centers during the compression of the hollow billet wall by anvils with a variable radius working surface have been determined. The stressed state of the mandrel during the production of steel hollow billets in a unit of combined continuous casting and deformation processes has also been established.

REFERENCES / СПИСОК ЛИТЕРАТУРЫ

- Lekhov O.S., Mikhalev A.V., Nepryakhin S.O. Stressed state of the billet – mandrel system during production of hollow steel billet in a unit of continuous casting and deformation. Part 1. *Izvestiya. Ferrous Metallurgy*. 2023;66(4):485–491. (In Russ.). <https://doi.org/10.17073/0368-0797-2023-4-485-491>
Лехов О.С., Михалев А.В., Непряхин С.О. Напряженное состояние системы заготовка – оправка при получении стальной полой заготовки на установке непрерывного литья и деформации. Часть 1. *Известия вузов. Черная металлургия*. 2023;66(4):485–491. <https://doi.org/10.17073/0368-0797-2023-4-485-491>
- Vyunnenberg K. Production of continuously cast billets with the highest quality. In: *Proceedings of the 6th Int. Congress of Iron and Steel*, vol. 3. Moscow: Mashinostroenie; 1990: 364–376.
Вюнненберг К. Производство непрерывнолитых заготовок, отвечающих высшим требованиям качества. В кн.: *Труды шестого международного конгресса железа и стали*. Т. 3. Москва: Машиностроение; 1990:364–376.
- Fujii H., Ohashi T., Hiromoto T. On the formation of the internal cracks in continuously cast slabs. *Tetsu-to-Hagane*. 1978;18(8):510–518. https://doi.org/10.2355/tetsutohagane1955.62.14_1813
- Sorimachi K., Emi T. Elastoplastic stress analysis of bulging as a major cause of internal cracks in continuously cast slabs. *Tetsu-to-Hagane*. 1977;63(8):1297–1304. https://doi.org/10.2355/tetsutohagane1955.63.8_1297
- Lekhov O.S., Mikhalev A.V. Continuous Casting and Deformation Unit for the Manufacture of Steel Sheets and Billets. Ekaterinburg: UPI; 2020:307. (In Russ.).
Лехов О.С., Михалев А.В. Установка непрерывного литья и деформации для производства стальных листов и сортовых заготовок. Екатеринбург: Изд-во УМЦ УПИ; 2020:307.
- Lekhov O.S., Guzanov B.N., Lisin I.V., Bilalov D.Kh. Study of combined continuous casting and cyclic deformation process for production of steel sheets. *Stal'*. 2016;(1):59–62. (In Russ.).
Лехов О.С., Гузанов Б.Н., Лисин И.В., Билалов Д.Х. Исследование совмещенного процесса непрерывной разливки и циклической деформации для получения листов из стали. *Сталь*. 2016;(1):59–62.
- Lekhov O.S., Mikhalev A.V., Shevelev M.M. Load and strain status of CCM backups and stripe deformation at production of steel sheets for welded pipes. Report 1. *Izvestiya. Ferrous Metallurgy*. 2018;61(4):268–273. (In Russ.). <https://doi.org/10.17073/0368-0797-2018-4-268-273>
Лехов О.С., Михалев А.В., Шевелев М.М. Нагруженность и напряженное состояние бойков установки непрерывного литья и деформации полосы при получении листов из стали для сварных труб. Сообщение 1. *Известия вузов. Черная металлургия*. 2018;61(4):268–273. <https://doi.org/10.17073/0368-0797-2018-4-268-273>
- ANSYS. Structural Analysis Guide. Rel. 15.0.
- Bogatov A.A., Nukhov D.Sh., P'yankov K.P. Finite element modeling of plate rolling. *Metallurg*. 2015;(2):19–23. (In Russ.).
Богатов А.А., Нухов Д.Ш., Пьянков К.П. Конечно-элементное моделирование процесса толстолистовой прокатки. *Металлург*. 2015;(2):19–23.
- Takashima Y., Yanagimoto I. Finite element analysis of flange spread behavior in H-beam universal rolling. *Steel Research International*. 2011;82(10):1240–1247. <https://doi.org/10.1002/srin.201100078>
- Karrech A., Seibi A. Analytical model of the expansion in of tubes under tension. *Journal of Materials Processing Technology*. 2010;210:336–362.
- Kazakov A.L., Spevak L.F. Numeral and analytical studies of nonlinear parabolic equation with boundary conditions of a special form. *Applied Mathematical Modelling*. 2013; 37(10–13):6918–6928. <https://doi.org/10.1016/j.apm.2013.02.026>
- Kobayashi S., Oh S.-I., Altan T. Metal Forming and Finite-Element Method. New York: Oxford University Press; 1989:377.
- Jansson N. Optimized sparse matrix assembly in finite element solvers with one-sided communication. In: *High Performance Computing for Computational Science – VECPAR 2012*. Springer: Berlin, Heidelberg; 2013:128–139.
- Matsumia T., Nakamura Y. Mathematical model of slab bulging during continuous casting. In: *Applied Mathematical and Physical Models in Iron and Steel Industry. Proceedings of the 3rd Process Tech. Conf., Pittsburgh, Pa, 28–31 March 1982*. New York; 1982:264–270.
- Park C.Y., Yang D.Y. A study of void crushing in large forgings: II. Estimation of bonding efficiency by finite-element analysis. *Journal of Materials Processing Technology*. 1997; 72(1):32–41.
- Efimenko L.A., Prygaev A.K. Determination of the Actual Mechanical Properties of Pipeline Metal Based on Hardness Measurement. Moscow: RTU nefti i gaza; 2007:18. (In Russ.).
Ефименко Л.А., Прыгаев А.К. Определение фактических механических свойств металла трубопроводов на основе измерения твердости. Москва: изд. РТУ нефти и газа; 2007:18.
- Kudrya A.V. Critical factors of metallurgical quality of high-strength steels. In: *Perspective Materials. Vol. V*. Tolyatti: TSU; 2013: 332–362. (In Russ.).
Кудря А.В. Критические факторы металлургического качества сталей повышенной прочности. В кн.: *Перспективные материалы. Т. V*. Тольятти: изд. ТГУ; 2013: 332–362.
- Kazakov A.A., Kiselev D.V. Modern methods for assessing the quality of the structure of materials based on panoramic studies based on the TXIXOMET image analyzer. In: *Perspective Materials. Vol. V*. Tolyatti: TSU; 2013:270–329. (In Russ.).
Казаков А.А., Киселев Д.В. Современные методы оценки качества структуры материалов на основе панорамных исследований на основе анализатора изображений TXIXOMET. В кн.: *Перспективные материалы. Т. V*. Тольятти: изд. ТГУ; 2013:270–329.
- Kyung-Moon L., Hu-Chul L. Grain refinement and mechanical properties of asymmetrically rolled low carbon steel. *Journal of Materials Processing Technology*. 2010;210(12):1574–1579. <https://doi.org/10.1016/j.jmatprotec.2010.05.004>

Information about the Authors

Oleg S. Lekhov, Dr. Sci. (Eng.), Prof. of the Chair of Engineering and Vocational Training in Machinery and Metallurgy, Russian State Professional Pedagogical University

E-mail: MXLehov38@yandex.ru

Aleksandr V. Mikhalev, Cand. Sci. (Eng.), General Director, JSC “Ural Pipe Plant”

E-mail: mialex@trubprom.com

Sergei O. Nepriakhin, Cand. Sci. (Eng.), Assist. Prof. of the Chair of Metal Forming, Ural Federal University named after the First President of Russia B.N. Yeltsin

E-mail: s.o.nepriakhin@urfu.ru

Сведения об авторах

Олег Степанович Лехов, д.т.н., профессор кафедры инжиниринга и профессионального обучения в машиностроении и металлургии, Российский государственный профессионально педагогический университет

E-mail: MXLehov38@yandex.ru

Александр Викторович Михалев, к.т.н., генеральный директор, ОАО «Уральский трубный завод»

E-mail: mialex@trubprom.com

Сергей Олегович Непряхин, к.т.н., доцент кафедры обработки металлов давлением, Уральский федеральный университет имени первого Президента России Б.Н. Ельцина

E-mail: s.o.nepriakhin@urfu.ru

Contribution of the Authors

O. S. Lekhov – formulation of the article idea, analysis of the calculation results, writing the text.

A. V. Mikhalev – conducting an experiment on a pilot unit.

S. O. Nepriakhin – conducting computer calculations.

Вклад авторов

О. С. Лехов – идея статьи, анализ результатов расчета, написание статьи.

А. В. Михалев – проведение эксперимента на опытной установке.

С. О. Непряхин – проведение компьютерных расчетов.

Received 15.03.2023

Revised 23.11.2023

Accepted 19.02.2024

Поступила в редакцию 15.03.2023

После доработки 23.11.2023

Принята к публикации 19.02.2024

INNOVATION IN METALLURGICAL
INDUSTRIAL AND LABORATORY EQUIPMENT,
TECHNOLOGIES AND MATERIALSИННОВАЦИИ В МЕТАЛЛУРГИЧЕСКОМ
ПРОМЫШЛЕННОМ И ЛАБОРАТОРНОМ
ОБОРУДОВАНИИ, ТЕХНОЛОГИЯХ И МАТЕРИАЛАХ

UDC 621.74.045

DOI 10.17073/0368-0797-2024-4-463-470



Original article

Оригинальная статья

STRESS-STRAIN STATE OF CERAMIC SHELL MOLD DURING FORMATION OF SPHERICAL STEEL CASTING IN IT. PART 2

V. I. Odinokov, A. I. Evstigneev[✉], E. A. Dmitriev,
A. N. Namokonov, A. A. Evstigneeva, D. V. Chernyshova

Komsomolsk-na-Amure State University (27 Lenina Ave., Komsomolsk-on-Amur, Khabarovsk Territory 681013, Russian Federation)

✉ diss@knastu.ru

Abstract. The paper presents the results of numerical calculations of the solution to the problem of modeling the process of possible cracking in a spherical shell mold when pouring liquid steel into it and cooling the solidifying casting. The numerical scheme of the axisymmetric problem and the algorithm for its solution were given in Part 1. The crack resistance is estimated by magnitude of the normal stresses in the ceramic shell during its co-cooling with a solidifying casting. The results detailed analysis considered: fields of displacement, stresses, and temperatures both on spherical surface and in growing crust of solidified metal. The solution took into account the change in the shear modulus of the mold material from temperature, and an assessment of this refinement was given. The problem was solved in two ways. The first – with a constant shift modulus of the shell mold; the second – with its temperature-dependent shift modulus. There is a significant difference between these variants in terms of magnitude of the normal stresses arising in the shell mold. The authors analyzed resistance of the shell mold spherical geometry to external influences from its support filler and filling funnel. The problem of determining the contact and free surfaces at the boundary of the shell mold and support filler was solved. The results are presented graphically in the form of diagrams of stresses and temperatures over the studied area in its different sections and time intervals for cooling of the growing metal crust. The role of compressive normal stresses σ_{22} , σ_{33} on the surface of contact of the shell mold with liquid metal at the initial moment of cooling on probability of cracking in a spherical mold is shown. The level of strain-stress state in a spherical shell mold when cooling a steel casting in it is significantly determined by dependence of shift modulus of the shell mold on temperature.

Keywords: investment casting, shell mold, stressed state, modeling, cracking

Acknowledgements: The research was supported by the Russian Science Foundation, grant No. 24-29-00214, <https://rscf.ru/project/24-29-00214/>.

For citation: Odinokov V.I., Evstigneev A.I., Dmitriev E.A., Namokonov A.N., Evstigneeva A.A. Chernyshova D.V. Stress-strain state of ceramic shell mold during formation of spherical steel casting in it. Part 2. *Izvestiya. Ferrous Metallurgy*. 2024;67(4):463–470. <https://doi.org/10.17073/0368-0797-2024-4-463-470>

НАПРЯЖЕННО-ДЕФОРМИРОВАННОЕ СОСТОЯНИЕ КЕРАМИЧЕСКОЙ ОБОЛОЧКОВОЙ ФОРМЫ ПРИ ФОРМИРОВАНИИ В НЕЙ СТАЛЬНОЙ ШАРООБРАЗНОЙ ОТЛИВКИ. ЧАСТЬ 2

В. И. Одиноков, А. И. Евстигнеев[✉], Э. А. Дмитриев,
А. Н. Намоконов, А. А. Евстигнеева, Д. В. Чернышова

Комсомольский-на-Амуре государственный университет (Россия, 681013, Хабаровский край, Комсомольск-на-Амуре, пр. Ленина, 27)

✉ diss@knastu.ru

Аннотация. В статье приведены результаты численного решения задачи по моделированию процесса возможного трещинообразования в оболочковой форме (ОФ) шарообразной конфигурации при заливке в нее жидкой стали и охлаждении затвердевающей отливки. Численная схема осесимметричной задачи и алгоритм решения были приведены в части 1. Трещиностойкость оценивается

по величине нормальных напряжений в керамической ОФ в процессе ее совместного охлаждения с затвердевающей отливкой. При детальном анализе результатов были учтены поля перемещений, напряжений, температур как в сферической ОФ, так и в нарастающей корочке затвердевшего металла. При решении учитывалось изменение модуля сдвига материала формы от температуры, и была дана оценка этого уточнения. Задачу решали двумя способами. Первый – с постоянным модулем сдвига ОФ; второй – с модулем сдвига ОФ, зависящим от температуры. Между этими вариантами есть существенная разница в величине нормальных напряжений, возникающих в ОФ. Авторы проанализировали стойкости ОФ сферической геометрии от внешних воздействий со стороны опорного наполнителя (ОН) оболочковой формы и заливочной воронки. Была решена задача по определению контактной и свободной поверхностей на границе ОФ и ОН. Результаты решения задачи представлены графически в виде эпюр напряжений, температур по исследуемой области в разных ее сечениях и временных интервалах охлаждения ОФ и нарастающей корочки металла. Показана роль сжимающих нормальных напряжений σ_{22} , σ_{33} на поверхности соприкосновения ОФ с жидким металлом в начальный момент охлаждения на вероятность трещинообразования в сферической форме. Уровень напряженно-деформированного состояния в сферической ОФ при охлаждении в ней стальной отливки существенно определяется зависимостью модуля сдвига ОФ от температуры.

Ключевые слова: литье по выплавляемым моделям, оболочковая форма, напряженное состояние, моделирование, трещинообразование

Благодарности: Исследование выполнено за счет гранта Российского фонда № 24-29-00214, <https://rscf.ru/project/24-29-00214/>.

Для цитирования: Одинокое В.И., Евстигнеев А.И., Дмитриев Э.А., Намоконов А.Н., Евстигнеева А.А., Чернышова Д.В. Напряженно-деформированное состояние керамической оболочковой формы при формировании в ней стальной шарообразной отливки. Часть 2. *Известия вузов. Черная металлургия*. 2024;67(4):463–470. <https://doi.org/10.17073/0368-0797-2024-4-463-470>

INTRODUCTION

Previous studies on the influence of the stress-strain state (SSS) on the crack resistance of shell molds (SM) during the pouring of liquid metal and subsequent cooling with the solidifying casting were conducted using shell molds for investment casting (IC) in the form of risers with both cylindrical and spherical (sump) shapes. Numerous theoretical and experimental investigations have been carried out to identify the features of the SSS in ceramic shell molds and the resulting castings in investment casting. These studies examined various factors, including the materials used in the investment models [1; 2], the shape and geometry of the SM [3; 4], the mold wall thickness [5; 6], the mold material [7; 8], the geometry of the castings [9 – 11], methods for testing mold strength, and more [12; 13].

Mathematical modeling of these processes has also been presented in other works, covering modeling methods [14], research [15 – 17], numerical modeling [18 – 20], specialized mathematical models [21 – 23], and software tools [24; 25].

The production of spherical and globular IC castings, and consequently the resistance of the SM to cracking during the formation of such castings, is of both scientific and practical interest. The materials in this study are focused on addressing this issue.

In [26], the general approach to constructing a mathematical model for determining the SSS and temperature in an SM during the cooling of a spherical casting was presented, along with the numerical scheme and algorithm for solving the problem using developed software packages [27; 28]. This study presents the results of theoretical and numerical research aimed at solving the outlined problem.

MAIN BODY

In [26], the general problem of cooling a spherical casting in a shell mold was described.

Fig. 1 illustrates the computational scheme of the process under study, considering axial symmetry (where the angle α defines the size of the gating window, and the angle φ defines the extent of the SM's coverage by the supporting filler (SF)).

Initial date

Geometric parameters: $S = 5$ mm, $R_1 = 20$ mm.

Time intervals $\Delta\tau_n$: 0.1; 1.0; 2.0; 4.0; 5.0; 5.0; 5.0; 10.0; 10.0; 1.0; 2.0; 5.0; 1.0; 1.0; 3.0; 3.0; 5.0; 10.0; 10.0 s; the friction parameter on surface S_3 (Fig. 1) is $\psi = 0.001$.

Domain partitioning: $N_1 \times N_2 = 10 \times 30$.

Accepted physical parameters of the cast steel at a temperature of $\theta > 1000$ °C ($\theta_m^* = 1500$ °C): $G = 1000$ kg/mm² (shear modulus); $\alpha = 12 \cdot 10^{-6}$ °C⁻¹ (coefficient of linear expansion); $\lambda = 0.0298$ W/(mm·°C) (thermal conductivity coefficient); $L = 270 \cdot 10^3$ J/kg (latent heat of fusion); $C = 444$ J/(kg·°C) (specific heat capacity); $\gamma = 7.80 \cdot 10^{-6}$ kg/mm³ (density); $\theta_s = 1450$ °C (solidification temperature).

Physical properties of the ceramic mold: $G_m = 2910$ kg/mm²; $\alpha = 0.51 \cdot 10^{-6}$ °C⁻¹; $\lambda = 0.000812$ W/(mm·°C); $C = 840$ J/(kg·°C); $\gamma = 2.0 \cdot 10^{-6}$ kg/mm³.

Some theoretical studies [29] have shown that during the cooling of steel in an SM with α angles of 10 and 30° and $\varphi = (180^\circ - \alpha)$, significant compressive stresses σ_{22} and σ_{33} can occur, potentially exceeding the compressive strength of the ceramic material. When $\alpha = 30^\circ$, the stresses σ_{ii} , $i = 2, 3$ are slightly lower in absolute value

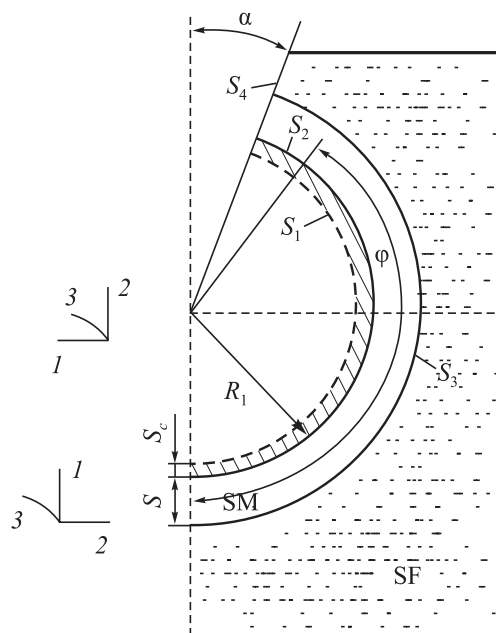


Fig. 1. Calculation scheme of a spherical ceramic shell mold molded in support filler and filled with liquid metal, taking into account axial symmetry:

LM – liquid metal; TM – solid metal; SM – shell mold;
SF – support filler; S_1 – inner contact surface of liquid and solidified metal; S_2 – inner contact surface of solidified metal and shell mold; S_3 – outer surface of shell mold; S_4 – free surface of the end face of casting cup; R_1 – radius of spherical casting; S – thickness of shell mold; S_T – thickness of solidified metal crust; α – slope angle of funnel; φ – angle of enclosing surface of shell mold with a support filler

Рис. 1. Расчетная схема шарообразной ОФ,

заформованной в опорный наполнитель и залитой жидким металлом, с учетом осевой симметрии:

LM – жидкий металл; TM – твердый металл;

SF – оболочковая форма; TM – опорный наполнитель;

S_1 – внутренняя поверхность контакта жидкого и затвердевшего металла; S_2 – внутренняя поверхность контакта затвердевшего металла и оболочковой формы; S_3 – внешняя поверхность оболочковой формы; S_4 – свободная поверхность торца литниковой чаши ОФ; R_1 – радиус шарообразной отливки;

S – толщина оболочковой формы; S_T – толщина корочки затвердевшего металла; α – угол наклона литниковой воронки;

φ – угол охвата поверхности оболочковой формы опорным наполнителем

than at $\alpha = 10^\circ$. Fig. 2 shows the distribution of normal stresses σ_{ii} in the SM at $\alpha = 10^\circ$: (a) after 7.1 s of cooling, (b) after 51.1 s.

Fig. 3 illustrates the distribution of stresses σ_{22} and σ_{33} in the solidified metal shell after 60.1 s of cooling; solid lines represent the distributions at $\alpha = 30^\circ$, while dashed lines represent those at $\alpha = 10^\circ$.

The values of σ_{22} and σ_{33} on the surface adjacent to the liquid metal are greater (in magnitude) than on the surface of the SM, which is explained by the constant shear modulus G_m of the forming solid metal (1000 kg/mm²), independent of temperature. As in the SM, the stresses σ_{22} and σ_{33} are compressive, and at $\alpha = 10^\circ$, they are higher than at $\alpha = 30^\circ$.

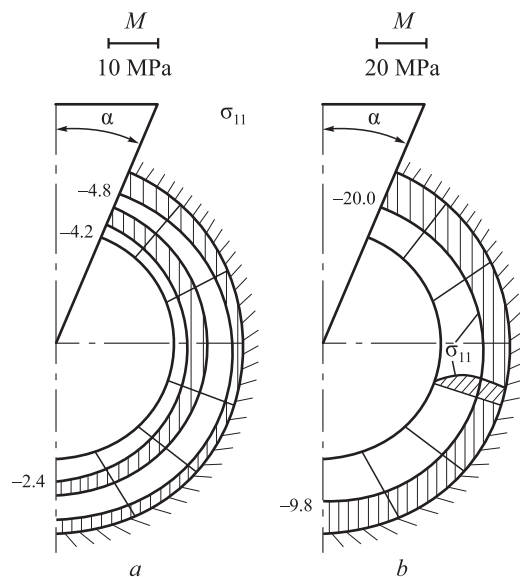


Fig. 2. Diagrams of normal stresses σ_{11} in shell mold at $\alpha = 10^\circ$ and time of casting cooling 7.1 s (a) and 51.1 s (b)

Рис. 2. Эпюры нормальных напряжений σ_{11} в ОФ при $\alpha = 10^\circ$ при времени охлаждения отливки 7,1 с (a) и 51,1 с (b)

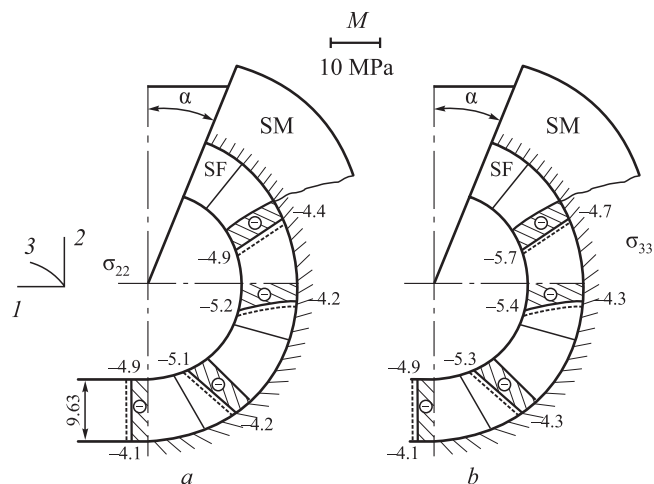


Fig. 3. Diagrams of normal stresses σ_{22} (a) and σ_{33} (b) in forming metal crust at $\alpha = 30^\circ$ (solid lines) and $\alpha = 10^\circ$ (dashed lines) and time of casting cooling 60.1 s

Рис. 3. Эпюры нормальных напряжений σ_{22} (a) и σ_{33} (b) в образующей корочки металла при $\alpha = 30^\circ$ (сплошные линии) и $\alpha = 10^\circ$ (штриховые линии) и времени охлаждения отливки 60,1 с

Fig. 4, a shows the distribution of stresses σ_{11} in the solidified metal skin after 60.1 s. The stresses σ_{11} are compressive throughout the cross-section: solid lines indicate σ_{11} at $\alpha = 30^\circ$, while dashed lines show them at $\alpha = 10^\circ$.

Fig. 4, b shows the growth curves of the skin thickness (S) and the stress σ_{33} over time. As the angle α increases, the normal stresses decrease slightly (in magnitude).

Further increasing α is unnecessary, as the metal skin continues to grow with only minor changes in normal stresses.

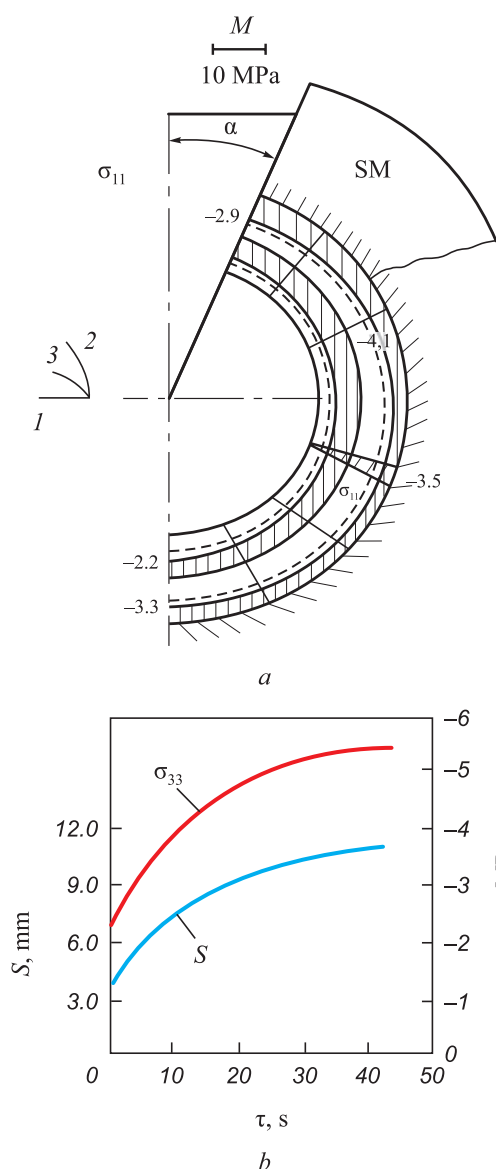


Fig. 4. Diagrams of normal stresses σ_{11} (a) in crystallized metal crust after casting cooling for 60.1 s and growth curves of metal crust (S) and stresses σ_{33} (b) with cooling time

Рис. 4. Эпюры нормальных напряжений σ_{11} (a) в закристаллизовавшейся корочке металла через время охлаждения отливки 60,1 с и кривые роста величины корочки металла (S) и напряжений σ_{33} (b) со временем охлаждения

The results were obtained assuming a constant (average) shear modulus for the SM (G_m).

As indicated in [29], the temperature in the SM adjacent to the solidifying metal is very high (around 1300 °C). At this temperature, the ceramic is practically in a softened state, meaning the shear modulus in this area will be much lower than the average value of G_m for the shell mold. We will use experimental data (Fig. 5) obtained in [30] from testing ceramic samples made from a binder material ($\text{SiO}_2 + \text{MgPO}_4$).

Approximating the results presented in Fig. 5, we obtain:

$$G_m = 6412 - 6.37\theta, \text{ kg/mm}^2 \text{ for } 300^\circ\text{C} < \theta < 1000^\circ\text{C};$$

$$G_m = 40 \text{ kg/mm}^2 \text{ for } \theta \geq 1000^\circ\text{C};$$

$$G_m = 4500 \text{ kg/mm}^2 \text{ for } \theta < 300^\circ\text{C}.$$

The results of the solution with a temperature-dependent shear modulus of the SM are shown in Fig. 6 at $\alpha = 10^\circ$ as distributions of σ_{ii} , $i = 1, 2, 3$ for $\tau = 1.12$ s (solid lines); $\tau = 7.12$ s (dashed lines).

During thermal shock and cooling at $\tau = 1.12$ s, the stresses σ_{22} and σ_{33} have the highest values (in absolute terms) in the SM's contact zone with the metal, but they change sharply with cooling time. All normal stresses are compressive. The stresses σ_{33} in the forming skin ($S = 6$ mm) after $\tau = 7.12$ s are shown in Fig. 7.

With further cooling, the stresses σ_{ii} decrease.

The most critical period for failure is the initial cooling phase ($0 < \tau < 8$ s) (Fig. 6).

Figs. 8 and 9 show the calculation results for $\alpha = 30^\circ$, $\tau = 1.12$ s (solid lines); $\tau = 7.12$ s (dashed lines).

As seen, the pattern is approximately the same, but the values of σ_{ii} , $i = 1, 2, 3$ are slightly lower than at

$\text{SiO}_2 + \text{MgPO}_4$				
T	E	$Et/E20$	G , MPa	Vol. expansion coefficient
20	11250000000	1.0000	45,000	4.44444 E-06
100	11250000000	1.0000	45,000	4.44444 E-06
200	11250000000	1.0000	45,000	4.44444 E-06
300	11250000000	1.0000	45,000	4.44444 E-06
400	9642857143	0.8571	38,571	5.18519 E-06
500	8437500000	0.7500	33,750	5.92593 E-06
600	5625000000	0.5000	22,500	8.88889 E-06
700	4218750000	0.3750	16,875	1.18519 E-05
800	2596153846	0.2308	10,385	1.92593 E-05
900	1687500000	0.1500	6750	2.96296 E-05
1000	96428571	0.0086	386	5.18519 E-04
1100	61363636	0.0055	245	8.14815 E-04

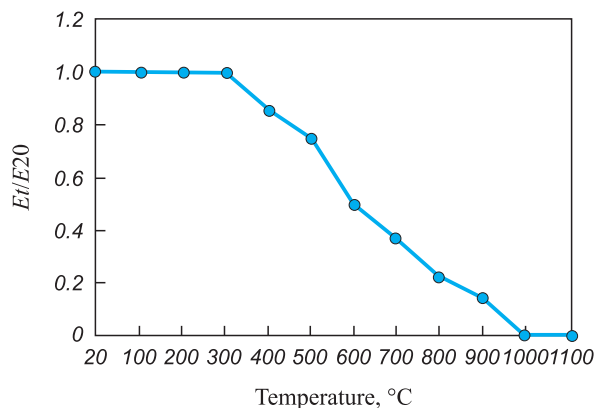


Fig. 5. Experimental data on tests of ceramic samples made of a binder ($\text{SiO}_2 + \text{MgPO}_4$)

Рис. 5. Экспериментальные данные при испытании керамических образцов, выполненных из связующего материала ($\text{SiO}_2 + \text{MgPO}_4$)

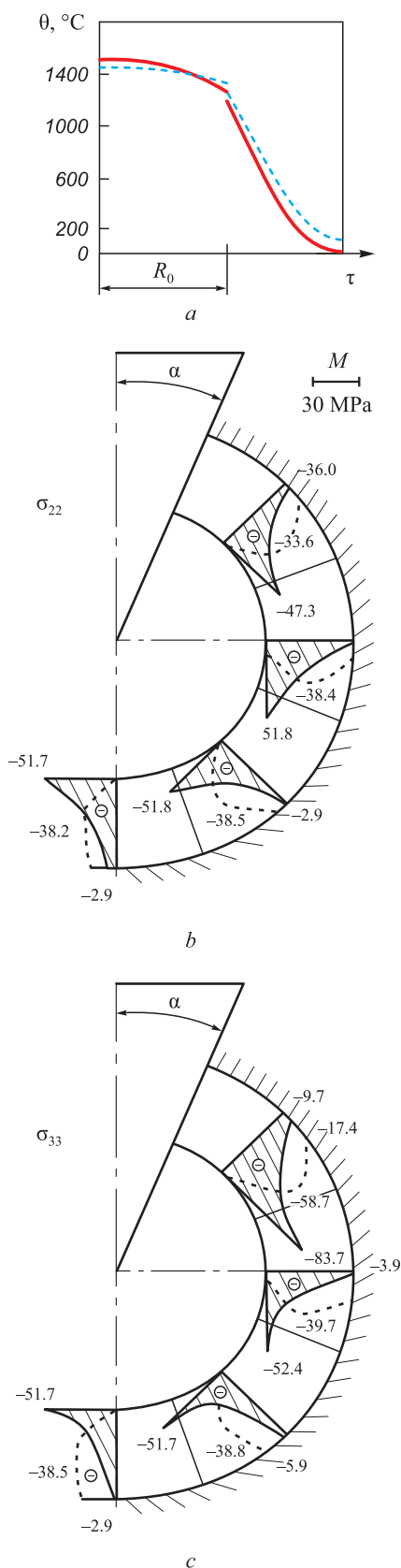


Fig. 6. Temperatures field (a), diagrams of normal stresses σ_{22} (b) and σ_{33} (c) in ceramic mold at time of casting cooling 1.12 s (—) and 7.12 s (---)

Рис. 6. Поле температур (а), эпюры нормальных напряжений σ_{22} (b) и σ_{33} (с) в ОФ при $\alpha = 10^{\circ}$ и времени охлаждения отливки 1,12 с (—) и 7,12 с (---)

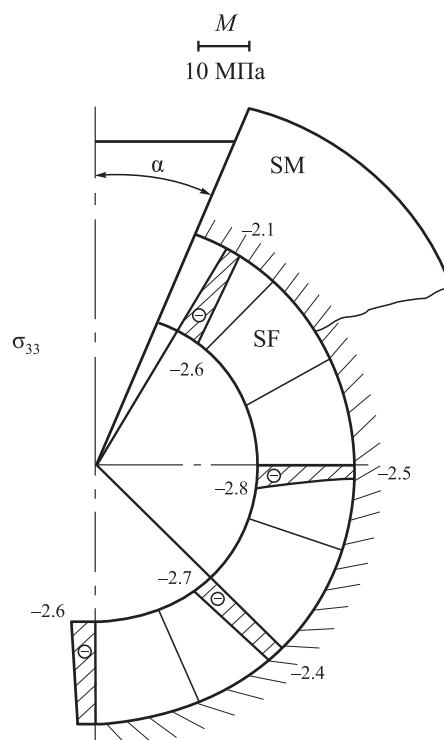


Fig. 7. Diagrams of normal stresses σ_{33} in resulting metal crust ($S = 6$ mm) at time of casting cooling 7.12 s

Рис. 7. Эпюры нормальных напряжений σ_{33} в образующейся металлической корочке ($S = 6$ мм) при времени охлаждения отливки 7,12 с

$\alpha = 10^{\circ}$, and small tensile stresses σ_{22} and σ_{33} have even appeared in the SM at the interface with the SF (Fig. 8). In the metal skin ($S = 6$ mm) after $\tau = 7.12$ s, the stresses σ_{33} are shown (Fig. 9), which are also lower than at $\alpha = 10^{\circ}$ (Fig. 3, b).

Further cooling shows that normal stresses decrease, and the distributions of σ_{ii} for $\tau = 32.12$ and 52.12 s are close to each other.

Regarding the effect of the cylindrical SM material on its durability, these results were presented in previous works by the authors, where in the case under consideration, the most critical factor for potential crack formation in the SM is the tensile normal stresses σ_{22} in the outer layer of the shell, which is in contact with the supporting filler.

Considering the temperature dependence of the shear modulus in the SM significantly affects the stress-strain state during the cooling of the steel casting within it. Under the given external conditions for the metal cooling process in a spherical SM, its durability at the initial moment of pouring is questionable.

CONCLUSIONS

A more accurate solution to the problem was obtained by considering the temperature-dependent change in

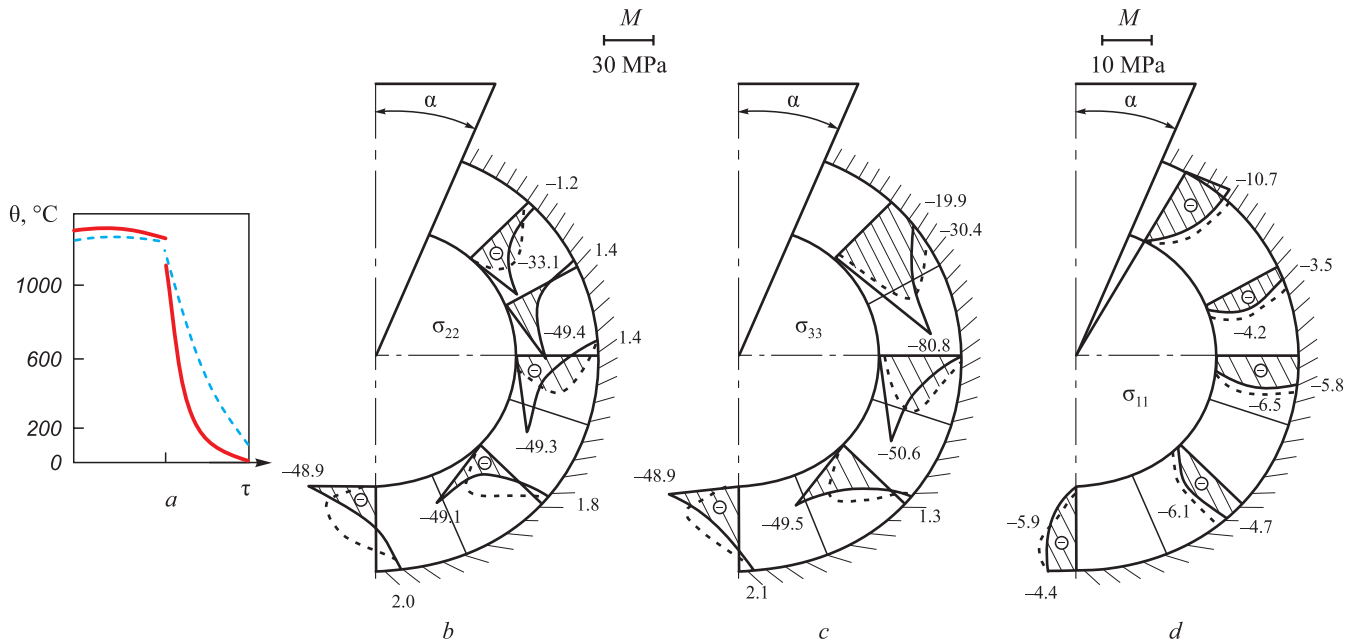


Fig. 8. Temperatures field (a), diagrams of normal stresses σ_{22} (b), σ_{33} (c) and σ_{11} (d) at $\alpha = 30^\circ$ after casting cooling for 1.12 s (—) and 7.12 s (---)

Рис. 8. Поле температур (a), эпюры нормальных напряжений σ_{22} (b), σ_{33} (c) и σ_{11} (d) в ОФ при $\alpha = 30^\circ$ через время охлаждения отливки 1,12 с (—) и 7,12 с (---)

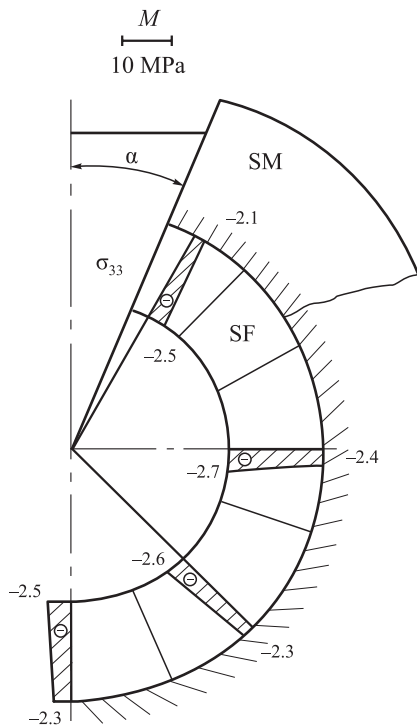


Fig. 9. Diagrams of normal stresses σ_{33} in formed metal crust after casting cooling for 7.12 s ($\alpha = 30^\circ$)

Рис. 9. Эпюры нормальных напряжений σ_{33} в образующейся корочке металла через время охлаждения отливки 7,12 с ($\alpha = 30^\circ$)

that compressive stresses σ_{22} and σ_{33} at the interface between the SM and the liquid metal at the initial cooling stage are critical. Significant compressive stresses σ_{11} (up to 10 MPa) at the interface between the SM and the SF indicate the possibility and necessity of further theoretical study of this process by modeling the surface coverage area of the SF.

REFERENCES / СПИСОК ЛИТЕРАТУРЫ

1. Bansode S.N., Phalle V.M., Mantha S.S. Optimization of process parameters to improve dimensional accuracy of investment casting using Taguchi approach. *Advances in Mechanical Engineering*. 2019;11(4):1–12. <https://doi.org/10.1177/1687814019841460>
2. Mittal Y.G., Kamble P., Gote G., Patil Y., Patel A. K., Bernard A., Karunakaran K.P. Mathematical modelling of pattern sublimation in rapid ice investment casting. *International Journal of Metalcasting*. 2022;16(2):1002–1009. <http://dx.doi.org/10.1007/s40962-021-00665-w>
3. Kanyo J.E., Schafföner S., Uwanyuze R.Sh., Leary K.S. An overview of ceramic molds for investment casting of nickel superalloys. *Journal of the European Ceramic Society*. 2020;40(15):4955–4973. <https://doi.org/10.1016/j.jeurceramsoc.2020.07.013>
4. Rafique M.M.A., Iqbal J. Modeling and simulation of heat transfer phenomena during investment casting. *International Journal of Heat and Mass Transfer*. 2009;52(7–8):2132–2139. <http://doi.org/10.1016/j.jheatmasstransfer.2008.11.007>
5. Singh R. Mathematical modeling for surface hardness in investment casting applications. *Journal of Mechanical Science and Technology*. 2012;26:3625–3629. <http://dx.doi.org/10.1007/s12206-012-0854-0>

the shear modulus of the mold material, which significantly impacted the results. The analysis of the SSS in a spherical SM during the pouring of a steel casting showed

6. Jafari H., Idris M. H., Ourdjini A. Effect of thickness and permeability of ceramic shell mould on in situ melted AZ91D investment casting. *Applied Mechanics and Materials*. 2014;465–466:1087–1092.
<http://dx.doi.org/10.4028/www.scientific.net/AMM.465-466.1087>
7. Bansode S.N., Phalle V.M., Mantha S. Taguchi approach for optimization of parameters that reduce dimensional variation in investment casting. *Archives of Foundry Engineering*. 2019;19(1):5–12.
<https://dx.doi.org/10.24425/afe.2018.125183>
8. Pattnaik S., Karunakar D.B., Jha P.K. Developments in investment casting process – A review. *Journal of Materials Processing Technology*. 2012;212(11):2332–2348.
<https://doi.org/10.1016/j.jmatprotec.2012.06.003>
9. Zhang J., Li K.W., Ye H.W., Zhang D.Q., Wu P.W. Numerical simulation of solidification process for impeller investment casting. *Applied Mechanics and Materials*. 2011;80–81: 961–964.
<https://doi.org/10.4028/www.scientific.net/AMM.80-81.961>
10. Dong Y.W., Li X.L., Zhao Q., Jun Y., Dao M. Modeling of shrinkage during investment casting of thin walled hollow turbine blades. *Journal of Materials Processing Technology*. 2017;244:190–203.
<https://doi.org/10.1016/j.jmatprotec.2017.01.005>
11. Rakoczy Ł., Cygan R. Analysis of temperature distribution in shell mould during thinwall superalloy casting and its effect on the resultant microstructure. *Archives of Civil and Mechanical Engineering*. 2018;18(4):1441–1450.
<https://doi.org/10.1016/j.acme.2018.05.008>
12. Yameng W., Zhigang L. The design of testing methods for strength of ceramic shell mold in investment casting. *Proceedings of the Asia-Pacific Conf. on Intelligent Medical 2018 & Int. Conf. on Transportation and Traffic Engineering*. 2018;336–341. <https://doi.org/10.1145/3321619.3321686>
13. Kolczyk J., Zych J. High temperature strength of ceramic moulds applied in the investment casting method. *Archives of Foundry Engineering*. 2011;11(3):121–124.
14. Anglada E., Meléndez A., Maestro L., Domínguez I. Finite element model correlation of an investment casting process. *Materials Science Forum*. 2014;797:105–110.
<http://dx.doi.org/10.4028/www.scientific.net/MSF.797.105>
15. Liu C., Sun J., Lai X., He B., Li F. Influence of complex structure on the shrinkage of part in investment casting process. *The International Journal of Advanced Manufacturing Technology*. 2015;77:1191–1203.
<https://doi.org/10.1007/s00170-014-6523-y>
16. Liu C., Wang F., Jin S., Li F., Lai X. Permafrost analysis methodology (PAM) for ceramic shell deformation in the firing process. *International Journal of Metalcasting*. 2019;13(4):953–968.
<http://dx.doi.org/10.1007/s40962-019-00317-0>
17. Everhart W.A., Lekakh S.N., Richards V., Chen J., Li H., Chandrashekhara K. Corner strength of investment casting shells. *International Journal of Metalcasting*. 2013;7:21–27.
<https://doi.org/10.1007/BF03355541>
18. Sabau A.S. Numerical simulation of the investment casting process. *Transactions of American Foundry Society*. 2005;113:407–417.
19. Zheng K., Lin Y., Chen W., Liu L. Numerical simulation and optimization of casting process of copper alloy water-meter shell. *Advances In Mechanical Engineering*. 2020;12(5):1–12.
<http://dx.doi.org/10.1177/1687814020923450>
20. Manzari M.T., Gethin D.T., Lewis R.W. Optimisation of heat transfer between casting and mould. *International Journal of Cast Metals Research*. 2000;13(4):199–206.
<https://doi.org/10.1080/13640461.2000.11819402>
21. Rafique M.M.A., Shah U. Modeling and simulation of heat transfer phenomenon related to mold heating during investment casting. *Engineering*. 2020;12(5):291–314.
<http://dx.doi.org/10.4236/eng.2020.125024>
22. Dong Y., Bu K., Zhang D. Numerical simulation of displacement field of solidification process for investment casting. In: *2008 Asia Simulation Conf. – 7th Int. Conf. on System Simulation and Scientific Computing*. 2008:715–720.
<https://doi.org/10.1109/asc-icsc.2008.4675453>
23. Upadhyay G.K., Das S., Chandra U., Paul A.J. Modelling the investment casting process: a novel approach for view factor calculations and defect prediction. *Applied Mathematical Modelling*. 1995;19(6):354–362.
[https://doi.org/10.1016/0307-904X\(95\)90001-0](https://doi.org/10.1016/0307-904X(95)90001-0)
24. Khan M.A.A., Sheikh A.K. Simulation tools in enhancing metal casting productivity and quality: A review. *Proceedings of the Institution of Mechanical Engineers, Part B: Journal of Engineering Manufacture*. 2016;230(10):1799–1817.
<https://doi.org/10.1177/0954405416640183>
25. Banerjee S., Sutradhar G. Analysis of casting defects in investment casting by simulation. *Advances in Materials, Mechanical and Industrial Engineering: Selected Contributions from the First Int. Conf. on Mechanical Engineering, Jadavpur University, Kolkata, India*. Springer International Publishing. 2019:247–271.
http://dx.doi.org/10.1007/978-3-319-96968-8_12
26. Одиноков В.И., Евстигнеев А.И., Дмитриев Э.А., Намоконов А.Н., Евстигнеева А.А., Чернышова Д.В. Напряженно-деформированное состояние керамической оболочковой формы при формировании в ней стальной шарообразной отливки. Часть 1. *Известия вузов. Черная металлургия*. 2024;67(2):211–218.
<https://doi.org/10.17073/0368-0797-2024-2-211-218>
27. Odinokov V.I., Evstigneev A.I., Dmitriev E.A., Namokov A.N., Evstigneeva A.A., Chernyshova D.V. Stress-strain state of ceramic shell mold during formation of spherical steel casting in it. Part 1. *Izvestiya. Ferrous Metallurgy*. 2024;67(2):211–218.
<https://doi.org/10.17073/0368-0797-2024-2-211-218>
Одиноков В.И., Прокудин А.Н., Сергеева А.М., Севастьянов Г.М. Свидетельство о государственной регистрации программы для ЭВМ № 2021111389. ОДИССЕЙ. Зарегистрировано в Реестре программ для ЭВМ 13.12.2012.
28. Odinokov V.I., Dmitriev E.A., Evstigneev A.I., Ivankova E.P. Certificate of state registration of the computer program No. 2021111121 “Program for mathematical modeling the optimization of choice of temperature of the support filler, material physical properties and structure of shell mold according to smelted models to increase its crack resistance when cooling the casting in it”. Registered in the Register of Computer programs on 04.11.2021. (In Russ.).
Одиноков В.И., Дмитриев Э.А., Евстигнеев А.И., Иванкова Е.П. Свидетельство о государственной регистрации программы для ЭВМ № 2021111121 «Программа математического моделирования оптимизации выбора температуры опорного наполнителя, физических свойств материала и структуры оболочковой формы по выплав-

ляемым моделям для повышения ее трещиностойкости при охлаждении в ней отливки». Зарегистрировано в Реестре программ для ЭВМ 11.04.2021 г.

29. Evstigneev A.I., Odinokov V.I., Dmitriev E.A., Chernyshova D.V., Evstigneeva A.A., Ivankova E.P. On the crack resistance of a ceramic shell mold according to smelted models when a spherical steel casting solidifies in it. *Liteinoe proizvodstvo*. 2022;(9):22–25. (In Russ.).

Евстигнеев А.И., Одинокое В.И., Дмитриев Э.А., Чернышова Д.В., Евстигнеева А.А., Иванкова Е.П. О тре-

щиностойкости керамической оболочковой формы по выплавляемым моделям при затвердевании в ней шарообразной стальной отливки. *Литейное производство*. 2022;(9):22–25.

30. Odinokov V.I., Kaplunov B.G., Peskov A.V., Bakov A.V. Mathematical Modeling of Complex Technological Processes. Moscow: Nauka; 2008:178. (In Russ.).

Одинокое В.И., Каплунов Б.Г., Песков А.В., Баков А.В. Математическое моделирование сложных технологических процессов. Москва: Наука; 2008:178.

Сведения об авторах

Information about the Authors

Валерий Иванович Одинокое, д.т.н., профессор, главный научный сотрудник Управления научно-исследовательской деятельностью, Комсомольский-на-Амуре государственный университет

ORCID: 0000-0003-0200-1675

E-mail: 79122718858@yandex.ru

Алексей Иванович Евстигнеев, д.т.н., профессор, главный научный сотрудник Управления научно-исследовательской деятельностью, Комсомольский-на-Амуре государственный университет

ORCID: 0000-0002-9594-4068

E-mail: diss@knastu.ru

Эдуард Анатольевич Дмитриев, д.т.н., доцент, ректор, Комсомольский-на-Амуре государственный университет

ORCID: 0000-0001-8023-316X

E-mail: rector@knastu.ru

Александр Николаевич Намоконов, аспирант, Комсомольский-на-Амуре государственный университет

ORCID: 0009-0003-9269-7713

E-mail: namokonovsasha@mail.ru

Анна Алексеевна Евстигнеева, студент, Комсомольский-на-Амуре государственный университет

ORCID: 0000-0003-0667-2468

E-mail: annka.ewstic@mail.ru

Дарья Витальевна Чернышова, аспирант, Комсомольский-на-Амуре государственный университет

ORCID: 0000-0001-5142-2455

E-mail: daracernysova744@gmail.com

Valerii I. Odinokov, Dr. Sci. (Eng.), Prof., Chief Researcher of the Department of Research Activities, Komsomolsk-on-Amur State University

ORCID: 0000-0003-0200-1675

E-mail: 79122718858@yandex.ru

Aleksei I. Evstigneev, Dr. Sci. (Eng.), Prof., Chief Researcher of the Department of Research Activities, Komsomolsk-on-Amur State University

ORCID: 0000-0002-9594-4068

E-mail: diss@knastu.ru

Eduard A. Dmitriev, Dr. Sci. (Eng.), Assist. Prof., Rector, Komsomolsk-on-Amur State University

ORCID: 0000-0001-8023-316X

E-mail: rector@knastu.ru

Aleksandr N. Namokonov, Postgraduate, Komsomolsk-on-Amur State University

ORCID: 0009-0003-9269-7713

E-mail: namokonovsasha@mail.ru

Anna A. Evstigneeva, Student, Komsomolsk-on-Amur State University

ORCID: 0000-0003-0667-2468

E-mail: annka.ewstic@mail.ru

Dar'ya V. Chernyshova, Postgraduate, Komsomolsk-on-Amur State University

ORCID: 0000-0001-5142-2455

E-mail: daracernysova744@gmail.com

Вклад авторов

Contribution of the Authors

В. И. Одинокое – научное руководство, анализ результатов исследований, редактирование и корректировка финальной версии статьи.

А. И. Евстигнеев – формирование концепции статьи, определение цели и задачи исследования, анализ результатов исследования, подготовка текста.

Э. А. Дмитриев – проведение расчетов, их анализ, подготовка и корректировка текста.

А. Н. Намоконов – проведение расчетов, подготовка библиографического списка, обработка графического материала.

А. А. Евстигнеева – проведение расчетов, подготовка текстового и графического материала.

Д. В. Чернышова – обработка расчетных результатов, подготовка графического материала.

V. I. Odinokov – scientific guidance, analysis of research results, editing and correction of the article final version.

A. I. Evstigneev – formation of the article concept, definition of the purpose and objectives of the study, analysis of research results, writing the text.

E. A. Dmitriev – conducting calculations and their analysis, writing and correction of the text.

A. N. Namokonov – conducting calculations, preparation of references, processing of graphic material.

A. A. Evstigneeva – conducting calculations, preparation of the text and graphic material.

D. V. Chernyshova – processing of calculated results, preparation of graphic material.

Поступила в редакцию 19.04.2024

После доработки 24.05.2024

Принята к публикации 25.05.2024

Received 19.04.2024

Revised 24.05.2024

Accepted 25.05.2024

INNOVATION IN METALLURGICAL
INDUSTRIAL AND LABORATORY EQUIPMENT,
TECHNOLOGIES AND MATERIALSИННОВАЦИИ В МЕТАЛЛУРГИЧЕСКОМ
ПРОМЫШЛЕННОМ И ЛАБОРАТОРНОМ
ОБОРУДОВАНИИ, ТЕХНОЛОГИЯХ И МАТЕРИАЛАХ

UDC 669.18

DOI 10.17073/0368-0797-2024-4-471-480



Original article

Оригинальная статья

DEVELOPMENT OF A METHODOLOGY FOR DETERMINING
THE CONTENT OF NON-METALLIC INCLUSIONS IN STEELA. O. Morozov¹ , O. A. Komolova¹, A. Yu. Em¹, A. A. Zhemkov¹,
K. V. Grigorovich¹, E. V. Yakubenko², T. I. Cherkashina², A. I. Dagman²¹ Baikov Institute of Metallurgy and Materials Science, Russian Academy of Sciences (49 Leninskii Ave., Moscow 119991, Russian Federation)³ PJSC “Novolipetsk Metallurgical Plant” (2 Metallurgov Sqr., Lipetsk 398040, Russian Federation)

morozov-morozov.an@yandex.ru

Abstract. As part of the study, a method was proposed for assessing the metal purity for non-metallic inclusions using optical emission spectrometry. To assess the content of non-metallic inclusions in the slabs, two columns of metal were selected from two slabs of low-alloy metal deoxidized with aluminum. Each column was divided into seven samples in the direction from the small radius of the continuously cast ingot to the large one. We studied these samples to assess metal contamination with non-metallic inclusions using quantitative optical metallography according to ASTM E1245-03, fractional gas analysis (FGA) and optical emission spectral analysis PDA. Analysis of the samples according to ASTM E1245-03 standard showed that in all samples the percentage of oxides and sulfides is on average 10 and 90 %, respectively. According to the results of FGA, it was concluded that such non-metallic oxide inclusions as aluminates predominate in the metal samples of both ingots. A comparison was made between the results of the determination of oxygen in non-metallic inclusions obtained by FGA method and the number of sparks in inclusions at the analysis by PDA method; analysis of the dependencies showed that there are two clearly defined point distributions. To carry out PDA analysis, a program was developed that allows determining the number of inclusions of various types and calculate their volume fraction.

Keywords: non-metallic inclusions, ASTM E1245-03, fractional gas analysis, PDA

For citation: Morozov A.O., Komolova O.A., Em A.Yu., Zhemkov A.A., Grigorovich K.V., Yakubenko E.V., Cherkashina T.I., Dagman A.I. Development of a methodology for determining the content of non-metallic inclusions in steel. *Izvestiya. Ferrous Metallurgy*. 2024;67(4):471–480. <https://doi.org/10.17073/0368-0797-2024-4-471-480>

РАЗРАБОТКА МЕТОДИКИ ОПРЕДЕЛЕНИЯ СОДЕРЖАНИЯ
НЕМЕТАЛЛИЧЕСКИХ ВКЛЮЧЕНИЙ В СТАЛИА. О. Морозов¹ , О. А. Комолова¹, А. Ю. Ем¹, А. А. Жемков¹,
К. В. Григорович¹, Е. В. Якубенко², Т. И. Черкашина², А. И. Дагман²¹ Институт металлургии и материаловедения им. А.А. Байкова РАН (Россия, 119991, Москва, Ленинский пр., 49)² ПАО «Новолипецкий металлургический комбинат» (Россия, 398040, Липецк, пл. Металлургов, 2)

morozov-morozov.an@yandex.ru

Аннотация. В рамках исследования предложена методика оценки чистоты металла по неметаллическим включениям (НВ) с использованием оптико-эмиссионной спектрометрии. Для оценки содержания НВ в сляхбах отобраны по два столбика металла от двух слывбов низколегированного металла, раскисленного алюминием. Каждый столбик поделен на семь образцов в направлении от малого радиуса непрерывнолитой заготовки к большому. На данных образцах проведены исследования по оценке загрязненности металла НВ методами количественной оптической металлографии по стандарту ASTM E1245-03, фракционного газового анализа (ФГА) и оптико-эмиссионного спектрального PDA анализа. Исследования по стандарту ASTM E1245-03 показали, что во всех образцах процентное соотношение содержания оксидов и сульфидов в среднем составляет 10 и 90 % соответственно. По результатам ФГА

сделан вывод о том, что в пробах металла обоих слитков преобладают такие оксидные НВ, как алюминаты. Проведено сравнение результатов определения содержания кислорода в НВ, полученного методом ФГА, и количества попаданий искр (спарков) во включения при анализе методом PDA. Анализ зависимостей показал, что есть два четко выраженных распределения точек. Для проведения анализа методом PDA разработана программа, позволяющая определить количество НВ различных типов в образцах металла и рассчитать их объемную долю.

Ключевые слова: неметаллические включения, ASTM E1245-03, фракционный газовый анализ, PDA

Для цитирования: Морозов А.О., Комолова О.А., Ем А.Ю., Жемков А.А., Григорович К.В., Якубенко Е.В., Черкашина Т.И., Дагман А.И. Разработка методики определения содержания неметаллических включений в стали. *Известия вузов. Черная металлургия*. 2024;67(4):471–480. <https://doi.org/10.17073/0368-0797-2024-4-471-480>

INTRODUCTION

The quality of steel is significantly influenced by non-metallic inclusions (NMI). The presence of NMI in the finished metal disrupts its homogeneity, degrades surface properties, fatigue strength, and plastic characteristics of the metal [1 – 3]. NMIs act as stress concentrators during deformation, rolling, and stamping of the steel sheet, which subsequently leads to the formation of surface defects [4 – 7]. A negative effect of increased NMI content in molten steel is also the clogging of steel casting nozzles, which drastically reduces casting speed and impairs production efficiency [8].

Various production factors affect the quantity, shape, size, and type of oxide NMIs in steel:

- chemical composition, oxidation state, temperature of the steel and slag;
- chemical and fractional composition of deoxidizers, slag-forming and alloying materials, and their introduction regime;
- inert gas blowing regime of the melt;
- vacuum treatment technology;
- chemical composition of the lining.

Inclusions larger than 50 μm are unevenly distributed and are significantly fewer in number. However, they substantially impact the quality of the finished product, as fatigue failure always occurs in the vicinity of large NMIs regardless of their composition [4; 9 – 11].

Most researchers consider NMIs as initiation sites for hydrogen cracking [12 – 14]. There is a correlation between $\text{CaO-Al}_2\text{O}_3$, $\text{MgO-Al}_2\text{O}_3$ inclusions and internal and external irregularity defects in the metal [15; 16].

The aim of this study is to compare methods for determining the contamination of metal by NMIs. One of the most common methods for quantitatively assessing NMI content in steel is metallographic analysis – comparing the sizes and shapes of NMIs found in the metal with standard scales using point-counting scales and quantitative optical microscopy as per ASTM E1245-03 standard, determining the volume fraction and size distribution of inclusions [17 – 20].

The fractional gas analysis (FGA) method allows determining the total oxygen content in various types of oxide NMIs and their volume fraction, providing a more comprehensive picture of the various types of NMIs present in the steel [21 – 23].

ASSESSING METAL CONTAMINATION BY NMIs USING OPTICAL MICROSCOPY AS PER ASTM E1245-03

The assessment of metal contamination by NMIs using optical microscopy according to ASTM E1245-03 standard was conducted with an optical microscope on a properly prepared polished specimen. Images were captured with a camera. The recognition and identification of inclusions were based on differences in grey level intensity when compared with each other and with the unetched matrix. The measurements and classification of NMIs depended on the nature (oxides, sulfides) of the identified elements in the image. These measurements were performed in each selected field of view. The polished specimen surface needed to be sufficiently large (at least 160 mm^2) to measure at least 100 fields of view at the required magnification.

For the study of NMI content, two columns from two continuously cast billets were selected. One column was taken from the middle of the continuously cast billet, and the other from the 1/4 width zone of the ingot. Each column was divided into seven samples. The sampling scheme is shown in Fig. 1. Table 1 presents the sample labeling.

Samples 1, 2, 4, 6, and 7 from each column were analyzed. Samples 3 and 5 were not examined.

To prepare samples for evaluating metal contamination by NMIs using optical microscopy as per ASTM E1245-03 standard, metal samples were ground and polished to achieve the required surface quality. The analysis per ASTM E1245-03 standard was conducted on a 200 mm^2 surface area for each sample. As a result of the analysis, two main types of NMIs were identified: oxides and sulfides. Oxide-sulfide compounds were also observed as oxysulfides. These oxysulfide inclusions were divided into two parts based on grey shades: oxide and sulfide. Table 2 presents the results

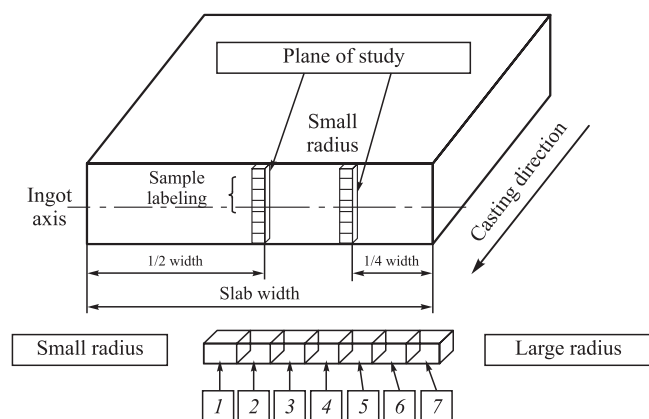


Fig. 1. Sampling scheme

Рис. 1. Схема отбора образцов

Table 1. Sample labeling

Таблица 1. Маркировка образцов

Sample label	Sample description
11X	Column from 1/2 width of slab 1, X – sample number in the column
12X	Column from 1/4 width of slab 1, X – sample number in the column
21X	Column from 1/2 width of slab 2, X – sample number in the column
22X	Column from 1/4 width of slab 2, X – sample number in the column

of the calculation of the total volume fraction of NMIs and separately the volume fractions of oxide and sulfide inclusions.

The study results indicated that the average percentage content of oxides and sulfides in the metal across all samples was 10 and 90 %, respectively. However, in samples 111 and 121, the relative oxide content was higher (31 and 17 % sulfides, respectively), indicating uneven distribution of NMIs. Uneven distribution of NMIs was also observed in samples located closer to the small radius (111, 121). The upper zone of the samples showed minimal NMI content, with their size not exceeding 10 μm , and the majority of inclusions located below 1/3 of the sample height. Thus, the upper 1/3 of the samples were cleaner in terms of inclusions than the lower 2/3. Samples (111, 112, 121, 122, 211, 212, 221, 222) closest to the small radius had a higher total volume fraction of NMIs compared to other samples. Figs. 2 – 5 compare the results of total volume fraction calculations of NMIs obtained from the same samples in the laboratories of PJSC “Novolipetsk Metallurgical Plant” (PCL and R&D) and Laboratory No. 17 of IMET RAS.

Figs. 2 – 5 show that the metal purity by NMIs in the second slab was slightly higher than in the first slab. The total volume fraction of NMIs in the metal of the second slab did not exceed 0.035 %, whereas in the first slab it varied from 0.020 to 0.055 %. It can be concluded that the second slab was more homogeneous in NMI content throughout its height and contained fewer inclusions than the first slab.

DETERMINING METAL CONTAMINATION BY NMIS USING FRACTIONAL GAS ANALYSIS (FGA)

To determine the content of oxide NMIs formed in the steel, fractional gas analysis (FGA) was conducted on the selected metal samples. The FGA method allows the determination of total oxygen and nitrogen content, the amount of oxygen in various types of oxide NMIs, and the calculation of the volume fraction of different types of oxide NMIs. The main advantage of the FGA method is that it provides rapid information on the total oxygen and nitrogen content in the metal, as well as the oxygen distributed in different types of oxide NMIs.

Table 2. Total volume fraction of non-metallic inclusions in the samples and volume fraction of oxide and sulfide inclusions, %

Таблица 2. Объемная доля всех НВ в образцах и объемная доля оксидных и сульфидных включений, %

Sample	NMIs total volume fraction	Oxide NMIs	Sulfide NMIs
111	0.0444	0.0139	0.0305
112	0.0447	0.0047	0.0400
114	0.0230	0.0020	0.0210
116	0.0220	0.0020	0.0200
117	0.0104	0.0007	0.0097
121	0.0553	0.0093	0.0460
122	0.0391	0.0031	0.0360
124	0.0379	0.0029	0.0350
126	0.0286	0.0026	0.0260
127	0.0219	0.0019	0.0200
211	0.0274	0.0024	0.0250
212	0.0298	0.0018	0.0280
214	0.0215	0.0025	0.0190
216	0.0265	0.0025	0.0240
217	0.0200	0.0020	0.0180
221	0.0250	0.0020	0.0230
222	0.0264	0.0014	0.0250
224	0.0292	0.0022	0.0270
226	0.0204	0.0024	0.0180
227	0.0186	0.0016	0.0170

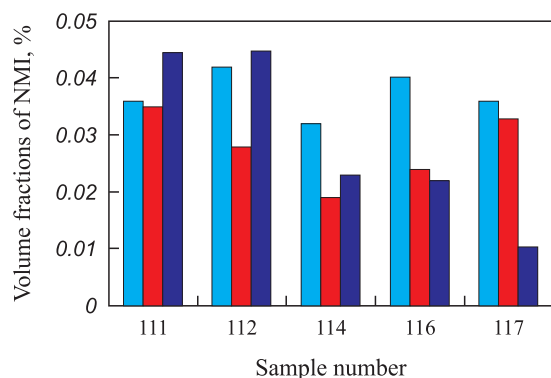


Fig. 2. Comparison of the results of calculating the volume fractions of non-metallic inclusions for the samples from the central column of 1 ingot:

— PCL; — R&D; — Laboratory No. 17

Рис. 2. Сравнения результатов расчета объемных долей НВ для образцов, отобранных от центрального столбика слитка 1:

— ЦЛК; — R&D; — Лаборатория № 17

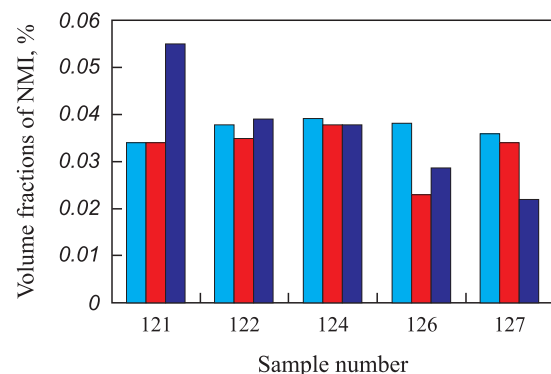


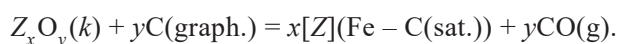
Fig. 3. Comparison of the results of calculating the volume fractions of non-metallic inclusions for the samples from the outer column of 1 ingot:

— PCL; — R&D; — Laboratory No. 17

Рис. 3. Сравнения результатов расчета объемных долей НВ для образцов, отобранных от крайнего столбика слитка 1:

— ЦЛК; — R&D; — Лаборатория № 17

FGA is a modification of the reduction melting method in a graphite crucible under a stream of carrier gas at a specified linear heating rate of the sample. The analysis method is based on the difference in the temperature dependence of the thermodynamic stability of oxides, which contain the majority of the bound oxygen in the metal. As the melt temperature increases, oxides are reduced by carbon, and oxygen is extracted from the melt as carbon monoxide according to the reaction



The reduction of oxide NMIs contained in the metal is a complex process involving several stages, such as:

- melting of the sample and spreading of the melt over the graphite crucible;

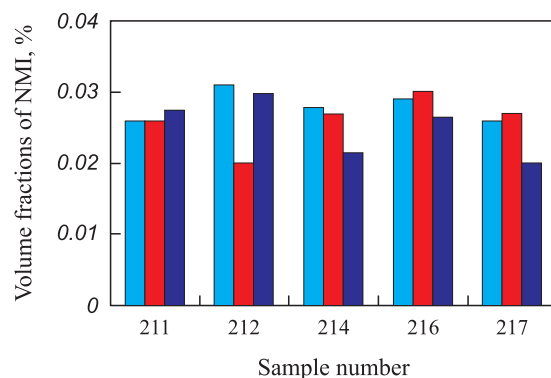


Fig. 4. Comparison of the results of calculating the volume fractions of non-metallic inclusions for the samples from the central column of 2 ingot:

— PCL; — R&D; — Laboratory No. 17

Рис. 4. Сравнения результатов расчета объемных долей НВ для образцов, отобранных от центрального столбика слитка 2:

— ЦЛК; — R&D; — Лаборатория № 17

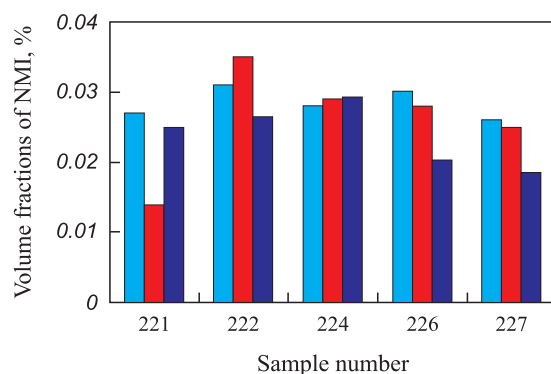


Fig. 5. Comparison of the results of calculating the volume fractions of non-metallic inclusions for the samples from the outer column of 2 ingot:

— PCL; — R&D; — Laboratory No. 17

Рис. 5. Сравнения результатов расчета объемных долей НВ для образцов, отобранных от крайнего столбика слитка 2:

— ЦЛК; — R&D; — Лаборатория № 17

- diffusion of carbon from the graphite crucible into the sample material;

- dissociation and reduction of oxide inclusions by carbon in the melt with the formation of CO molecules and bubbles;

- internal mass transfer of reaction products to the sample surface;

- removal of reaction products from the reaction surface and mass transfer in the gas phase.

A typical curve of carbon dioxide emission intensity from a metal sample depending on the melt temperature is shown in Fig. 6. The FGA results, processed using the proprietary software “Oxide Separation Pro” are shown in Fig. 7.

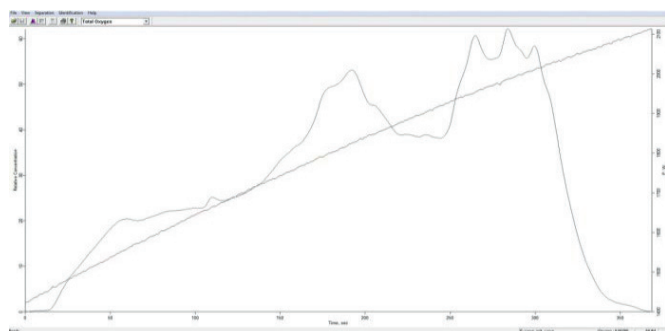


Fig. 6. Gas emission curve from the sample (evologram)

Рис. 6. Кривая газовыделения из образца (эволюграмма)

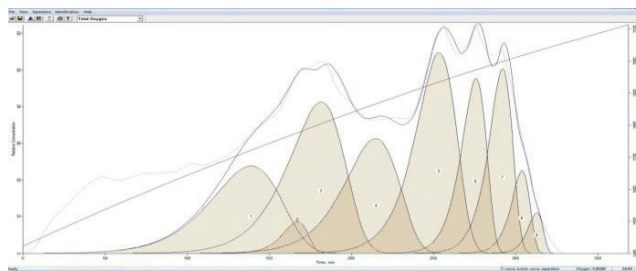


Fig. 7. Processing PGA results in Oxide Separation Pro program

Рис. 7. Обработка результатов ФГА в программе Oxide Separation Pro

For the FGA studies, three samples weighing 1.0 – 1.5 g were cut from each metal sample. Their surface was cleaned with a file to remove the oxide film and contaminants. After mechanical cleaning, the samples were

washed with alcohol and dried. The FGA results are presented in Figs. 8 – 11.

The average values and standard deviations (SD) of the results for total oxygen and nitrogen, as well as

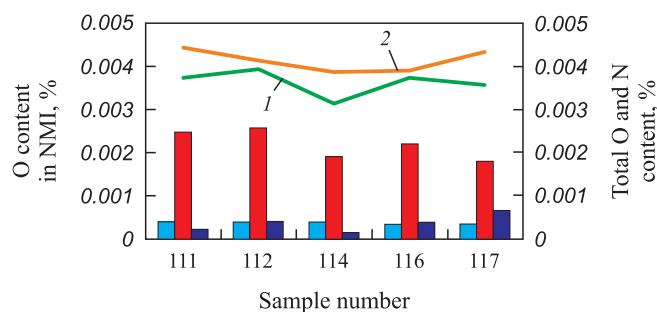


Fig. 8. FGA results of the samples from the central column of ingot 1:
— silicates; — aluminates; — spinel;
1 – oxygen; 2 – nitrogen

Рис. 8. Результаты ФГА образцов от центрального столбика слитка 1:
— силикаты; — алюминаты; — шпинель;
1 – кислород; 2 – азот

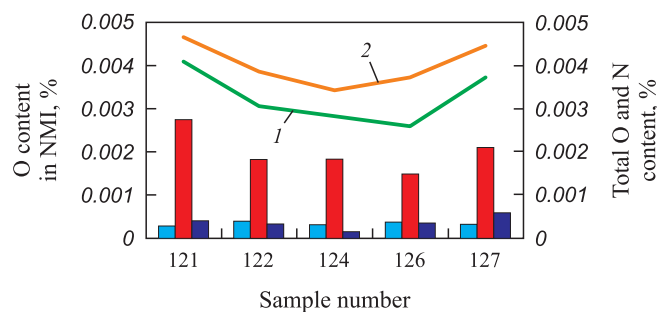


Fig. 9. FGA results of the samples from the outer column (1/4 width) of ingot 1:
— silicates; — aluminates; — spinel;
1 – oxygen; 2 – nitrogen

Рис. 9. Результаты ФГА образцов крайнего столбика (1/4 ширины) слитка 1:
— силикаты; — алюминаты; — шпинель;
1 – кислород; 2 – азот

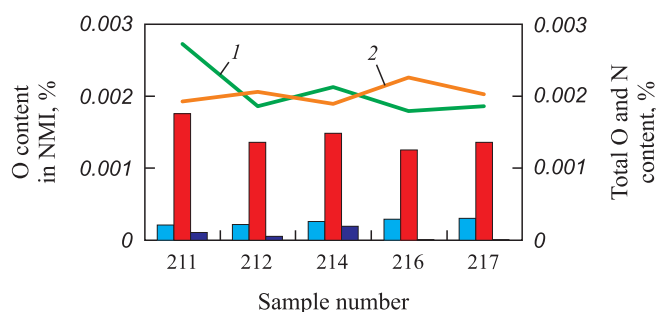


Fig. 10. FGA results of the samples from the central column of ingot 2:
— silicates; — aluminates; — spinel;
1 – oxygen; 2 – nitrogen

Рис. 10. Результаты ФГА образцов центрального столбика слитка 2:
— силикаты; — алюминаты; — шпинель;
1 – кислород; 2 – азот

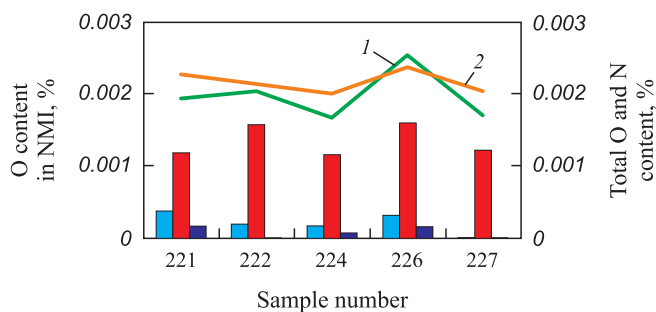


Fig. 11. FGA results of the samples from the outer column (1/4 width) of ingot 2:
— silicates; — aluminates; — spinel;
1 – oxygen; 2 – nitrogen

Рис. 11. Результаты ФГА образцов крайнего столбика (1/4 ширины) слитка 2:
— силикаты; — алюминаты; — шпинель;
1 – кислород; 2 – азот

Table 3. Average values and SD of total oxygen and nitrogen, oxygen in non-metallic inclusions for ingots 1 and 2, %

Таблица 3. Средние значения и СКО общего кислорода и азота, кислорода в НВ для слитков 1 и 2, %

Ingot	O	O (SD)	N	N (SD)	O in NMIs	O in NMIs (SD)
1	0.0034	0.0005	0.0041	0.0004	0.0028	0.0004
2	0.0020	0.0004	0.0021	0.0002	0.0016	0.0002

oxygen in NMIs, for samples from ingots 1 and 2 are presented in Table 3.

The FGA results indicate that the metal samples from both ingots predominantly contain oxide NMIs such as aluminates (Figs. 8 – 11). Fig. 8 and 9 for ingot 1 show an increasing trend in spinel content from the central part of the columns (samples 114, 124) to the large radius of the ingot (samples 116, 117, 126, 127). In the samples of ingot 2 (Figs. 10, 11), unlike ingot 1, spinel-type inclusions are virtually absent. The average total oxygen con-

tent in ingot 1 is 0.0036 % for samples 11X and 0.0033 % for samples 12X. The average nitrogen content is 0.0041 and 0.0040 %, respectively. In ingot 2, the average total oxygen content is 0.0021 % for samples 21X and 0.0020 % for samples 22X. The average nitrogen content is 0.0020 and 0.0022 %, respectively.

Based on the average oxygen, nitrogen, and oxygen in NMIs, it can be concluded that ingot 2 is cleaner than ingot 1. This corresponds to the results obtained when calculating the volume fractions of inclusions using the metallographic method. Fig. 12 and 13 present correlations between the oxygen content in NMIs obtained by the FGA method in the studied samples and the number of sparks in inclusions during optical-emission spectrometric PDA analysis for identical samples on two different spectrometers (R&D and PCL). Fig. 14 shows the correlation between the total oxygen content in NMIs and the oxygen content in aluminates obtained by the FGA method. Fig. 15 shows the correlation between the oxygen content in NMIs obtained by the FGA method and the oxide content obtained from polished specimens analyzed by optical microscopy according to ASTM E1245-03 standard in Laboratory No. 17.

Fig. 12 and 13 highlight two regions of data points. The first region corresponds to the results from ingot 2, and the second to ingot 1.

A clear correlation is observed between the oxygen content in NMIs and the oxygen content in aluminates obtained by FGA (Fig. 14).

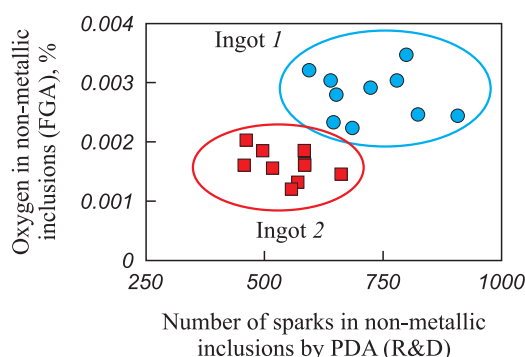


Fig. 12. Correlation between the oxygen content in non-metallic inclusions obtained by FGA method and number of sparks in inclusions by PDA (R&D) method for the samples of different ingots

Рис. 12. Корреляция между содержанием кислорода в НВ, полученного методом ФГА, и количеством попаданий спарков во включения методом PDA (R&D) для образцов разных слитков

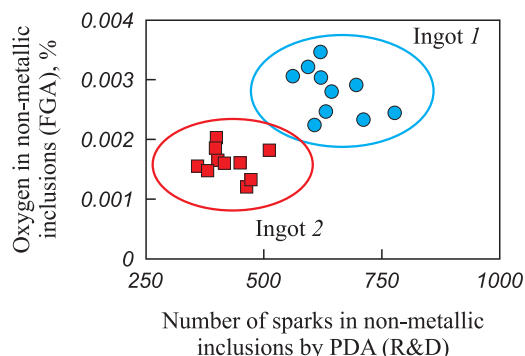


Fig. 13. Correlation between oxygen content in non-metallic inclusions obtained by FGA method and number of sparks in inclusions by PDA method (Plant Central Laboratory – PCL)

Рис. 13. Корреляция между содержанием кислорода в НВ, полученного методом ФГА, и количеством попаданий спарков во включения методом PDA (ЦЛК) для образцов разных слитков

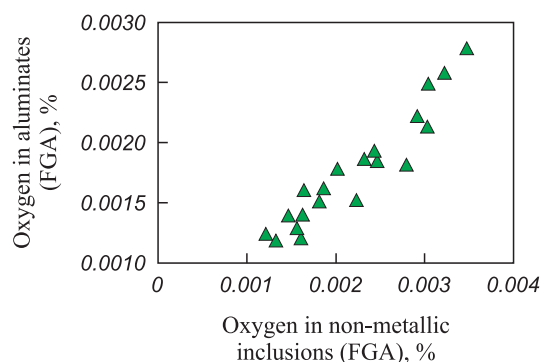


Fig. 14. Correlation between oxygen content in non-metallic inclusions and amount of oxygen in aluminates obtained by FGA method

Рис. 14. Корреляция между общим содержанием кислорода в НВ и количеством кислорода, содержащегося в алюминатах, полученных методом ФГА

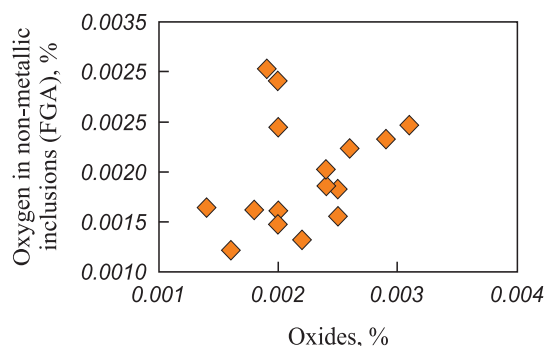


Fig. 15. Correlation between oxygen content in non-metallic inclusions obtained by FGA method and content of oxides obtained by ASTM method in Laboratory No. 17

Рис. 15. Корреляция между общим содержанием кислорода в НВ, полученного методом ФГА и содержанием оксидов, полученного методом ASTM в лаборатории № 17

An analysis of the spectral data array of metal samples on spectrometers was conducted. The files display the emission intensities of spectral wavelengths of various elements for each spark (I_{el}).

Based on the results of metal contamination assessment by NMIs according to ASTM E1245-03 standard, a correlation equation was found linking the area of NMIs with I_{el} .

Using the obtained equation, the volume fractions of NMIs for the studied samples were calculated.

All calculation variants were compared with the results of determining the volume fraction of NMIs using optical microscopy (VD-NMI – total volume fraction of NMIs based on spectral analysis data from two spectrometers at the plant) (Fig. 16).

Fig. 16 shows that the results of determining the volume fraction of NMIs in metal samples according to ASTM E1245-03 standard and the PDA method are consistent. The metal sample analyses show significant differences in NMI content in different parts of the slabs.

CONCLUSIONS

Studies of samples using quantitative optical metallography methods according to ASTM E1245-03 standard showed that in all samples, the percentage ratio of oxides to sulfides in the total volume fraction averaged 10 and 90 %, respectively. However, in samples 111 and 121, the oxide content was higher at 31 and 17 %, respectively, and these samples also exhibited uneven NMI distribution. In samples located closer to the small radius (111, 121), uneven NMI distribution was also observed. The upper zone of the samples showed minimal NMI content, with their size not exceeding 10 μm , and most inclusions were located below 1/3 of the sample height. Thus, the upper 1/3 of the samples were cleaner in terms of inclusions than the lower 2/3.

Samples (111, 112, 121, 122, 211, 212, 221, 222) closest to the small casting radius had the highest volume

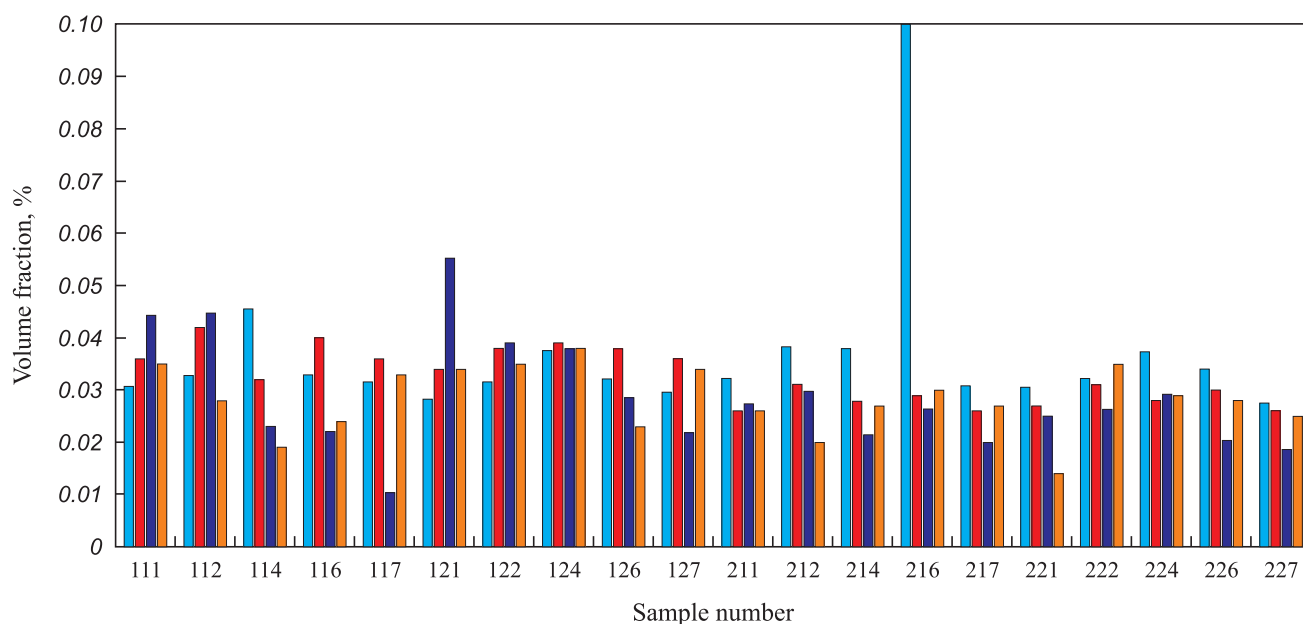


Fig. 16. Comparison of the results of determining the volume fraction of non-metallic inclusions according to ASTM E1245-03 standard (PCL – Laboratory No. 17, R&D) and by PDA method (total volume fraction of non-metallic inclusions, %):

■ – VF of NMI; ■ – PCL; ■ – Laboratory No. 17; ■ – R&D

Рис. 16. Сравнение результатов определения объемной доли НВ по стандарту ASTM E1245-03 (ЦЛК, лаборатория № 17, R&D) и методом PDA (ОД-НВ, %):

■ – ОД НВ; ■ – ЦЛК; ■ – лаборатория № 17; ■ – R&D

fraction of NMIs compared to other samples. The total volume fractions of NMIs in the samples and the separate volume fractions of oxide and sulfide inclusions were determined.

Comparison of the results of volume NMI fraction determination by quantitative optical metallography according to ASTM E1245-03 standard by PCL, R&D, and Laboratory No. 17 staff showed good measurement consistency.

To determine the content of major types of oxide NMIs in different parts of the slabs, fractional gas analysis was conducted on the selected metal samples. The analysis concluded that oxide NMIs, such as aluminates, predominantly occur in the metal samples from both ingots.

For ingot 1, there was an increasing trend in spinel content from the central part of the columns (samples 114, 124) to the large radius of the ingot (samples 116, 117, 126, 127). In the samples from ingot 2, unlike ingot 1, spinel-type inclusions were practically absent. The average total oxygen content in ingot 1 was 0.0036 % for samples 11X and 0.0033 % for samples 12X. The average nitrogen content was 0.0041 and 0.0040 %, respectively. In ingot 2, the average total oxygen content was 0.0021 % for samples 21X and 0.0020 % for samples 22X. The average nitrogen content was 0.0020 and 0.0022 %, respectively. Based on the average results for oxygen, nitrogen, and oxygen in NMIs content data, it can be concluded that ingot 2 is significantly cleaner in terms of oxide NMIs than ingot 1.

A comparison of the results of oxygen in NMIs determined by FGA and the number of spark hits in inclusions during PDA optical-emission spectral analysis (data from PJSC “NLMK” R&D and PCL) was conducted. The analysis showed two distinct distributions of data points. The first distribution corresponds to ingot 2, and the second to ingot 1. The research results also showed a clear correlation between the oxygen content in NMIs and the oxygen content in aluminates obtained by FGA.

An analysis of the spectral data array of selected metal samples, obtained on the workshop spectrometer, was conducted. For the analysis, software was developed to determine the number of inclusions of various types and calculate their volume NMI fractions. The analysis showed good consistency between the results of the PDA optical-emission spectral analysis and the quantitative optical metallography methods according to ASTM E1245-03 standard.

REFERENCES / СПИСОК ЛИТЕРАТУРЫ

1. Xue H.B., Cheng Y.F. Characterization of inclusions of X80 pipeline steel and its correlation with hydrogen-induced cracking. *Corrosion Science*. 2011;53(4):1201–1208. <http://dx.doi.org/10.1016/j.corsci.2010.12.011>
2. Huang F., Liu J., Deng Z.Y., Cheng J.H., Lu Z.H., Li X.G. Effect of microstructure and inclusions on hydrogen induced cracking susceptibility and hydrogen trapping efficiency of X120 pipeline steel. *Materials Science and Engineering*. 2010;527(26):6997–7001. <http://dx.doi.org/10.1016/j.msea.2010.07.022>
3. Kim W.K., Koh S.U., Yang B.Y., Kim K.Y. Effect of environmental and metallurgical factors on hydrogen induced cracking of HSLA steels. *Corrosion Science*. 2008;50(12):3336–3342. <https://doi.org/10.1016%2Fj.corsci.2008.09.030>
4. Bate P.S. Texture development in the cold rolling of IF steel. *Materials Science and Engineering: A*. 2004;380(1-2):365–377. <https://doi.org/10.1016/j.msea.2004.04.007>
5. Ma J., Zhang B., Xu D., Han E., Ke W. Effects of inclusion and loading direction on the fatigue behavior of hot rolled low carbon steel. *International Journal of Fatigue*. 2010;32(7):1116–1125. <http://dx.doi.org/10.1016/j.ijfatigue.2009.12.005>
6. Ikäheimonen J., Leiviskä K., Ruuska J., Matkala J. Nozzle clogging prediction in continuous casting of steel. In: *15th Triennial World Congress, July 21–26 Barcelona, Spain*. 2002:143–147.
7. Tehovnik F., Burja J., Arh B., Knap M. Submerged entry nozzle clogging during continuous casting of al-killed steel. *Metallurgija*. 2015;54(2):371–374.
8. Shchukina L.I., Tuvaev V.F., Komolova O.A., Grigorovich K.V. Investigation of the causes of reduced pourability of sheet steel at domestic enterprises. In: *Proceedings of XV Int. Congress of Steelmakers*. 2018:357–362. (In Russ.).
Щукина Л.И., Туваев В.Ф., Комолова О.А., Григорович К.В. Исследование причин снижения разливаемости листовой стали на отечественных предприятиях. *Материалы XV Международного конгресса сталеплавыльщиков. Конгресс металлургов*. 2018:357–362.
9. Xiaolei Z., Zhe S., Guifang Z. The evolution of non-metallic inclusions in IF steel. *Applied Mechanics and Materials*. 2015;696:62–65. <http://dx.doi.org/10.4028/www.scientific.net/AMM.696.62>
10. Zaitsev A.I., Rodionova I.G., Khoroshilov A.D., Mezin F.I., Semernin G.V., Mishnev P.A., Zhironkin M.V., Bikin K.B. Analysis of surface defects occurrence in cold-rolled products from IF-steels. *Elektrometallurgiya*. 2012;(7):36–40. (In Russ.).
Зайцев А.И., Родионова И.Г., Хорошилов А.Д., Мезин Ф.И., Семернин Г.В., Мишнев П.А., Жиронкин М.В., Бикин К.Б. Анализ возникновения поверхностных дефектов в холоднокатаных изделиях из IF-сталей. *Электromеталлургия*. 2012;(7):36–40.
11. Shiozawa K., Lu L. Effect of non-metallic inclusion size and residual stresses on gigacycle fatigue properties in high strength steel. *Advanced Materials Research*. 2008;44–46:33–42. <https://doi.org/10.4028/www.scientific.net/AMR.44-46.33>
12. Liu Z.Y., Li X. G., Du C. W., Lu L., Zhang Y. R., Cheng Y.F. Effect of inclusions on initiation of stress corrosion cracks in X70 pipeline steel in an acidic soil environment. *Corrosion Science*. 2009;51(4):895–900. <https://doi.org/10.1016/j.corsci.2009.01.007>
13. Maiti R., Hawbolt E.B. The effect of inclusion parameters on the fracture toughness of two X-70 Pipeline steels. *Journal of Materials for Energy Systems*. 1985;6(4):242–250. <https://doi.org/10.1007/BF02833513>
14. Dong C.F., Liu Z.Y., Li X.G., Cheng Y.F. Effects of hydrogen-charging on the susceptibility of X100 pipeline steel

- to hydrogen-induced cracking. *International Journal of Hydrogen Energy*. 2009;34(24):9879–9884.
<https://doi.org/10.1016/j.ijhydene.2009.09.090>
15. Li B.S., Zhu H.Y., Xue Z.L., Qin Z.F., Sun J. Analysis of inner fold and bulge defects on J55 steel for oil casing pipe. *AIP Advances*. 2019;9:085109.
<http://dx.doi.org/10.1063/1.5100889>
 16. Zhu H.Y., Wang L.Q., Li J.L., Zhao J.X., Yu Y. Effects of metallurgical factors on reticular crack formations in Nb-bearing pipeline steel. *High Temperature Materials and Processes*. 2020;39(1):81–87.
<http://dx.doi.org/10.1515/htmp-2020-0043>
 17. Vander-Voort G.F. Materials Characterization. “Image Analysis”: Metals Handbook. ASM, Metals Park, OH; 1986;10(9):309–322.
 18. Karasev A.V., Suito H. Analysis of size distributions of primary oxide inclusions in Fe-10 mass pct Ni-M (M = Si, Ti, Al, Zr, and Ce) alloy. *Metallurgical and Materials Transactions B*. 1999;30(2):259–270.
<https://doi.org/10.1007/s11663-999-0055-0>
 19. Ohta H., Suito H. Characteristics of particle size distribution of deoxidation products with Mg, Zr, Al, Ca, Si/Mn and Mg/Al in Fe10 mass % Ni alloy. *ISIJ International*. 2006;46(1):14–21.
<http://dx.doi.org/10.2355/isijinternational.46.14>
 20. Kanbe Y., Karasev A., Todoroki H., Jönsson P.G. Application of extreme value analysis for two- and three-dimensional determinations of the largest inclusion in metal samples. *ISIJ International*. 2011;51(4):593–602.
<http://dx.doi.org/10.2355/isijinternational.51.593>
 21. Pande M.M., Guo M. Determination of steel cleanliness in ultra-low carbon steel by pulse discrimination analysis optical emission spectroscopy technique. *ISIJ International*. 2011;51(11):1778–1787.
<http://dx.doi.org/10.2355/isijinternational.51.1778>
 22. Gorkusha D.V., Grigorovich K.V., Karasev A.V., Komolova O.A. Content modification of different types of nonmetallic inclusions during low-carbon IF steel ladle treatment. *Izvestiya. Ferrous Metallurgy*. 2019;62(5):345–352. (In Russ.). <http://dx.doi.org/10.17073/0368-0797-2019-5-345-352>
Горкуша Д.В., Григорович К.В., Карасев А.В., Комолова О.А. Изменение содержания различных типов неметаллических включений при обработке низкоуглеродистой стали в ковше. *Известия вузов. Черная металлургия*. 2019;62(5):345–352.
<http://dx.doi.org/10.17073/0368-0797-2019-5-345-352>
 23. Komolova O.A., Grigorovich K.V. Mathematical models, algorithms and software for dynamic simulation of ladle treatment technology. *Metallurgia Italiana*. 2019;111(3):20–24.

Information about the Authors

Сведения об авторах

Anton O. Morozov, Junior Researcher of the Laboratory of Materials Diagnostics, Baikov Institute of Metallurgy and Materials Science, Russian Academy of Sciences

ORCID: 0000-0002-0810-4088

E-mail: morozov-morozov.an@yandex.ru

Ol'ga A. Komolova, Cand. Sci. (Eng.), Senior Researcher of the Laboratory of Materials Diagnostics, Baikov Institute of Metallurgy and Materials Science, Russian Academy of Sciences

ORCID: 0000-0001-9517-8263

E-mail: o.a.komolova@gmail.com

Anton Yu. Em, Junior Researcher of the Laboratory of Materials Diagnostics, Baikov Institute of Metallurgy and Materials Science, Russian Academy of Sciences

ORCID: 0000-0002-9743-5996

E-mail: tony.yem1994@gmail.com

Anton A. Zhemkov, Junior Researcher of the Laboratory of Materials Diagnostics, Baikov Institute of Metallurgy and Materials Science, Russian Academy of Sciences

E-mail: zhemkov96@mail.ru

Konstantin V. Grigorovich, Academician, Dr. Sci. (Eng.), Head of the Laboratory of Materials Diagnostics, Baikov Institute of Metallurgy and Materials Science, Russian Academy of Sciences

ORCID: 0000-0002-5669-4262

E-mail: grigorov@imet.ac.ru

Elena V. Yakubenko, Head of the Department, PJSC “Novolipetsk Metallurgical Plant”

E-mail: yakubenko_ev@nlmk.com

Tat'yana I. Cherkashina, Head of the Laboratory, PJSC “Novolipetsk Metallurgical Plant”

E-mail: cherkashina_ti@nlmk.com

Aleksey I. Dagman, Cand. Sci. (Eng.), Head of the Expert Direction of the Directorate of Development of New Process Technologies, PJSC “Novolipetsk Metallurgical Plant”

E-mail: dagman_ai@nlmk.com

Антон Олегович Морозов, младший научный сотрудник лаборатории диагностики материалов, Институт металлургии и материаловедения им. А.А. Байкова РАН

ORCID: 0000-0002-0810-4088

E-mail: morozov-morozov.an@yandex.ru

Ольга Александровна Комолова, к.т.н., старший научный сотрудник лаборатории диагностики материалов, Институт металлургии и материаловедения им. А.А. Байкова РАН

ORCID: 0000-0001-9517-8263

E-mail: o.a.komolova@gmail.com

Антон Юрьевич Ем, младший научный сотрудник лаборатории диагностики материалов, Институт металлургии и материаловедения им. А.А. Байкова РАН

ORCID: 0000-0002-9743-5996

E-mail: tony.yem1994@gmail.com

Антон Алексеевич Жемков, младший научный сотрудник лаборатории диагностики материалов, Институт металлургии и материаловедения им. А.А. Байкова РАН

E-mail: zhemkov96@mail.ru

Константин Всеволодович Григорович, академик РАН, д.т.н., заведующий лабораторией диагностики материалов, Институт металлургии и материаловедения им. А.А. Байкова РАН

ORCID: 0000-0002-5669-4262

E-mail: grigorov@imet.ac.ru

Елена Всеволодовна Якубенко, начальник отдела, ПАО «Новолипецкий металлургический комбинат»

E-mail: yakubenko_ev@nlmk.com

Татьяна Игоревна Черкашина, начальник лаборатории, ПАО «Новолипецкий металлургический комбинат»

E-mail: cherkashina_ti@nlmk.com

Алексей Алексей Дагман, руководитель экспертного направления дирекции по разработке новых технологий процесса, ПАО «Новолипецкий металлургический комбинат»

E-mail: dagman_ai@nlmk.com

Contribution of the Authors

Вклад авторов

A. O. Morozov – conducting research by optical microscopy according to ASTM E1245-03 standard, preparing text, forming conclusions.

O. A. Komolova – development of an algorithm and software for processing the radiation intensities of elements, text correction.

A. Yu. Em – conducting research by fractional gas analysis.

A. A. Zhemkov – conducting research by fractional gas analysis.

K. V. Grigorovich – scientific guidance, analysis of research results, text revision, correction of conclusions.

E. V. Yakubenko – conducting research using optical emission spectral analysis.

T. I. Cherkashina – conducting research using optical emission spectral analysis.

A. I. Dagman – work organization, analysis of research results.

А. О. Морозов – проведение исследования методом оптической микроскопии по стандарту ASTM E1245-03, подготовка текста, формирование выводов.

О. А. Комолова – разработка алгоритма и программного обеспечения обработки интенсивностей излучения элементов, корректировка текста.

А. Ю. Ем – проведение исследования методом фракционного газового анализа.

А. А. Жемков – проведение исследования методом фракционного газового анализа.

К. В. Григорович – научное руководство, анализ результатов исследований, доработка текста, корректировка выводов.

Е. В. Якубенко – проведение исследований методом оптико-эмиссионного спектрального анализа.

Т. И. Черкашина – проведение исследований методом оптико-эмиссионного спектрального анализа.

А. И. Дагман – организация работ, анализ результатов исследований.

Received 14.03.2024
Revised 30.06.2024
Accepted 05.07.2024

Поступила в редакцию 14.03.2024
После доработки 30.06.2024
Принята к публикации 05.07.2024



UDC 669.187.2:621.365.21

DOI 10.17073/0368-0797-2024-4-481-489



Original article

Оригинальная статья

AUTOMATED PROCESS CONTROL IN ELECTRIC ARC FURNACES IN THE ASPECT OF DIGITAL TWIN TECHNOLOGY

A. V. Sivtsov¹, O. Yu. Sheshukov^{1, 2}, D. K. Egiazar'yan^{1, 2},
M. M. Tsymbalist¹, P. P. Orlov²

¹ Institute of Metallurgy, Ural Branch of the Russian Academy of Sciences (101 Amundsena Str., Yekaterinburg 620016, Russian Federation)

² Ural Federal University named after the first President of Russia B.N. Yeltsin (19 Mira Str., Yekaterinburg 620002, Russian Federation)

✉ aws2004@mail.ru

Abstract. An approach to managing the main modes of smelting steel in heavy-duty electric arc furnaces (EAF) using digital twin technology was defined and formulated. It was noted, that the existing power regulators do not have the function of balancing the effective power of phases and, accordingly, electric arcs because they are focused on working with a certain average value of the signal. It is proposed to use the analysis of dynamic characteristics based on instantaneous values of input parameters instead of operating ones, as it's usually implemented in most devices. This allows us to obtain more accurate data on the arc state and reduce the amount of time and computing power required to obtain a result and form recommendations. Based on the data obtained as a result of long - term observations of the heavy-duty EAF-135 operation, the relationship of the constant component of the arc voltage (CCAV) with the metal oxidation is shown. An example of its use as a criterion for controlling the melting oxidative stage is given. This reduces the consumption of electrochemical sensors for each melting in the case of serial metal production. Based on the recorded data, it is possible to timely determine the unevenness of the arc power release between the furnace electrodes and issue recommendations on gas burners operation regulating to equalize the rate of scrap melting at electrodes with less power release. The authors propose the idea of using digital twins based on models of the active power distribution across the melting bath zones and dependence of metal oxidation on oxygen blowing for monitoring and controlling the electric mode and the oxygen blast mode at the oxidative stage of the melting process. Simplified schemes of these twins are given.

Keywords: electric arc furnace, digital twin, control system, electric mode, electric arc, refining period, constant component of arc voltage

Acknowledgements: The work was performed within the state assignment of the Institute of Metallurgy of the Russian Academy of Sciences.

For citation: Sivtsov A.V., Sheshukov O.Yu., Egiazar'yan D.K., Tsymbalist M.M., Orlov P.P. Automated process control in electric arc furnaces in the aspect of digital twin technology. *Izvestiya. Ferrous Metallurgy*. 2024;67(4):481–489. <https://doi.org/10.17073/0368-0797-2024-4-481-489>

ПРОБЛЕМЫ АВТОМАТИЗИРОВАННОГО УПРАВЛЕНИЯ ТЕХНОЛОГИЧЕСКИМ ПРОЦЕССОМ В ДУГОВЫХ СТАЛЕПЛАВИЛЬНЫХ ПЕЧАХ В АСПЕКТЕ ПРИМЕНЕНИЯ ТЕХНОЛОГИИ ЦИФРОВЫХ ДВОЙНИКОВ

А. В. Сивцов¹, О. Ю. Шешуков^{1,2}, Д. К. Егизарьян^{1,2},
М. М. Цымбалист¹, П. П. Орлов²

¹ Институт металлургии Уральского отделения РАН (Россия, 620016, Екатеринбург, ул. Амундсена, 101)

² Уральский федеральный университет имени первого Президента России Б. Н. Ельцина (Россия, 620002, Екатеринбург, ул. Мира, 19)

✉ aws2004@mail.ru

Аннотация. В работе определен и сформулирован подход к управлению основными режимами выплавки стального полупродукта в сверхмощных дуговых сталеплавильных печах (ДСП) с использованием технологии цифровых двойников. Существующие регуляторы мощности не обладают функцией симметрирования полезных мощностей фаз и, соответственно, электрических дуг, так как они ориентированы на работу со средней величиной сигнала. Авторы предлагают использовать анализ динамических характеристик, построенных на мгновенных значениях входных параметров вместо действующих, как принято в большинстве реализованных устройств. Это дает возможность получить более точные данные о состоянии столба дуги и снизить количество требуемых времени и вычислительных мощностей на получение результата и формирование рекомендаций. Длительная регистрация данных при работе сверхмощной ДСП-135 показала связь постоянной составляющей напряжения дуги с окисленностью металлического расплава. Приведен пример ее использования в качестве критерия управления окислительной стадией плавки, что позволяет снизить расход электрохимических датчиков на каждую плавку в случае серийности выплавляемого металла. На основе регистрируемых данных подтверждена возможность своевременного определения неравномерности выделения дуговой мощности между электродами печи и выдачи рекомендаций по регулированию работы газогорелочных устройств для выравнивания скорости осаждения лома у электродов с меньшим выделением мощности. Авторами предложена идея использования цифровых двойников на базе моделей распределения активной мощности по зонам ванны и зависимости окисленности металла от расхода кислорода для контроля и управления электрическим режимом и режимом газового дутья на окислительной стадии процесса. Приведены упрощенные схемы этих двойников.

Ключевые слова: дуговая сталеплавильная печь, цифровой двойник, система управления, электрический режим, электрическая дуга, рафинировочный период, постоянная составляющая напряжения дуги

Благодарности: Работа выполнена в рамках государственного задания Института металлургии Уральского отделения РАН.

Для цитирования: Сивцов А.В., Шешуков О.Ю., Егизарьян Д.К., Цымбалист М.М., Орлов П.П. Проблемы автоматизированного управления технологическим процессом в дуговых сталеплавильных печах в аспекте применения технологии цифровых двойников. *Известия вузов. Черная металлургия*. 2024;67(4):481–489. <https://doi.org/10.17073/0368-0797-2024-4-481-489>

INTRODUCTION

Currently, many industries and economic sectors exhibit a clear trend towards the large-scale adoption of digital twin technology for process management [1; 2]. This approach has proven effective in numerous cases by reducing energy consumption and saving raw materials. The essence of this approach involves creating a virtual counterpart, essentially a digital twin of the controlled unit, technological mode, or process, achieved through mathematical modeling [3 – 5].

One of the key prerequisites for applying this approach is ensuring bidirectional communication between the object and its virtual counterpart. In general, this communication can be implemented either through direct impact on the furnace control elements or in the form of advice to the technologist or operator of electric arc furnaces (EAF) regarding the application of specific control actions to the process. It is quite likely that the development of automated process control systems with advisory functions can be considered part of digital twin techno-

logy, at least as prerequisites for their creation. Therefore, studying the features of processes occurring in electric arc furnaces to develop methods for controlling key technological parameters remains relevant.

In steel and cast-iron production, digital twin technologies have not yet found significant application. Preliminary work on mathematical modeling of technological processes in steelmaking [6; 7] and blast furnaces [8 – 10] could serve as the basis for their creation. One of the first significant steps in applying digital twins to EAF control is the work of scientists from Nosov Magnitogorsk State Technical University (NMSTU) [11], which describes the algorithm in detail and provides an example of its use in a power regulator.

The electric mode of EAFs changes significantly during melting [12 – 15]. As regulatory practice shows, operators and technologists very rarely use such an effective control lever as changing the voltage tap during the melting process. Having set a certain tap at the beginning of a technological stage, they operate on it almost

throughout the entire stage, regardless of changes in the technological situation and arc burning conditions.

Using the digital twin algorithm and the results of their previous research [16; 17], the authors implemented the tracking of situations where the PI controller settings are not optimal and iteratively selected new, optimal settings corresponding to the current state of the system. This significantly stabilized the electrical mode by reducing the standard deviations of currents and arc powers by 15.9 and 4.8 %, respectively, decreased the specific energy consumption (SEC) by 3 %, and reduced the furnace operating time under current by 2 min.

However, this approach involves controlling the electrode movement based on the parameters of the conditionally average phase and does not ensure the symmetry of the furnace's useful load. This leads to significant uneven distribution of arc power in the areas of individual electrodes, given the asymmetry of the short network inherent in almost all steelmaking furnaces. This issue requires a rather complex technical solution involving the organization of voltage signal sampling points directly from the furnace electrodes. It is desirable that in their further research, the authors address this aspect of optimizing the electrical mode.

METHODOLOGY FOR RECORDING SIGNALS

FROM THE RESEARCH OBJECT

The purpose of the electric mode is to deliver and rationally distribute electrical power within the working space of the furnace. In this context, the electric arc serves as the main component of the useful electrical load – an element with distinctly pronounced properties and features. The efficiency of the melting process and the main technical and economic indicators (TEI) depend on the degree of development (power) and stability of the arc discharge. The root mean square (standard) deviations of the actual values of arc current and phase power from certain values set according to the stage of the process can undoubtedly

serve successfully as indicators of discharge stability and even the thermal state of the furnace. For the digital twin model of the power regulator, this approach is acceptable. However, for the control subsystem of the electric mode, which aims to ensure the rational distribution of power in the furnace bath, more detailed information about the characteristics of the electric arc is required.

Therefore, it is proposed to use instantaneous values of input parameters in the electric mode model rather than actual values. The feasibility of this approach is confirmed by the recent interest in hybrid models of the alternating current Cassie-Mayer arc, based on solving the equations of electrical conductivity of the arc column [18 – 21]. However, using such models involves a rather complex mathematical framework and calculations, requiring significant time and computational resources. Moreover, model representations do not always correspond to the real characteristics of the object, particularly the oscillograms of the arc current and voltage. Therefore, preference should be given to analyzing dynamic characteristics constructed from instantaneous signal values:

- dynamic voltage-current characteristic (VAC-characteristic): the dependence of the active component of phase voltage on current;
- phase trajectory: dependence of the current derivative on the arc current.

Their typical forms are shown in Fig. 1.

Based on the shape of the dynamic VAC characteristic, particularly the slopes of its linear sections relative to the current axis, it is possible to uniquely determine the values of the resistances connected in series with and shunting the arc. This forms the basis of the dynamic VAC characteristic method, which is thoroughly detailed in [22].

Using this method, one can determine the parameters of the equivalent electrical circuit in the EAF's working space. These parameters include the voltage drop across the arc, the resistance connected in series with

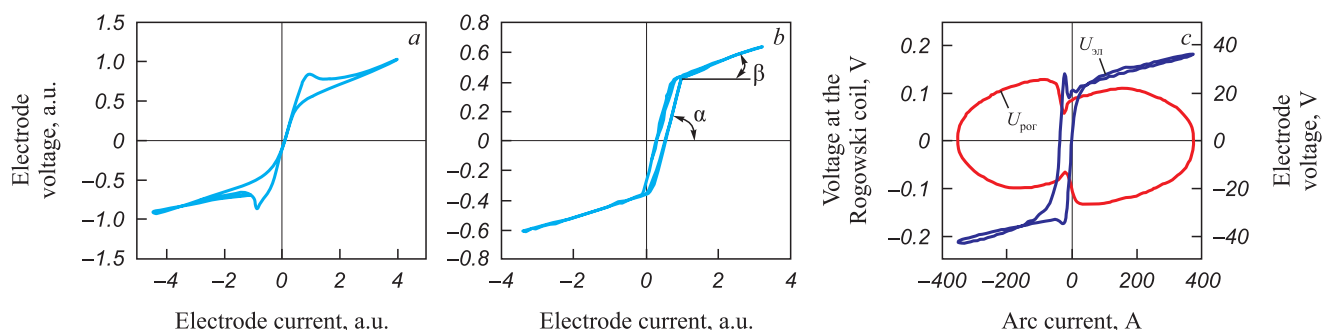


Fig. 1. Typical forms of dynamic VAC and phase trajectory of circuits with non-shunted (a) and shunted (b) electric arc; data from a real EAF during the combustion period for liquid metal (averaging) (c)

Рис. 1. Типичные формы динамической ВАХ и фазовой траектории цепей со свободно горящей (a) и шунтированной (b) электрической дугой, а также данные с реальной ДСП в период горения на жидкий металл (усреднение) (c)

it, the short network segment, and the arc power. During the refining stage, when the arcs are shunted by slag, it is possible to determine the currents in both the slag and arc branches, as well as the power released in these zones. Additionally, the analysis of the phase trajectory has practical applications in developing a mathematical model for automated control of the EAF's electric mode parameters.

Unlike the use of standard deviations of power and actual values of electrode current and phase voltage to assess the stability of the arc discharge, analyzing the forms of phase trajectories and dynamic VAC characteristics provides more illustrative information. It allows for monitoring the thermal state of the furnace during melting and timely applying control actions to the process. To assess arc plasma instability over specific time intervals, effective signal processing methods are used, including short-time Fourier transform (STFT) [22]. The arc instability index

$$\tilde{v}_a = \frac{1}{N} \sum_{i=1}^N \sqrt{\frac{u_{\phi i}^2 - \tilde{u}_{\phi i}^2}{U_1^2}} \quad (1)$$

employed by the authors represents the mean quadratic deviation of the phase voltage signal from its averaged Fourier representation $\tilde{u}_{\phi i}$ over several (8 – 12) periods, normalized to the amplitude of the first harmonic (U_1), across the digital realization ($i = 1 \dots N$) of the signal $u_{\phi i}$. The procedure for the averaged Fourier transform is described in more detail in [23].

EXPERIMENTAL TESTING OF THE METHODOLOGY

Fig. 2 shows the real and averaged dynamic VAC characteristics and phase trajectories typical for various stages of melting, from the beginning to the end of the melting process. These were obtained by sampling and analog-to-digital conversion of electrical voltage signals from the furnace transformer outputs and derivatives of currents in the electrodes, sampled using Rogowski coils. The dynamic VAC characteristic exhibits hysteresis since it is constructed for the values of the total phase voltage. It is evident that as the charge heats, melts, and forms a single bath of liquid alloy, the thermal content of the furnace increases, and the characteristics stabilize, concentrating in an increasingly narrow area.

This process is reflected in the changes in the arc instability indicators for individual phases, presented in Fig. 3. The data were obtained on a heavy-duty EAF-135 during the smelting of a steel semi-product. The charge was loaded in two stages, so the first section of the characteristic corresponds to the melting of the first batch of the charge, the second section to the melting of the second batch and the refining period. The practical significance of monitoring this indicator lies in providing advice

to the steelmaker on changing the electric mode settings, switching the voltage tap, and making decisions about turning off the furnace for loading the second batch or starting the oxidation stage of the process.

Timely decision-making will reduce the melting time and specific energy consumption (SEC). It is also noted

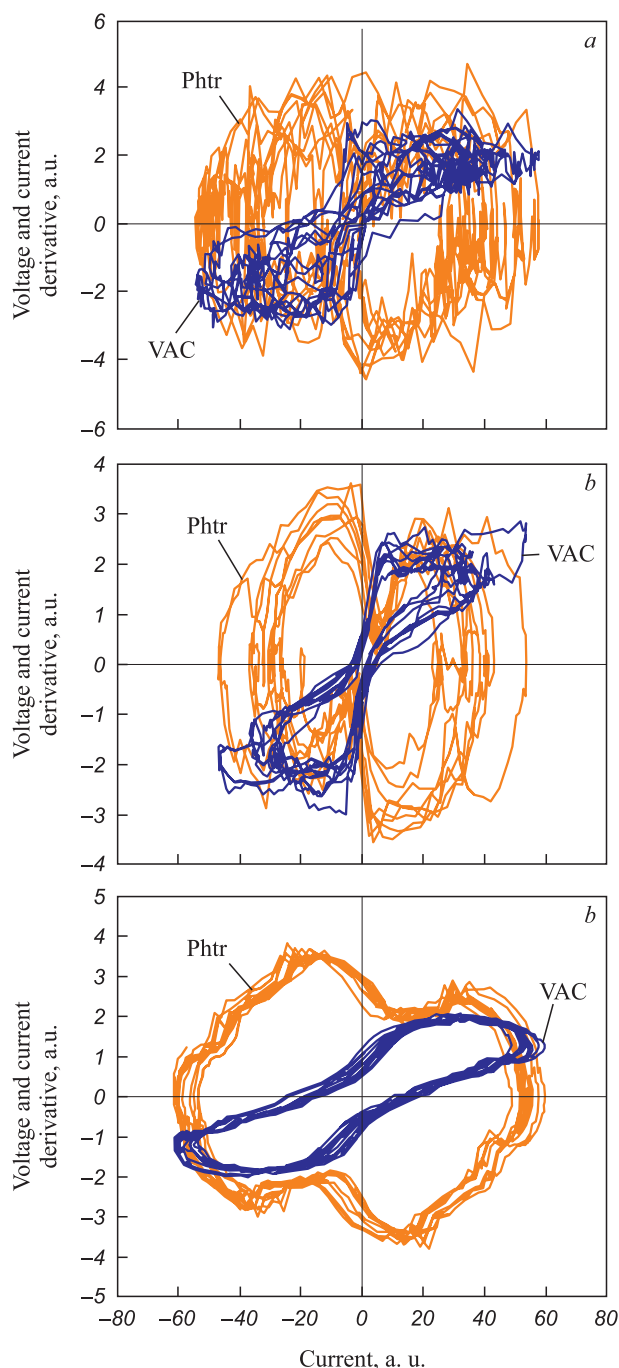


Fig. 2. Change in dynamic characteristics of a circuit with electric arc at the stages of scrap melting (a), liquid metal bath forming (b) and oxidative refining (c)

Рис. 2. Изменение динамических характеристик цепи с электрической дугой на стадиях плавления лома (a), горения дуги на ванну жидкого металла (b) и окислительного рафинирования (c)

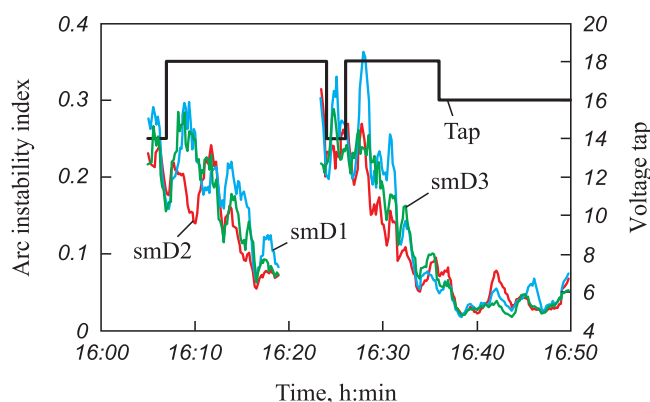


Fig. 3. Changes in arc instability index during melting

Рис. 3. Изменения показателя нестабильности дуги в ходе плавки

that there is a delay in voltage stabilization on the first phase. Due to the asymmetry of the arc power, the instability indicator reaches values characteristic of the other electrodes only after a few minutes. To compensate for the energy deficit and accelerate the melting process, it is necessary to increase the gas consumption in the burners operating in the area of the lagging phase.

Regarding the development of the digital twin for the electric mode control subsystem, its simplified schematic can be presented in Fig. 4.

According to this scheme, signals of phase voltage and currents in the electrodes (or, in the presence of Rogowski coils, the derivatives of the current) from each phase are fed into the subsystem. They are normalized, digitized using an analog-to-digital converter, subjected to discrete Fourier transform (DFT) with subsequent determination of the arc instability index, and processed using the dynamic VAC characteristic method. The output characteristics – arc power and instability index – are sent to the mode asymmetry determination block and directly to the advisory block for the technologist. The advice formed based on the state of the object includes recommendations for the operator on applying

specific control actions, such as changing the voltage tap, adjusting current setpoints (conductance or phase impedance), or altering gas flow intensity.

Regulating the electric mode is an important but not the primary task in managing the steelmaking process. The quality of the produced steel has always been the highest priority among the main production goals. With the continuously decreasing quality of scrap metal, its importance only increases.

The quality of the steel produced in heavy-duty furnaces largely depends on the oxidation period during melting. This period also impacts the energy efficiency of the process, particularly the specific energy consumption (SEC) and the furnace operating time. An under-oxidized alloy increases the phosphorus content in the final product, while excessive oxidation leads to higher consumption of ferroalloys during the ladle furnace treatment stage, extending this stage and increasing both oxygen and specific energy consumption. Therefore, continuous monitoring of the oxidation degree of the metal melt during the refining period is crucial for effective process management.

In practice, the oxidation of the metal is determined episodically (2 – 3 times per melt) using disposable electrochemical probes. Due to the irregularity of measurements and frequent probe failures, this control method can be considered as an estimate and not meeting the needs of operational control. Hence, an alternative method based on measuring an electrical parameter closely related to the oxidation of the metal is required [24; 25].

This parameter is the constant component of the arc voltage (CCAV), which arises in AC circuits due to the difference in thermionic emission currents from electrodes of different chemical compositions [26 – 29]. The thermionic emission current density is described by the Richardson-Dushman equation

$$j = AT^2 \exp\left(-\frac{\Phi_e}{kT}\right), \quad (2)$$

where A is the emission constant; Φ_e is the work function of the electron; k is the Boltzmann constant, and T is the absolute temperature.

As the equation suggests, the difference in emission currents is influenced by two factors: temperature and chemical composition. Since the electrode temperatures are limited by the sublimation of graphite and the evaporation of iron, the chemical factor – the difference in electron work functions – exerts the greatest influence on the current difference, especially since this parameter is in the exponent. Impurities significantly affect the work function. While the chemical composition of graphite does not change during melting, the metal melt always contains impurities whose concentrations vary. Thus,

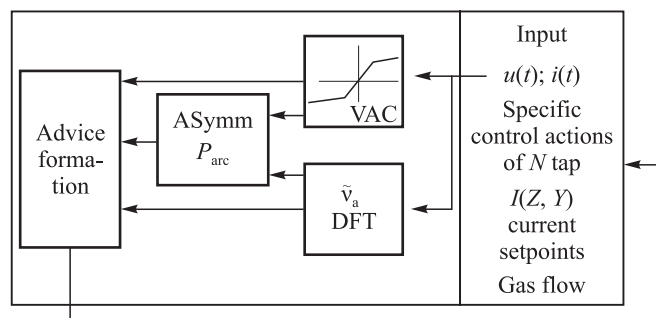


Fig. 4. Simplified block diagram of a digital twin of electrical mode control subsystem in the “Advice to the technologist” function

Рис. 4. Упрощенная блок-схема цифрового двойника подсистемы управления электрическим режимом в функции «Совет технологу»

during the oxidation stage, changes in the CCAV will most often be related to changes in the melt composition.

The refining stage of steel melting is organized such that after the melting of the scrap, slag-forming materials and a reductant, in the form of coke or anthracite, are added to the furnace. Coke is used to promote slag foaming. The dissolution of carbon in the liquid metal increases the work function of electrons from the melt, thereby reducing the CCAV. Conversely, saturating the melt with oxygen increases the CCAV.

Thus, continuous monitoring of the CCAV during the oxidation period allows for real-time assessment of the oxidation state of the metal in the furnace bath. In works [30 – 32], the authors comprehensively describe the methodology for determining oxidation based on the CCAV. Here, only a brief description of the algorithm for establishing the relationship between these characteristics is provided, along with the resulting dependence

of the metal oxidation degree on oxygen consumption (Fig. 5). Furthermore, it is shown how this can be used in the digital twin technology for the refining stage of steel melting in heavy-duty furnaces.

The foundation of the digital twin mathematical model is a statistical relationship linking the average values of CCAV and metal oxidation. As shown in [31], its graph represents a rather broad cloud of points stretched along an upward linear trend. The correlation coefficient of this relationship is low, not exceeding 0.5. Nevertheless, this approximation is used in the model as a static characteristic, serving as an initial approximation for the desired relationship.

The dependence shown in Fig. 5 initially represented a time series that was smoothed using a moving average filter, reflecting changes in CCAV during the oxidation stage of the process and approximated by an exponential function (Exp). Based on the exponential nature of the alloy decarburization process and the linearity of the oxidation process, we use linear approximations of the final segments to derive the function $[O] = f(G_{O_2})$ from the initial Exp characteristic. By accounting for changes in the oxygen lance parameters, the time axis is transformed into an oxygen consumption axis.

Individual points on the graph represent the oxidation values of the melt obtained using electrochemical sensors. It is evident that these points, while qualitatively mirroring the characteristic jump, lay significantly higher than the initial Exp curve. However, after the transformations, they nearly matched the corrected function $[O] = f(G_{O_2})$. The block diagram of the digital twin for metal oxidation control and oxygen lance regulation is presented in Fig. 6.

The digital twin receives electrical signals from all phases (instantaneous values), the oxygen consumption rate at the burners, time, and the mass of corrective charge

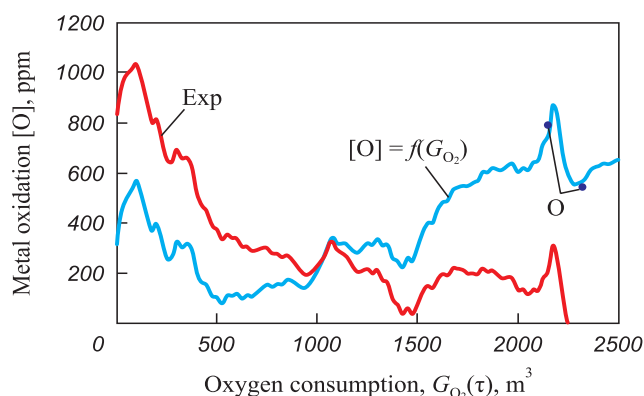


Fig. 5. Dependence of metal oxidation degree on oxygen consumption at refining stage

Рис. 5. Зависимость степени окисления металлического расплава от расхода кислорода на стадии рафинирования

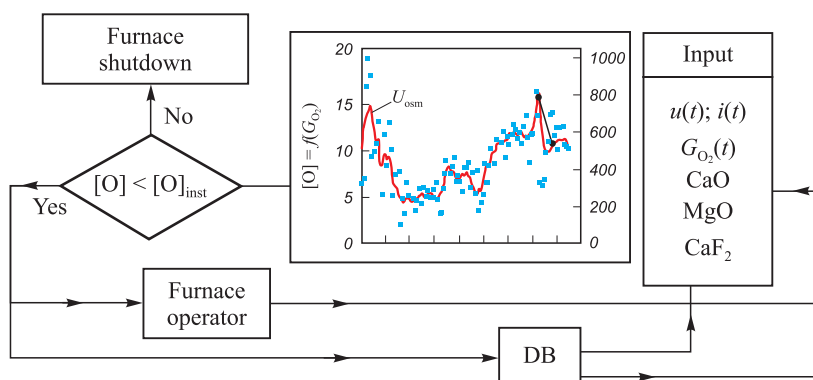


Fig. 6. Simplified block diagram of a digital twin for regulating the oxidative stage parameters:
 $u(t); i(t)$ – input electrical signals of phase voltages and electrode currents; $G_{O_2}(t)$ – oxygen consumption;
 CaO, MgO, CaF₂ – magnesia-lime additives; fluorspar; DB – database

Рис. 6. Упрощенная блок-схема цифрового двойника регулирования параметров окислительной стадии процесса:
 $u(t); i(t)$ – входные электрические сигналы фазных напряжений и токов электродов; $G_{O_2}(t)$ – расход кислорода;
 CaO, MgO, CaF₂ – магнезиально-известковые добавки, плавиковый шпат; DB – база данных

materials. The algorithm determines the oxidation level of the melt, checks if the current value meets the setpoint, and provides advice to the operator, who then decides on the control actions to take. Simultaneously, the information is recorded in a database for further statistical processing to refine the algorithm's adjustable parameters. The parameter settings should be adapted to the specific unit, considering the quality of the raw materials, furnace characteristics, the nature and magnitude of the response to control actions, and possibly the grade of the product being produced.

CONCLUSIONS

Effective management of the electric mode requires a broader approach than simply ensuring the reliable operation of the power regulator at set voltage taps and control parameter setpoints. Issues such as phase and arc active power asymmetry, which remain unresolved even with modern regulators, can be effectively addressed using a digital twin of the electric mode control subsystem. This will significantly expand both the range of controllable parameters and the functional capabilities of the control system.

The most rational way to monitor and regulate the oxidation stage of the steel semi-product melting process is by using a digital twin based on the relationship between metal oxidation and the constant component of the arc voltage, as well as analyzing its dependence on oxygen consumption by the gas burners. This approach, combined with the accumulation and systematization of statistical information in a database, will significantly reduce the system's adaptation time to a specific unit.

Digital twin technology is still a new and continuously evolving field in process and equipment management within the metallurgical complex. Its potential for saving material and energy resources and improving the technical and economic indicators of production is vast and particularly valuable as we transition from automated control systems to automatic regulators of technological modes and individual units in steelmaking production.

REFERENCES / СПИСОК ЛИТЕРАТУРЫ

1. Shvedenko V.N., Mozokhin A.E. Concept of digital twins at life cycle stages of production systems. *Scientific and Technical Journal of Information Technologies, Mechanics and Optics*. 2020;20(6):815–827. <https://doi.org/10.17586/2226-1494-2020-20-6-815-827>
2. Xiang F., Zhi Z., Jiang G. Digital twins technology and its data fusion in iron and steel product life cycle. In: *2018 IEEE 15th Int. Conf. on Networking, Sensing and Control (ICNSC)*, 27–29 March 2018. Zhuhai: 1–5. <https://doi.org/10.1109/ICNSC.2018.8361293>
3. Ueda S., Natsui S., Nogami H., Yagi J., Airuama T. Recent progress and future perspective on mathematical modeling of blast furnace. *ISIJ International*. 2010;50(7):913–923. <https://doi.org/10.2355/isijinternational.50.914>
4. Takatani K., Inada T., Ujisawa Y. Three-dimensional dynamic simulator for blast furnace. *ISIJ International*. 1999;39(1): 15–22. <https://doi.org/10.2355/isijinternational.39.15>
5. Matsuzaki S., Nishimura T., Shinotake A., Kunimoto K., Naito M., Sugiyama T. Development of mathematical model of blast furnace. *Nippon Steel Technical Report*. 2006; 94:87–95.
6. Chistyakova T.B., Novozhilova I.V., Kozlov V.V., Laktionov N.V. Software complex for control of electro-steel process in the arc furnaces. *Izvestiya SPbGTI(TU)*. 2019;51(77):82–89. (In Russ.). <https://doi.org/10.36807/1998-9849-2019-51-77-82-89>
7. Nikolaev A.A. Improving the Efficiency of Electric Arc Furnaces and Ladle Furnace Units using Advanced Algorithms for Controlling Electrical Modes: Monograph. Magnitogorsk: Nosov MSTU; 2015:161. (In Russ.).
Николаев А.А. Повышение эффективности работы дуговых сталеплавильных печей и установок ковша-печь за счет применения усовершенствованных алгоритмов управления электрическими режимами: Монография. Магнитогорск: Издательство МГТУ им. Носова; 2015:161.
8. Dmitriev A.N., Zolotykh M.O., Vit'kina G.Yu. Monitoring the Condition of Blast Furnace Refractory Lining based on Digital Technologies. Yekaterinburg: AMB; 2022:156. (In Russ.).
Дмитриев А.Н., Золотых М.О., Витькина Г.Ю. Мониторинг состояния огнеупорной футеровки горна доменной печи на основе цифровых технологий. Екатеринбург: АМБ; 2022:156.
9. Spirin N.A., Lavrov V.V., Rybolovlev V.Yu., Krasnobaev A.V., Onorin O.P., Kosachenko I.E. Model Decision Support Systems in the Automated Process Control System of Blast Furnace Melting. Yekaterinburg: UrFU; 2011:462. (In Russ.).
Спирин Н.А., Лавров В.В., Рыболовлев В.Ю., Краснобаев А.В., Онорин О.П., Косаченко И.Е. Модельные системы поддержки принятия решений в АСУ ТП доменной плавки. Екатеринбург: УрФУ; 2011:462.
10. Dmitriev A.N., Chen' K., Zolotykh M.O., Vit'kina G.Yu. Mathematical Modeling of Blast-Furnace Process. Yekaterinburg: AMB; 2023:232. (In Russ.).
Дмитриев А.Н., Чэнь К., Золотых М.О., Витькина Г.Ю. Математическое моделирование доменного процесса. Екатеринбург: АМБ; 2023:232.
11. Nikolaev A.A., Dema R.R., Tulupov P.G., Ryzhev S.S. Development of an algorithm for energy-efficient control of an arc steelmaking furnace using a digital twin. *Chernye metally*. 2023;(8):4–12. (In Russ.). <https://doi.org/10.17580/chm.2023.08.01>
Николаев А.А., Дема Р.Р., Тулупов П.Г., Рыжевол С.С. Разработка алгоритма энергоэффективного управления дуговой сталеплавильной печью с использованием цифрового двойника. *Черные металлы*. 2023;(8):4–12. <https://doi.org/10.17580/chm.2023.08.01>
12. Mironov Yu.M., Mironova A.N. Analysis of characteristics of electric arc furnaces as control objects. *Russian Electrical*

- Engineering*. 2017;88(7):395–399.
<https://doi.org/10.3103/S1068371217070124>
13. Mironov Yu.M., Mironova A.N. Analysis of electrical conditions of electric arc furnaces during different periods of melting. *Metallurgist*. 2021;65:177–184.
<https://doi.org/10.1007/s11015-021-01146-5>
 14. Raisz D., Sakulin M., Renner H., Tehlivets Y. Recognition of the operational states in electric arc furnaces. In: *Ninth Int. Conf. on Harmonics and Quality of Power. Proceedings (Cat. No.00EX441), 1–4 Oct. 2000, Orlando, Florida USA*. IEEE; 2:475–480. <https://doi.org/10.1109/ichqp.2000.897725>
 15. Zhao H., Chen F., Zhao Z. Study about the methods of electrodes motion control in the EAF based on intelligent control. In: *2010 Int. Conf. on Computer, Mechatronics, Control and Electronic Engineering 24–26 Aug. 2010 Changchun, China*. IEEE; 4:68–71. <https://doi.org/10.1109/cmce.2010.5610213>
 16. Nikolaev A.A., Kornilov G.L., Yakimov I.A. Investigation of the operating modes of electric arc furnaces in combination with static thyristor reactive power compensators. Part 2. *Elektrometallurgiya*. 2014;(6):9–13. (In Russ.).
Николаев А.А., Корнилов Г.Л., Якимов И.А. Исследование режимов работы дуговых сталеплавильных печей в комплексе со статическими тиристорными компенсаторами реактивной мощности. Часть 2. *Электрометаллургия*. 2014;(6):9–13.
 17. Kornilov G.P., Nikolaev A.A., Yachikov I.M., Yakimov I.A., Karandaev A.S. High-speed control system for the electric mode of an arc steelmaking furnace. *Izvestiya vuzov. Elektromekhanika*. 2017;60(6):45–54. (In Russ.).
<https://doi.org/10.17213/0136-3360-2017-6-45-54>
Корнилов Г.П., Николаев А.А., Ячиков И.М., Якимов И.А., Карандаев А.С. Быстродействующая система управления электрическим режимом дуговой сталеплавильной печи. *Известия вузов. Электромеханика*. 2017;60(6):45–54.
<https://doi.org/10.17213/0136-3360-2017-6-45-54>
 18. Yang F., Tang Z., Shen Y., Su L., Yang Z. Parameter determination method of cassie-mayr hybrid arc model based on magnetohydrodynamics plasma theory. *Frontiers in Energy Research*. 2022;10.
<https://doi.org/10.3389/fenrg.2022.808289>
 19. Guardado J.L., Maximov S.G., Melgoza E., Naredo J.L., Moreno P. An improved arc model before current zero based on the combined Mayr and Cassie arc models. *Transactions on Power Delivery*. 2005;20(1):138–142.
<https://doi.org/10.1109/TPWRD.2004.837814>
 20. Chittora P., Singh A., Singh M. Modeling and analysis of power quality problems in electric arc furnace. In: *Annual IEEE India Conf. (INDICON). New Delhi: 17-20 December 2015*. IEEE; 1–6. <https://doi.org/10.1109/INDICON.2015.7443638>
 21. King-Jet T., Yaoming W., Vilathgamuwa D.M. An experimentally verified hybrid Cassie-Mayr electric arc model for power electronics simulations. *IEEE Transactions on Power Electronics*. 1997;12(3):429–436.
<https://doi.org/10.1109/63.575670>
 22. Shakti P.S., Debi P.D., Santosh K.B., Nigamananda R. Instability and fault analysis of arc plasma using advanced signal processing methods. *Review of Scientific Instruments*. 2023;94(10):104710. <https://doi.org/10.1063/5.0161187>
 23. Sivtsov A.V., Sheshukov O.Yu., Tsymbalist M.M., Nekrasov I.V., Egiazar'yan D.K., Makhnutin A.V., Orlov P.P. Steel semiproduct melting intensification in electric arc furnaces using coordinated control of electric and gas conditions: II. On-line control of the state of the charge and melt zones in electric arc furnaces. *Russian Metallurgy (Metally)*. 2019;2019(6):565–569.
<https://doi.org/10.1134/S003602951906017X>
 24. Sivtsov A.V., Egiazar'yan D.K., Sheshukov O.Yu., Tsymbalist M.M., Orlov P.P., Mikheenkova M.A. Method for controlling the parameters and characteristics of an electric arc to evaluate the efficiency of using briquetted metallized scale for steel smelting. *Metallurgist*. 2022;66:11–18.
<https://doi.org/10.1007/s11015-022-01296-0>
 25. Sivtsov A.V., Sheshukov O.Yu., Tsymbalist M.M., Nekrasov I.V., Egiazar'yan D.K. The valve effect of an electric arc and problems in controlling electric-arc furnaces *Metallurgist*. 2015;59(5–6):380–385.
<https://doi.org/10.1007/s11015-015-0113-6>
 26. Nikol'skii V.N. Rectifying effect of arc of a three-phase steel-making furnace. *Elektrichestvo*. 1951;(11):34–37. (In Russ.).
Никольский В.Н. Выпрямляющее действие дуги трехфазной сталеплавильной печи. *Электричество*. 1951;(11):34–37.
 27. Markov N.A., Barannik O.V. Effect of a constant component of electrode currents on operation of an electric arc steelmaking furnace. *Elektricheskie apparaty: Tr. Kuibyshevskogo politekhnicheskogo instituta*. 1970;(2):145–150. (In Russ.).
Марков Н.А., Баранник О.В. Влияние на работу дуговой сталеплавильной электропечи постоянной составляющей токов электродов. *Электрические аппараты: Труды Куйбышевского политехнического института*. 1970;(2):145–150.
 28. Pedro A.A., Suslov A.P. Valve effect in an electrode furnace. *Tsvetnye metally*. 2012;(12):91–95. (In Russ.).
Педро А.А., Суслов А.П. Вентильный эффект в электродной печи. *Цветные металлы*. 2012;(12):91–95.
 29. Beloglazov I.I., Pedro A.A. On valve effect in an ore-thermal furnace. *Elektrometallurgiya*. 2016;(2):20–27. (In Russ.).
Белоглазов И.И., Педро А.А. О природе вентильного эффекта в рудно-термической печи. *Электрометаллургия*. 2016;(2):20–27.
 30. Sivtsov A.V., Tsymbalist M.M., Sheshukov O.Yu., Nekrasov I.V. A method for controlling the oxidation of slag and metal during the smelting of iron-based alloys in alternating current electric arc furnaces. Patent RF no. 2485185. MPK C21C 5/52, G01N 27/26. *Bulleten' izobretenii*. 2013;(17). (In Russ.).
Пат. RU 2485185. Способ контроля окисленности шлака и металла при выплавке сплавов на основе железа в электродуговых печах переменного тока / Сивцов А.В., Цымбалист М.М., Шешуков О.Ю., Некрасов И.В.; заявлено 13.09.2011; опубликовано 20.06.2013, Бюллетень № 17.
 31. Sivtsov A.V., Sheshukov O.Yu., Nekrasov I.V., Tsymbalist M.M., Egiazar'yan D.K., Orlov P.P. On some features of application of arc voltage constant component to control metal oxidation during steel refining. *Elektrometallurgiya*. 2020;(1):2–8. (In Russ.).
Сивцов А.В., Шешуков О.Ю., Некрасов И.В., Цымбалист М.М., Егизарьян Д.К., Орлов П.П. О некоторых особенностях применения постоянной составляющей напряжения дуги для контроля окисленности металла на стадии рафинирования стали. *Электрометаллургия*. 2020;(1):2–8.

32. Sivtsov A.V., Sheshukov O.Yu., Egiazar'yan D.K., Tsymbalist M.M., Lobanov D.A. Slag mode regulation in electric arc furnace based on electrical parameters control during melting oxidation period. *Izvestiya. Ferrous Metallurgy*. 2022;65(9):619–628. (In Russ.).
<https://doi.org/10.17073/0368-0797-2022-9-619-628>

Сивцов А.В., Шешуков О.Ю., Егиазарьян Д.К., Цымбалист М.М., Лобанов Д.А. Регулирование шлакового режима выплавки стали в электродуговой печи на основе контроля электрических параметров в ходе окислительного периода плавки. *Известия вузов. Черная металлургия*. 2022;65(9): 619–628. <https://doi.org/10.17073/0368-0797-2022-9-619-628>

Information about the Authors

Сведения об авторах

Andrei V. Sivtsov, Dr. Sci. (Eng.), Leading Researcher of the Laboratory of Technogenic Formations Problems, Institute of Metallurgy, Ural Branch of the Russian Academy of Sciences
ORCID: 0000-0002-7840-1088
E-mail: aws2004@mail.ru

Oleg Yu. Sheshukov, Dr. Sci. (Eng.), Chief Researcher, Institute of Metallurgy, Ural Branch of the Russian Academy of Sciences; Prof., Director of the Institute of New Materials and Technologies, Ural Federal University named after the first President of Russia B.N. Yeltsin
ORCID: 0000-0002-2452-826X
E-mail: o.j.sheshukov@urfu.ru

Denis K. Egiazar'an, Cand. Sci. (Eng.), Senior Researcher, Head of the Laboratory of Technogenic Formations Problems, Institute of Metallurgy, Ural Branch of the Russian Academy of Sciences; Assist. Prof. of the Chair of Metallurgy of Iron and Alloys of the Institute of New Materials and Technologies, Ural Federal University named after the first President of Russia B.N. Yeltsin
ORCID: 0000-0002-9833-7191
E-mail: avari@mail.ru

Mikhail M. Tsymbalist, Cand. Sci. (Eng.), Senior Researcher of the Laboratory of Pyrometallurgy of Reduction Processes, Institute of Metallurgy of Ural Branch of the Russian Academy of Sciences
ORCID: 0000-0002-9570-040X
E-mail: cherknimne@yandex.ru

Pavel P. Orlov, Cand. Sci. (Eng.), Engineer, Senior Lecturer of the Chair of Metallurgy of Iron and Alloys of the Institute of New Materials and Technologies, Ural Federal University named after the first President of Russia B.N. Yeltsin
ORCID: 0000-0003-4616-306X
E-mail: p.p.orlov@urfu.ru

Андрей Владиславович Сивцов, д.т.н., ведущий научный сотрудник лаборатории проблем техногенных образований, Институт металлургии Уральского отделения РАН
ORCID: 0000-0002-7840-1088
E-mail: aws2004@mail.ru

Олег Юрьевич Шешуков, д.т.н., главный научный сотрудник, Институт металлургии Уральского отделения РАН; профессор, директор Института новых материалов и технологий, Уральский федеральный университет имени первого Президента России Б.Н. Ельцина
ORCID: 0000-0002-2452-826X
E-mail: o.j.sheshukov@urfu.ru

Денис Константинович Егиазарьян, к.т.н., старший научный сотрудник, заведующий лабораторией, Институт металлургии Уральского отделения РАН; доцент кафедры металлургии железа и сплавов Института новых материалов и технологий, Уральский федеральный университет имени первого Президента России Б.Н. Ельцина
ORCID: 0000-0002-9833-7191
E-mail: avari@mail.ru

Михаил Михайлович Цымбалист, к.т.н., старший научный сотрудник лаборатории пирометаллургии восстановительных процессов, Институт металлургии Уральского отделения РАН
ORCID: 0000-0002-9570-040X
E-mail: cherknimne@yandex.ru

Павел Петрович Орлов, к.т.н., инженер, старший преподаватель кафедры металлургии железа и сплавов института новых материалов и технологий, Уральский Федеральный Университет им. Первого Президента России Б.Н. Ельцина
ORCID: 0000-0003-4616-306X
E-mail: p.p.orlov@urfu.ru

Contribution of the Authors

Вклад авторов

A. V. Sivtsov – general scientific guidance, conducting theoretical research, planning experiments, conducting industrial tests, writing the text.

O. Yu. Sheshukov – setting the research task, planning industrial tests, correcting and editing the article.

D. K. Egiazaryan – conducting laboratory research, discussing the results.

M. M. Tsymbalist – software for experimental research, conducting industrial tests.

P. P. Orlov – conducting laboratory research.

А. В. Сивцов – общее руководство исследованием, теоретические изыскания, планирование эксперимента, проведение промышленных испытаний, написание статьи.

О. Ю. Шешуков – постановка задачи исследований, планирование промышленных испытаний, корректировка и редактирование статьи.

Д. К. Егиазарьян – проведение лабораторных исследований, обсуждение результатов.

М. М. Цымбалист – программное обеспечение экспериментальных исследований, проведение промышленных испытаний.

П. П. Орлов – проведение лабораторных исследований.

Received 28.02.2024
Revised 09.04.2024
Accepted 19.06.2024

Поступила в редакцию 28.02.2024
После доработки 09.04.2024
Принята к публикации 19.06.2024

Над номером работали:

Л.И. Леонтьев, главный редактор

Е.В. Протопопов, заместитель главного редактора

Е.А. Ивани, ответственный секретарь

Л.П. Бащенко, заместитель ответственного секретаря

Е.Ю. Потапова, заместитель главного редактора по развитию

О.А. Долицкая, научный редактор

Е.М. Запольская, ведущий редактор


А.О. Гашникова, ведущий редактор

В.В. Расенец, верстка, иллюстрации

Г.Ю. Острогорская, менеджер по работе с клиентами

Подписано в печать 20.08.2024. Формат 60×90 ¹/₈. Бум. офсетная № 1.
Печать цифровая. Усл. печ. л. 14,25. Заказ 20334. Цена свободная.

Отпечатано в типографии Издательского Дома МИСИС.
119049, Москва, Ленинский пр-кт, д. 4, стр. 1.
Тел./факс: +7 (499) 236-76-17



Thermodynamic modeling of cobalt and nickel reduction using hydrometallurgical enrichment concentrates for steel alloying

Complex electron-ion-plasma surface modification of high-alloy stainless steel

Gradient of microhardness in the contact zone coating (HEA CoCrFeNiMn) – substrate (alloy 5083)

Phase composition and microstructure of intermetallic alloys obtained using electron-beam additive manufacturing

Low-cycle fatigue of welded joint from steel of X70 strength class

Influence of inhomogeneities in chemical composition and porosity of sintered steel on development of martensitic transformation

Physics of hardening of the rolling surface of rail head from hypereutectoid steel after operation

Effect of electric arc surfacing on the structure and properties of coatings

Molecular dynamics study of the influence of carbon impurity on austenite nanoparticles crystallization during rapid cooling

Thermodynamic aspects of WO_3 tungsten oxide reduction by carbon, silicon, aluminum and titanium

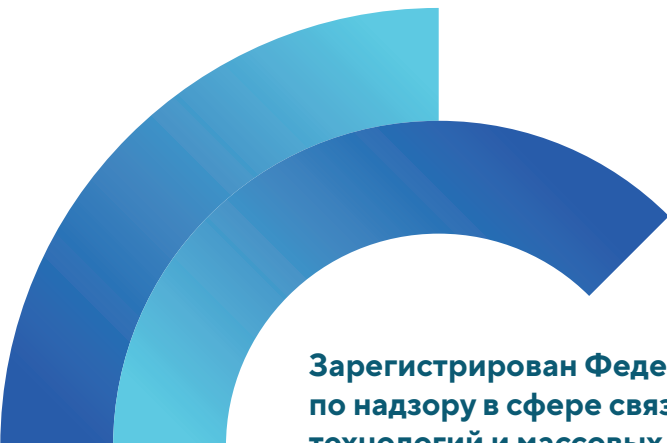
Stress state of billet – mandrel system during production of hollow steel billet in a unit of continuous casting and deformation. Part 2

Stress-strain state of ceramic shell mold during formation of spherical steel casting in it

Development of a methodology for determining the content of non-metallic inclusions in steel

Automated process control in electric arc furnaces in the aspect of digital twin technology

To the 90th Anniversary of Leonid Andreevich Smirnov



**Зарегистрирован Федеральной службой
по надзору в сфере связи, информационных
технологий и массовых коммуникаций.
Свидетельство о регистрации
ПИ № ФС77-35456.**

Подписной индекс 70383.

